Mixed oxygen ionic and electron conducting perovskite oxides:
issues and possible solutions

Von der Naturwissenschaftlichen Fakultät

der Gottfried Wilhelm Leibniz Universität Hannover

zur Erlangung des Grades

Doktor der Naturwissenschaften

Dr. rer. nat.

genehmigte Dissertation

von

Dipl.-Chem. Konstantin Efimov

geboren am 29. März 1980 in Iwanowo (Russland)

2011

Referent: Priv.-Doz. Dr. Armin Feldhoff

Korreferent: Prof. Dr. Klaus-Dieter Becker

Tag der Promotion: 29.09.2011

Abstract

Alkaline-earth and cobalt-based perovskite oxides stand out in the family of mixed oxygen ionic and electron conducting (MIEC) materials as a result of their extraordinary transport properties. These cubic perovskites are renowned for their potential applications toward oxygen separating membranes used in membrane reactors, as well as for cathodes in solid-oxide fuel cells. However, their reliable use can be hindered by phase decomposition of the cubic perovskite structure at intermediate temperatures (773-1073 K), as well as poor chemical stability in the presence of CO_2. Within the scope of the presented thesis, both of these major issues were extensively studied. Seven original research articles were produced during the course of this work, including a discussion of how these problems can be solved.

In chapter 2, the decomposition process of $(Ba_{0.5}Sr_{0.5})(Co_{0.8}Fe_{0.2})O_{3-\delta}$ and $(Ba_{0.8}Sr_{0.2})(Co_{0.8}Fe_{0.2})O_{3-\delta}$ at temperatures below 1173 K was elucidated using powder X-ray diffraction (XRD) and various transmission electron microscopy (TEM) techniques. Transformation of the cubic perovskite structure into hexagonal or hexagon-related perovskite phases was observed in both systems. This process was driven by a combined valence and spin-state transition of cobalt cations, leading to considerable diminution of their effective ionic radii. Large effective ionic radii are not tolerated in cubic perovskite structures that contain large barium and strontium cations.

Hence, the cubic perovskite structure of alkaline earth-based perovskite at intermediate temperatures can be stabilized by the substitution of cobalt with iron in the crystal lattice. This aspect is discussed in chapter 3 via the introduction of a novel cobalt-free perovskite material $(Ba_{0.5}Sr_{0.5})(Fe_{0.8}Cu_{0.2})O_{3-\delta}$. Apart from its excellent phase stability at relevant temperatures, the $(Ba_{0.5}Sr_{0.5})(Fe_{0.8}Cu_{0.2})O_{3-\delta}$ membrane exhibits the highest oxygen permeation flux of known cobalt-free materials so far.

Chapter 4 summarizes the effect of CO_2 on $(Ba_{0.5}Sr_{0.5})(Fe_{0.8}Zn_{0.2})O_{3-\delta}$ and $Ba(Co_xFe_yZr_z)O_{3-\delta}$ perovskites, which were developed as an alternative to cobaltites because of their enhanced phase stability at intermediate temperatures and because of their desirable thermo-mechanical properties. It was found that the oxygen permeation performance of both membrane materials broke down completely in the presence of CO_2. Furthermore, the perovskites were partially decomposed into carbonates and distorted perovskite phases after contact with CO_2, which was accompanied by the segregation of zinc or cobalt, respectively, as confirmed through (*in-situ*) XRD and TEM investigation. It was also discovered that the oxygen permeation and membrane microstructures were fully recovered under CO_2-free conditions.

The assumption that calcium-containing, perovskite-like $(La_{0.6}Ca_{0.4})(Co_{0.8}Fe_{0.2})O_{3-\delta}$ and $(La_{0.6}Ca_{0.4})FeO_{3-\delta}$ may provide CO_2-stable membrane materials, owing to the lower thermodynamic stability of calcium carbonate compared with barium- and strontium-carbonate, is discussed and finally confirmed in chapter 5. An alternative approach to overcome CO_2-intolerance lies in the concept of alkaline-earth free dual-phase membranes. This concept is also presented in chapter 5. Membranes containing 40 wt. % $NiFe_2O_4$, as the electronic conductor, and 60 wt. % $Ce_{0.9}Gd_{0.1}O_{2-\delta}$, as the electrolyte, can be considered promising materials for applications that require the presence of CO_2.

ii

Zusammenfassung

Oxide mit Perowskitstruktur, die Erdalkalimetalle sowie Cobalt enthalten, ragen aufgrund ihrer außergewöhnlichen Transport-Eigenschaften in der Klasse der gemischt Sauerstoff-Ionen und elektronenleitenden Materialien heraus. Allerdings wird ihre großtechnische Anwendung, z.B. in Membranreaktoren oder als Kathode in Fest-Oxid Brennstoffzellen, erschwert, da sich die kubischen Perowskit Strukturen im mittleren Temperaturbereich (773-1073 K) zersetzen. Desweiteren zeigen Erdalkalimetall-haltige Oxide eine schlechte chemische Stabilität gegenüber CO_2. Im Rahmen der vorgelegten Dissertation werden die genannten Problemstellungen sowie mögliche Lösungsansätze intensiv diskutiert, woraus sieben Forschungsarbeiten resultierten.

In Kapitel 2 wird der Zersetzungsprozess, der unterhalb von 1173 K eintritt, von $(Ba_{0.5}Sr_{0.5})(Co_{0.8}Fe_{0.2})O_{3-\delta}$ und $(Ba_{0.8}Sr_{0.2})(Co_{0.8}Fe_{0.2})O_{3-\delta}$ mit Hilfe der Röntgenpulverdiffraktometrie (XRD) und der Transmissionselektronenmikroskopie (TEM) untersucht. In beiden Systemen findet eine Umwandlung in hexagonale oder hexagonal verzerrte Phasen statt. Triebkraft dieser Umwandlung ist ein gekoppelter Valenz- und Spinübergang der Cobaltkationen, wodurch der Ionenradius verringert wird, was durch die kubische Perowskitstruktur nicht toleriert wird.

Die kubische Perowskitstruktur kann im mittleren Temperaturbereich stabilisiert werden, indem Cobalt durch Eisen ersetzt wird. Dies wird in Kapitel 3 anhand des neuen Cobalt-freien Perowskitmaterials $(Ba_{0.5}Sr_{0.5})(Fe_{0.8}Cu_{0.2})O_{3-\delta}$ gezeigt. Neben exzellenter Stabilität im relevanten Temperaturbereich, weist die $(Ba_{0.5}Sr_{0.5})(Fe_{0.8}Cu_{0.2})O_{3-\delta}$ Membran den höchsten Sauerstofffluss aller bekannten Cobalt-freien Materialien auf.

Kapitel 4 behandelt den Einfluss von CO_2 auf die Perowskite $(Ba_{0.5}Sr_{0.5})(Fe_{0.8}Zn_{0.2})O_{3-\delta}$ und $Ba(Co_xFe_yZr_z)O_{3-\delta}$. Diese wurden als Alternative zu Cobaltiten entwickelt, da sie erhöhte Phasenstabilität im mittleren Temperaturbereich sowie verbesserte thermomechanische Eigenschaften besitzen. In Anwesenheit von CO_2 jedoch brach die Sauerstoffionenleitfähigkeit beider Membranmaterialien komplett ein. (*In-situ*) XRD sowie TEM Untersuchungen zeigten, dass sich die Perowskite unter CO_2-Einwirkung teilweise in Carbonate und verzerrte Perowskitphasen zersetzten. Unter CO_2-freien Bedingungen wurden die Mikrostruktur und die Sauerstoffionenleitfähigkeit beider Membranen vollständig regeneriert.

In Kapitel 5 wird die Annahme bestätigt, dass die Calcium-haltigen Perowskite $(La_{0.6}Ca_{0.4})(Co_{0.8}Fe_{0.2})O_{3-\delta}$ und $(La_{0.6}Ca_{0.4})FeO_{3-\delta}$ CO_2-stabil sind, was auf die schlechtere thermodynamische Stabilität von Calciumcarbonat gegenüber Barium- und Strontiumcarbonat zurückgeführt werden kann. In diesem Kapitel wird zusätzlich das Konzept Erdalkali-freier Dual-Phasen Membranen vorgestellt, um dem Problem der CO_2-Intoleranz zu begegnen. Das Material mit der neuen Zusammensetzung aus 40 Gew.-% $NiFe_2O_4$ (Elektronenleiter) und 60 Gew.-% $Ce_{0.9}Gd_{0.1}O_{2-\delta}$ (Elektrolyt) kann in Anwendungen unter CO_2-haltiger Atmosphäre als besonderes vielversprechend angesehen werden.

Preface

The presented thesis summarizes the results, which were achieved in the past three years during my work as scientific co-worker at the Institut für Physikalische Chemie und Elektrochemie of the Gottfried Wilhelm Leibniz Universität Hannover. Financial support for this work was granted by the department chair Prof. Dr. Jürgen Caro, by the Deutsche Forschungsgemeinschaft (DFG, Grant FE 928/ 1-2), as well as from the State of Lower Saxony (Germany, NTH bottom-up project, No. 21-71023-25-7/09) under the guidance of Priv. Doz. Dr. Armin Feldhoff.

Seven selected research articles are presented within this thesis; I am the first author in four of these papers. The following statements assign my contributions to the articles included in this thesis. For all articles, I greatly acknowledge the beneficial encouragement of my co-authors, in particular from Priv. Doz. Dr. Armin Feldhoff and Prof. Dr. Jürgen Caro.

The two articles presented in chapter 2 deal with the inherent phase instability of $(Ba_{0.5}Sr_{0.5})(Co_{0.8}Fe_{0.2})O_{3-\delta}$ (BSCF) and $(Ba_{0.8}Sr_{0.2})(Co_{0.8}Fe_{0.2})O_{3-\delta}$ perovskites at temperatures below 1173 K. In the first article, entitled *TEM study of BSCF perovskite decomposition at intermediate temperatures*, experimental investigations and data interpretation were carried out by me. I appreciate the collaboration of Dr. Qiang Xu from TU Delft (Netherlands), who provided me with the opportunity to work with an FEI Titan transmission electron microscope (TEM), according to the 026019 ESTEEM integrated infrastructure initiative from the European Union. The second article in this assembly, *Oxygen-vacancy related structural phase transition of $Ba_{0.8}Sr_{0.2}Co_{0.8}Fe_{0.2}O_{3-\delta}$*, was written by Dr. Zhèn Yáng from ETH Zurich (Switzerland). I am very glad to have contributed to this publication, which includes refinements of the X-ray diffraction (XRD) patterns for this material and the interpretation of data achieved from the XRD and TEM investigations.

The experimental work for the article *A long-term stable cobalt-free oxygen-permeable perovskite-type membrane* in chapter 3 was conducted by the competent student apprentice Torben Halfer and me in equal shares. I carried out the data interpretation and manuscript preparation for this study. I would like to thank Dipl.-Chem. Alexander Kuhn for electrical conductivity measurements and Prof. Dr. Paul Heitjans for fruitful discussions.

Chapter 4 provides an understanding of studies concerning the poisoning effect of CO_2 on $Ba(Co_xFe_yZr_z)O_{3-\delta}$ (BCFZ) and $(Ba_{0.5}Sr_{0.5})(Fe_{0.8}Zn_{0.2})O_{3-\delta}$. The article *In-situ X-ray diffraction study of carbonate formation and decomposition in perovskite-type BCFZ* arose from the successful and very pleasant cooperation of my colleague Dr. Oliver Czuprat, who carried out oxygen permeation experiments on BCFZ hollow fiber. I performed *in-situ* XRD and TEM investigations, as well as the data analysis and manuscript development for this work. Within the second article, *Performance of zinc-doped perovskite-type membranes at intermediate temperatures for long term oxygen permeation and under carbon dioxide atmosphere*, I carried out scanning electron microscopy (SEM) and TEM examinations. Furthermore, Dr. Lars Robben from the Institut für Mineralogie of the Gottfried Wilhelm

Leibniz Universität Hannover and I conducted the XRD measurements and data interpretation in similar shares. I am grateful to Dr. Julia Martynczuk for writing the manuscript and for her cooperation during this research.

The last two articles in chapter 5 introduce CO_2-tolerant, mixed oxygen-ionic and electron-conducting materials (MIEC). I am the first author for the publication entitled *Ca-containing CO_2-tolerant perovskite materials for oxygen separation*. I express gratitude to my colleagues Dipl.-Chem. Tobias Klande and MSc. Nadine Juditzki, who supported me by carrying out membrane fabrication and oxygen permeation flux measurements.

The article *CO_2-stable and cobalt-free dual-phase membrane for oxygen separation* was written by my esteemed colleague MSc. Huixia Luo. My contribution to this publication was in conducting the XRD investigations for this work, as well as performing *in-situ* XRD experiments in different gaseous atmospheres. Additionally, I provided data interpretation and manuscript preparation support.

Contents

1 Introduction

1.1 Motivation

The global consumption of energy continues to rise steadily, while global energy resources are becoming more and more restricted. Because of the increasing world population and economic growth of developing countries, the energy supply problem will become an acute challenge in the near future. Furthermore, about 80% of the world currently uses energy that is produced from fossil fuels [1]. This use may lead to incalculable consequences for the environment, like global climate change. Hence, a challenge of material sciences-oriented chemistry research is to develop materials that transform the present technical processes into more energy-saving and environmentally friendly methods, as well as to invent novel and energy-efficient procedures. A class of materials that could meet these requirements is mixed oxygen ionic and electron conducting (MIEC) ceramics that are based on complex oxides with perovskite or perovskite-related structures.
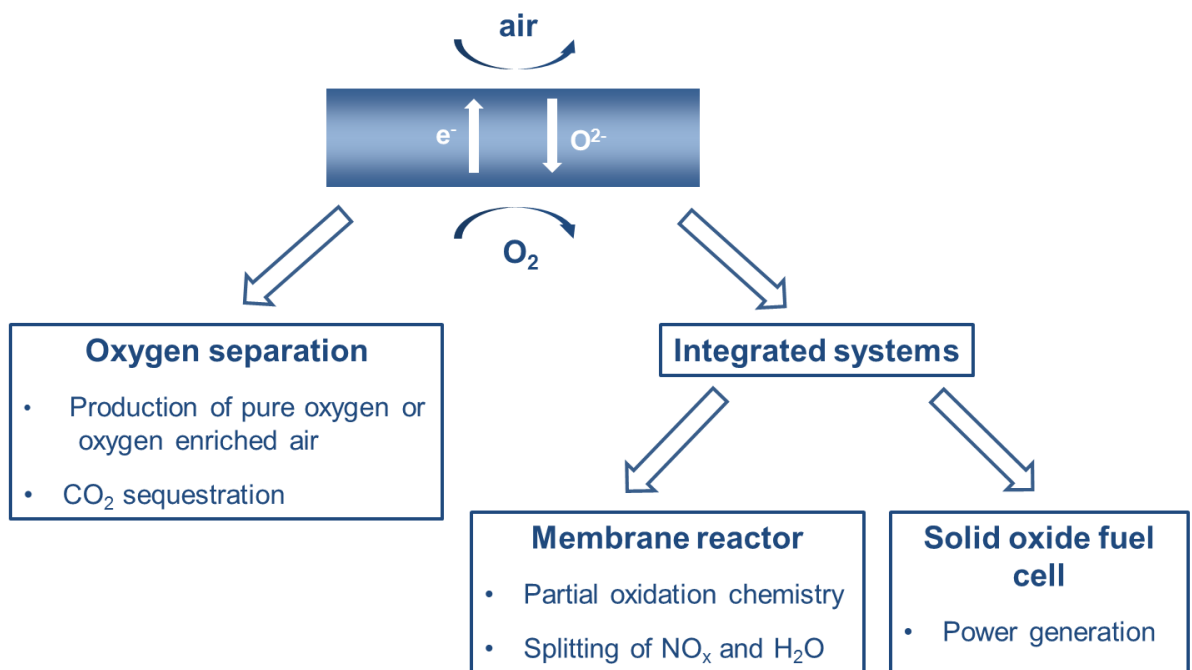
Figure 1.1: Application fields of MIEC membrane materials.

Over the last two decades, MIEC ceramics have gained a lot of attention in industry and from academia as a result of their versatile application potential as membrane materials [2]. Owing to their ability to separate oxygen from gas mixtures with infinite selectivity, MIEC membrane materials with a perovskite structure can be applied in many industrial processes where a constant supply or removal of oxygen is required [8]. Figure 1.1 summarizes exemplary application fields of MIEC materials, when used as membranes and as crucial components of integrated systems. Recently, MIEC membranes

have gained additional interest because of their potential application for CO_2 capture in the oxygen supply of power stations, according to the pre-combustion and oxyfuel concepts [9]. Both processes utilize air separation to obtain pure oxygen prior to fuel combustion. In pre-combustion, pure oxygen is used to perform a CO-CO_2 shift reaction [10]. On the other hand, in the oxyfuel process, fuel is burned with nitrogen-free oxygen, which allows ideal capturing of the CO_2 as a single product after steam condensation [11,12].

Furthermore, the MIEC perovskites can be used in membrane reactors that are integrated with a catalyst. This method enables combination of the chemical reaction and product separation steps in one device unit. This process results in energy and raw materials savings, as well as in reduced costs [13]. Important catalytic processes, such as partial oxidation and oxidative dehydrogenation of hydrocarbons, as well as the splitting of nitrogen oxides and water, can be successfully carried out in MIEC perovskite-based membrane reactors [14-17].
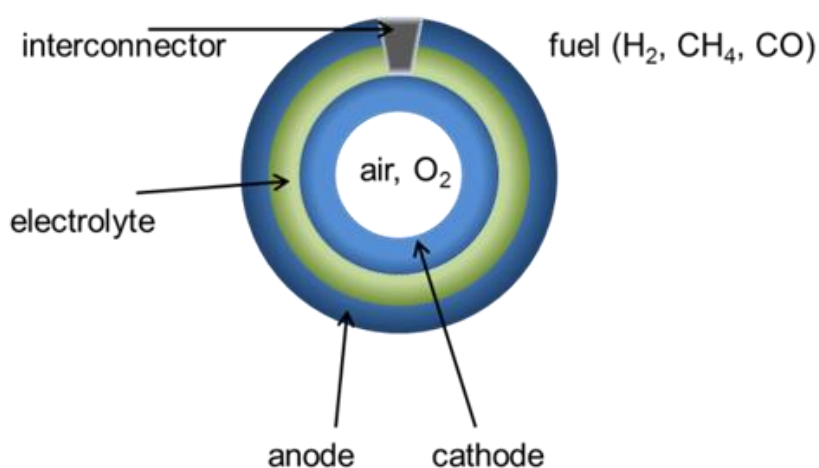
Figure 1.2: *Schematic of a solid oxide fuel cell with the Siemens–Westinghouse tubular design [13].*

Solid oxide fuel cells (SOFCs) can be considered one of the most important fields of application for MIEC materials [13,14]. The main advantage of fuel cells is their ability to convert chemical energy directly into electricity, resulting in higher efficiency energy production compared with conventional methods [15]. A fully ceramic SOFC that is operated in the temperature range 773-1273 K can utilize hydrogen, natural gas, or hydrocarbons without the Carnot limitation [16]. Figure 1.2 schematically illustrates an SOFC with a tubular design, which consists of MIEC electrodes, a ceramic electrolyte, and an interconnector. The electrodes are separated by gas-tight electrolytes. The oxygen in the oxidant is reduced into ions at the cathode side and incorporated in the cathode material, because of its MIEC properties. The oxygen ions are then transported through the electrolyte, which is an ionic conductor, to the anode side. At this location, oxygen ions combine with the fuel in a cold combustion process. The electrons, which form during this oxidation reaction, will be routed via an interconnector back to the cathode side, where further reduction of oxygen takes place. Thus, electrical power can be generated using the cell. A key factor for the performance of an SOFC lies in its high catalytic activity for oxygen reduction and high electrical conductivity of the cathode material [17]. Because some

perovskite ceramics exhibit good oxygen reduction properties, as well as high oxygen ionic and electrical conductivities, they can be considered promising SOFC cathode materials.

The pioneering work of Teraoka et al. in the 1980s initiated extensive investigations into MIEC materials by many research groups around the world up to the present time [18,19]. During this time, a number of materials were developed that may be applied in the aforementioned industrial processes [20]. However, some general issues were also revealed that hindered the final breakthrough of MIEC materials. These problems often related to the high operating temperatures of devices that contain MIEC components, like SOFC and membrane reactors. Conventionally, SOFCs are usually operated at temperatures around 1273 K. This high operating temperature is required to improve the electrode reaction kinetics. However, among other things these temperatures can lead to interfacial reactions between the electrolyte, electrode, and interconnector, as well as induce crack formation owing to different degrees of thermal dilatation in the cell components [21]. In MIEC-based membrane reactors, the high operating temperatures are responsible for interactions during the catalytic partial oxidation of hydrocarbons by thermal cracking, coking, and dehydrogenation of educts, apart from the poor thermomechanical stability of the reactor [22]. By reducing the operating temperatures into the so-called intermediate range, between 773 and 1073 K, some of these issues can be avoided. At lower temperatures, however, the traditional MIEC materials (e.g., strontium-doped lanthanum manganite) are unsuitable because of their poor transport properties [23,24]. Thus, alternative materials exhibiting sufficiently high oxygen-ion and electron conductivities at intermediate temperatures are needed.

In the year 2000, Shao et al. developed a novel perovskite material with compositions of $(Ba_{0.5}Sr_{0.5})(Co_{0.8}Fe_{0.2})O_{3-\delta}$ (BSCF). These materials exhibited superior oxygen transport behavior accompanied by excellent short-time phase stability over a wide temperature range under both high and low oxygen partial pressures [25]. Since that time, BSCF perovskite has been investigated in detail regarding its application as a material for ceramic oxygen separation membranes and membrane reactors [26-29]. More recently, Shao and Haile have reported the high power density of a symmetric single SOFC using BSCF as the electrode and a samaria-doped ceria (SDC) electrolyte, due to the very low polarization resistance of the cathode at temperatures between 773 and 873 K [31,32]. Since then, BSCF perovskite has been considered one of the most promising cathode materials for use in SOFCs that are operated in the intermediate temperature regime (IT-SOFC) [32].

Unfortunately, the wide application of BSCF may be hindered by two major problems. The first regards the inherent phase instability of BSCF perovskite at temperatures below 1023 K, as discussed in detail in section 1.5.1 [33]. The second serious issue, which also applies to the majority of barium- and strontium-containing perovskite materials, is the poisoning effect of CO_2 on the perovskite, due to the high potential of A-site cations to form carbonates [34]. The intolerance toward CO_2 may inhibit the use of the membrane materials in the CO_2 capture processes or in the partial oxidation of hydrocarbons, where some CO_2 is formed as the by-product of an undesired deeper oxidation. Moreover, the applications in IT-SOFC can also be threatened by the presence of small amounts of CO_2 in the air due to the high thermodynamic stability of corresponding barium and strontium carbonates at lower temperatures (see also section 1.5.2).

In the presented thesis, issues including the inherent phase instability of cobalt-based perovskite at intermediate temperatures and the instability against CO_2 of barium- and strontium-containing

perovskite are addressed. Chapter 2 presents a detailed study of the phase transition of high-performance perovskite $(Ba_{0.5}Sr_{0.5})(Co_{0.8}Fe_{0.2})O_{3-\delta}$ (BSCF) and $(Ba_{0.8}Sr_{0.2})(Co_{0.8}Fe_{0.2})O_{3-\delta}$ at relevant temperatures. Chapter 3 introduces a novel cobalt-free perovskite material $(Ba_{0.5}Sr_{0.5})(Fe_{0.8}Cu_{0.2})O_{3-\delta}$, which exhibits excellent phase stability that leads to constant and desirable functional properties over intermediate temperature ranges. In Chapter 4, the stability of $(Ba_{0.5}Sr_{0.5})(Fe_{0.8}Zn_{0.2})O_{3-\delta}$, $Ba(Co_xFe_yZr_z)O_{3-\delta}$ (x+y+z = 1) perovskites, developed as an alternative to BSCF, in CO_2-containing atmospheres is discussed. Finally, Chapter 5 discusses MIEC materials that have a high tolerance toward CO_2.

1.2 Perovskite oxide structure

1.2.1 Ideal cubic perovskite structure

The mineral $CaTiO_3$ is an eponym for perovskite-type oxides. This mineral was discovered during the expedition of Alexander von Humboldt in the Ural Mountains in the year 1829 and was named in honor of Count Lev Alexeyevich Perovsky, who at that time was a local politician and sponsor of mineralogy science [35,36].

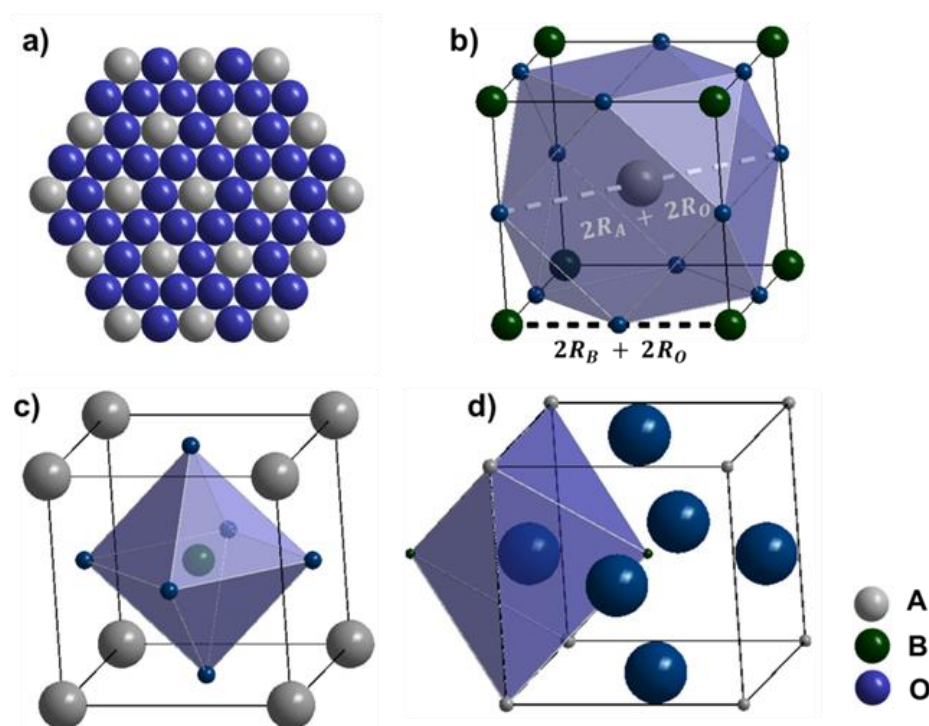**Figure 1.3**: *a) A hexagonal close-packed layer of O anions and A-site cations in the ABO₃ structure. b) Unit cell of the ABO₃ perovskite structure showing the AO₁₂ polyhedron. Alternative representations of the cubic perovskite structure showing c) octahedral coordination by B-site cations and d) coordination of O anions by two apical B cations and four coplanar A cations. The radii of ions are not drawn to scale.*

Ideal perovskite oxides have the general formula ABO_3, in which A is a large cation (alkaline, alkaline-earth, or rare earth cation) and B is a small or middle-sized cation (mostly transition metals). The O^{2-} anions, with one quarter of these replaced by A cations in an ordered way, form a cubic close-packed array of hexagonal layers that are perpendicular to the body diagonals of the cubic cell and have the stacking sequence **ABC**. Figure 1.3a shows the lay-out of one close-packed hexagonal layer. The A cations are surrounded by twelve anions as an integral part of the close packing (Figure 1.3b). The small B cations occupy one quarter of the octahedral interstices in the cubic close-packed arrays (Figure 1.3c). The O^{2-} anions are also octahedrally coordinated by two apical B cations and four coplanar A cations (Figure 1.4 d). The ideal cubic perovskites, having the cell parameter a_p, adopt the space group $Pm3m$ (No.: 221). The B cation is located at the origin of the unit cell with atomic coordinates 0,0,0 (Wyckoff position 1*a*). The A cation is situated at coordinates 1/2,1/2,1/2 (Wyckoff position 1*b*) and the O^{2-} anion is located at 1/2,0,0 (Wyckoff position 3*d*) [37].

In the year 1926, Goldschmidt considered perovskite to be an ionic compound that consisted to a first approximation of hard spheres with ionic radii R (Å). He also declared that the A-site cations exactly fit the twelvefold site if the A cations have the same size as the anions. Correspondingly, the edge of the ideal cubic cell (shown in Figure 2.1b), which can be described as $2R_B + 2R_O$, is equal to $2^{1/2}$ times the length of a line joining O-A-O ($2R_A + 2R_O$), according to the concept of closest packing and the Pythagorean theorem. In real structures, the A, B and X cations have different sizes. As a result, Goldschmidt modified this relationship by a parameter known as the tolerance factor *t*:

$$t = \frac{R_O + R_A}{2^{1/2}(R_O + R_B)} \tag{1}$$

Thus, for ideal cubic perovskite t, is unity. The tolerance factor should be considered a rough guide to whether the ABO_3 compound will crystallize in the cubic perovskite structure. This crystallization is due to partly covalent bonding, as well as to the stabilizing effect of a cubic symmetry. Despite this crystallization, adoption of $Pm3m$ the space group can be expected with *t* values in the range 0.9-1.05 [38].

1.2.2 Distorted perovskite structure

The majority of ABO_3 compounds, including the mineral $CaTiO_3$, exhibit lower symmetries than the ideal cubic perovskite structure. However, Megaw has proposed to include these structures in the term *perovskite-type* structure. These compounds maintain a pseudo-cubic cell that is derived from an ideal structure that has a small deformation of the cell parameters or interaxial angles [39].

The geometrical approach of the Goldschmidt tolerance factor based on ionic radii is considered to be an approved method to predict whether a given package of ions will arrange in the distorted perovskite-type structure. In this context, the source for reliable ionic radii is especially significant. For this purpose, Shannon carried out an extraordinary series of experiments to establish a set of empirical ionic radii while considering the valence, spin-state and coordination of corresponding ions [40,41]. Table 1.1 lists the effective radii of relevant cations in perovskite-type oxides, which are based on an oxygen-ion radius of 140 pm, and includes the effects of partially covalent metal-oxygen bonding. Obviously, only the Sr^{2+} cation provides a close match with the twelvefold A-site. Occupation

of the A-site with smaller cations (e.g., Ca^{2+} and La^{3+}) or bigger cations (e.g., Ba^{2+}) may lead to distortion of the cubic perovskite structure.

Table 1.1: *Effective ionic radii of some cations based on $r(O^{2-}) = 140$ pm from [40,41]. The radii of A- and B-site cations are provided according to twelvefold and sixfold coordinations, respectively. For cobalt and iron, the spin state is considered by providing values for the low-spin* ‖ *high-spin configuration.*

A-site cations	Ionic radius / pm	B-site cations	Ionic radius / pm	
Ba^{2+}	161	Co^{2+}	65 ‖	74.5
Sr^{2+}	144	Co^{3+}	54.5 ‖	61
Ca^{2+}	135	Co^{4+}	53	
La^{3+}	136	Fe^{2+}	61 ‖	78
		Fe^{3+}	55 ‖	64.5
		Fe^{4+}	58.5	
		Cu^{2+}	73	
		Cu^{3+}	54	
		Zn^{2+}	74	
		Ti^{4+}	60.5	
		Zr^{4+}	72	

The most common type of distortion was found to be a tilting and/or rotation of the BO_6 octahedron [42-45]. In the ideal cubic perovskite, the A-site cation is surrounded by eight regular BO_6 octahedra, which share all of their corners with neighboring octahedra, as shown in Figure 1.4a. All A-O bonds in the twelvefold site are equal. When the A-site cations in real perovskite are undersized, resulting in $t < 1$, the lengths of some A-O bonds will be contracted, leading to a tilt of the BO_6 octahedra. Consequently, the correlated tilting of surrounding octahedra results in a change of the A-site coordination, as well as a reduction in symmetry from the $Pm3m$ space group. Glaser suggests a description of the tilt systems in terms of rotations of BO_6 octahedra about three orthogonal Cartesian axes, which are conformable with three axes of the pseudo-cubic unit cell. The type of rotation is specified as a, b, and c degrees. The sense of the rotation of sequenced octahedra layers perpendicular to the rotation axis is defined via superscript, whereby a positive superscript means that neighboring octahedra are tilted in the same direction and a negative superscript indicates the opposite tilt of octahedra in successive layers [42].

Using crystallographic principles, Glaser identified 23 possible tilt systems arising via the rotation of octahedra [42]. Howard and Stokes, however, reduced that number to 15 space groups, which can be observed in the real perovskites according to group theory [46]. Apart from cubic structures, the orthorhombic and rhombohedral distorted perovskite systems, as described in detail below, are relevant for this thesis.

Figure 1.4b illustrates the structure of orthorhombic perovskite produced by a $a^+ b^- b^-$ tilt of the octahedral and leading to symmetry in the $Pnma$ space group [42]. The unit cell of orthorhombic perovskite can be transformed from a cubic unit cell with cell edge length a_p using a geometrical relationship [47]:

$$a \approx c \approx 2^{1/2}a_p, \; b \approx 2a_p \tag{2}$$
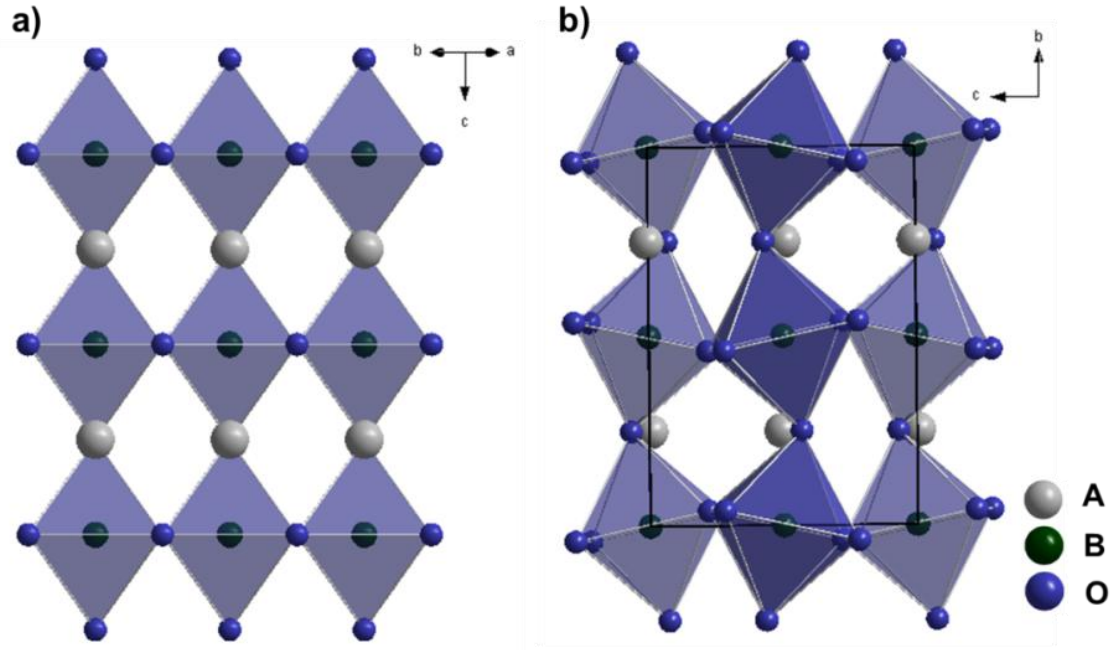
Figure 1.4: *Perspective view of a) an ideal cubic structure and b) an orthorhombic perovskite structure with $a^+ b^- b^-$ a tilt system of BO$_6$ octahedra.*

Thereby, the number of formula units per unit cell Z increases from unity for a cubic cell to $Z = 4$. The dimension of the orthorhombic strain of this perovskite structure can then be evaluated using the orthorhombicity parameter, as defined by [48]:

$$\sigma = 2(a - c)/(a + c) \tag{3}$$

The rhombohedral distortion arises through a $a^- a^- a^-$ tilt, which is equivalent to the rotation of octahedra about the body diagonal of a pseudo-cubic cell [42,44]. The relationship of the rhombohedral cell to the cubic cell can be depicted using a hexagonal setting:

$$a_H \approx 2^{1/2}a_p; \; c_H \approx 2 \cdot 3^{1/2}a_p; \; Z = 6 \tag{4}$$

Figure 1.5a,b schematically depicts how the ideal perovskite structure (tilt system $a^0 a^0 a^0$) transforms to the rhombohedral configuration due to rotation of the octahedra. Thus, the parameter of rhombohedral rotation ω can be determined directly from c-axis projection of the hexagonal unit cell (Figure 1.5b) or calculated from the cell parameters using the relationship [47]:

$$\frac{c_H}{a_H} = \frac{6^{1/2}}{cos\omega} \tag{5}$$
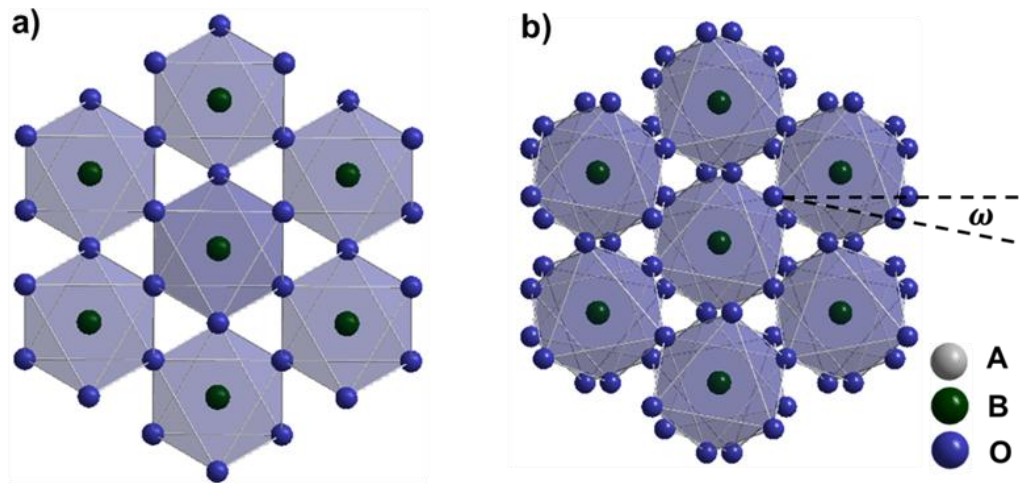
Figure 1.5*: Transformation of cubic perovskite (a) to rhombohedral perovskite by rotation of octahedra about a triad [1,1,1] cubic axis with the angle ω.*

Apart from its chemical composition, the degree of octahedral framework tilt in distorted perovskite is strongly affected by the temperature. In general, increasing temperature leads to a decrease in tilt angle and leads, as a final consequence, to a transition into a cubic structure [47].
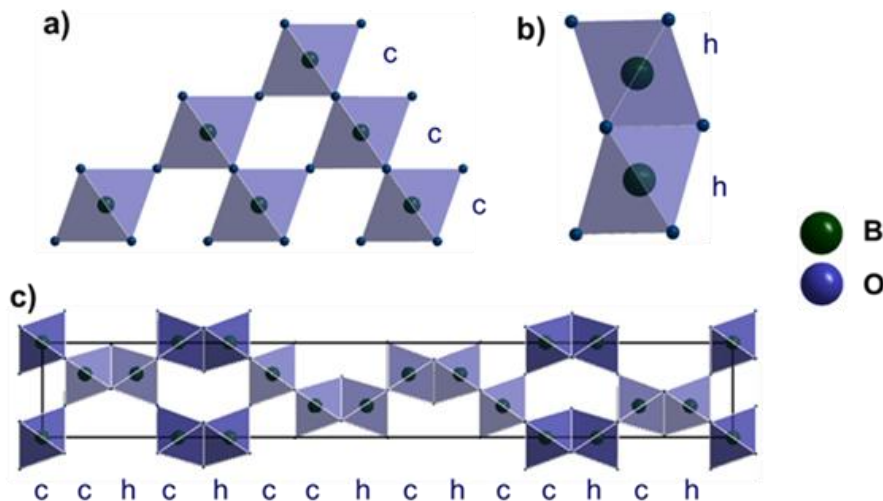
Figure 1.6*: a) Cubic perovskite structure viewed along [1,1,0] axis showing the 3C stacking sequence of BO_6 octahedra. b,c) Projections along [0,1,0] axis of hexagonal perovskite polytypes showing b) 2H and c) 15R stacking sequence of BO_6 octahedra.*

The hexagonal modification of perovskite structures, which typically forms when the A-site cation is too large and/or B-site cation is too small for an ideal cubic structure (*i.e.*, $t > 1$) cannot be derived

from a tilting of the BX_6 octahedra [47]. The structure of hexagonal perovskites also consists of close-packed AO_3 layers, as in a cubic structure; whereas, the layers are arranged in hexagonal close-packing with the stacking sequence **AB** [49,50]. In this structure, BO_6 octahedra share faces and form chains along the hexagonal axis, resulting in shortened B-O and B-B bond lengths. Figure 1.6a,b illustrates the structural characteristics of ideal cubic and hexagonal perovskites in terms of cubic-stacking of AO_3 layers, which leads to corner-sharing octahedra (3C polytype), and hexagonal-stacking, which leads to face-sharing octahedra (2H polytype), respectively. Between the two ideal stacking schemes, a large number of packing structures that contain both corner-sharing (denoted by *c*) and face-sharing octahedra (denoted by *h*) can be observed in the same perovskites oxides when the Goldschmidt tolerance factor is greater than unity [49]. The 15R hexagonal polytype, which plays an important role in Section 2.2, consists of close-packed layers arranged in a (*cchch*)$_3$ stacking sequence, as shown in Figure 1.6c [51].

1.3   Preparation of perovskite oxide membranes

1.3.1 Sol-gel process

Starting materials for the processing of dense MIEC ceramics are usually perovskite oxides that are in powder form. Diverse methods exist for the synthesis of ceramic powders, which can be subdivided in solid-state reactions, liquid precursor methods, and vapor phase reactions. The liquid-phase method, as for the sol-gel process, is thereby the most appropriate for preparation of highly pure and homogenous perovskite materials with complex compositions [52]. For this reason, most perovskite materials discussed in this thesis were fabricated using the sol-gel method. Figure 1.7 displays a flow chart of the sol-gel synthetic procedure [53,54].
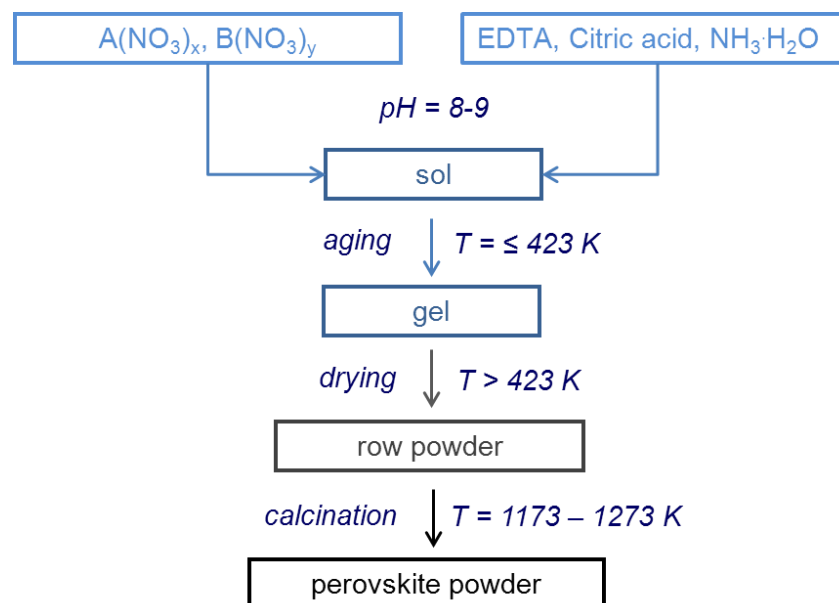
Figure 1.7: A schematic of sol-gel synthetic route in order to prepare perovskite oxides.

The first step of a sol-gel process is the preparation of a sol, which contains highly dispersed solid particles in the size range of 1-100 nm in water or organic solution. In our practical case, the sol was prepared by adding solutions of metal nitrates in water in stoichiometric amounts, allowing very fine intermixing of the educts following supplementation of the organic ligands and network formers. Owing to its high complex formation ability with almost any metal cation, ethylene-diamine-tetraacetic acid (EDTA) was used as the organic ligand [55]. The citric acid was added to the solution as a network former to prevent the segregation and precipitation of metal compounds during transformation of the sol into a gel. A gel is a viscous substance that contains three-dimensional, metal-organic, polymer networks with a very fine distribution of metal cations. This gel forms after the aging or heat treatment of the sol. During drying of the gel at temperatures above 423 K, the predominant portion of the organic component decomposes, leading to the formation of a dispersed mixture that consists of nano-scale metal oxides and carbonates as precursors for further reactions [53,54]. The amorphous powder mixture is then transformed into the desired perovskite via calcination at temperatures in the range of 1123-1223 K. In this process, a solid state reaction between metal oxides and carbonates leads to the formation of the perovskite [56].

1.3.2 Solid state reactions

The solid state reaction is initialized by formation of a product layer on the contact surface between the educts, when the free enthalpy of the system is reduced. Consequently, the product layer separates the educts from each other. Further reaction involves mass transport through the contact zone and product layer, as promoted by the presence of a chemical potential gradient between the phase boundaries [57]. The growth of product is controlled by reaction on the contact zone with a sufficiently low thickness of product layer. In this case, the reaction rate can be described as lineal low, where x is the product layer thickness and t is the time:

$$x \sim t \tag{6}$$

With an increase in product layer thickness, the mass diffusion becomes a rate-limited step. Thus, the growth of the product phase follows a parabolic law, to a first approximation [58-60]:

$$x \sim t^{1/2} \tag{7}$$

Although the solid state reactions are exothermic, owing to low reaction entropy values, high temperatures are required for the activation of a solid state process. Temperatures in the range of 973-1273 K initiate the contact zone reactions and increase the diffusion coefficients of the compounds D_i:

$$D_i = \frac{u_i RT}{z_i F} \tag{8}$$

where u_i is the ionic mobility and z_i is the charge of the corresponding ion. On the other hand, the concentration of the defects N_v in the product layer, through which the mass transport occurs, increases with increasing temperature according to the following equation, where ΔH_v is the formation enthalpy of point defects [61]:

$$N_v = const \cdot \exp - \frac{\Delta H_v}{RT} \tag{9}$$

Despite the presence of high temperatures, the solid state reaction rates are low because of the long diffusion pathways, which particles must pass through to achieve their appropriate positions in the product lattice. According to kinetic considerations, it is obvious that preferably small particle sizes of educts and high concentrations in contact zones are crucial for optimum solid state processes to occur. To obtain these conditions, the liquid-phase precursors like sol/gel outstand in the last time [52].

1.3.3 Preparation of dense perovskite membranes

To achieve gas-tight membranes, the as-synthesized powder will be consolidated in the desired shape, following by sintering into a dense ceramic. Sintering refers to processes involving heat treatment of powder compacts at temperatures near the melting point of the material [62]. Two competitive processes, densification and coarsening, occur in the sintering process and are driven by a reduction in free energy of the system, which can be mostly accomplished by reducing the surface free energy. The grain growth or coarsening is effected by the mass transport trough surface and lattice diffusion, as well as by evaporation and condensation (vapor transport) of the matter. Processes like grain boundary diffusion and plastic flow lead to the densification of powder compacts [62].

During the initial stage of sintering, the powder particles can be relocated and the number of nearest neighbors can increase. Furthermore, the grain boundaries are formed, and the large unevenness on the particle surfaces is removed. Up to 65 % of the maximum density is achieved at this stage. In the intermediate step, combined coarsening and densification processes result in a reduction in pore cross-section. Isolated pores replace the previously continuous porosity and an intermediate stage can be considered complete if the density reaches approximately 90% of the theoretical density. Finally, the grains grow at the cost of smaller grains and isolated pores, leading to the formation of coarse grains. The density is further increased up to 95-98%. The discrepancy in maximum density occurs if some pores get trapped inside the grain; these are difficult to remove from the ceramic [62].

In this thesis, dense perovskite disk-membranes with dimensions of 16 mm diameter and approximately 1 mm thickness were obtained by uniaxially pressing the powder with 140-150 kN in the green compacts followed by sintering. The sintering temperature and time for this process were empirically determined to achieve gas-tight ceramics with the desired compositions and densities close to the maximum.

1.3.4 Preparation of asymmetric membranes

In MIEC membrane technology, a decrease in membrane thickness often leads to an increase in oxygen flux, if oxygen permeation is limited by bulk-diffusion (see section 1.4.3). One method to achieve thin membranes with sufficient mechanical strength is the asymmetric membrane approach. Asymmetric membranes refer to the composite-structured membranes that consist of a thin dense layer that is deposited on a porous support, as shown schematically in Figure 1.8. The selection of materials, which can be applied for porous support and a dense layer, is a key factor for the

successful manufacturing of asymmetric membranes. Apart from good chemical compatibility, the materials should exhibit similar thermal expansion coefficients, because differences in the expansion between substrate and thin layer may result in thermal stress, and this stress may lead to cracking of the membrane at high operating temperatures. The smart solution for this issue is to use self-supported membranes that consist of a support and dense layers made from the same material introduced by Teraoka et al., who were the first to fabricate self-supported membranes [63-64].
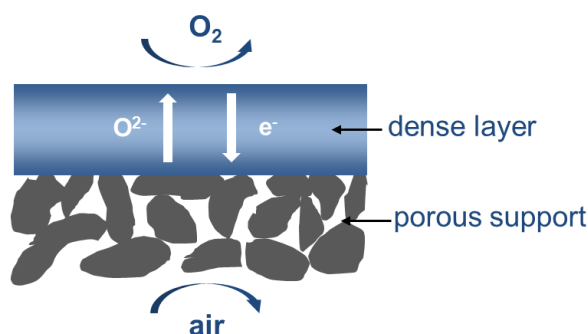
Figure 1.8: *Schematic of an asymmetric membrane, consisting of a dense layer and porous support.*

Diverse methods exist to fabricate self-supported membranes. These methods typically involve multiple preparation steps for the porous substrate and deposition of a thin dense layer. In our practical case, the support and dense layers discussed in section 4.1 were fabricated from the same powders as synthesized by the sol-gel method [63-66]. Porous substrates containing a high amount of open pores with sizes in the range of 0.5-10 µm were prepared using 20 wt.% of organic polymer pore former Pluronic F 127, which was intermixed with the powder and then removed by heat treatment. Dense layers with approximately 10 µm thicknesses were obtained via spin-coating of a 3 ml slurry containing 15 wt.% powder in ethanol, drying, and sintering.

1.4   Mixed oxygen ion and electron conductors

1.4.1 Defect chemistry of perovskite oxides.

The mixed oxygen ion and electron-conducting properties of perovskites are strongly affected by their defect chemistry. The formation of defects not only in perovskite but also in all inorganic materials is caused by a considerable increase in entropy leading to a minimum in the Gibbs free energy [67,68]:

$$\Delta G = \Delta H - T\Delta S \qquad (10)$$

Although many type of defects may occur in inorganic compounds, the perovskite oxides are usually dominated by oxygen vacancy and electronic defects (electron holes), preserving the overall electrical neutrality [69,70]. The perovskite oxides relevant for this thesis contain A-site cations with fixed valence states (Ba^{2+}, Sr^{2+}, Ca^{2+} and/or La^{3+}). The B-sites are occupied by multivalent transition metal cations. Even at room temperature and ambient oxygen partial pressure, the average valence of

the B-site cation is lower than the highest possible state. This occurrence results in the presence of oxygen vacancies in the perovskite lattice. Further oxygen vacancies form upon the heating of the perovskite materials, accompanied by reduction of the B-site cations. The removal of oxygen and formation of oxygen vacancies can be described using Kröger-Vink defect notation, as follows [71]:

$$O_O^X + 2B_B^X \ \rightarrow \ V_O^{\bullet\bullet} + 2B_B' + \frac{1}{2} \, O_{2\,(g)} \tag{11}$$
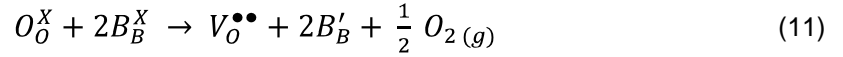
In cubic non-stoichiometric perovskite, the oxygen vacancies are statistically introduced in the lattice. Thus, the disordered vacancies are crystallographic in nature and energetically equivalent to occupied oxygen sites [72]. Some perovskite materials can exhibit a high degree of disordered oxygen vacancies. For a current state-of-the-art BSCF material (see page 3), for example, an oxygen stoichiometry of 2.48 was observed at room temperature. The amount of oxygen in this perovskite declines at operating temperatures above 1173 K to approximately 2.2, which relates to one quarter of the oxygen site being vacant, without a collapse of perovskite structure [69].

1.4.2 Electrical conductivity of perovskite oxides

The majority of perovskite oxides containing transition metal cations at the B-site exhibit positive Seebeck coefficients consistent with p-type conduction. Owing to this, the electron holes ($h^\bullet$) can be considered charge carriers [73]. The electron holes form by reduction of B-site cations, as caused by oxygen loss:

$$B_B^X \ \rightarrow \ B_B' + h^\bullet \tag{12}$$

At low temperatures, the electronic conduction occurs through thermally activated migration of electron holes along B-O-B bonds. This hopping mechanism involves interactions with small polarons of the lattice (phonons) and follows the relation [74]:

$$\sigma = \ \frac{C}{T} \ \exp \ \frac{-E_A}{kT} \tag{13}$$

where σ is electrical conductivity, E_A is the activation energy, and k is the Boltzmann constant. The pre-exponential constant C includes the carrier concentration, as well as other material-dependent parameters. The electrical conductivity increases with increasing temperature, and a maximum of σ can be observed [70, 73]. Further increases in temperature lead to metal-like conductivity. In other words, the conductivity decreases with temperature, which cannot be explained by a small-polaron hopping mechanism. This behavior can result from the transition of localized d-electrons of B-site cations at atomic lattice site, due to coulombic repulsion at low temperatures, into delocalized d-electrons. This transition is caused by hybridizations with oxygen p-electrons and/or by spin-state transitions of the transition metal d-electrons at high temperatures [75-78]. The delocalized charge carriers dominate the electrical conductivity of perovskite oxides at high temperatures, leading to metal-like conductivity.

1.4.3 Oxygen permeation through perovskite membranes

MIECs perovskite membranes can selectively separate oxygen from air or other gas mixtures by the lattice diffusion of oxygen ions [3]. The driving force of oxygen transport through the perovskite membranes is the difference in chemical potential of oxygen between the two surfaces of the membrane owing to sufficiently high temperatures for the diffusion. The chemical potential gradient forces oxygen to move from the location with the higher oxygen partial pressure toward the side with lower partial pressure. Figure 1.9 schematically illustrates the basic principle of the oxygen permeation process. The chemical potential gradient of oxygen across the membrane is subdivided into a central (bulk) zone and adjoining interfacial zones, emphasizing the combination of both solid state diffusion and surface exchange reactions in the oxygen permeation process [79].
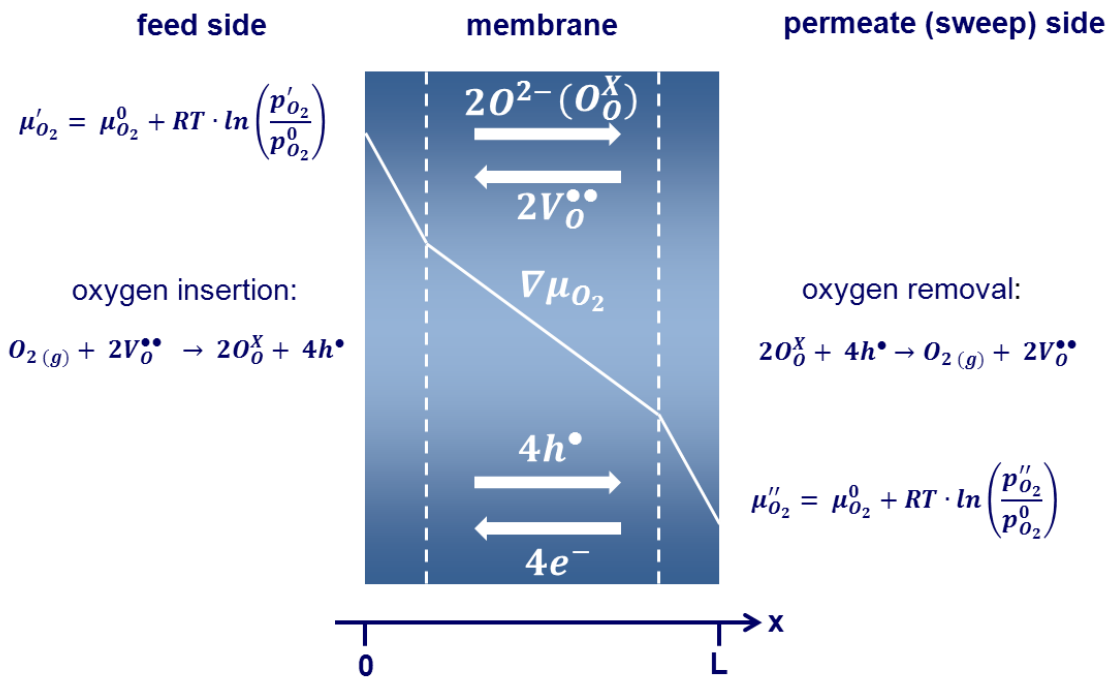
Figure 1.9: The basic principle of oxygen permeation through dense perovskite membranes of thickness L driven by the gradient between the oxygen chemical potentials of the feed side and the permeate side.

Oxygen transport trough the bulk zone can occur either via diffusion of oxygen in the perovskite lattice or across grain boundaries in the polycrystalline membrane [80,81]. Oxygen diffusion in the lattice of oxygen-deficient perovskite can be described in terms of oxygen-ion hopping from occupied sites to neighboring empty sites, which are energetically equivalent on the time scale of the oxygen ion jump. The wandering oxygen-ion must merely negotiate a motional enthalpy ΔH_m with a value lower than 1 eV for relevant perovskites. The motional enthalpy can be regarded as the activation energy for oxygen vacancy diffusion directly associated with the diffusion coefficient [80]:

$$D_{V_O^{\bullet\bullet}} \sim \exp\left(\frac{-\Delta H_m}{kT}\right) \tag{14}$$

Thus, the oxygen ionic conductivity can be defined, using the Nernst-Einstein equation, as [79,80]:

$$\sigma_{ion} = \frac{4F^2}{RT} c_{V_O^{\bullet\bullet}} D_{V_O^{\bullet\bullet}} \qquad (15)$$

where F is the Faraday constant and $c_{V_O^{\bullet\bullet}}$ is the concentration of oxygen vacancies.

The oxygen transport in the lattice of MIEC perovskites is accompanied by a counteracting flux of electrons caused by charge compensation. The Wagner theory is commonly used to describe the simultaneous flux of ions and electrons [82]. According to Wagner, the single particle flux of the charge carrier is proportional both to the conductivity of each charge carrier and the chemical potential gradient:

$$jo_2 \sim - \frac{\sigma_{el}\sigma_{ion}}{\sigma_{el}+\sigma_{ion}} \nabla\mu o_2 \qquad (16)$$

The electrical conductivity of most MIEC perovskite oxides is much higher than the oxygen ion conductivity [83]. Accordingly, oxygen permeation diffusion through a perovskite lattice in a membrane with a thickness *L* depends only on the oxygen ion conductivity. In other words, the concentration of oxygen vacancies and the chemical potential of oxygen across the membrane:

$$jo_2 \sim - \frac{D_{V_O^{\bullet\bullet}}}{L} \int_{\mu'o_2}^{\mu''o_2} c_{V_O^{\bullet\bullet}} \, d\mu o_2 \qquad (17)$$

Furthermore, the ambipolar transport of oxygen ions and electrons through a polycrystalline membrane can be directly affected by grain boundaries. Mayer et al. suggest that the grain boundaries exhibit their own defect chemistry, which can impact the transport properties in a positive way, because of the presence of fast pathways for the diffusion, or in a negative way, because of the formation of space charge layers blocking the charge carrier's migration [81].

As long as the membrane thickness is appropriately high, the oxygen permeation process is dominated by bulk transport. With decreasing membrane thickness, the surface-exchange reaction would become the limiting step of the oxygen permeation process. Furthermore, the surface exchange gains importance if oxygen transport resistance in the bulk phase is small because of the high ionic conductivity [84]. In general, the reversible oxygen surface exchange can be expressed with the following equation:

$$O_{2\,(g)} + 2V_O^{\bullet\bullet} \leftrightarrow 2O_O^X + 4h^\bullet \qquad (18)$$
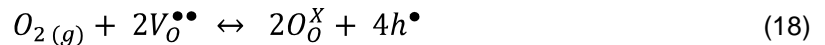
This reaction is composed of successive steps that might limit the overall reaction rate. It may involve the chemisorption of oxygen as a molecule at the surface, a charge transfer reaction between an adsorbed molecule and the bulk (oxygen reduction), and the incorporation of oxygen in the oxide lattice [85]:

$$O_{2\,(g)} \leftrightarrow O_{2\,abs} \qquad (19)$$

$$O_{2\,abs} + V_O^{\bullet\bullet} \leftrightarrow O_{abs} + O_O^X + 2h^\bullet \qquad (20)$$

$$O_{abs} + V_O^{\bullet\bullet} \leftrightarrow O_O^X + 2h^\bullet \qquad (21)$$
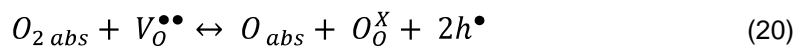
The transport parameters used to describe the surface exchange are a surface exchange coefficient k and the balanced oxygen exchange rate j_{ex}^O. In the absence of an oxygen chemical

potential gradient, these parameters correlate directly with the given oxygen partial pressure and, thus, with the concentration of oxygen anion c_O on the surface at equilibrium [86]:

$$j_{ex}^{O} = \frac{1}{2} k c_O \qquad (22)$$

Note that oxygen surface-exchange reactions may be affected by factors like surface morphology or the presence in the gas phase, for example, of CO_2, CO, and H_2O. These compounds can be absorbed on the surface, leading to a reduction in rates of oxygen exchange with the solid [87,88].
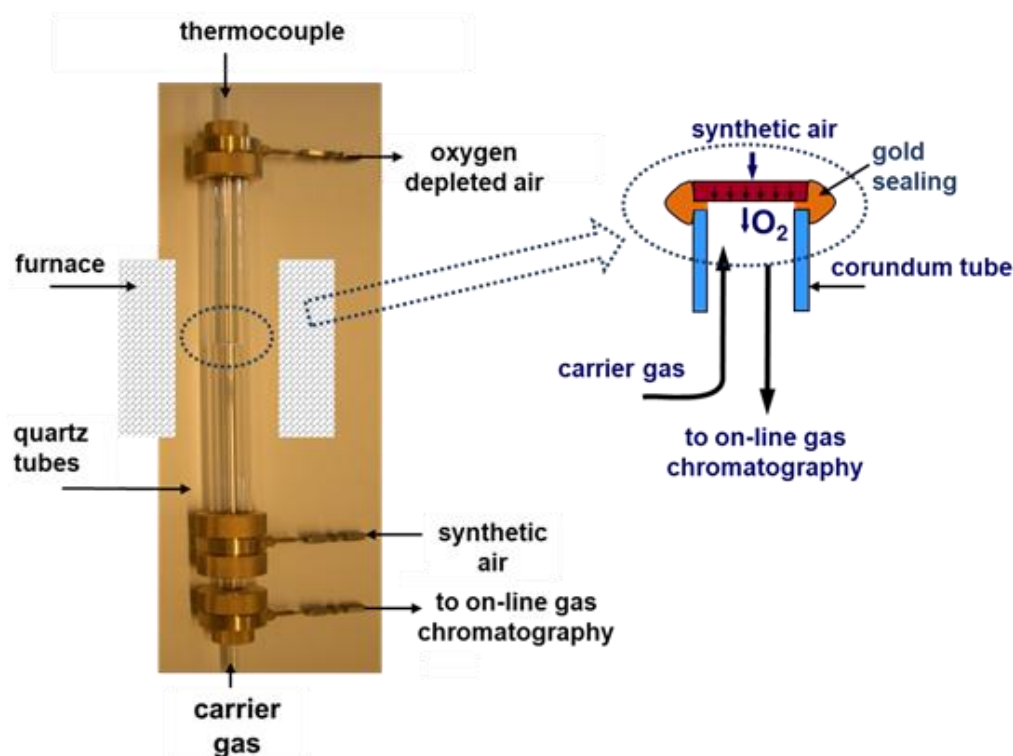
Figure 1.10: *Set up to measure the oxygen permeability of disc membranes with on-line gas chromatography [89].*

1.4.4 Measurement of oxygen permeation

Oxygen permeation measurements were based on the analysis of oxygen concentrations in the carrier gas by on-line gas chromatography. A high-temperature permeation cell, as shown in Figure 1.10, was used for the experiments [89]. To expose the perovskite materials to an oxygen chemical potential gradient, the disk-shaped membranes were sealed with a gold paste onto the ceramic tube and synthetic air was flushed from the upper side (feed side). A stream of inert carrier gas (He) or CO_2 was supplied from the lower membrane side (sweep side) to transport the permeated oxygen away from the membrane. In the case of asymmetric membranes, the dense layer was fixed onto the ceramic pipe. Afterward, the porous support (feed side) was purged with synthetic air and the dense layer (sweep side) was purged with the carrier gas. Gas concentrations in the effluent stream were

calculated from a gas chromatograph calibration. The relative leakage of O_2, which was evaluated by measuring the amount of N_2 in the effluent stream, was subtracted in the calculation of the oxygen permeation flux. The absolute flux rate of the effluents F was determined using neon as an internal standard. The oxygen permeation flux could then be calculated by the fraction of oxygen in the effluent gas and by determination of an effective area for the permeation S, as follows:

$$J_{O_2} \ ml \cdot min^{-1} \cdot cm^{-2} \ = \ C_{O_2} - \frac{C_{N_2}}{4.02} \cdot \frac{F}{S} \tag{23}$$

where the factor 4.02 relates to the ratio of leaked oxygen and nitrogen, according to Knudsen diffusion.

1.5 MIEC perovskite oxides: issues and possible solutions

1.5.1 Inherent phase instability of BSCF perovskite at intermediate temperatures

In the first report concerning BSCF perovskite, Shao et al. already referred to the slow decline of oxygen flux through a BSCF membrane after long operation times at 1023 and 1098 K, as caused by material decomposition [25]. This observation, however, did not prevent BSCF perovskite from becoming one of the "hottest" materials for intermediate temperature applications. Only a few critical reports about the degradation of functional properties of BSCF were published [90,91]. To gain a deeper understanding of these phenomena, Švarcová et al. have investigated the long-term stability of BSCF in the intermediate temperature range [92]. A slow transition of the single cubic perovskite phase into a 2H hexagonal polytype was detected in BSCF powders that were annealed below the crucial temperature of 1123 K in air. The oxidation of B-site cations, which leads to a decrease in the effective ionic radii and gives the structure a Goldschmidt tolerance factor higher than unity, was declared as a reason for the BSCF phase transition [92]. Furthermore, Arnold et al. have reported an increase of cobalt valence in BSCF from 2.2+ at 1223 K to 2.6+ at 298 K. The valence of iron remained predominantly at a state of 3+ over the whole temperature range [93]. Hence, they assumed that the oxidation of cobalt cations, combined with their spin-state transition, results in a dramatic diminution of their ionic radius, as shown in Table 1.1. This diminution is the real driving force of the BSCF phase transition [93]. The conclusion of Arnold et al. was confirmed by the extensive study of BSCF decomposition, as detailed in Chapter 2. It was found that cubic BSCF partially transforms into several hexagonal perovskite-related phases. This transformation is accompanied by the strong segregation of Co in these phases during annealing at temperatures below 1123 K. Moreover, the investigation of the phase transition in the cubic $(Ba_{0.8}Sr_{0.2})(Co_{0.8}Fe_{0.2})O_{3-\delta}$ perovskite (Chapter 2), which contained more barium on the A-site than BSCF, showed a very fast and pronounced cubic to hexagonal phase transformation, providing a destabilizing effect of high barium content on the phase stability of cubic cobalt-based perovskite, according to the concept of the Goldschmidt tolerance factor.

Knowing the reasons for the inherent phase instability of BSCF perovskite, strategies can be developed to design materials that are stable at intermediate temperatures. For example, doping of

the B-site of BSCF with zirconium considerably reduces the cubic to hexagonal transformation kinetics, as reported by Yakovlev et al. [94]. The high 4+ valence state of zirconium cations prevents the oxidation and spin-state transition of cobalt cations. Further, the zirconium cations stabilize the cubic structure because they are too large for octahedral coordination in the face-shared octahedra framework. The efforts to steady cobalt-based perovskite with zirconium led to the development of materials with the composition $BaCo_xFe_yZr_zO_{3-\delta}$ (x+y+z = 1), which exhibited improved inherent phase stability and thermo-mechanical strength apart from good conducting properties [95]. However, cobalt has several disadvantages, including its high cost, toxicity, and easy evaporation during material synthesis and operation. Owing to these disadvantages, cobalt-free perovskite with appropriate oxygen transport properties, like $(Ba_{0.5}Sr_{0.5})(Fe_{0.8}Zn_{0.2})O_{3-\delta}$ perovskite oxide, which was recently developed in our group, can be considered real alternatives to cobalt-based perovskites [96]. A novel perovskite $(Ba_{0.5}Sr_{0.5})(Fe_{0.8}Cu_{0.2})O_{3-\delta}$ is presented in chapter 3 as another promising cobalt-free MIEC membrane material, as it has the highest oxygen permeation performance of known cobalt-free materials.

1.5.2 Intolerance of alkaline-earth containing perovskite against CO_2

The poisoning effect of CO_2 on the alkaline earth-containing perovskite is based on the high affinity of A-site cations to form carbonates [34,88,97]. This is in accordance with the high thermodynamic stability of carbonates at certain temperatures and CO_2 partial pressures, which can be evaluated by the Ellingham diagram in Figure 1.11. The dashed lines in the diagram represent the temperature dependency of CO_2 chemical potential at different partial pressures. The compact lines with positive slope relate to chemical potentials of CO_2 during the decomposition of corresponding carbonates. These compact lines are calculated with thermodynamic data or determined experimentally. Thus, the carbonates are thermodynamically stable if the CO_2 chemical potential of the carbonate decomposition reaction at the given temperature is lower than at the corresponding partial pressure. It becomes obvious that barium and strontium carbonates remain stable, even in air (p(CO_2) ≈ 30 Pa) up to 1170 K and 1000 K, respectively. The stability of carbonates correlates directly with the ionic radii of the cations because the binding strength between the polyatomic carbonate anion and the metal cation increase with decreasing polarization power of the cation, which is inversely proportional to the ionic size [99]. Hence, it follows that the thermal stability of carbonates containing smaller cations, like Ca^{2+}, La^{3+} or transition metal cations, is lower than that of barium and strontium carbonates. This conclusion is hereby confirmed by the thermodynamic data shown in Figure 1.11.

Applied to perovskite oxides, the Ellingham diagram may give a rough estimation of the possible tolerance of the materials against CO_2 at relevant conditions. However, the stabilization energy of perovskite should be considered, which has been defined by Yokokawa et al. as [100]:

$$\Delta_r H(ABO_3) = \Delta_f H^0(ABO_3) - \Delta_f H^0(AO_n) - \Delta_f H^0(BO_m) \qquad [24]$$

Further, they postulated that the stabilization energy depends strongly on the chemical composition of perovskite and correlates well with the Goldschmidt tolerance factor, providing a large stabilization for materials with a cubic symmetry ($t = 1$). Thus, if the stabilization energy of the perovskite exhibits a highly negative value, the stability against carbonate formation is strong. On the basis of

thermodynamic data, the resistance toward CO_2 can be predicted for some binary perovskite oxides at relevant conditions [99]. Because many advanced perovskite oxides have complex chemical compositions, thermodynamic data is often not available. Therefore, the CO_2 stability of the materials should be empirically investigated in each individual case.
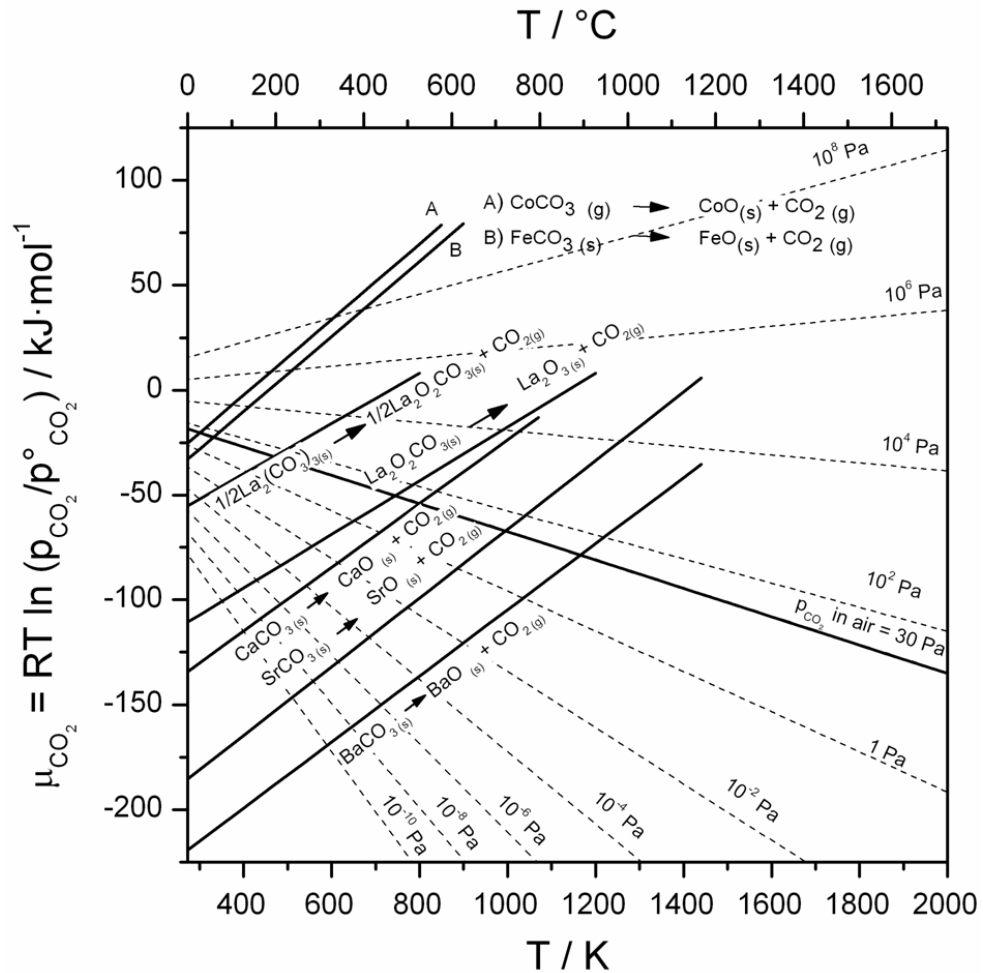
Figure 1.11: *Ellingham diagram for the decomposition of carbonates under different partial pressures calculated with thermodynamic data from [98] or determined experimentally [56].*

The BSCF perovskite exhibits high intolerance toward CO_2. The perovskite structure of the BSCF membrane breaks down at a depth of up to approximately 50 µm in the presence CO_2. This break down is caused by the formation of a mixed barium/strontium carbonate [34]. Both the functional properties and microstructures of alternative perovskite materials $(Ba_{0.5}Sr_{0.5})(Fe_{0.8}Zn_{0.2})O_{3-\delta}$ and $BaCo_xFe_yZr_zO_{3-\delta}$ (x+y+z = 1) are also strongly impaired after contact with CO_2, as represented in chapter 4. According to the above-mentioned thermodynamic considerations, the lanthanum- and calcium-based perovskites can provide CO_2-stable MIEC materials. This issue will be discussed in detail in chapter 5.

Additionally, the problem of CO_2-intolerance can be overcome by using alkaline-earth, free dual phase MIEC membranes. The dual phase concept is based on the presence of an oxygen ionic and electronic conductor in the membrane. These phases form two interpenetrating percolated networks of solid oxide electrolyte and an internally short-circuiting electrode, providing MIEC properties of the

membrane. Chapter 5 presents a novel CO_2-stable composite dual phase membrane containing 40 wt.% $NiFe_2O_4$ with a spinel structure as the electronic conductor and 60 wt.% $Ce_{0.9}Gd_{0.1}O_{2-\delta}$ with a fluorite structure as the electrolyte.

1.6 Bibliography

[1]   International energy agency. World energy outlook 2010.

[2]   J. Sunarso, S. Baumann, J.M. Serrac, W.A. Meulenberg, S. Liu, Y.S. Lin, J.C. Diniz da Costa, Mixed ionic–electronic conducting (MIEC) ceramic-based membranes for oxygen separation, *J. Membr. Sci.* 320 (2008) 13-41.

[3]   H.J.M. Bouwmeester, A.J. Burggraaf, Dense ceramic membranes for oxygen separation, in: A.J. Burggraaf, L. Cot (Eds.), Fundamentals of inorganic membrane science and technology, Elsevier, Amsterdam, 1996.

[4]   R. Bredesen, K. Jordal, O. Bolland, High-temperature membranes in power generation with CO_2 capture, *Chem. Eng. Processes* 43 (2004) 1129-1158.

[5]   S.P. Kaldis, G. Skodras, G.P. Sakellaropoulos, Energy and capital cost analysis of CO_2 capture in coal IGCC processes via gas separation membranes, *Fuel Process. Technol.* 85 (2004) 337-346.

[6]   M. Modigell, R. Kneer, H. Maier, N. Peters, D. Abel, R. Niehuis, Oxycoal AC - Entwicklung eines CO_2 emissionsfreien thermischen Kraftwerkprozesses, *Chem. Ing. Technik* 77 (2005)1147-1148.

[7]   E. Blomen, C. Hendriks, F. Neele, Capture technologies: Improvements and promising developments, *Energy Procedia* 1 (2009) 1505-1512.

[8]   A.G. Dixon, Recent research in catalytic inorganic membrane reactors, *Int. J. Chem. Reactor Eng.* 1 (2003) R6.

[9]   W. Yang, H. Wang, X. Zhu, L. Lin, Development and application of oxygen permeable membrane in selective oxidation of light alkanes, *Topics Catal.* 35 (2005) 155-167.

[10] O. Czuprat, S. Werth, J. Caro, T. Schiestel, Oxidative dehydrogenation of propane in a perovskite membrane reactor with multi-step oxygen insertion, *AIChE J.* 56 (2010) 2390-2396.

[11] H. Jiang, F. Liang, O. Czuprat, K. Efimov, A. Feldhoff, S. Schirrmeister, S. Schiestel, H. Wang, J. Caro, "Hydrogen production by water dissociation in surface-modified $BaCo_xFe_yZr_{1-x-y}O_{3-\delta}$ hollow-fiber membrane reactor with improved oxygen permeation", *Chem. Eur. J.* 16 (2010) 7898-7903.

[12] H. Jiang, H. Wang, F. Liang, S. Werth, T. Schiestel, J. Caro, Direct decomposition of nitrous oxide to nitrogen by in situ oxygen removal with a perovskite membrane, *Angew. Chem. Int. Ed.* 48 (2009) 2983-2986.

[13] B.C.H. Steele, A. Heinzel, Materials for fuel-cell technologies, *Nature* 414 (2001) 345-352.

[14] K. Huang, J. Wan, J.B. Goodenough, Oxide-ion conducting ceramics for solid oxide fuel cells, *J. Mater. Sci.* 36 (2001) 1093-1098.

[15] L. Carrette, K.A. Friedrich, U. Stimming, Fuel cells – fundamentals and applications, *Fuel Cells* 1 (2001) 5-39.

[16] J. Richter, P. Holtappels, T. Graule, T. Nakamura, L.J. Gauckler, Materials design for perovskite SOFC cathodes, *Monatsh. Chem.* 140 (2009) 985-999.

[17] S.C Singhal, Advances in solid oxide fuel cell technology, *Solid State Ionics* 135 (2000) 305-313.

[18] Y. Teraoka, H. Zhang, S. Furukawa, N. Yamazoe, Oxygen permeation through perovskite oxides, *Chem. Lett.* 11 (1985) 1743-1746.

[19] Y. Teraoka, T. Nobunaga, N. Yamazoe, Effect of cation substitution on the oxygen semipermeability of perovskite-type oxides, *Chem. Lett.* 3 (1988) 503-506.

[20] Y. Liu, X. Tan, K. Li, Mixed conducting ceramics for catalytic membrane processing, *Catal. Rev.* 48 (2) (2006) 145-198.

[21] N.P. Brandon, S. Skinner, B.C.H. Steele, Recent advances in materials for fuel cells. *Annu. Rev. Mater. Res.* 33 (2003) 183-213.

[22] J. Caro, Membranreaktoren für die katalytische Oxidation, *Chem. Ing. Technik* 78 (2006) 899-912.

[23] S.P. Simner, J.F. Bonnett, N.L. Canfield, K.D. Meinhardt, J.P. Shelton, V.L. Sprenkle, J.W. Stevenson, Development of lanthanum ferrite SOFC cathodes, *J. Power Sources* 113 (2003) 1-10.

[24] S.P. Jiang, Development of lanthanum strontium manganite perovskite cathode materials of solid oxide fuel cells: a review, *J. Mater. Sci.* 43 (2008) 6799-6833.

[25] Z.P. Shao, W.S. Yang, Y. Cong, H. Dong, J.H. Tong, G.X. Xiong, Investigation of the permeation behavior and stability of a $Ba_{0.5}Sr_{0.5}Co_{0.8}Fe_{0.2}O_{3-delta}$ oxygen membrane, *J. Membr. Sci.* 172 (2000) 177-188.

[26] Z.P. Shao, G.X. Xiong, J.H. Tong, H. Dong, W.S. Yang, Synthesis, oxygen permeation study and membrane performance of a $Ba_{0.5}Sr_{0.5}Co_{0.8}Fe_{0.2}O_{3-delta}$ oxygen-permeable dense ceramic reactor for partial oxidation of methane to syngas, *Sep. Purif. Tech.* 25 (2001) 97-116.

[27] H.H. Wang, Y. Cong, W.S. Yang, Investigation on the partial oxidation of methane to syngas in a tubular $Ba_{0.5}Sr_{0.5}Co_{0.8}Fe_{0.2}O_{3-delta}$ membrane reactor, *Catal. Today* 82 (2003) 157-166.

[28] C.S. Chen, S.J. Feng, S. Ran, D.C. Zhu, W. Liu, H.J.M. Bouwmeester, Conversion of methane to syngas by a membrane-based oxidation-reforming process *Angew. Chem. Int. Ed.* 42 (2003) 5196-5198.

[29] W. Zhu, W. Han, G. Xiong, W. Yang, Mixed reforming of heptane to syngas in the $Ba_{0.5}Sr_{0.5}Co_{0.8}Fe_{0.2}O_3$ membrane reactor, *Catal. Today* 104 (2005) 149-153.

[30] Z.P. Shao, S. M. Haile, A high-performance cathode for the next generation of solid-oxide fuel cells, *Nature* 431 (2004) 170-173.

[31] Z.P. Shao, S.M. Haile, J. Ahn, P.D. Ronney, Z.L. Zhan, S.A. Barnett, A thermally self-sustained micro solid-oxide fuel-cell stack with high power density, *Nature* 435 (2005) 795-798.

[32] W. Zhou, R. Ran, Z.P. Shao, Progress in understanding and development of $Ba_{0.5}Sr_{0.5}Co_{0.8}Fe_{0.2}O_{3-\delta}$-based cathodes for intermediate-temperature solid-oxide fuel cells: A review, *J. Power Sources* 192 (2009) 231-246.

[33] M. Arnold, T.M. Gesing, J. Martynczuk, A. Feldhoff, Correlation of the formation and the decomposition process of the BSCF perovskite at intermediate temperatures, *Chem. Mater.* 20 (2008) 5851-5858.

[34] M. Arnold, H. Wang, A. Feldhoff, Influence of CO_2 on the oxygen permeation performance and the microstructure of perovskite-type $(Ba_{0.5}Sr_{0.5})(Co_{0.8}Fe_{0.2})O_{3-\delta}$ membranes, *J. Membr. Sci.* 293 (2007) 44-52.

[35] G. Rose, Reise nach dem Ural, dem Altei und dem Kaspischen Meere (Mineralogisch-geognostischer Teil und historischer Bericht der Reise), Verlag der Sanderschen Buchhandlung (G.E. Reimer), Berlin 1842.

[36] G. Rose, Beschreibung einiger neuen Minerale des Urals, *Poggendorff's Annalen (Annalen der Physik und Chemie)*,Verlag Johann Ambrosius Barth, Leipzig, Band 48 (1839) 551-573.

[37] T. Barth, Die Kristallstruktur von Perowskit und verwandten Verbindungen, *Norsk geol. Tiddskr.* 8 (1925) 201-216.

[38] V.M. Goldschmidt, Die Gesetze der Kristallchemie, *Naturwiss.* 14 (1926) 477-485.

[39] H.D. Megaw, Crystal structure of double oxides of the perovskite type, *Proc. Phys. Soc.* 58 (1946) 133-152.

[40] R.D. Shannon, C.T. Prewitt, Effective ionic radii in oxides and fluorides, *Acta Cryst. Sect B* 25 (1969) 925-946.

[41] R.D. Shannon, Revised effective ionic radii and systematic studies of interatomic distances in halides and chalcogenides, *Acta Cryst. Sect. A* 32 (1976) 751-767.

[42] A.M. Glazer, The classification of tilted octahedra in perovskites, *Acta Cryst. Sect B* 28 (1972) 3384-3392.

[43] A.M. Glazer, Simple Ways of Determining Perovskite Structures, *Acta Cryst. Sect A* 31 (1975) 756-762.

[44] H.D. Megaw, Crystal structures: A working approach, W.B. Saunders Co., Philadelphia, PA, 1973.

[45] K.S. Aleksandrov, The sequences of structural phase transitions in perovskites, *Ferroelectrics* 18 (1976) 801-805.

[46] C.J. Howard, H.T. Stokes, Group-Theoretical Analysis of Octahedral Tilting in Perovskites, *Acta Cryst. Sect B* 54 (1998) 782-789.

[47] R.H. Mitchell, Perovskites: Modern and Ancient; Almaz Press Inc.: Ontario, Canada, 2002

[48] M. Ain, J.M. Delrieu, A. Menelle, G. Parette, J. Jegoudez, Orthorhombicity and oxygen uptake by $YBa_2Cu_3O_{6+x}$, *J. Phys. France* 50 (1989) 1455-1461.

[49] L. Katz, R. Ward, Structure Relations in Mixed Metal Oxides, *Inorg. Chem.* 3 (1964) 205-211.

[50] M. O'Keeffe, B.G. Hyde, Crystal structures. 1. Patterns and symmetry. Mineralogical Soc. America, Washington DC,1996.

[51] E.J. Cussen, J. Sloan, J.F. Vente, P.D. Battle, T.C. Gibb, 15R $SrMn_{1-x}Fe_xO_{3-\delta}$ (x ≈ 0.1); A new perovskite stacking sequence, *Inorg. Chem.* 37 (1998) 6071-6077.

[52] Y.G. Metlin and Y.D. Tretyakov. Chemical routes for preparation of oxide high-temperature superconducting powders and precursors for superconductive ceramics, coatings and composites, *J. Mater. Chem.* 4 (1994) 1659–1665.

[53] A. Feldhoff, M. Arnold, J. Martynczuk, T.M. Gesing, H. Wang. The sol-gel synthesis of perovskites by an EDTA/citrate complexing method involves nanoscale solid state reactions, *Solid State Sciences* 10 (2008) 689-701.

[54] A. Feldhoff, J. Martynczuk, H.H. Wang, Advanced $Ba_{0.5}Sr_{0.5}Zn_{0.2}Fe_{0.8}O_{3-\delta}$ perovskite-type ceramics as oxygen selective membranes: Evaluation of the synthetic process, *Progress Solid State Chem.* 35 (2007) 339–353.

[55] R.H.E. van Doorn, H. Kruidhof, A. Nijmeijer, L. Winnubst, A. J. Burggraaf, Preparation of $La_{0.3}Sr_{0.7}CoO_{3-\delta}$ perovskite by thermal decomposition of metal-EDTA complexes, *J. Mater. Chem* 8 (1998) 2109-2112.

[56] K. Efimov, M. Arnold, J. Martynczuk, A. Feldhoff, Crystalline Intermediate Phases in the Sol–Gel-Based Synthesis of $La_2NiO_{4+\delta}$, *J. Am. Ceram. Soc.* 92 (2009) 876-880.

[57] H. Schmalzried. Reaktionen im festen Zustand, *Angew. Chem.* 8 (1963) 353–392.

[58] R. Pretorius, C.C. Theron. Compound phase formation in thin film structures, *Crit. Rev. Solid State Mater. Sci.* 24 (1999) 1-62.

[59] U. Gösele, K.N. Tu. Growth kinetics of planar binary diffusion couples: Thin-film case versus bulk case, *J. Appl. Phys.* 53 (1982) 3252-3260

[60] F.M. d'Heurle. Nucleation of a new phase from the interaction of two adjacentphases: Some silicides, *J. Mater. Res.* 3 (1988) 167-195.

[61] R.A. Swalin, Thermodynamics of solids, John Wiley and Sons, New York, 2 edition, 1972.

[62] M.N. Rahaman. Ceramic processing and sintering. CRC Press/Taylor and Francis Group, Boca Raton, 2nd edition, 2003.

[63] Y. Teraoaka, T Fukuda, N. Miura, N. Yamazoe, Development of oxygen semipermeable sembrane using mixed conductive perovskite-type oxides (Part 1) - Preparation of porous sintered discs of perovskite oxides, *J. Ceram. Soc. Jpn., Int. Ed.* 97 (1989) 467-472.

[64] Y. Teraoaka, T Fukuda, N. Miura, N. Yamazoe, Development of oxygen semipermeable sembrane using mixed conductive perovskite-type oxides (Part 2) - Preparation of dense film of perovskite type oxide on porous substrate, *J. Ceram. Soc. Jpn., Int. Ed.* 97 (1989), 523–529.

[65] K. Watanabe, M. Yuasa, T. Kida, K. Shimanoe, Y. Teraoka, N. Yamazoe, Dense/porous asymmetric-structured oxygen permeable membranes based on $La_{0.6}Ca_{0.4}CoO_3$ perovskite-type oxide, *Chem. Mater.* 20 (2008) 6965-6973.

[66] M.L. Fontaine, J.B. Smith, Y. Larring, R. Bredesen, On the preparation of asymmetric $CaTi_{0.9}Fe_{0.1}O_{3-\delta}$ membranes by tape-casting and co-sintering process, *J. Membr. Sci.* 326 (2009) 310–315

[67] W.D. Kingery, H.K. Bowen, D.R. Uhlmann, Introduction to Ceramics, John Wiley & Sons, Toronto, 1976.

[68] A.R. West, Solid State Chemistry and Its Applications, John Wiley & Sons, Chichester, 1984.

[69] S. McIntosh, J.F. Vente, W.G. Haije, D.H.A. Blank, H.J.M. Bouwmeester, Oxygen stoichiometry and chemical expansion of $Ba_{0.5}Sr_{0.5}Co_{0.8}Fe_{0.2}O_{3-delta}$ measured by in situ neutron diffraction, *Chem. Mater.* 18 (2006) 2187-2193.

[70] Z.Yáng, A.S. Harvey, A. Infortuna, J. Schoonman, L.J. Gauckler, Electrical conductivity and defect chemistry of $Ba_xSr_{1-x}Co_yFe_{1-y}O_{3-\delta}$ perovskites, *J. Solid State Electrochem.* 15 (2010) 277-284.

[71] F.A. Kröger and H.J. Vink. Relations between the concentrations and imperfections in crystalline solids, *Solid State Phys.* 3 (1956) 307-435.

[72] V.M. Goodenough, Electronic and ionic transport properties and other physical aspects of perovskites, *Rep. Prog. Phys.* 67 (2004) 1915-1993.

[73] J.W. Stevenson, T.R. Armstrong, R.D. Carneim, L.R. Pederson, W. J. Weber, Electrochemical properties of mixed conducting perovskites $La_{1-x}M_xCo_{1-y}Fe_yO_{3-\delta}$ (M = Sr, Ba, Ca), *J. Electrochem. Soc.* 143 (1996) 2722–2729.

[74] D.P. Karim, A.T. Aldred, Localized level hopping transport in $La(Sr)CrO_3$, *Phys. Rev. B* 20 (1979) 2255–2263

[75] Y. Tokura, Correlated-electron physics in transition-metal oxides, *Phys. Today* 56 (2003) 50-55.

[76] A. Feldhoff, J. Martynczuk, M. Arnold, M. Myndyk, I. Bergmann, V. Šepelák, W. Gruner, U. Vogt, A. Hähnel, J. Woltersdorf, Spin-state transition of iron in $(Ba_{0.5}Sr_{0.5})(Fe_{0.8}Zn_{0.2})O_{3-\delta}$ perovskite, *J. Solid State Chem.* 182 (2009) 2961–2971.

[77]   P.M. Raccah, J.B. Goodenough, First-order localized-electron ⇆ Collective-electron transition in LaCoO$_3$, *Phys. Rev.* 155 (1967) 932–943.

[78]   A.G Bhide, D.S. Rajoria, G. Rama Rao, C.N.R. Rao, Mössbauer studies of the high-spin-low-spin equilibria and the localized-collective electron transition in LaCoO$_3$, *Phys. Rev.B.* 6 (1972) 1021-1032.

[79]   Y.S. Lin, W. Wang, J. Han, Oxygen permeation through thin mixed-conducting solid oxide membranes, *AIChE J.* 40 (5) (1994) 786-798.

[80]   J.B. Goodenough, Crystalline solid electrolytes. Part 2. Material design, in: Solid state electrochemistry, ed. By P.G. Bruce, Cambridge University Press., Cambridge 1995.

[81]   J. Maier, Festkörper — Fehler und Funktion, Prinzipien der Physikalischen Festkörperchemie. Teubner, Stuttgart-Leipzig, 1st edition, 2000.

[82]   C. Wagner, Equations for transport in solid oxides and sulfides of transition metals. *Prog. Solid State Chem.* 10 (1975) 3-16.

[83]   H.J.M Bouwmeester. Dense ceramic membranes for methane conversion, *Catal. Today* 82 (2003) 141-150

[84]   H.J.M. Bouwmeester, H. Kruidhof, A.J. Burggraaf, Importance of the surface exchange kinetics as rate limiting step in oxygen permeation through mixed conducting oxides, *Solid State Ionics* 72 (1994) 185-194.

[85]   S. Dou, C.R. Masson, P.D. Pacey, Mechanism of oxygen permeation through lime-stabilized zirconia, *J. Electrochem. Soc.* 132 (8) (1985) 1843-1849.

[86]   Z. Adamczyk, J. Nowotny, Effect of the surface on gas/solid equilibration kinetics on nonstoichiometric compounds, *Solid State Phenom.* 15&16 (1991) 285-336.

[87]   J.A. Lane, J.A. Kilner, Oxygen surface exchange on gadolinia doped ceria, *Solid State Ionics*, 137 (2000) 927-932.

[88]   I.V. Khromushin, T.I. Aksenova, Zh.R. Zhotabaev, *Solid State Ionics* 162–163 (2003) 37–40

[89]   H. Wang, C. Tablet, A. Feldhoff, J. Caro. Investigation of phase structure, sintering, and permeability of perovskite-type (Ba$_{0.5}$Sr$_{0.5}$)(Co$_{0.8}$Fe$_{0.2}$)O$_{3-\delta}$ membranes, *J. Membr. Sci.* 262 (2005) 20-26.

[90]   A.C. van Veen, M. Rebeilleau, D. Farrusseng, C. Mirodatos, Studies on the performance stability of mixed conducting BSCFO membranes in medium temperature oxygen permeation, *Chem. Commun.*1 (2003) 32-33.

[91]   M. Rebeilleau-Dassonneville, S. Rosini, A.C. van Veen, D. Farruseng, C. Mirodatos, Oxidative activation of ethane on catalytic modified dense ionic oxygen conducting membranes, *Catal. Today* 104 (2005) 131-137.

[92]   S. Švarcová, K. Wiik, J. Tolchard, H.J.M. Bouwmeester, T. Grande. Structural instability of cubic perovskite Ba$_x$Sr$_{1-x}$Co$_{0.8}$Fe$_{0.2}$O$_{3-\delta}$, *Solid State Ionics* 178 (2008) 1787–1781.

[93] M. Arnold, Q Xu, F.D. Tichelaar, A. Feldhoff, Local charge disproportion in a high-performance perovskite, *Chem. Mater.* 21 (2009) 635-640.

[94] S. Yakovlev, C.Y. Yoo, S. Fang, H.J.M. Bouwmeester, Phase transformation and oxygen equilibration kinetics of pure and Zr-doped $Ba_{0.5}Sr_{0.5}Co_{0.8}Fe_{0.2}O_{3-\delta}$ perovskite oxide probed by electrical conductivity relaxation, *Appl. Phys.Lett.* 96 (2010) 254101.

[95] J. Tong, W. Yang, B. Zhu, R. Cai, Investigation of ideal zirconium-doped perovskite-type ceramic membrane materials for oxygen separation, *J. Membr. Sci.* 203 (2002) 175-189.

[96] H. Wang, C. Tablet, A. Feldhoff, J. Caro. A cobalt-free oxygen-permeable membrane based on the perovskite-type oxide $(Ba_{0.5}Sr_{0.5})(Fe_{0.8}Zn_{0.2})O_{3-\delta}$. *Adv. Mater.* 17 (2005) 1785-1788.

[97] S.J. Benson, D. Waller, J.A. Kilner, Degradation of $La_{0.6}Sr_{0.4}Fe_{0.8}Co_{0.2}O_{3-delta}$ in carbon dioxide and water atmospheres, *J. Electrochem. Soc.* 146 (4) (1999) 1305–1309.

[98] I. Barin, F. Sauert, G. Patzki, "Thermochemical data of pure substances", third ed., vols. I and II, VCH, Weinheim, 1995.

[99] K.H. Stern, E.L. Weise, „ High temperature properties and decomposition of inorganic salts. Part 2. Carbonates", NSDRS, Washington, 1969.

[100] H. Yokokawa, N. Sakai, T. Kawada, M. Dokiya, Thermodynamic stabilities of perovskite xides for electrodes and other electrochemical materials, *Solid State Ionics* 52 (1992) 43-56.

2 Inherent phase instability of BSCF perovskite at intermediate temperatures

2.1 Summary

Here, we deal with the decomposition of cubic perovskites $(Ba_{0.5}Sr_{0.5})(Co_{0.8}Fe_{0.2})O_{3-\delta}$ (BSCF) and $(Ba_{0.8}Sr_{0.2})(Co_{0.8}Fe_{0.2})O_{3-\delta}$ in the intermediate temperature range (773-1073 K). The compounds differ only in their Ba/Sr ratio. Section 2.2 presents the results of a detailed TEM study on BSCF annealed for 180-240 h at temperatures below 1173 K. The slow phase transitions of cubic perovskite into hexagonal perovskite $Ba_{0.6}Sr_{0.4}CoO_{3-\delta}$, a previously unknown $Ba_{1-x}Sr_xCo_{2-y}Fe_yO_{5-\delta}$ complex oxide and $Ba_{0.4}Sr_{0.6}O$ was observed both in ceramic and powder samples. Already, the presence of small amounts of non-cubic phases in the BSCF system at intermediate temperatures has a steep negative effect on oxygen permeation performance. The reason for this behavior is the lamellar-shape of the $Ba_{1-x}Sr_xCo_{2-y}Fe_yO_{5-\delta}$ phase, which is structurally related to the 15R rhombohedral perovskite polymorph. The several micrometer-long $Ba_{1-x}Sr_xCo_{2-y}Fe_yO_{5-\delta}$ lamellae grew through the cubic perovskite grains and can be considered as barriers to oxygen transport because of their shape, low crystal symmetry, and low amount of mobile oxygen vacancies. Furthermore, a change in composition of the cubic phase due to cobalt enrichment in the lamellae states was an additional factor responsible for degradation of the BSCF functional properties.

The decomposition process of the $(Ba_{0.8}Sr_{0.2})(Co_{0.8}Fe_{0.2})O_{3-\delta}$ system was found to be more pronounced. The metastable cubic structure, which can be obtained upon quenching from 1223 K to room temperature, transforms into about 70% hexagonal and lamella-shaped rhombohedral phases upon furnace cooling at a rate of 3 K/min. Using differential thermal analysis and thermal gravimetry, abrupt changes in the oxygen stoichiometry of 1 wt.%, corresponding to a $\Delta\delta = 0.14$, were observed in the sample between 1073 and 1173 K. The massive phase conversion in the $(Ba_{0.8}Sr_{0.2})(Co_{0.8}Fe_{0.2})O_{3-\delta}$ system additionally resulted in mechanical stresses exceeding the strength of the material, as well as the formation of cracks in the ceramic.

The driving force of decomposition in both cubic perovskites BSCF and $(Ba_{0.8}Sr_{0.2})(Co_{0.8}Fe_{0.2})O_{3-\delta}$ at intermediate temperatures can be declared as a coupled valence and spin-state transition of cobalt-cations induced by oxygen insertion, which leads to a considerable decrease of their ionic radii. The oxidized cobalt-cations, which are smaller in size, are not tolerated in a cubic perovskite structure, especially when large barium cations occupy the A-sites in the perovskite lattice, according to the concept of the Goldschmidt tolerance factor.

2.2   TEM study of BSCF perovskite decomposition at intermediate temperatures

Konstantin Efimov, Qiang Xu, and Armin Feldhoff

CHEMISTRY OF MATERIALS

Article

Transmission Electron Microscopy Study of $Ba_{0.5}Sr_{0.5}Co_{0.8}Fe_{0.2}O_{3-\delta}$ Perovskite Decomposition at Intermediate Temperatures

Konstantin Efimov,*[†] Qiang Xu,[‡,§] and Armin Feldhoff[†]

[†]*Institute of Physical Chemistry and Electrochemistry, Leibniz Universität Hannover, Callinstrasse 3-3a, 30167 Hannover, Germany,* [‡]*National Centre for HREM, Kavli Institute of Nanoscience, Delft University of Technology, 2628 CJ Lorentzweg 1, Delft, The Netherlands, and* [§]*Vision Lab, University of Antwerp, 2020 Antwerp Groenenborgerlaan, 171, U316, Belgium*

The cubic perovskite $Ba_{0.5}Sr_{0.5}Co_{0.8}Fe_{0.2}O_{3-\delta}$ (denoted BSCF) is the state-of-the-art ceramic membrane material used for oxygen separation technologies above 1150 K. BSCF is a mixed oxygen-ion and electron conductor (MIEC) and exhibits one of the highest oxygen permeabilities reported so far for dense oxides. Additionally, it has excellent phase stability above 1150 K. In the intermediate temperature range (750−1100 K), however, BSCF suffers from a slow decomposition of the cubic perovskite into variants with hexagonal stacking that are barriers to oxygen transport. To elucidate details of the decomposition process, both sintered BSCF ceramic and powder were annealed for 180−240 h in ambient air at temperatures below 1123 K and analyzed by different transmission electron microscopy techniques. Aside from hexagonal perovskite $Ba_{0.6}Sr_{0.4}CoO_{3-\delta}$, the formation of lamellar noncubic phases was observed in the quenched samples. The structure of the lamellae with the previously unknown composition $Ba_{1-x}Sr_xCo_{2-y}Fe_yO_{5-\delta}$ was found to be related to the 15R hexagonal perovskite polytype. The valence and spin-state transition of cobalt leading to a considerable diminution of its ionic radius can be considered a reason for BSCF's inherent phase instability at intermediate temperatures.

Introduction

Cubic perovskite $Ba_{0.5}Sr_{0.5}Co_{0.8}Fe_{0.2}O_{3-\delta}$ (BSCF) is prominent in the family of mixed ionic and electronic conducting materials.[1,2] Owing to an exceptionally large amount of mobile oxygen defects in the highly symmetric perovskite lattice, BSCF exhibits very high oxygen-ionic transport rates over a wide temperature range.[3,4] Its extraordinary conducting properties combined with excellent phase stability at high temperatures make BSCF very promising for potential applications as semipermeable membranes in major processes like the separation of oxygen from air and the catalytic conversion of hydrocarbons.[5−8] Furthermore, the employment of BSCF as a cathode material in solid-oxide fuel cells (SOFCs) has also attracted a lot of attention.[9] In 2004, Shao and Haile reported the high power density of a symmetric single SOFC using BSCF as electrodes and a samaria-doped ceria (SDC) electrolyte at 773 and 873 K.[1] Since then, BSCF has been considered to be one of the most auspicious cathode materials for use in SOFCs operated in an intermediate temperature regime (IT-SOFC, T = 773−1073 K).[10]

Nevertheless, the wide applications of BSCF may be inhibited because of two major problems. First, the poor thermomechanical stability of the BSCF, namely low creep resistance and large coefficient of thermal expansion (CTE), can lead to the failure of the operation process in the worst case.[3,8,11] Second, the desired cubic structure of BSCF collapses at temperatures below 1123 K under long-term condition. In 2000, Shao et al. observed a slow decline of oxygen flux through a BSCF membrane after a long operation time at 1023 and 1098 K that was caused by an inherent phase transition.[4] A similar degradation of the oxygen permeation performance at 973 and 1023 K was also observed by van Veen et al. in 2003.[12] In order to elucidate this issue, Rebeilleau-Dassonneville et al. carried out an in situ X-ray diffraction (XRD) experiment and found the formation of noncubic phases in BSCF if the temperature was kept below 1073 K.[7] Moreover, Švarcová et al. investigated the long-term stability of BSCF at and below the crucial temperature of 1123 K by XRD.[13] Slow decomposition of the single cubic

*Corresponding author. E-mail: konstantin.efimov@pci.uni-hannover.de.
(1) Shao, Z.; Haile, S. M. *Nature* **2004**, *431*, 170.
(2) Chen, C.; Feng, S.; Ran, S.; Zhu, D.; Liu, W.; Bouwmeester, H. J. M. *Angew. Chem., Int. Ed.* **2003**, *115*, 5196.
(3) McIntosh, S.; Vente, J. F.; Haije, W. G.; Blank, D. H. A.; Bouwmeester, H. J. M. *Chem. Mater.* **2006**, *18*, 2187.
(4) Shao, Z.; Yang, W.; Cong, Y.; Dong, H.; Tong, J.; Xiong, G. *J. Membr. Sci.* **2000**, *172*, 177.
(5) Wang, H.; Cong, Y.; Xang, W. *Catal. Today* **2003**, *82*, 157.
(6) Caro, J.; Wang, H.; Tablet, C.; Kleinert, A.; Feldhoff, A.; Schiestel, T.; Kilgus, M.; Kölsch, P.; Werth, S. *Catal. Today* **2006**, *118*, 128.
(7) Rebeilleau-Dassonneville, M.; Rosini, S.; van Veen, A. C.; Farruseng, D.; Mirodatos, C. *Catal. Today* **2005**, *104*, 131.
(8) Vente, J. F.; Haije, W. G.; Rak, Z. S. *J. Membr. Sci.* **2006**, *177*, 2245.
(9) Shao, Z.; Haile, S. M.; Ahn, J.; Ronney, P. D.; Zhan, Z.; Barnett, S. A. *Nature* **2005**, *435*, 795.

(10) Zhou, W.; Ran, R.; Shao, Z. *J. Power Sources* **2009**, *192*, 231.
(11) Yi, J. X.; Lein, H. L.; Grande, T.; Yakovlev, S.; Bouwmeester, H. J. M. *Solid State Ionics* **2009**, *180*, 1564.
(12) van Veen, A. C.; Rebeilleau, M.; Farrusseng, D.; Mirodatos, C. *Chem. Commun.* **2003**, *1*, 32.
(13) Švarcová, S.; Wiik, K.; Tolchard, J.; Bouwmeester, H. J. M.; Grande, T. *Solid State Ionics* **2008**, *178*, 1787.

perovskite phase into a 2H hexagonal polytype was detected in a BSCF powder that had been annealed for 24 h at 1023 K in ambient air. The phase transition process was observed to be much more pronounced after annealing of the BSCF samples for 240 h in flowing oxygen between 1073 and 1123 K. In this study, the hexagonal phase ratio expanded with decreasing temperature. The oxidation of the B-site cations (B = transitions metals), which leads to a change of effective ionic radii and gives the structure the Goldschmidt tolerance factor higher than one, was declared the reason for the inherent BSCF phase instability at intermediate temperatures.[13,14] In 2009, Arnold et al. reported the valence transition of cobalt in cubic BSCF from the predominantly 2+ state at 1223 K to the mixed 2+/3+ state at 298 K according to in situ electron energy loss spectroscopy (EELS).[15] Hence, they concluded that the oxidation of cobalt cations combined with their spin-state transition resulting in dramatic diminution of their ionic radius is the real driving force of the BSCF decomposition.[15]

Recently, Mueller et al. investigated the phase transition of cubic BSCF perovskite by combining XRD with transmission electron microscopy (TEM).[16] Their TEM micrograph of a BSCF ceramic that had been annealed for 8 days at 1073 K showed a grain boundary phase and lamellae that ran through the grains. The grain boundary phase was described as $2H-Ba_{0.5+x}Sr_{0.5-x}CoO_{3-\delta}$ based on energy dispersive X-ray spectroscopy (EDXS) and selected area electron diffraction (SAED) along the *c*-axis. The latter is not sensitive to different stacking sequences, especially if they occur only at the very interface of the cubic phase, which can be expected accordingly to Arnold et al.[17] These lamellae were not addressed further. On the basis of their analysis, Mueller et al. proposed a simplistic phase diagram that put BSCF in a miscibility gap between the cubic and hexagonal phases, which were the only phases considered.[16]

Švarcová has suggested that the decomposition of BSCF might be reversible because annealed BSCF samples contain some of the same phases as the raw powder obtained after annealing for 240 h at 1023 K.[13] The relationship between the formation and decomposition processes of BSCF was also discussed by Arnold et al., who investigated the sol–gel synthesis of BSCF in detail.[17] XRD and high-resolution transmission electron microscopy (HRTEM) were applied to characterize crystalline intermediate phases in raw BSCF powder. A phase attribution of a sample quenched at 1023 K was provided in that report. Aside from the cubic (3C) and 2H hexagonal phases, the sample consisted of an additional phase of lower symmetry, which was described as a disordered hexagonal perovskite polymorph.

The findings of Arnold et al. offered inspiration to conduct a transmission electron microscopy (TEM) study of BSCF's decomposition process. For this reason, both sintered BSCF ceramic and powder were annealed for 180–240 h in ambient air at temperatures below 1123 K and extensively analyzed by several TEM techniques. Additionally, the functional properties of BSCF ceramic were tested by time-dependent oxygen permeation experiments under the aforementioned conditions.

Experimental Section

The BSCF powder was synthesized by a sol–gel route using ethylenediaminetetraacetic acid (EDTA) and citric acid as the organic ligand and network former, respectively. Given amounts of $Ba(NO_3)_2$, $Sr(NO_3)_2$, $Co(NO_3)_2$, and $Fe(NO_3)_3$ were dissolved in water, followed by the addition of EDTA and citric acid. The pH value of the solution was adjusted to the range of 7–9 with $NH_3 \cdot H_2O$. The transparent reaction solution was then heated at 423 K under constant stirring for several hours until a purple-colored gel was obtained. The gel was then pre-calcined in the temperature range of 573–673 K. Following, the precalcined powders were ground and fired at 1223 K for 10 h. To obtain the BSCF ceramic, the powder was uniaxially pressed under 140–150 kN for 20 min into green bodies. The pellets were then calcined for 10 h at 1423 K with a heating and cooling rate of 3 K/min.

An oxygen permeation measurement was performed on a dense membrane disk with a diameter of 16 mm and a thickness of 1.1 mm in a high-temperature permeation cell according to the method described elsewhere.[18,19] The reactor temperature was kept constant at 1023 K for more than 240 h. Air was fed at a rate of 150 mL min^{-1} to the feed side; He (29.0 mL min^{-1}, 99.995%) and Ne (1.0 mL min^{-1}, 99.995%), which were used to determine the absolute flux rate of the effluents, were fed to the sweep side. The effluents were analyzed by gas chromatography on an Agilent 6890 instrument equipped with a Carboxen 1000 column. Gas concentrations in the effluent stream were calculated from a gas chromatograph calibration.

A powder XRD sample was obtained from the BSCF ceramic after annealing at 1023 K for 240 h and subsequent grinding. The XRD data were collected in a $\Theta/2\Theta$ geometry on a Philips X'pert-MPD instrument with monochromated Cu Kα radiation at 40 kV and 40 mA and a receiving slit of 0.05 mm using a step–scan mode in the 2Θ range of 15°–90° with intervals of 0.02°.

In order to obtain a TEM sample, the annealed BSCF ceramic was cut into rectangular pieces of 1 mm × 1.5 mm × 3 mm. The BSCF powder sample was epoxy glued between two pieces of silicon wafer before cutting. Subsequently, the pieces were polished on polymer-embedded diamond lapping films to approximately 0.01 mm × 1 × 2.5 mm (Allied High Tech, Multiprep). Finally, Ar$^+$ ion sputtering was employed at 3 kV (Gatan, model 691 PIPS, precision ion polishing system) under shallow incident angles in the range of 4–8° until electron transparency was achieved.

Scanning TEM (STEM) and TEM, as well as SAED, were conducted at 200 kV on a JEOL JEM-2100F-UHR field-emission instrument equipped with an ultrahigh-resolution pole piece that provided a point-resolution better than 0.19 nm (spherical

(14) Goldschmidt, V. M. *Naturwissenschaften* **1926**, *14*, 477.
(15) Arnold, M.; Xu, Q.; Tichelaar, F. D.; Feldhoff, A. *Chem. Mater.* **2009**, *21*, 635.
(16) Mueller, D. N.; De Souza, R. A.; Weirich, T. E.; Roehrens, D; Mayer, J.; Martin, M. *Phys. Chem. Chem. Phys.* **2010**, *12*, 10320.
(17) Arnold, M.; Gesing, T. M.; Martynczuk, J.; Feldhoff, A. *Chem. Mater.* **2008**, *20*, 5881.

(18) Wang, H.; Tablet, C.; Feldhoff, A.; Caro, J. *J. Membr. Sci.* **2005**, *262*, 20.
(19) Martynczuk, J.; Arnold, M.; Feldhoff, A. *J. Membr. Sci.* **2008**, *322*, 375.
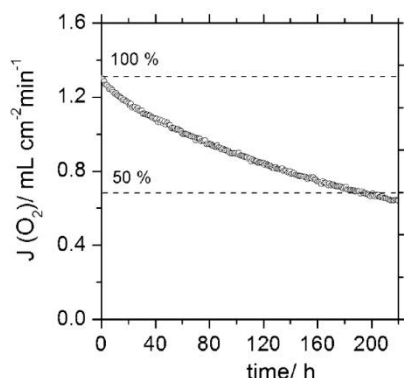
Efimov et al.

Figure 1. Oxygen permeation flux through BSCF membrane as a function of time at 1023 K.

aberration constant C_S = 0.5 mm; chromatic aberration constant C_C = 1.2 mm) and allowed high-resolution TEM (HRTEM) acquisition. A light element EDX spectrometer, Oxford Instruments INCA-200 TEM, was used for elemental analysis. An energy filter of the type Gatan GIF 2001 was employed to acquire electron energy-loss spectra (EELS). HR-STEM high angle annular dark field (HAADF) experiments were conducted with an FEI Titan electron microscope equipped with an aberration image corrector at 300 kV

Results and Discussion

The oxygen permeation performance of the BSCF ceramic was tested at 1023 K. As demonstrated in Figure 1, the oxygen flux through the BSCF membrane decayed continuously to about 50% after 240 h. This result was in good agreement with the results reported by Shao et al.[4] and van Veen et al.[12] The degradation of the BSCF functional properties at intermediate temperatures can be due to several reasons. First, the concentration of mobile oxygen vacancies in the perovskite lattice can be decreased due to a change in oxidation state of the B-cations, as recently reported.[12,20] Second, the continuously decreasing oxygen permeation performance of BSCF under long-term conditions can be explained by the growth of noncubic phases during operation, which might act as barriers, and by a change of stoichiometry of the cubic phase.

Figure 2a,b shows the XRD data taken from the BSCF powder as well as from ground BSCF ceramic after annealing at 1073 K for 180 h and at 1023 K for 240 h, respectively. Obviously, the cubic perovskite remained as the major phase in both samples. However, the presence of noncubic phases was evident on the basis of the weak additional intensities between 25° and 28° and 42.5° 2Θ, which are marked with an asterisk. Rebeilleau-Dassonneville et al. observed additional reflections at the same positions in the BSCF diffraction pattern during in situ XRD experiments at temperatures below 1023 K.[7] Thus, it may be concluded that the noncubic phases arose before quenching of the sample. Due to the restricted number of reflections from the noncubic phases and those weak intensities, the
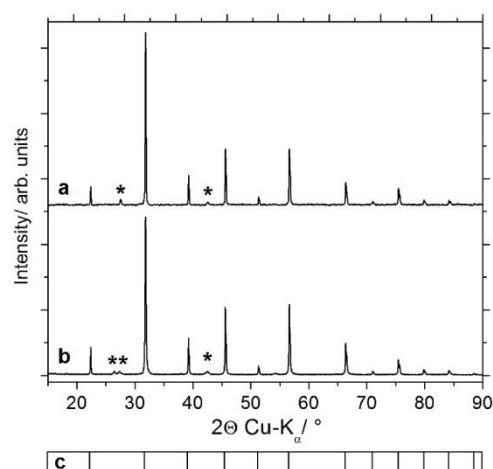
(20) Kriegel, R; Kircheisen, R; Töpfer, J. *Solid State Ionics* **2010**, *181*, 64.

Figure 2. (a) XRD pattern of the BSCF powder after annealing at 1073 K for 180 h. (b) XRD pattern of the BSCF ceramic after annealing at 1023 K for 240 h. The intensities corresponding to noncubic phases are marked with asterisks. (c) The Bragg positions correspond to cubic perovskite with a = 0.398 nm.

noncubic phases could not be identified by XRD in this work either.

Nevertheless, with help of several TEM methods, it was possible to detect and analyze the noncubic phases in the annealed BSCF powder and ceramic samples. A TEM dark-field micrograph in Figure 3a shows an area of the powder sample. An interface between two grains is clear in this image. A HRTEM (Figure 3b) micrograph of the marked grain showed a hexagonal symmetry of the grain structure. Furthermore, the fast Fourier transform (FFT) in Figure 3c can be explained by the reciprocal lattice of hexagonal perovskite being viewed along the $[0,1,0]_{hex}$ orientation due to a spacing of 0.49 nm between the $(100)_h$ planes and $(010)_h$ planes. The chemical composition of the hexagonal phase was determined by EDX spectroscopy to be $Ba_{0.6}Sr_{0.4}CoO_{3-\delta}$. Hexagonal perovskites with similar composition have been previously reported by Gushee et al.[21] and Taguchi et al.[22] Accordingly, the transition of cubic BSCF into a hexagonal perovskite phase after annealing at intermediate temperatures, as reported by Švarcová et al.[13] and Mueller et al.,[16] was confirmed during the current TEM study.

Furthermore, the partial transformation of cubic BSCF to noncubic phases, which had the shape of lamellae, was observed in the treated powder sample. Similar lamellae could be seen in the TEM micrograph of Mueller et al., but they were not addressed further there.[16] A HRTEM micrograph in Figure 4a shows one lamella and the parent phases. The structure of the lamella, which was approximately 50 nm wide, consisted mainly of periodically ordered segments with a distance of 1.19 nm between them. As can be observed in the SAED pattern of the corresponding sample area in Figure 4b, which was acquired from the

(21) Gushee, B. E.; Katz, L.; Ward, R. *J. Am. Ceram. Soc.* **1957**, *79*, 5601.
(22) Taguchi, H.; Takeda, Y.; Kanamaru, F.; Shimada, M.; Koizumi, M. *Acta Crystallogr., Sect. B* **1977**, *33*, 1299.
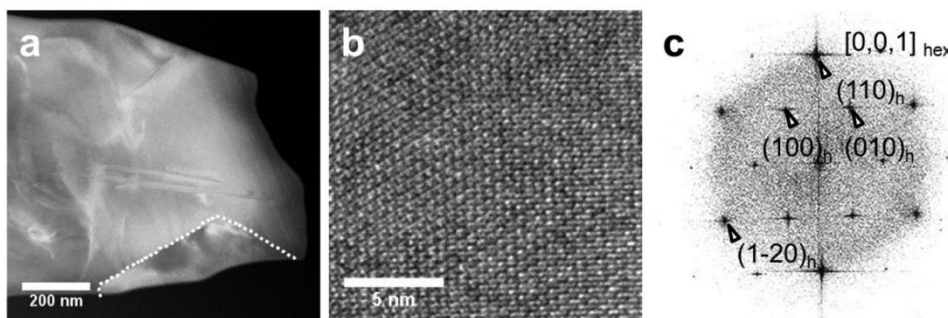
Figure 3. (a) STEM annular dark-field micrograph showing an interface between two grains in the BSCF powder sample annealed at 1073 K for 180 h. (b) HRTEM micrograph of the marked grain. (c) Power spectrum of (b).
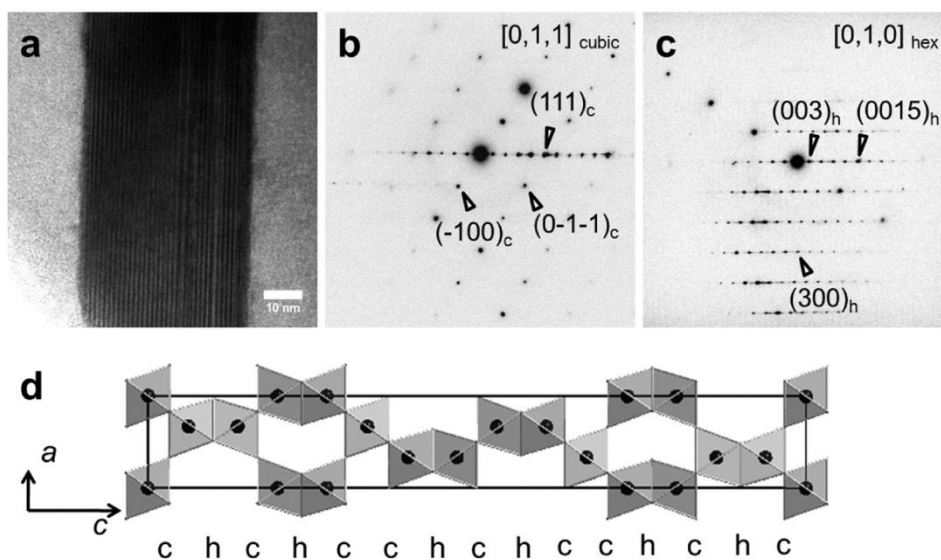

Figure 4. (a) HRTEM micrograph showing a lamella in the BSCF powder sample after annealing at 1073 K for 180 h. (b) SAED pattern from the corresponding area. (c) SAED pattern from the lamella achieved by tilting of the sample. (d) 15R structural model viewed along the [0,1,0] direction using $(cchch)_3$ stacking sequences of BO_6 octahedra.

selected sample area with a size of approximately 260 nm, the lamella grew in the cubic perovskite grain oriented along the $[0,1,1]_{cubic}$ direction. The segments of the lamella were arranged parallel to the $(111)_{cubic}$ plane. The spacing between the lamella segments was approximately equal to a 5-fold (111) spacing of cubic perovskite ($d_{(111)} = 0.23$ nm), which corresponds to the spacing between cubic-close packed AO_3 layers. Hence, it can be concluded that one segment of the lamella consisted of five close-packed layers. Note that these five close-packed layers were not necessarily all cubic-close stacked. Some of them may have been hexagonal-close stacked, making the whole structure a noncubic phase. Similar structures containing five-layered segments were once described for hexagonal perovskite polytypes of 5H $BaCoO_{3-\delta}$ by Miranda et al., as well as 15R $SrMn_{1-x}Fe_xO_{3-\delta}$ by Cussen et al.[23,24] The

SAED pattern from the lamella shown in Figure 4c was obtained by tilting of the sample. The intensity distribution of the diffraction data revealed the rhombohedral symmetry of the lamella, which can be explained using a hexagonal unit cell. The rhombohedral symmetry of the lamella structure appeared if the close-packed layers were arranged in a $(cchch)_3$ stacking sequence along the c_{hex} axis, as shown in the Figure 4d. Moreover, the lamella's diffraction pattern exhibited a distinct correlation with the diffraction pattern of 15R $SrMn_{1-x}Fe_xO_{3-\delta}$ with the $(cchch)_3$ stacking sequence viewed along the $[0,1,0]_{hex}$ direction.[24] Consequently, the lamella can be considered a 15R related phase with a hexagonal unit cell. The lattice parameter $c_{hex} \approx 3.57$ nm of the unit cell was estimated from the HRTEM and SAED. The parameter $a_{hex} \approx 0.56$ nm was estimated using the formula $a_{hex} = a_{cubic}((2)^{1/2})$.[25] The relationship between cubic perovskite and hexagonal perovskite polytypes in terms of the cubic-closed and

(23) Miranda, L.; Feteira, A.; Sinclair, D. C.; Hernández, M. G.; Boulahya, K.; Hernando, M.; Varela, A.; González-Calbet, J. M.; Parras, M. *Chem. Mater.* **2008**, *20*, 2818.

(24) Cussen, E. J.; Sloan, J.; Vente, J. F.; Battle, P. D.; Gibb, T. C. *Inorg. Chem.* **1998**, *37*, 6071.

(25) Mitchell, R. H. *Perovskites: Modern and Ancient*; Almaz Press Inc.: Ontario, Canada, 2002.
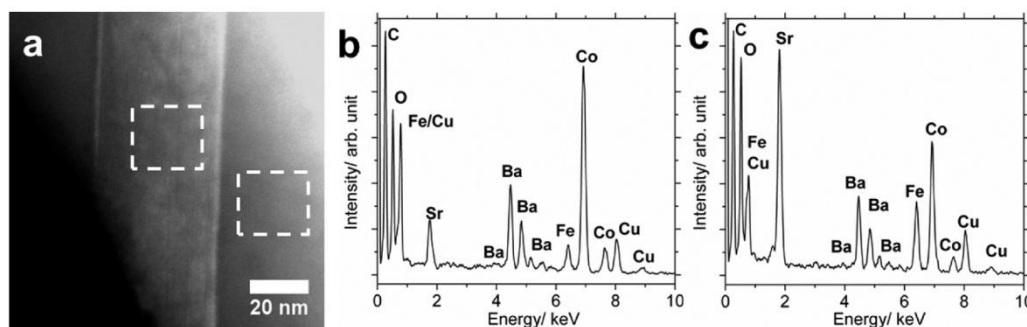
Figure 5. (a) STEM annular dark-field micrograph with labeling of scanned areas for elemental analysis. (b) EDX spectrum of the lamella. (c) EDX spectrum of the parent cubic phase. C and Cu lines appear due to a narrow TEM pole piece.
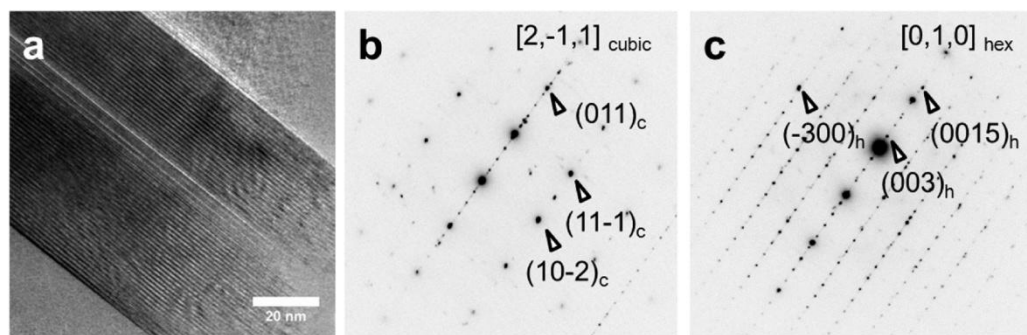

Figure 6. (a) HRTEM micrograph showing the lamella in the BSCF ceramic sample annealed at 1023 K for 240 h. (b) SAED pattern from the lamella and the matrix. (c) SAED pattern from the lamella achieved by tilting of the sample as compared to (b).

hexagonal-closed stacking of AO_3 was described by Katz et al. in detail.[26] A possible pathway of the transition from cubic perovskite to hexagonal polymorphs via a shear of the AO_3 layers has been reported by Arnold et al.[15,27] In terms of the cubic cell, the AO_3 layers oriented perpendicular to the [1,1,1] cubic zone axis form cubic-close packing. B-cations occupy the octahedral holes, and octahedra generate a three-dimensional corner-sharing array. The shear of some AO_3 layers leads to the formation of hexagonal-close packing and face-shared octahedral columns along the [1,1,1] cubic orientation. The arrangement of the five-layered sequences of the lamella parallel to the (111) cubic plane can be explained with this pathway.

By STEM high angle annular dark-field (HAADF) and EDXS experiments, anomalies of the lamellar chemical composition could be observed. The STEM HAADF micrograph in Figure 5a shows inhomogeneous elemental distribution inside of the lamella in spots with a bright Z-contrast. Figure 5b shows an EDX spectrum acquired from a wide area of lamella labeled in Figure 5a. Using Cliff-Lorimer quantification, a considerable accumulation of cobalt of up to 63 atom % of the total value of cations was detected in the lamella. A moderate enrichment of barium of up to 30 atom % as well as a strong

depletion of strontium and iron was also observed. On average, the amount of the B-cations exceeded the content of A-cations in the lamella by 2-fold. Thus, the EDX spectroscopy delivered surprising results, because hexagonal perovskite-related phases with such stoichiometry are not known. In contrast, the spectrum of the matrix phase (Figure 5c) showed the expected intensity distribution of element lines for the cubic BSCF perovskite.

Lamellar phases were also found in the BSCF ceramic sample annealed at 1023 K for 240 h. One of them is displayed in the HRTEM micrograph in Figure 6a. The lamella were mainly organized in periodically stacked segments. Furthermore, in the middle of the lamella, a thin area with a nonperiodic arrangement of the segments was observed. The SAED pattern from the lamella and the matrix acquired from the selected sample area with a size of approximately 260 nm (Figure 6b) revealed that the lamellae grew in the cubic perovskite grain oriented along the $[2,\bar{1},1]_{cubic}$ zone axis. The segments of the lamella were arranged parallel to the (011) cubic plane. The spacing between periodic segments was 1.19 nm, which is the same distance between segments of the lamella found in the powder sample. By tilting of the sample, the lamella were oriented along the $[0,1,0]_{hex}$ direction. The intensity distribution in the SAED pattern in Figure 6c shows rhombohedral symmetry of the lamellar structure. The comparison of the diffraction data from the lamella in the ceramic sample with the SAED pattern from the

(26) Katz, L.; Ward, R. *Inorg. Chem.* **1964**, *3*, 205.
(27) Arnold, M.; Wang, H.; Martynczuk, J.; Feldhoff, A. *J. Am. Ceram. Soc.* **2007**, *90*, 3651.

lamella in the powder sample (Figure 4c) lead to the conclusion that the lamellae were isostructural with each other. However, the lamella formed in the annealed ceramic did not grow parallel to the close-packed layer of the cubic matrix; the regular part of the lamella can instead be explained by a 15R-related structure. Diffraction spots that cannot be attributed to the 15R setting are likely related to the stacking faults in the middle area of the lamella in Figure 6a.

EDX spectroscopy investigations of the chemical composition indicated the presence of twice the amount of B-cations compared to A-cations in the lamella in the ceramic sample. In order to elucidate structural information in accordance with the chemical composition of the lamellae, which is unusual for hexagonal perovskite-related compounds, high resolution (HR) STEM HAADF experiments were carried out that determine the positions of atoms by mass-density contrast distribution. The HR-STEM HAADF micrograph in Figure 7a and Fourier averaged HRSTEM micrograph in Figure 7b show further lamella in the annealed ceramic sample. The lamella is viewed along the $[\bar{1},1,0]_{hex}$ direction. In this projection, it is clearly evident that the regular segments of the lamella structure contain five layers: three layers consisting of bright dots and two dark rows separated by chains with lower contrast in between. The dots with a bright Z-contrast relate to the positions of A-cations due to their atomic weight, and the two dark rows indicate missing A-cation positions. The Z-contrast intensity distribution of the layers achieved from the marked area in the Fourier averaged STEM micrograph is plotted in Figure 7c. The average contrast ratio between the chain with medium contrast and three layers with bright contrast was 0.67. According to the relationship of the lamella structure to the 15R setting and the results of EDX spectroscopy, the three layers with bright contrast in Figure 7a,b relate to columns containing A-cations (mostly barium) and oxygen. The chain with medium contrast corresponds to double B-cation (mostly cobalt) columns. The contrast ratio between the columns was calculated as follows: ratio = $Z(Co + Co)^2/Z(Ba + O)^2 = 0.71$, which is consistent with the measured contrast ratio. As suggested by the Z-contrast pattern and intensity distribution, a structural model of the five-layered segment of the regular part of the lamella viewed along the $[\bar{1},10]$ orientation, as shown in Figure 7d, was proposed. The lamella structure is assembled from three AO_3 layers and two O_3 layers, which are in a quasi-close-packed arrangement along the c_{hex} axis. B-cations occupy a quarter of the octahedral sites between the layers, as in the perovskite structure. Additionally, a quarter of the disordered octahedral sites between the two O_3 layers is occupied by extra B-cations. In the structural model, the circles point to columns with A-cation vacancies and the arrows mark the double B-cation columns. The chemical composition of the lamella can be described with the general formula of $(A_3B_6O_{15})_3$, corresponding to the 15R setting. According to results of EDX spectroscopy and HRSTEM, as well as the expected presence of oxygen vacancies, an empirical formula of
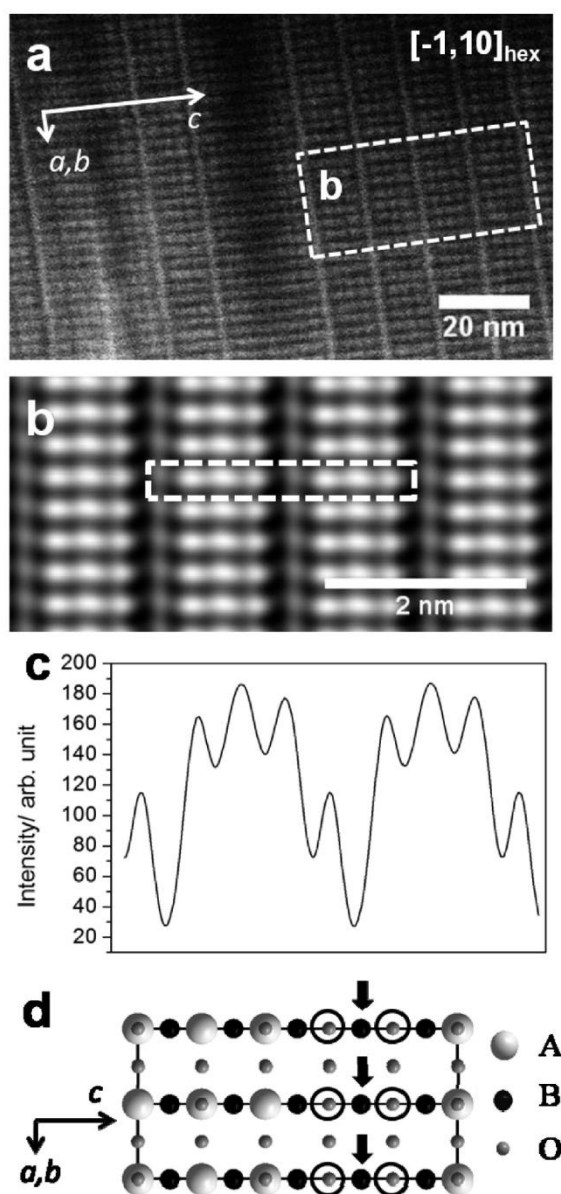
Figure 7. (a) HR-STEM annular dark-field micrograph of the lamella viewed along the $[\bar{1},1,0]_{hex}$ direction. (b) Fourier averaged HR-STEM micrograph from the area labeled in (a). (c) Z-contrast intensity distribution taken from the area labeled in (b). (d) Schematic representation of the five-layered segment of the $Ba_{1-x}Sr_xCo_{2-y}Fe_yO_{5-\delta}$ structure as suggested by the Z-contrast pattern. Circles mark A-cation vacancies, and arrows point to double B-cations columns.

$Ba_{1-x}Sr_xCo_{2-y}Fe_yO_{5-\delta}$ of the lamella phase is proposed. The report from Sun et al. concerning new barium cobaltite $Ba_3Co_{10}O_{17}$ gives a further insight into the development of a $Ba_{1-x}Sr_xCo_{2-y}Fe_yO_{5-\delta}$ structure model, because $Ba_3Co_{10}O_{17}$ exhibits the 15R related structure containing close-packed BaO_3 and an oxygen layer array with completely occupied octahedral sites with cobalt cations in the oxygen layer.[28]

(28) Sun, J.; Yang, M.; Li, G.; Yang, T.; Liao, F.; Wang, Y.; Xiong, M.; Lin, J. *Inorg. Chem.* **2006**, *45*, 9151.
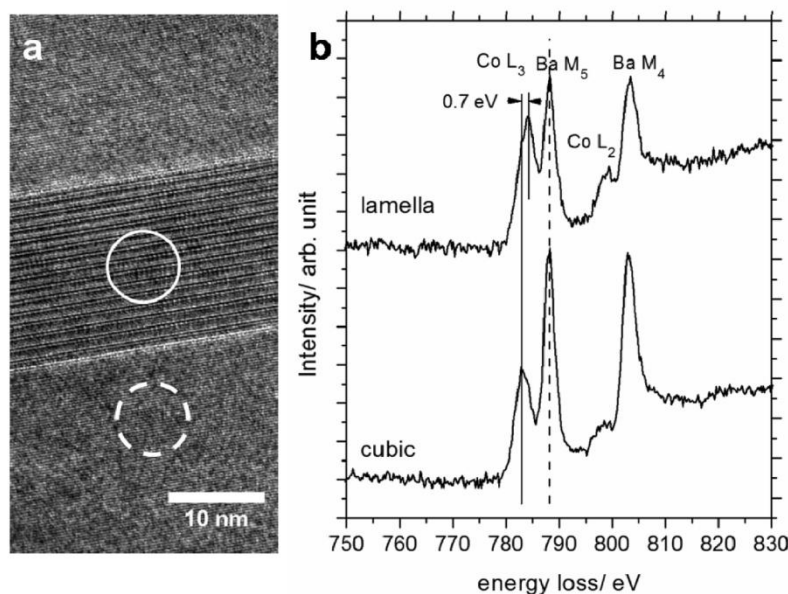
Figure 8. (a) HRTEM micrograph with labeling of area for EELS. (b) Electron energy-loss spectra showing cobalt-$L_{2,3}$ and barium-$M_{4,5}$ ionization edges of lamella and the cubic phase.

Furthermore, with the help of the HR-STEM HAADF micrograph in the Figure 7a, the above-mentioned inhomogeneous elemental distribution in the lamellae can be explained. Obviously, in some areas of the lamella, all barium sites in the close-packed layer remained occupied.

The significant difference between phases with hexagonal stacking of close-packed layers from the cubic perovskites is the up to 10 pm closer B-site cation−oxygen distances in the octahedral sites. Accordingly, smaller cations favor occupation at the octahedral sites in the hexagonal stacking. The ionic radius of multivalent B-cations is strongly connected with their valence and spin state.[29] Because the structure of the lamellae contains hexagonal-close packed layers, an average higher valence of B-cations, especially cobalt, compared to cubic perovskite is expected. In order to verify this assumption, EEL spectra were acquired from the cubic phase and $Ba_{1-x}Sr_xCo_{2-y}$-$Fe_yO_{5-\delta}$ lamella of the ceramic sample annealed at 1023 K for 240 h corresponding to the marked areas in a Figure 8a. The cobalt $L_{2,3}$ and barium $M_{4,5}$-edges from the cubic phase and lamella are plotted in the Figure 8b. The EEL spectrum of the lamella showed a significant increase in the cobalt-L_3/barium-M_5 and cobalt-L_2/barium-M_4 intensity ratios as compared to the spectra from the cubic phase. This fact confirms the accumulation of cobalt in the lamella. An additional feature of the EEL spectra from the lamella was the shift of the cobalt L_3-edge position at approximately 0.7 eV to a higher energy loss, which was determined using the barium M_5-edge (788 eV at maximum) as an internal standard.[15] A reason for the L_3-edge shift is the increase in the average cobalt valence in the lamellae.[30] Arnold et al.

determined the mixed 2+/3+ valence state of cobalt with absolute value of 2.6+ in the cubic BSCF perovskite at room temperature by comparing the cobalt L_3-edge of cubic BSCF with those of well-known materials.[26] However, the measured value of cobalt valence may be slightly higher due to the long-term annealing at intermediate temperatures, as reported by Kriegel et al.[16] In comparison, the valence state of cobalt in the $Ba_{1-x}Sr_xCo_{2-y}$-$Fe_yO_{5-\delta}$ lamella was close to +3 and was measured in the same way that the shift of the cobalt L_3-edge was monitored. Then, the predominantly valence state of cobalt of 3+ in the lamella phase can be estimated. The presence of a certain amount of Co^{4+} in the lamella phase is expected also.[31] As a consequence of the rising valence of cobalt, the amount of oxygen vacancies (δ) in the lamella should be considerably lower than that in the cubic matrix. Combined with the low crystal symmetry, the presence of lamellae in BSCF can be considered to be unfavorable for its oxygen conducting properties. Because lamellae are several micrometers long, they can be considered as barriers to ionic oxygen transport through a BSCF membrane.

The findings of the EELS experiments confirmed the driving force of the BSCF decomposition postulated by Arnold et al.,[15] who suggested that it was a temperature-dependent change of cobalt valence coupled with a partial spin-state transition of cobalt ions.[31,32] The oxidation of cobalt leads to a diminution of its ionic radius from Co^{2+}-(high spin) = 74.5 pm to Co^{3+}(high spin) = 61 pm, Co^{3+}-(low spin) = 54.5 pm, and Co^{4+}(high spin) = 53 pm.[29] The

(29) Shannon, R. D. *Acta Crystallogr., Sect. A* **1976**, *32*, 751.
(30) Yoon, W. S.; Kim, K. B.; Kim, M. G.; Lee, M. K.; Shin, H. J.; Lee, J. M.; Lee, J. S. *J. Phys. Chem. B* **2002**, *106*, 2526.

(31) Harvey, A. S.; Yáng, Z.; Infortuna, A.; Beckel, D.; Purton, J. A.; Gauckler, L. J. *J. Phys.: Condens. Matter* **2009**, *21*, 015801.
(32) Harvey, A. S.; Litterst, F. J.; Yáng, Z.; Rupp, J. L. M.; Infortuna, A.; Gauckler, L. J. *Phys. Chem. Chem. Phys.* **2009**, *11*, 3090.

small cobalt cations are not tolerated in the cubic perovskite structure because they favor occupying the face-shared octahedral sites in the hexagonal stacking with a closer B−O distance. The observation of Nagai et al. suggests a labile cobalt valence and spin state as being responsible for BSCF decomposition, because many cobalt-based cubic perovskites break down via the formation of hexagonal/cubic phase mixtures at temperatures below 1173 K.[33] Furthermore, the cobalt-free iron-based cubic perovskites of the compositions $(Ba_{0.5}Sr_{0.5})$-$(Fe_{0.8}Cu_{0.2})O_{3-\delta}$ and $(Ba_{0.5}Sr_{0.5})(Fe_{0.8}Zn_{0.2})O_{3-\delta}$, which are related to BSCF, show good stability under long-term conditions at temperatures below 1173 K, owing to the less flexible redox behavior of iron.[34−36]

We observed about 20 sample areas in both the BSCF powder annealed at 1073 K for 180 h and the sintered ceramic annealed at 1023 K for 240 h. We observed that the growth of lamellae often occurred in various directions in the cubic perovskite grain. Such a situation is obvious in the TEM bright field micrograph in Figure 9a, which shows several micrometer-long lamellae arranged in three different directions in the ceramic sample. The matrix phase was characterized by the HRTEM micrograph in Figure 9b combined with the two-dimensional fast Fourier transformation (FFT) from the corresponding area (Figure 9c) to be a cubic perovskite grain, viewed along the $[0,1,1]_{cubic}$ zone axis. Note that the lamellae grew through the BSCF grain bulk and not along the grain boundaries. The lamellae marked in Figure 9a with a dashed line are also shown in Figure 9b under high resolution magnification. The FFT from the related area in Figure 9d exhibited a reciprocal lattice of the $Ba_{1-x}Sr_{x}$-$Co_{2-y}Fe_{y}O_{5-\delta}$ structure viewed along the $[\bar{1},1,0]_{hex}$ orientation. The segments of the lamella formed parallel to the (100) cubic plane. The lamella marked in Figure 9a with the dotted line were located at an angle of approximately 25°. Because the angle between the (100) and $(3\bar{1}1)$ cubic planes amounted to 25.24°, the growth direction of the lamella was indicated to be parallel to the $(3\bar{1}1)$ cubic plane. The growth direction of the lamella marked with the dashed-dotted line parallel to the $(2,\bar{1},1)$ cubic direction was determined analogously to the angle between the lamellae of approximately 35° and the angle between the (100) and $(2,\bar{1},1)$ cubic directions of 35.26°. The formation of lamellae along the (100), $(2\bar{1}1)$, and $(3\bar{1}1)$ cubic directions cannot be explained by the shear of close-packed layers of the cubic parent phase. A geometrical approach considering tilting of the coordination polyhedrons does not provide a solution either. It appears that complex reconstructive transformations influenced by the change of chemical composition occurred during the BSCF decomposition process. Recently, Yi et al. attested high creep rates of BSCF at the
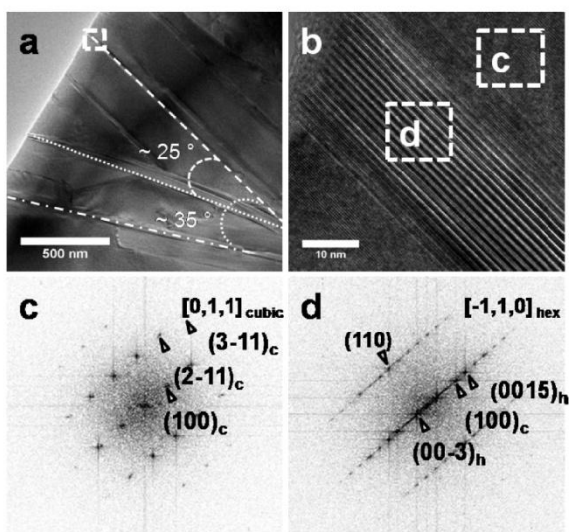
Figure 9. (a) TEM bright-field micrograph of the annealed BSCF ceramic sample showing lamellae grown along different directions. (b) HRTEM micrograph of the marked area in (a). (c, d) Two-dimensional fast Fourier transformed related to the marked areas in (b).
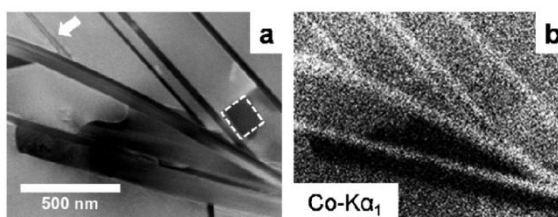
Figure 10. (a) STEM annular dark-field micrograph showing platelike phases adjacent to lamellae. Arrow marks the lamella shown in Figure 11. Rectangle marks the area of the $Ba_{0.6}Sr_{0.4}CoO_{3-\delta}$ composition. (b) Cobalt distribution by EDX spectroscopy using the Co $K\alpha_1$ line.

relevant temperatures. The creep was found to be controlled by cation diffusion.[11] Hence, the high cation mobility in the BSCF delivers a possible explanation for the BSCF phase transition into compounds with unusual compositions via complex pathways.

Due to the fact that the lamellae are cobalt enriched, the presence of phases with low cobalt concentrations were expected in the annealed BSCF samples. Indeed, cobalt-depleted phases were detected by EDXS. Figure 10a shows the STEM HAADF micrograph that was acquired from the detail of the sample area presented in Figure 9a showing platelike phases adjacent to the lamellae. In the elemental distribution by EDXS in Figure 10b, a strong depletion of cobalt in the platelike phases is clearly evident. Furthermore, the Cliff-Lorimer quantification of the EDXS data indicated a slight accumulation of strontium of up to 60 atom % of the total value of cations, as well as an absence of iron in these phases. According to the EDXS results, the platelike phases are related to a mixed barium strontium oxide with the stoichiometry $Ba_{0.4}Sr_{0.6}O$. With help of EDX spectroscopy, a phase was detected (marked by a rectangle in the STEM HAADF

(33) Nagai, T.; Ito, W.; Sakon, T. *Solid State Ionics* **2007**, *177*, 3433.
(34) Efimov, K.; Halfer, T.; Kuhn, A.; Heitjans, P.; Caro, J.; Feldhoff, A. *Chem. Mater.* **2010**, *22*, 1540.
(35) Martynczuk, J.; Efimov, K.; Robben, L.; Feldhoff, A. *J. Membr. Sci.* **2009**, *344*, 62.
(36) Feldhoff, A.; Martynczuk, J.; Arnold, M.; Myndyk, M.; Bergmann, I.; Šepelák, V.; Gruner, W.; Vogt, U.; Hähnel, A.; Woltersdorf, J. *J. Solid State Chem.* **2009**, *182*, 2961.

Figure 11. HRTEM micrograph showing the presence of cubic phase inside the lamella.

micrograph in Figure 10a) that contained barium, strontium, and cobalt in proportions similar to the hexagonal perovskite $Ba_{0.6}Sr_{0.4}CoO_{3-\delta}$. Further, a lower amount of cobalt in one lamella marked by an arrow in Figure 10a compared to other lamellae was found by quantification of the EDXS data. This lamella is shown in the HRTEM micrograph in Figure 11. Obviously, the lamella contained areas with different structures. The areas "I" on the edges of the lamella exhibited the 15R-related $Ba_{1-x}Sr_x$-$Co_{2-y}Fe_yO_{5-\delta}$ structure viewed along the $[\bar{1},1,0]_{hex}$ orientation. The areas "II" in the middle of the lamella had a cubic structure and are viewed along the $[1,0,0]_{cubic}$ zone axis, different from the parent cubic phase oriented along the $[0,1,1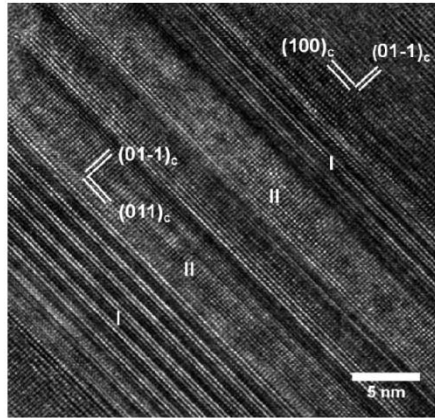]_{cubic}$ zone axis. The presence of cubic phase inside the lamella explains its lower cobalt content and emphasizes the complex transformation process of cubic perovskite into the $Ba_{1-x}Sr_xCo_{2-y}Fe_yO_{5-\delta}$ structure. It is clearly seen that the diffusion of metal ions play a decisive role in the decomposition process of BSCF. Hence, under the present conditions, BSCF does not exhibit a rigid cationic lattice in that only the oxygen is mobile. This observation supports the interpretation of high creep rates in the intermediate temperature range by Yi et al.[11]

On the basis of the annealing times of the BSCF samples, we assume that the phases reached equilibrium at the conditions under consideration. Figure 12 summarizes the decomposition process of BSCF. The products of BSCF phase transition, cobalt-enriched hexagonal perovskite $Ba_{0.6}Sr_{0.4}CoO_{3-\delta}$, 15R-related $Ba_{1-x}Sr_xCo_{2-y}$-$Fe_yO_{5-\delta}$ complex oxide, and barium, strontium mixed oxide were detected in the TEM study. Because no phases strongly enriched in strontium and iron were found in the annealed BSCF samples, the remaining of strontium and iron in the cubic perovskite may be proposed. Recently, Yáng et al. developed a phase map of a quasi-quaternary Ba−Sr−Co−Fe oxide system at 1273 K, which we adapted in Figure 13.[37] According to this phase map, the end members of the quasi-quaternary system reject to form
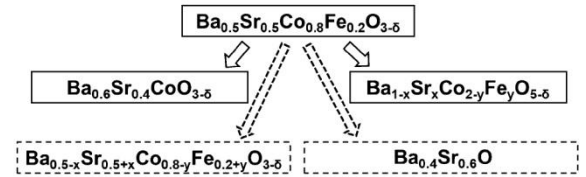
Figure 12. Schematic representation of the BSCF decomposition process.
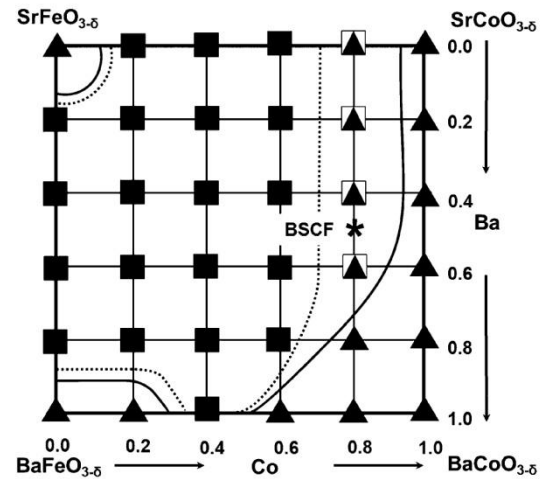
Figure 13. Schematic phase diagram of the quasi-quaternary Ba−Sr−Co−Fe oxide system. Adapted with permission from ref 37. Copyright 2009 International Union of Crystallography. The cubic phases are marked with square symbols; triangle symbols relate to the multiphase compounds. The borderlines each of which is associated with miscibility gap are drawn tentatively as solid lines at 1273 K and as dashed lines at temperatures below 1073 K.

the pure cubic phase. However, the cubic phase prevailed after the mixing of Ba/Sr at the A-site and Co/Fe at the B-site apart from barium- and cobalt-rich compositions. Furthermore, the cubic perovskite can be considered as more stable in the strontium- and iron-rich composition. However, then, it might exhibit poorer transport properties as compared to the initial BSCF composition. Each of the borderlines between the cubic phase field and multiphase compounds in Figure 13 is associated with a miscibility gap, which occurs between phases of dissimilar crystal structures according to the Hume−Rothery rules.[38] The results of the TEM study of BSCF decomposition point out, that the multiphase compound's area to the right of BSCF expands in the direction of strontium- and iron-rich composition in the intermediate temperature range as marked by a dashed line in Figure 13; i.e., the cubic phase field becomes narrowed as temperature decreases from, e.g., 1273 to 1073 K or lower. At temperatures below 1073 K, the parent BSCF phase is located in a miscibility gap between cubic phase and multiphase compounds, which is in good agreement with the report of Mueller et al.[16] Looking again at the Hume−Rothery rules,

(37) Yáng, Z.; Harvey, A. S.; Infortuna, A.; Gauckler, L. J. *J. Appl. Crystallogr.* **2009**, *42*, 153.

(38) Hume-Rothery, W.; Smallman, R. W.; Haworth, C. W. *The Structure of Metals and Alloys*; The Institute of Metals: London, 1969.

we may conclude that effective ionic radii influence the location of the miscibility gap (i.e., the borderlines in Figure 13). In this context, we emphasize that the multiphase formation is initialized by the coupled oxidation and spin-state transition of cobalt cations diminishing their effective ionic radii, which are not tolerated in the cubic perovskite structure. This view is supported by the postulations given by Švarcová et al. and Arnold et al.[13,15,17] In consequence, the cubic BSCF breaks down into the above-mentioned phases involving diffusion of the metal cations.

Conclusions

The current research attests the inherent phase instability of BSCF during heating at intermediate temperatures. We observed that cubic perovskite decomposed into hexagonal perovskite $Ba_{0.6}Sr_{0.4}CoO_{3-\delta}$, lamellar-shaped $Ba_{1-x}Sr_xCo_{2-y}Fe_yO_{5-\delta}$ complex oxide, and $Ba_{0.4}Sr_{0.6}O$. The structure of the previously unknown $Ba_{1-x}Sr_xCo_{2-y}Fe_yO_{5-\delta}$ phase was found to be related to the structure of the 15R hexagonal perovskite polymorph. The several micrometer-long $Ba_{1-x}Sr_xCo_{2-y}Fe_yO_{5-\delta}$ lamellae grew along different directions through the parent cubic phase and can be considered as barriers to oxygen transport due to their shape, low crystal symmetry, and low amount of mobile oxygen vacancies. A change in stoichiometry of the cubic phase is another reason for the degradation of the functional properties. The results of the TEM study support the postulated reason for BSCF decomposition at intermediate temperatures, which has been suggested to be coupled to the valence and spin-state transitions of cobalt ions.

2.3 Oxygen-vacancy related structural phase transition of Ba$_{0.8}$Sr$_{0.2}$Co$_{0.8}$Fe$_{0.2}$O$_{3-\delta}$

Zhèn Yáng, Julia Martynczuk, Konstantin Efimov, Ashley S. Harvey,

Anna Infortuna, Peter Kocher, and Ludwig J. Gauckler

Oxygen-vacancy related structural phase transition of Ba$_{0.8}$Sr$_{0.2}$Co$_{0.8}$Fe$_{0.2}$O$_{3-\delta}$

Zhèn Yáng [1], Julia Martynczuk [1], Konstantin Efimov [2], Ashley S. Harvey [1], Anna Infortuna [1], Peter Kocher [1], and Ludwig J. Gauckler [1]

1. Nonmetallic Inorganic Materials, Department of Materials, ETH Zurich, 8093 Zurich, Switzerland

2. Institute of Physical Chemistry and Electrochemistry, Leibniz Universitaet Hannover, D-30167 Hannover, Germany

Abstract

Ba$_{0.8}$Sr$_{0.2}$Co$_{0.8}$Fe$_{0.2}$O$_{3-\delta}$ exists as a single cubic phase at 1000 °C in air. Upon slow cooling it transforms, between 900 and 700 °C, to a mixture of cubic, hexagonal, and rhombohedral phases, as evidenced by X-ray diffraction and transmission electron microscopy. The reversible phase change is accompanied by a large change of the oxygen content ($\Delta\delta$ = 0.14) of Ba$_{0.8}$Sr$_{0.2}$Co$_{0.8}$Fe$_{0.2}$O$_{3-\delta}$ and a volume change of 1.2 vol.% at 700-900 °C. The multiphase material shows lamellar shaped structures in the HRTEM micrographs due to the partial transformation of the material from the cubic to the hexagonal and rhombohedral symmetry. The electrical conductivity changes from *p*-type semiconductivity between room temperature and 700 °C to metal-like conductivity at higher temperatures up to 1000 °C. The electrical conductivity of ceramic components is irreversibly changed upon thermal cycling due to the formation of microcracks caused by the phase change.

Keywords: BSCF; Phase transition; X-ray diffraction; Transmission electron microscopy; Electrical conductivity; Thermal expansion coefficient; Mixed ionic-electronic conductor; Perovskite.

1. Introduction

Perovskite-type materials have been widely studied in the recent several decades because of their multiple functional properties in electrical, optical, and magnetic applications.[1,2] Some of the perovskite-type materials have been studied for their good oxygen catalytic activity, high electrical conductivity and required oxygen ionic conductivity, especially as cathodes in the field of the solid oxide fuel cell (SOFC) and oxygen permeation membranes.[3-5] One perovskite-type com-position Ba$_{0.5}$Sr$_{0.5}$Co$_{0.8}$Fe$_{0.2}$O$_{3-\delta}$ of the family of the more general system Ba$_x$Sr$_{1-x}$Co$_y$Fe$_{1-y}$O$_{3-\delta}$ (BSCF) was reported for the first time in 2000 as an oxygen permeation ceramic membrane material [6] and in 2004 as a high performance cathode material for SOFCs with low polarization resistance in the intermediate temperature range 500–700 °C.[7] An isothermal phase study for 1000 °C showed cubic phase, hexagonal phase, and other symmetries existing in the BSCF system depending on different Ba/Sr and Co/Fe ratios.[8] Ba$_{0.5}$Sr$_{0.5}$Co$_{0.8}$Fe$_{0.2}$O$_{3-\delta}$ exhibits a pure cubic phase at 1000 °C.[9] The temperature-dependent electrical conductivity of Ba$_{0.5}$Sr$_{0.5}$Co$_{0.8}$Fe$_{0.2}$O$_{3-\delta}$ exhibits a transition from semiconductivity to metal-like conductivity at 400-500 °C.[10-15] This transition is not due to any structural phase change.[16] However, only the long-term electrical conductivity of Ba$_{0.5}$Sr$_{0.5}$Co$_{0.8}$Fe$_{0.2}$O$_{3-\delta}$ at 800 °C slowly degrades and a slow phase transformation from the cubic to mixed cubic, hexagonal, and hexagonal related phases at temperatures below 850 °C was reported in several studies of the long-term phase stability. [17,18] Aside from the hexagonal phase the formation of lamellar non-cubic cobalt-rich phases was observed due to oxygen vacancy ordering, but the

structure of these phases was not completely resolved so far. Such, in some cases several micrometer-long lamellae are considered as barriers to oxygen transport due to their layered shape, low crystalline symmetry, and tiny amount of mobile oxygen vacancies.[19, 20]

The electrical conductivity of $Ba_xSr_{1-x}Co_{0.8}Fe_{0.2}O_{3-\delta}$ (x = 0.3–0.7) decreases with increasing barium content.[21] Ba-rich BSCF compositions do not exhibit pure cubic phase at room temperature, for example, $Ba_{0.8}Sr_{0.2}Co_{0.8}Fe_{0.2}O_{3-\delta}$ is composed of mixed phases, one being cubic and others being hexagonal symmetry.[8] Early research predicted that Ba-rich BSCF compositions might undergo a phase transition from highly symmetric cubic to less symmetric hexagonal below 825-875 °C.[22] BSCF materials with the cubic phase exhibit good electrical conductivity at high temperatures, but degrade when being held at lower temperatures, i.e., below 800 °C and a slowly transformation from cubic to a hexagonal symmetry.[17] The phase relations in this system lower than 1000 °C is still unclear.

In this work, we present the phase information of $Ba_{0.8}Sr_{0.2}Co_{0.8}Fe_{0.2}O_{3-\delta}$ using crystalline phase and microstructure analyses by X-ray diffraction (XRD) and transmission electron microscopy (TEM). The electrical conductivity and the thermal expansion of bulk materials show abrupt changes corresponding to the phase transition of $Ba_{0.8}Sr_{0.2}Co_{0.8}Fe_{0.2}O_{3-\delta}$.

2. Experimental

$Ba_{0.8}Sr_{0.2}Co_{0.8}Fe_{0.2}O_{3-\delta}$ powder specimens were synthesized by the solid-state reaction method as described in detail in previous work.[8] The finely ground green powder was calcined at 1000 °C for 10 hours in air. The crystalline phase of the calcined powder was identified by means of XRD. XRD data from the furnace-cooled and quenched-powder specimens were recorded on a Siemens Bruker D8 Advance X-ray Diffractometer using Cu $K\alpha_{1,2}$ radiation in the $2\theta°$ range of 20°-80° with step sizes of 0.04° and of 0.02°, respectively. The phase analysis of furnace-cooled specimen was carried out by combined Rietveld and Pawley methods using the TOPAS 4.0 (Bruker AXS) software. Because all observed phases exhibit related chemical compositions, we assume that the phases have similar X-ray mass absorption

coefficients. Thus, the amounts of the phases can be estimated by calculating the areas of the corresponding phases in the XRD patterns using the Pawley method. The ratio of the areas of the integrated intensities delivers an approximate amount of the phase under consideration. The reliability of the method was controlled by XRD experiments on furnace cooled powders using known amounts of $BaZrO_3$ as internal standard. Calcined furnace-cooled powders were uni-axially pressed to shape the bulk specimen bars of 55×5×2.5 mm.[3] These green bars were cold iso-statically pressed for 3 minutes at a pressure of 280 MPa and then sintered at 1100 °C for 6 hours in air. A four-probe dc method was used to measure the electrical conductivity of the sintered specimen bars. Platinum wires (0.25 mm in diameter) were used as four electrodes glued to the sample with platinum paste for a better contact. Keithley 2000 and 2001 multimeters together with a self-programmed Labview software and a K-type thermocouple were used to record the experimental parameters of the specimen temperature and resistance. The sample was heated in a tube furnace with a ramp rate of 1 °C/min from room temperature up to 1060 °C with three heating and cooling cycles in air.

Differential thermal analysis and thermal gravimetry (DAT/TG) on powder and bulk specimens were performed as a function of temperature in synthetic air by mixing pure argon and pure oxygen (PanGas, 99.999% purity) gases in a DTA/TG (Netzsch STA 449 C). The heating and cooling rates were 1 °C/min. The thermal expansion of the same sintered bulk specimen bars after the electrical conductivity measurement was measured in air in a differential dilatometer (Baehr DIL 802) at a rate of 1 °C/min during heating and cooling cycles. TEM was used to characterize the furnace cooled powder specimens that were heated at 1000 °C for 10 hours. The microscope was a FEI Tecnai F30 operated at 300 kV with a post-column Gatan image filter (GIF) and an EDAX SUTW Si (Li) detector and Phoenix EDAM III controller. The energy resolution was 134 eV. Some of the powder was mixed into 2 mL of ethanol and sonicated for 10 minutes to make a suspension. Drops of the suspension were applied from a pipette to a Cu TEM grid with perforated 100 holey carbon films. Images were collected in

standard TEM mode and high-resolution (HRTEM). Energy-dispersive X-ray spectroscopy (EDXS) and mappings were taken in the scanning (STEM) mode with an electron-probe of about 2.5 nm in diameter.

3. Results and discussions

The powder specimen calcined at 1000 °C for 100 hours in air exhibited different phases at room temperature. Quenched samples showed pure cubic phase (Figure 1a), whereas the furnace cooled specimen (3 °C/min) exhibited a mixed phase (Figure 1b) at room temperature.

The phase analysis by combining Rietveld and Pawley methods (Figure 1b) shows that at least two additional phases besides the cubic phase (a = 4.044 Å) are present in the sample. Thus, a hexagonal phase (space group P63/mmc) with lattice parameters a = 5.657 Å and c = 28.434 Å as well as a rhombohedral phase (space group R-3m; a = 5.825 Å, c = 37.157 Å) were deducted and included in the refinement by the Pawley fit. The mentioned phase symmetries are typical for the hexagonal perovskite polymorph as well as for hexagonal perovskite related barium cobalt oxides as described elsewhere.[20,23,24] Structure data for the known cubic perovskite phase were taken from the ICSD-database PDF 109462. The amounts of cubic phase of about 30%, hexagonal phase of about 40%, and rhombohedral phase of approximately 30% were estimated by considering the integrated scattering intensities of the respective phases. This mixed phase composition exists from room temperature up to 960 °C as evidenced by *in-situ* high-temperature XRD where the amount of cubic phase was found to increase with increasing temperature.[25] The results show that a pure cubic phase of this material is preferred at temperatures above 960 °C. However, the cubic phase is not stable at temperatures below 960 °C for this composition. The facts that the fast cooling prevents the phase transition from cubic to hexagonal and upon slow cooling this phase transition occurs indicate that it is diffusion controlled. High temperature *in situ* XRD analysis showed these non-cubic phases continue to develop at the expense of the cubic phase at lower temperatures.[25]
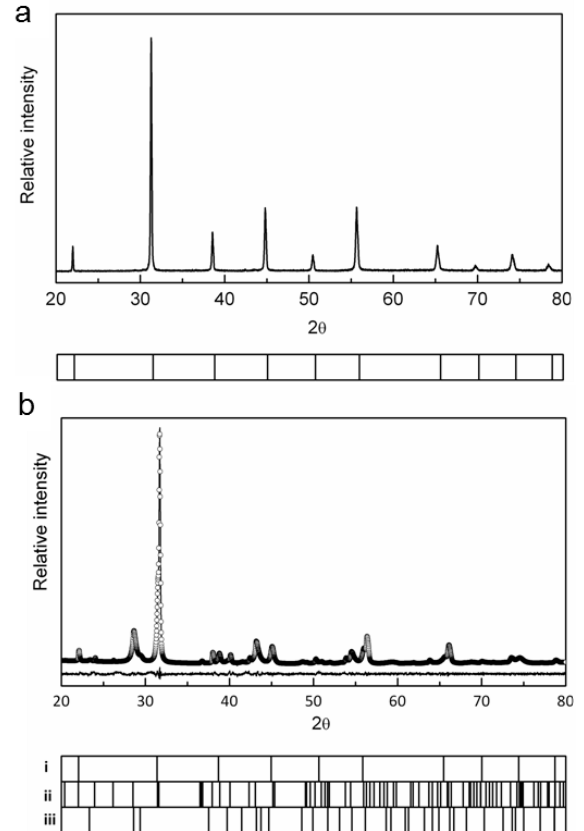
Figure 1*: (a) XRD-pattern of the quenched powder specimen. The calculated Bragg-positions of the cubic perovskite phase are given at the bottom. (b) XRD-patterns of the furnace cooled powder specimen: observed (full line), calculated (points), and difference. The calculated Bragg-positions are given at the bottom of the figure for (i) cubic phase, (ii) hexagonal phase, and (iii) rhombohedral phase.*

From HRTEM images of the powder specimen calcined at 1000 °C for 10 hours in air and furnace cooled, a clear cubic phase (space group Pm-3m; a = 4.044 Å), image viewed along [0,1,1] direction, d(100) = a ≈ 4 Å and d(0-11) ≈ 2.9 Å, angle (100):(0-11) = 90° (Figure 2a) and a lamellar structure rhombohedral phase (space group R-3m; a = 5.825 Å, c = 37.157 Å), image viewed along [-1,1,0] direction, d(003) = 1/3 c ≈ 12 Å and d(110) ≈ 2.8 Å, angle (003):(110) = 90° (Figure 2b) were observed. Those lamellar shaped structures occur due to the partial transformation of the cubic BSCF phase to non-cubic phases like the hexagonal and rhombohedral phases already found in the XRD patterns. Similar lamellar structures were found in the studies of

Efimov et al. and Mueller et al. for the $Ba_{0.5}Sr_{0.5}Co_{0.8}Fe_{0.2}O_{3-\delta}$ composition.[19,20] Here we have an insight into a non-equilibrium reaction sequence since the current sample was furnace cooled and not held in the intermediate temperature range for several hours like in the above mentioned studies.

and Table 1) and with small deviation on side d (Figure 3a and Table 1). However, the site b in Figure 3a shows a cobalt-rich composition (Figure 3a, 3b, and Table 1), which presumably is part of the more complex oxide phases leading to the multiple phase composition of the specimen.
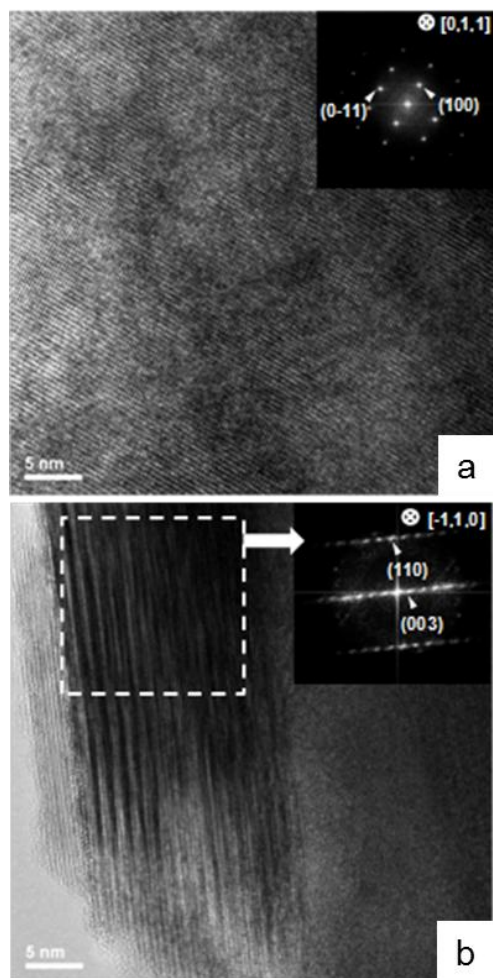
Figure 2: High-resolution transmission electron microscopy (HRTEM) images and diffraction patterns (insets) after Fast Fourier Transformation (FFT) calculations of the $Ba_{0.8}Sr_{0.2}Co_{0.8}Fe_{0.2}O_{3-\delta}$ calcined at 1000 °C for 10 hours in air and then furnace cooled. (a) cubic phase and (b) lamellar structure rhombohedral phase coexisting in one grain with areas of cubic symmetry.

Figure 3 and Table 1 present chemical elemental information of three sites of one particle of the specimen giving the chemical stoichiometry of the metal ions by EDXS results. The $Ba_{0.8}Sr_{0.2}Co_{0.8}Fe_{0.2}O_{3-\delta}$ nominal composition is found on site c (Figure 3a, 3c,

Figure 3: (a) TEM bright field image on three sites (b, c, and d) of one particle of the $Ba_{0.8}Sr_{0.2}Co_{0.8}Fe_{0.2}O_{3-\delta}$ powder calcined at 1000 °C for 10 hours in air and furnace cooled, (b) and (c) present the chemical elemental information by EDXS of site b and site c, respectively.

Table 1: *Local chemical compositions of each site (b, c, and d) of Figure 3a by showing metal ions in atomic percentage, on one particle of the Ba$_{0.8}$Sr$_{0.2}$Co$_{0.8}$Fe$_{0.2}$O$_{3-\delta}$ powder calcined at 1000 °C for 10 hours in air and furnace cooled.*

	Ba (atm%)	Sr (atm%)	Co (atm%)	Fe (atm%)
nominal	40	10	40	10
b	14	4	78	4
c	39	11	39	11
d	36	12	41	11

In a detailed STEM high angle annular dark field (HAADF) micrograph in Figure 4, this cobalt-rich and Ba-/Sr-/Fe-depleted area is more pronounced. It becomes evident that the chemical constituents are not homogeneously distributed across the grain. The alkali earth deficient site b of the grain shows a higher Co concentration than the nominal composition. Combining the XRD data, we confirm that the crystalline phase of this composition after slow cooling to room temperature is not pure, but multiple phases exist in this specific composition, even locally in one grain. We can conclude that the Ba-rich composition Ba$_{0.8}$Sr$_{0.2}$Co$_{0.8}$Fe$_{0.2}$O$_{3-\delta}$ of the Ba$_x$Sr$_{1-x}$Co$_y$Fe$_{1-y}$O$_{3-\delta}$ system undergoes a phase transformation at intermediate temperatures with local demixing of the cations and ordering of the oxygen vacancies. With the ordering and disordering states of oxygen vacancies, many oxides show different phases from brownmillerite (ordering) to cubic (disordering) perovskite phase, e.g., Ca$_2$AlFeO$_5$, Bi$_2$O$_3$, La$_2$Mo$_2$O$_9$, and Ba$_2$In$_2$O$_5$.[26-29] Here, an oxygen vacancy related phase transition was also found in the Ba$_{0.8}$Sr$_{0.2}$Co$_{0.8}$Fe$_{0.2}$O$_{3-\delta}$ composition, in similar cobalt-containing perovskites, and in SrCo$_{0.8}$Fe$_{0.2}$O$_{3-\delta}$.[30,31]

A possible pathway of the transition from cubic perovskite to hexagonal has been reported already earlier.[19,20] The cubic ABO$_3$ perovskite consists of AO$_3$ layers arranged in cubic-close packing perpendicular to the [1,1,1] cubic zone axis. B-cations occupy the octahedral holes and octahedra generate a three dimensional corner-sharing array. The shear of some AO$_3$ layers inducted by the

change of valence and spin-state of cobalt leads to the formation of hexagonal-close packing. Furthermore, the complex reconstructive transformations influenced by cation demixing occurred during the slow cooling of BSCF. Recently, Yi et al. reported high creep rates of Ba$_{0.5}$Sr$_{0.5}$Co$_{0.8}$Fe$_{0.2}$O$_{3-\delta}$ controlled by cation diff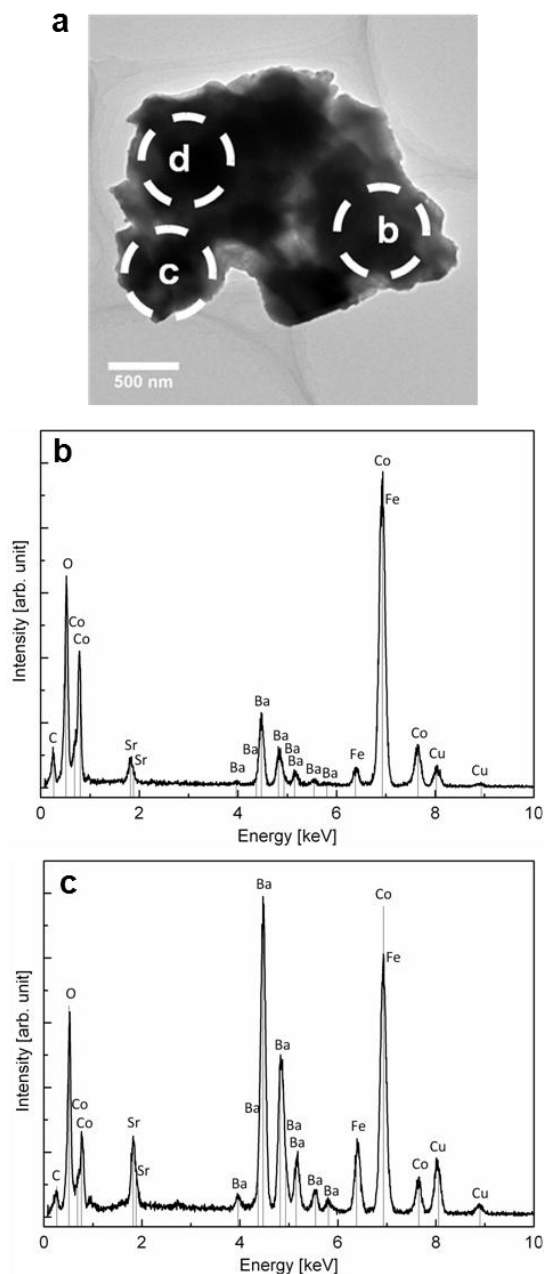usion.[32] Hence, the high cation mobility delivers a possible explanation for the phase transition into compounds with non-perovskite compositions via complex pathways. However, we want to point out that the phase transformation is reversible in a rather short time of ca. 1 hour as evidenced by the dilatometer measurements. As oxygen vacancy mobility is rather fast in this material, the latter points towards a phase transformation due to the fast rearrangement of oxygen vacancies.
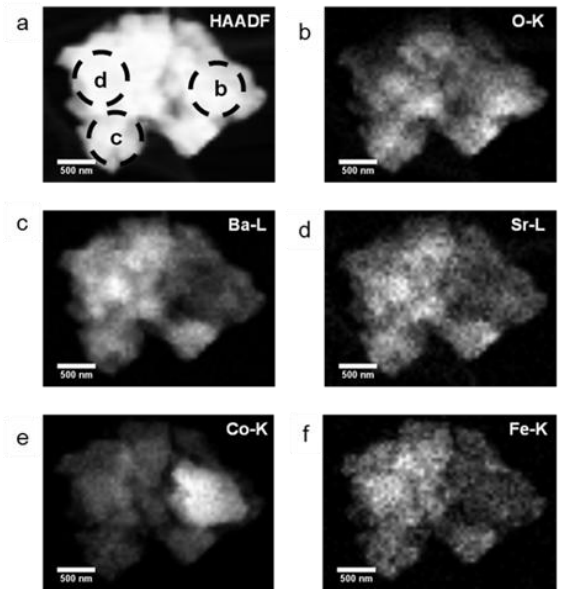
Figure 4: *Scanning transmission electron microscopy (STEM) high angle annular dark field (HAADF) image (a) and the elemental distributions by EDX mapping (b-f) on the same particle of the Ba$_{0.8}$Sr$_{0.2}$Co$_{0.8}$Fe$_{0.2}$O$_{3-\delta}$ powder calcined at 1000 °C for 10 hours in air and furnace cooled as shown in Figure 3.*

The change in oxygen content of the sintered bulk specimen (furnace cooled) during two heating and cooling cycles from room temperature to 1000 °C is shown in wt.% in Figure 5. The initial oxygen content at room temperature was taken as 3-δ = 2.48 referenced from the similar composition Ba$_{0.5}$Sr$_{0.5}$Co$_{0.8}$Fe$_{0.2}$O$_{3-\delta}$ in the literature.[33]
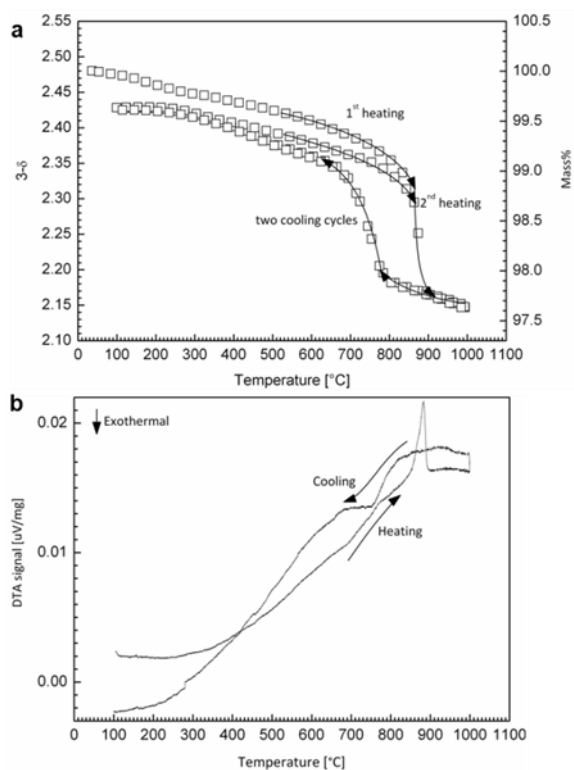
Figure 5: *(a) Oxygen stoichiometry and (b) DTA signal of $Ba_{0.8}Sr_{0.2}Co_{0.8}Fe_{0.2}O_{3-\delta}$ as a function of temperature in synthetic air.*

In the first heating cycle, the oxygen content of the sample continuously decreases with increasing temperature. An abrupt oxygen loss of 1 wt.% was observed in a rather small temperature interval of 20 °C between 880 and 900 °C upon heating. During further heating the sample further loses oxygen. Upon cooling from 1000 °C, the sample re-oxidizes with decreasing temperature down to 800 °C when an abrupt oxygen gain occurs. With further cooling more oxygen is incorporated into the material. The second thermal cycle shows similar behavior as the first thermal cycle including the hysteresis behavior in the temperature regime from 800-900 °C. The abrupt oxygen changes are accompanied by endo- and exothermic signals as shown in Figure 5b. Upon heating the onset temperature is 855 °C and an onset temperature is 820 °C for the exothermal event during cooling. Such a reversible phase transformation was reported for a similar cobalt-containing oxide BaSrCo₂O₅ already earlier.[34] The Fe-free BaSrCo₂O₅ transforms from a cubic symmetry below 900 °C into a rhombohedral phase upon cooling. The temperatures of endothermic and

exothermic reactions are very similar for both $Ba_{0.8}Sr_{0.2}Co_{0.8}Fe_{0.2}O_{3-\delta}$ and $BaSrCo_2O_5$.
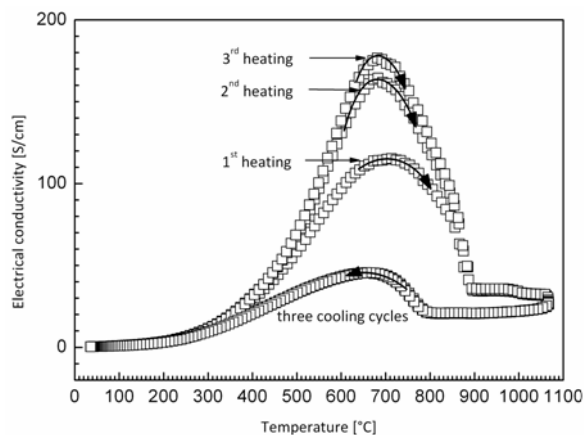
Figure 6: *The electrical conductivity of the bulk specimen $Ba_{0.8}Sr_{0.2}Co_{0.8}Fe_{0.2}O_{3-\delta}$ in air at a rate of 1 °C/min. Note the discontinuity of the conductivity at 895 °C upon heating and at 790 °C upon cooling.*

The electrical conductivity of a sintered bulk specimen bar (furnace cooled) as a function of temperature in air is shown in Figure 6 during three heating and cooling cycles. The electrical conductivity increases with increasing temperature, and reaches a maximum at 670–710 °C and then decreases upon further heating to 895 °C where a sharp discontinuity of the conductivity can be observed. The electrical conductivity does not change much with further heating up to 1060 °C. The discontinuity in electrical conductivity starts at 895 °C upon heating and at 790 °C during cooling. The maximum electrical conductivity occurs at 660 °C in the cooling cycles, and increases with the number of cycles. During the cooling cycles identical conductivities were observed. In the temperature range between room temperature and 660 °C the material exhibits *p*-type semiconductivity, which can be described as a small polaron hopping mechanism at elevated temperatures.[13, 15, 35] It then undergoes a transition above 660 °C to metal-like conductivity. The latter can be understood when considering the increasing overlap of the transition metal *d* orbitals and oxygen *p* orbitals as already reported earlier.[15]

The sharp discontinuity in the conductivity upon heating at 895 °C correlates with the phase transitions from mixed hexagonal and rhombohedral phases to the cubic symmetry

and is correlated with the abrupt oxygen loss at the same temperature shown in Figure 5a. The corresponding DTA signal (see Figure 5b) is endothermic. Obviously oxygen vacancies are formed and the transition metal cations (mainly Co) become reduced changing their radii.[36] This leads to the phase change from mixed hexagonal and rhombohedral phases to the cubic symmetry. The state of oxygen vacancies, being ordered (rhombohedral and hexagonal phases) or disordered (cubic phase) in the lattice, obviously plays a crucial role on the electrical conductivity and presumably on the oxygen ion conduction. However, the transition from ordered to disordered vacancy states cannot explain the discontinuity in the conductivity alone, e.g., at 895 °C upon heating as it is shown in Figure 6.
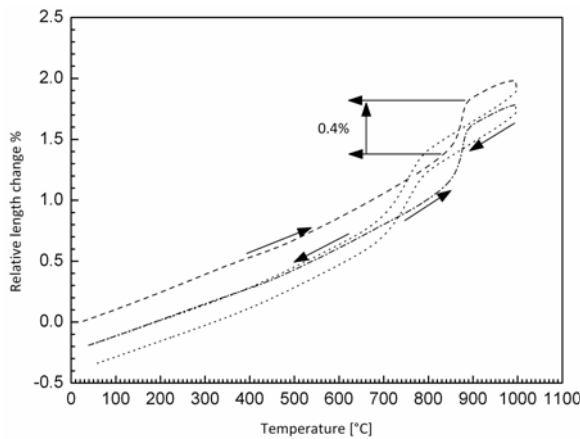
Figure 7: Relative length change of the bulk ceramic specimen of Ba$_{0.8}$Sr$_{0.2}$Co$_{0.8}$Fe$_{0.2}$O$_{3-\delta}$ as a function of temperature in air with two thermal cycles at a rate of 1 °C/min.

In order to elucidate this point further, we will now consider the relative length change of the ceramic specimen during heating and cooling cycles. Figure 7 shows the relative length change of the specimen during two subsequent heating and cooling cycles. Besides the usual length increase upon heating due to thermal and chemical expansion of 15.6×10^{-6} (1/°C), the material expands abruptly between 790-890 °C, with an onset at 850 °C during heating and contracts upon cooling with an onset at 790 °C. The onset temperature becomes slightly shifted to higher temperatures during the second cycle. The abrupt length change is ± 0.4% linear corresponding to 1.2 vol.%. After thermal

cycling the specimen was still mechanically intact but exhibited many microcracks in the microstructure as it is shown in the optical micrograph in Figure 8.
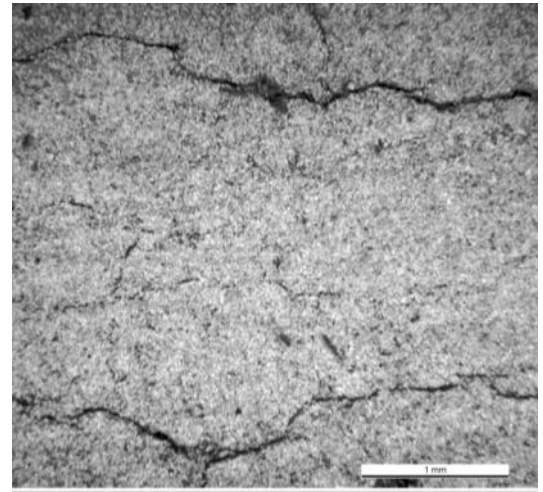
Figure 8: Microcracks in the Ba$_{0.8}$Sr$_{0.2}$Co$_{0.8}$Fe$_{0.2}$O$_{3-\delta}$ ceramic specimen bar predominantly running parallel to the long side of the specimen after 10 thermal cycles between room temperature and 1000 °C in air. (Optical micrograph, scale bar = 1 mm).

The redox-reaction of the transition metals between 700 and 900 °C causing the phase change leads to mechanical stresses exceeding the strength of the material and therefore cause microcracks in the microstructure of the ceramic which were observed on the surface of La$_{0.5}$Sr$_{0.5}$Co$_{0.5}$Fe$_{0.5}$O$_{3-\delta}$ as well reported by Lein et al. [37] They attributed this mechanical fracture to the considerable stress gradients developing in the materials due to gradient in oxygen concentration or valance of Co.[37] Therefore, the crack formation reported here does not necessarily come due to the phase transition, but might be caused by the considerable chemical expansion (oxidation of Co/Fe) during cooling. The hysteresis and the discontinuity of the electrical conductivity are a direct consequence of the disintegration of a coherent microstructure in this material.

4. Conclusions

The Ba$_{0.8}$Sr$_{0.2}$Co$_{0.8}$Fe$_{0.2}$O$_{3-\delta}$ composition of the Ba$_x$Sr$_{1-x}$Co$_y$Fe$_{1-y}$O$_{3-\delta}$ system shows a cubic symmetry (a = 4.044 Å) at 1000 °C when synthesized in air that can be retained in a

metastable state at room temperature upon quenching. During slow cooling, the material transforms at 790 °C into a mixed phase state characterized by cubic, hexagonal, and rhombohedral symmetries. The latter exhibits a lamellar structure, sometimes coexisting with areas of cubic symmetry in the same grain. The phase change is reversible and associated with the oxidation and reduction of the transition metal cations (mainly Co). The phase change is associated with a rather abrupt mass change of 1 wt.% corresponding to a $\Delta\delta = 0.14$ in the formula unit. The redox-reaction of the transition metal cations cause a reversible volume change of ~1.2 vol.% of the ceramic specimen leading to microcracks in the microstructure during thermal cycling. From room temperatures to ~670 °C the material shows small polaron hopping *p*-type semiconductivity up to 180 S/cm changing then to a metal-like conductivity. The conductivity is abruptly reduced by the microcracks forming when the material transforms into the cubic symmetry at temperatures above 900 °C.

5. Acknowledgements

References

1. R. J. H. Voorhoeve, D. W. Jr. Johnson, J. P. Remeika and P. K. Gallagher, Science, 1977, 195, 827-833.

2. A. S. Bhalla, R. Guo and R. Roy, Materials Research Innovations, 2000, 4, 3-26.

3. L. J. Gauckler, D. Beckel, B. E. Buergler, E. Jud, U. P. Muecke, M. Prestat, J. L. M. Rupp and J. Richter, CHIMIA International Journal for Chemistry, 2004, 58, 837-850.

4. N. Q. Minh, Journal of the American Ceramic Society, 1993, 76, 563-588.

5. K. Efimov, T. Halfer, A. Kuhn, P. Heitjans, J. Caro and A. Feldhoff, Chemistry of Materials, 2010, 22, 1540-1544.

6. Z. Shao, W. Yang, Y. Cong, H. Dong, J. Tong and G. Xiong, Journal of Membrane Science, 2000, 172, 177-188.

7. Z. Shao and S. M. Haile, Nature, 2004, 431, 170-173.

8. Z. Yáng, A. S. Harvey, A. Infortuna and L. J. Gauckler, Journal of Applied Crystallography, 2009, 42, 153-160.

9. B. Wei, Z. Lu, S. Li, Y. Liu, K. Liu and W. Su, Electrochemical and Solid-State Letters, 2005, 8, A428-A431.

10. H. Zhao, W. Shen, Z. Zhu, X. Li and Z. Wang, Journal of Power Sources, 2008, 182, 503-509.

11. G. S. Jiang, C. L. Song, D. C. Li, S. J. Feng, L. Wei and C. S. Chen, Chinese Journal of Chemical Physics, 2004, 17, 75-78.

12. P. Zeng, Z. Chen, W. Zhou, H. Gu, Z. Shao and S. Liu, Journal of Membrane Science, 2007, 291, 148-156.

13. Z. Chen, R. Ran, W. Zhou, Z. Shao and S. Liu, Electrochimica Acta, 2007, 52, 7343-7351.

14. Y. Zhang, J. Liu, X. Huang, Z. Lu and W. Su, Solid State Ionics, 2008, 179, 250-255.

15. Z. Yáng, A. S. Harvey, A. Infortuna, J. Schoonman and L. J. Gauckler, Journal of Solid State Electrochemistry, 2011, 15, 277-284.

16. H. Wang, C. Tablet, W. Yang and J. Caro, Materials Letters, 2005, 59, 3750-3755.

17. S. Svarcova, K. Wiik, J. Tolchard, H. J. M. Bouwmeester and T. Grande, Solid State Ionics, 2008, 178, 1787-1791.

18. M. Arnold, T. M. Gesing, J. Martynczuk and A. Feldhoff, Chemistry of Materials, 2008, 20, 5851-5858.

19. D. N. Mueller, R. A. De Souza, T. E. Weirich, D. Roehrens, J. Mayer and M. Martin, Physical Chemistry Chemical Physics, 2010, 12, 10320-10328.

20. K. Efimov, Q. Xu and A. Feldhoff, Chemistry of Materials, 2010, 22, 5866-5875.

21. B. Wei, Z. Lu, X. Huang, J. Miao, X. Sha, X. Xin and W. Su, Journal of the

European Ceramic Society, 2006, 26, 2827-2832.

22. Z. Shao, G. Xiong, J. Tong, H. Dong and W. Yang, Separation and Purification Technology, 2001, 25, 419-429.

23. M. Parras, A. Varela, H. Seehofer and J. M. González-Calbet, Journal of the Solid State Chemistry, 1995, 120, 327.

24. A. J. Jacobson and J. L. Hutchison, Journal of the Solid State Chemistry, 1980, 35, 334.

25. A. S. Harvey, F. J. Litterst, Z. Yang, J. L. M. Rupp, A. Infortuna and L. J. Gauckler, Physical Chemistry Chemical Physics, 2009, 11, 3090-3098.

26. A. A. Colville and S. Geller, Acta Crystallographica Section B, 1971, 27, 2311-2315.

27. H. A. Harwig and A. G. Gerards, Journal of Solid State Chemistry, 1978, 26, 265-274.

28. P. Lacorre, F. Goutenoire, O. Bohnke, R. Retoux and Y. Laligant, Nature, 2000, 404, 856-858.

29. M. Yoshinaga, M. Yamaguchi, T. Furuya, S. Wang and T. Hashimoto, Solid State Ionics, 2004, 169, 9-13.

30. Z. Q. Deng, W. S. Yang, W. Liu and C. S. Chen, Journal of Solid State Chemistry, 2006, 179, 362-369.

31. L. M. Liu, T. H. Lee, L. Qiu, Y. L. Yang and A. J. Jacobson, Materials Research Bulletin, 1996, 31, 29-35.

32. J. X. Yi, H. L. Lein, T. Grande, S. Yakovlev and H. J. M. Bouwmeester, Solid State Ionics, 2009, 180, 1564-1568.

33. S. McIntosh, J. F. Vente, W. G. Haije, D. H. A. Blank and H. J. M. Bouwmeester, Solid State Ionics, 2006, 177, 1737-1742.

34. K. Boulahya, J. C. Ruiz-Morales, M. Hernando, J. M. Gonzalez-Calbet and M. Parras, Chemistry of Materials, 2009, 21, 2045-2054.

35. R. Koc and H. U. Anderson, Journal of the European Ceramic Society, 1995, 15, 867-874.

36. R. Shannon, Acta Crystallographica Section A, 1976, 32, 751-767.

37. H. Lein, Ø. Andersen, P. Vullum, E. Lara-Curzio, R. Holmestad, M.-A.

Einarsrud and T. Grande, Journal of Solid State Electrochemistry, 2006, 10, 635-642.

3 Novel cobalt-free perovskite for intermediate temperatures applications

3.1 Summary

This chapter introduces a cobalt-free oxygen-permeable perovskite-type oxide with the novel composition $(Ba_{0.5}Sr_{0.5})(Fe_{0.8}Cu_{0.2})O_{3-\delta}$ (denoted BSFCu). This material was designed to be an alternative to Co-based perovskites (e.g., BSCF), which suffer from inherent phase instabilities in the intermediate temperature range (773-1073 K; see Chapter 2).

The sol-gel route was applied to synthesize the BSFCu material. XRD and TEM investigations revealed that this system crystallizes in the cubic perovskite structure. Furthermore, *in-situ* XRD experiments, carried out between room temperature and 1227 K, proved that the BSFCu perovskite remained in a cubic structure over the whole temperature range. The coefficient of thermal expansion (CTE) of the BSFCu was estimated by high resolution *in-situ* XRD to be ca. 16×10^{-6} K^{-1} between room temperature and 773 K and ca. 23×10^{-6} K^{-1} between 773 K and 1173 K, providing a lower dilatation in the intermediate temperature range compared with the CTE values of cobaltites and BSCF. The transport properties of the BSFCu membrane material were studied by measurements of electrical conductivity using the four-probe method and oxygen permeation. A maximum in BSFCu electrical conductivity of 45 S cm^{-1} was observed at 890 K, which is just as good as the electrical conductivity of the BSCF material. With regard to the oxygen ionic conductivity, the BSFCu material exhibited the highest permeation flux of all known cobalt-free materials. The permeation flux of BSCF perovskite, however, remains unrivalled.

Long-term stability of the BSFCu membrane was proven using time-dependent oxygen permeation experiments at 1023 K and compared with the performance of state-of-the-art BSCF material at the same conditions. It was clearly shown that BSFCu perovskite is preferable for intermediate temperature applications, as compared with BSCF, because of its improved inherent phase stability.

.

3.2 A novel cobalt-free oxygen-permeable perovskite-type membrane

Konstantin Efimov, Torben Halfer, Alexander Kuhn, Paul Heitjans,
Jürgen Caro, and Armin Feldhoff

CHEMISTRY OF
MATERIALS
Article

Novel Cobalt-Free Oxygen-Permeable Perovskite-Type Membrane

Konstantin Efimov,* Torben Halfer, Alexander Kuhn, Paul Heitjans, Jürgen Caro, and
Armin Feldhoff

*Institute of Physical Chemistry and Electrochemistry, and Center for Solid State Chemistry and New
Materials, Leibniz Universität Hannover, Callinstrasse 3-3A, 30167 Hannover, Germany*

Cobalt-free perovskite with the novel composition $(Ba_{0.5}Sr_{0.5})(Fe_{0.8}Cu_{0.2})O_{3-\delta}$ (BSFCu) was synthesized via a sol–gel method and studied with respect to the crystallographic structure as well as the oxygen ionic and the electronic conductivity. In situ X-ray diffraction (XRD) was applied to investigate the thermal dilatation and the phase stability of the BSFCu at high and intermediate temperatures. Additionally, time-dependent oxygen permeation performance measurements were carried out for BSFCu and Co-based $(Ba_{0.5}Sr_{0.5})(Co_{0.8}Fe_{0.2})O_{3-\delta}$ membranes at 1023 K for 200 h. The BSFCu phase was found to be a cubic perovskite by XRD and transmission electron microscopy. The BSFCu membrane exhibits a very high oxygen permeation and electrical conductivity as compared to known perovskite membranes. The oxygen permeation of the BSFCu membrane maintains its value for 200 h at 1023 K unlike $(Ba_{0.5}Sr_{0.5})(Co_{0.8}Fe_{0.2})O_{3-\delta}$, whose oxygen flux was reduced by one-half during the same interval.

Introduction

For many fields of application as cathode in solid-oxide fuel cells (SOFCs), in the production of oxygen-enriched air, and in the conversion of hydrocarbons to synthesis gas,[1–3] mixed ionic–electronic conductors (MIECs) are on the verge of a breakthrough. Nevertheless, membrane materials with improved qualities for industrial processes are needed. Cobalt-based perovskite oxides like $(La_xSr_{1-x})(Co_yFe_{1-y})O_{3-\delta}$ or $(Ba_xSr_{1-x})(Co_yFe_{1-y})O_{3-\delta}$ are often thought to be the most promising materials because they show very good oxygen permeability due to the extremely high amount of disordered oxygen vacancies and their excellent phase stability above 1173 K.[4,5] The flexible redox behavior of cobalt, however, leads to two considerable disadvantages. First, the large coefficient of thermal expansion (CTE) of cobaltites, with values between 20 and 24×10^{-6} K^{-1} over a wide temperature range,[6,7] is responsible for huge thermal stresses and can result in cracking of the ceramic products during operation in the worst case. Second, the cubic structure of Co-based perovskites at intermediate temperatures

(IT, approximately $T = 773-1073$ K) breaks down under long-term conditions.[5,8–10] The driving force for this conversion is a temperature-dependent coupled valence and spin-state transition of cobalt (between high spin Co^{2+} and low spin Co^{3+}). The small ionic radius of trivalent cobalt in low-spin configuration favors the formation of the hexagonal perovskite phase.[11,12] This fact excludes cobaltites from use as membrane materials in the IT range. Thus, the development of Co-free perovskite systems is of large and persistent interest.

Due to the less flexible redox behavior of iron, Fe-based perovskite oxides attracted much attention as possible alternatives to cobaltites in the past few years. Teraoka et al.[13] and Zhen et al.[14] reported that $Ba_xSr_{1-x}FeO_{3-\delta}$ systems reveal a high oxygen permeation flux accompanied with an exceedingly high phase stability. Furthermore, Wang et al.[15] and Martynczuk et al.[16] established an increase of the oxygen permeation rate by substituting $(Ba_xSr_{1-x})FeO_{3-\delta}$ with lower valence cations like Zn^{2+} and Al^{3+} for the B-site of the perovskite. Continuing the research on Co-free perovskite systems, we have

*Corresponding author. E-mail: konstantin.efimov@pci.uni-hannover.de.

(1) Shao, Z.; Haile, S. M. *Nature* **2004**, *431*, 170.
(2) Wang, H.; Werth, S.; Schiestel, T.; Caro, J. *Angew. Chem., Int. Ed.* **2005**, *44*, 6906.
(3) Chen, C.; Feng, S.; Ran, S.; Zhu, D.; Liu, W.; Bouwmeester, H. J. M. *Angew. Chem., Int. Ed.* **2003**, *115*, 5196.
(4) Teraoka, Y.; Zhang, H.; Furukawa, S.; Yamazoe, N. *Chem. Lett.* **1985**, *11*, 1743.
(5) Shao, Z.; Yang, W.; Cong, Y.; Dong, H.; Tong, J.; Xiong, G. *J. Membr. Sci.* **2000**, *172*, 177.
(6) McIntosh, S.; Vente, J. F.; Haije, W. G.; Blank, D. H. A.; Bouwmeester, H. J. M. *Chem. Mater.* **2006**, *18*, 2187.
(7) Vente, J. F.; Haije, W. G.; Rak, Z. S. *J. Membr. Sci.* **2006**, *177*, 2245.

(8) Švarcová, S.; Wiik, K.; Tolchard, J.; Bouwmeester, H. J. M.; Grande, T. *Solid State Ionics* **2008**, *178*, 1787.
(9) Teraoka, Y.; Nobunaga, T.; Namazoe, Y. *Chem. Lett.* **1988**, *3*, 503.
(10) Nagai, T.; Ito, W.; Sakon, T. *Solid State Ionics* **2007**, *177*, 3433.
(11) Arnold, M.; Gesing, T. M.; Martynczuk, J.; Feldhoff, A. *Chem. Mater.* **2008**, *20*, 5881.
(12) Arnold, M.; Xu, Q.; Tichelaar, F. D.; Feldhoff, A. *Chem. Mater.* **2009**, *21*, 635.
(13) Teraoka, Y.; Shimokawa, H.; Kang, C. Y.; Kusaba, H.; Sasaki, K. *Solid State Ionics* **2006**, *177*, 2245.
(14) Chen, Z.; Ran, R.; Zhou, W.; Shao, Z.; Liu, S. *Electrochim. Acta* **2007**, *52*, 7343.
(15) Wang, H.; Tablet, C.; Feldhoff, A.; Caro, J. *Adv. Mater.* **2005**, *17*, 1785.
(16) Martynczuk, J.; Liang, F.; Arnold, M.; Šepelák, V.; Feldhoff, A. *Chem. Mater.* **2009**, *21*, 1586.

developed a Cu-doped perovskite with the novel composition $(Ba_{0.5}Sr_{0.5})(Fe_{0.8}Cu_{0.2})O_{3-\delta}$ (BSFCu), which is the focus of this paper. The Fe ion normally takes a mixed oxidation state between 3+ and 4+ in perovskite oxides.[16,17] Replacing of Fe ions with divalent and trivalent Cu ions[18] in a perovskite lattice can lead to an increase of oxygen vacancies, from which one would expect to observe improved oxygen-conducting behavior. Already in 1988 and 1991, Teraoka et al. have shown the positive effect of Cu-doping on the $(La_xSr_{1-x})CoO_{3-\delta}$ oxygen permeability.[9,19] Similarly, Cu-containing Sr-$(Fe_xCu_{1-x})O_{3-\delta}$ perovskites with a high oxygen conductivity are reported in the literature.[20,21] Because SrFeO$_{3-\delta}$-based perovskite oxides tend to form a brownmillerite phase like $Sr_2Fe_2O_5$, their large-scale application would be inhibited.[20,22]

Experimental Section

A sol−gel route using metal nitrates, citrate, and ethylenediaminetetraacetic acid (EDTA) as described in detail elsewhere[23−25] was applied to prepare the BSFCu material. A powder obtained after heat treatment for 10 h at 1223 K was uniaxially pressed under 140−150 kN for 20 min into green bodies. The pellets were calcined for 10 h at 1323 K with a heating and cooling rate of 3 K/min to form dense membrane disks with a diameter of 16 mm and a thickness of 1.1 mm.

The XRD was carried out in a Θ/2Θ geometry on a Philips X'pert-MPD instrument using Cu Kα radiation at 40 kV and 40 mA, with a receiving slit of 0.05 mm. For Pawley refinement, the data were collected in a 2Θ range of 15°-90° in a step-scan mode with a step width of 0.04° and count time of 25 s per step. The Pawley refinement was performed by using Topas V4.1 software (Coehlo Software). During in situ high-temperature XRD measurements, data were collected in 2Θ ranges of 30°-33° and 20°-60° with intervals of 0.02° and count times of 33 s/step and 5 s/step, respectively. The tests were conducted in a high temperature cell (HDK 2.4 with REP 2000) with Pt−Rh holder in the temperature range of 308−1173 K in steps of 100 K with a heating and cooling rate of 3 K/min in air. Before each data acquisition, an equilibration time of 30 min was used.

Scanning electron microscopy (SEM) imaging was performed on a JEOL JSM-6700F field-emission instrument at a low excitation voltage of 2 kV. An energy-dispersive X-ray spectrometer (EDXS), Oxford Instruments INCA-300, with an ultrathin window was used for the elemental analysis at an excitation voltage of 15 kV.

Transmission electron microscopy (TEM) investigations were made at 200 kV on a JEOL JEM-2100F-UHR field-emission instrument (C_S = 0.5 mm, C_C = 1.2 mm). The microscope was operated as a high-resolution TEM (HRTEM) as well as a scanning TEM (STEM) in bright-field mode. The preparation method of the TEM specimen is described in detail elsewhere.[26] Additionally, HRTEM micrographs were simulated by using the electron microscopy software JEMS (Java version V3-3526U2008 s, P. Stadelmann, CIME-EPFL).

Conductivity measurements by impedance spectroscopy were performed using a four terminal configuration in the temperature range from room temperature to 1173 K with a heating rate of about 10 K/min in air. Pellets of about 1 mm thickness were prepared by room temperature pressing and subsequent sintering. Long sticks were cut from the pellet to enable low impedance measurements. Silver conductive paste was used as electrode material. The frequency dependence of the conductivity was negligible in the frequency range from 10 Hz to 100 kHz. Data shown here were recorded at a frequency of 50 Hz using a HP 4192 A impedance analyzer. The setup including the sample holder is described in detail elsewhere.[27]

Oxygen permeation was measured in a high-temperature permeation cell[28] according to the method described elsewhere.[29] Air was fed at a rate of 150 mL min^{-1} to the feed side; He (29.0 mL min^{-1}, 99.995%) and Ne (1.0 mL min^{-1}, 99.995%) gases were fed to the sweep side. The effluents were analyzed by gas chromatography on an Agilent 6890 instrument equipped with a Carboxen 1000 column. The gas concentrations in the effluent stream were calculated from a gas chromatograph calibration. The absolute flux rate of the effluents was determined by using neon as an internal standard. The relative leakage of O_2, which was evaluated by measuring the amount of N_2 in the effluent stream, was subtracted in the calculation of the oxygen permeation flux.

Results and Discussion

The stoichiometric $(Ba_{0.5}Sr_{0.5})(Fe_{0.8}Cu_{0.2})O_{3-\delta}$ perovskite oxide was synthesized via a sol−gel method, which affords a fine intermixing of the cations during all processing steps, thus leading to a pure product phase at comparably low synthesis temperatures and dwell times. Figure 1 displays an XRD pattern of the BSFCu powder. The desired product was found to be a pure perovskite phase. The cubic symmetry in the $Pm\overline{3}m$ space group (Nr. 221) with a = 3.9434(4) Å (lattice parameter) was determined by Pawley-analysis.[30] The refinement converged to reliability factors of R_{WP} = 11.162, R_{SP} = 8.91 and to a goodness of the fit of 1.253. Obviously, Cu ions ($r(Cu^{2+})$ = 0.73 Å, $r(Cu^{3+})$ = 0.54 Å)[31] can be incorporated at the B-position of the ABO_3 perovskite (A: $r(Ba^{2+})$ = 1.61 Å, $r(Sr^{2+})$ = 1.44 Å, B: $r(Fe^{3+}$, high spin) = 0.645 Å, $r(Fe^{4+}$, high spin) = 0.585 Å, $r(O^{2-})$ = 1.40 Å)[31]

(17) Feldhoff, A.; Martynczuk, J.; Arnold, M.; Myndyk, M.; Bergmann, I.; Šepelák, V.; Gruner, W.; Vogt, U.; Hähnel, A.; Woltersdorf, J. *J. Solid State Chem.* **2009**, *182*, 2961.
(18) Bringley, J. F.; Scott, B. A.; Laplaca, S. J.; Boehme, R. F.; Shaw, T. M.; McElfresh, M. W.; Trail, S. S.; Cox, D. E. *Nature* **1990**, *347*, 263.
(19) Teraoka, Y.; Nobunaga, T.; Okamoto, K.; Miura, N.; Yamazoe, N. *Solid State Ionics* **1991**, *48*, 207.
(20) Zhang, H.; Wang, T.; Dong, X.; Lin, W. *J. Nat. Gas Chem.* **2009**, *18*, 45.
(21) Nie, H.; Zhang, H.; Yu, G.; Yang, N. *Sep. Pur. Technol.* **2001**, *25*, 415.
(22) McIntosh, S.; Vente, J. F.; Haije, W. G.; Blank, D. H. A.; Bouwmeester, H. J. M. *Solid State Ionics* **2006**, *177*, 833.
(23) Martynczuk, J.; Arnold, M.; Caro, J.; Wang, H.; Feldhoff, A. *Adv. Mater.* **2007**, *19*, 2134.
(24) Feldhoff, A.; Arnold, M.; Martynczuk, J.; Gesing, T. M.; Wang, H. *Solid State Sci.* **2008**, *10*, 689.
(25) Feldhoff, A.; Martynczuk, J.; Wang, H. *Prog. Solid State Chem.* **2007**, *35*, 339.

(26) Arnold, M.; Wang, H.; Feldhoff, A. *J. Membr. Sci.* **2007**, *293*, 44.
(27) Indris, S.; Heitjans, P.; Roman, H. E.; Bunde, A. *Phys. Rev. Lett.*, **2000**, *84*, 2889; S. Indris, Thesis, University of Hannover, Germany, **2001**.
(28) Wang, H.; Tablet, C.; Feldhoff, A.; Caro, J. *J. Membr. Sci.* **2005**, *262*, 20.
(29) Martynczuk, J.; Arnold, M.; Feldhoff, A. *J. Membr. Sci.* **2008**, *322*, 375.
(30) Pawley, G. S. *J. Appl. Crystallogr.* **1981**, *14*, 357.
(31) Shannon, R. D. *Acta Crystallogr., Sect. A: Found. Crystallogr.* **1976**, *32*, 751.
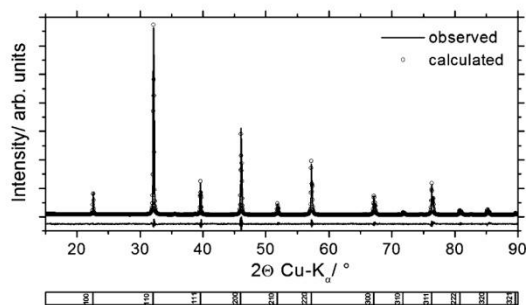
Figure 1. XRD pattern of BSFCu: observed, calculated by the Pawley method, and difference (bottom line). The calculated Bragg positions are marked with ticks at the bottom of the figure.
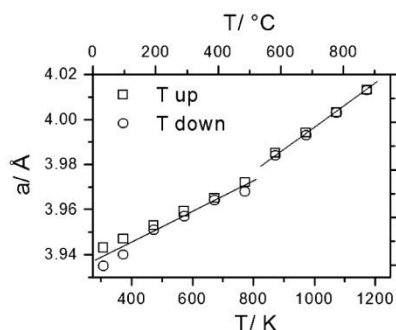
Figure 2. Lattice parameter of BSFCu as a function of the temperature during heating and cooling.

Figure 3. a) SEM of the BSFCu membrane surface. b) STEM and c) HRTEM showing an interface of two BSFCu perovskite grains. Insets show images calculated with −32 nm defocus for [2,2,3] and [0,0,1] zone axis for BSFCu, respectively. d) Selected area diffraction of the grain on the left in Figure 3c. e) Two-dimensional fast Fourier transformed from the grain on the right in Figure 3c.

without distorting the cubic structure. This is in agreement with Goldschmidt's tolerance factor of BSFCu calculated to be in the range of $t = 1.003-1.046$ for various ratios of Fe^{4+}/Fe^{3+} ions and Cu^{3+}/Cu^{2+} ions. Therefore, the cubic space group $Pm\overline{3}m$ was expected for BSFCu because the tolerance factor lies close to unity, which is a benchmark for cubic symmetry.[32]

In order to examine the behavior of the BSFCu powder at high temperatures, in situ XRD experiments were carried out in the temperature range of 308−1173 K with steps of 100 K under ambient air. Confirmed by measurements in the angle interval 20°-60° 2Θ, the cubic perovskite was found to be stable in the entire temperature range, since no reflexes of other phases appeared. The shift of the lattice parameters with temperature was derived in particular from the (110) reflex of the cubic structure in the 30°-33° 2Θ range. Figure 2 shows the change of the lattice parameter, determined from the 2Θ angular position of the peak under consideration, during heating and cooling. From these measurements, the CTE of BSFCu could be estimated to be approximately 16 × 10^{-6} K^{-1} between room temperature and 773 K as well as approximately 23 × 10^{-6} K^{-1} between 773 and 1173 K. Thus, the CTE of BSFCu gives a lower dilatation in the IT range and a similar dilatation at high temperatures compared to the CTE values of cobaltites reported by McIntosh et al.,[6] Vente et al.,[7] and Wei et al.[33]

After sintering, the BSFCu ceramic was investigated by electron microscopy. The SEM micrograph in Figure 3a shows the surface of the membrane. No cracks and only a few pores are visible on the membrane surface. The pores are not running throughout the membrane as evidenced by SEM of the cross-section. To verify the chemical composition of the membrane, EDX spectra were acquired from the surface and the cross-section. A Cliff-Lorimer quantification of the EDX spectra confirmed the desired $(Ba_{0.5}Sr_{0.5})(Fe_{0.8}Cu_{0.2})O_{3-\delta}$ stoichiometry. Furthermore, the BSFCu ceramic strikes by large grains with an average size of about 100 μm. The grain size distribution and the nature of the grain boundaries might be key factors in the oxygen permeation performance. The bright-field STEM micrograph and HRTEM micrograph in Figure 3b and Figure 3c, respectively, present the grain boundary between two perovskite grains revealed by selected area electron diffraction (SAED) (Figure 3d) or due to two-dimensional fast Fourier transformation (FFT) (Figure 3e). Both perovskite grains are in close contact. No amorphous phase, or any other substance, was observed at the interface. The grain on the left-hand side is oriented along the zone axis [2,2,3], and the grain on the right-hand side is oriented along the zone axis [0,0,1]. Additionally, the HRTEM micrograph in Figure 3c was extended by contrast simulations

(32) Goldschmidt, V. M. *Naturwissenschaften* **1926**, *14*, 477.
(33) Wei, B.; Lu, Z.; Huang, X.; Miao, J.; Sha, X.; Xin, X.; Su, W. *J. Eur. Ceram. Soc.* **2006**, *26*, 2827.

Table 1. Comparison of Oxygen Permeation Flux Through Several Related Perovskite Membranes

perovskite membranes	oxygen permeation flux/mL cm^{-2} min^{-1}		E_A/kJ mol^{-1}
	1023 K	1223 K	
$(Ba_{0.5}Sr_{0.5})(Fe_{0.8}Zn_{0.2})O_{3-\delta}$	0.36	0.98	55
$(Ba_{0.5}Sr_{0.5})(Fe_{0.9}Al_{0.1})O_{3-\delta}$[16]	0.41[a]	1.19	44
$(Ba_{0.5}Sr_{0.5})(Fe_{0.8}Cu_{0.2})O_{3-\delta}$	0.53	1.60	47
$(Ba_{0.5}Sr_{0.5})(Co_{0.8}Fe_{0.2})O_{3-\delta}$	1.31	2.66	46

[a] Value is extrapolated with the assumption of a linear progress of the oxygen permeation flux depending on the temperature.

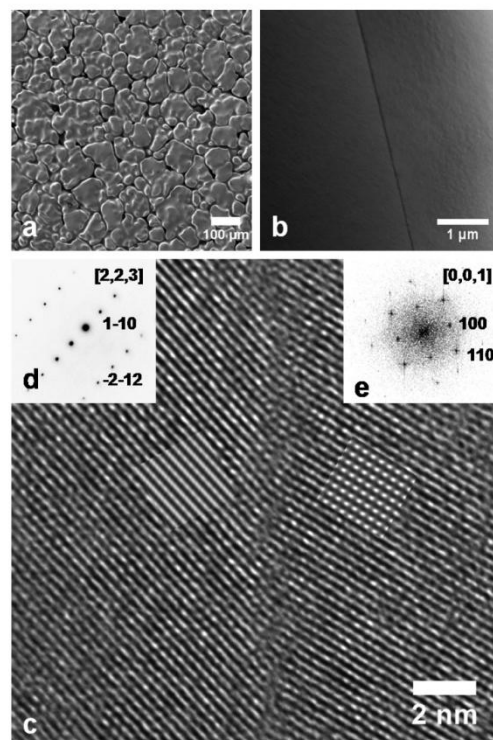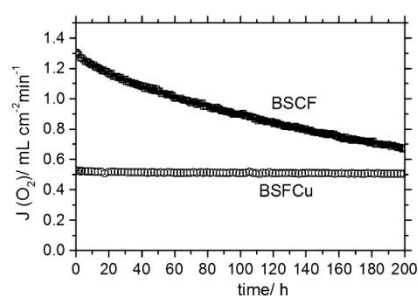**Figure 4.** Oxygen permeation flux through $(Ba_{0.5}Sr_{0.5})(Fe_{0.8}Cu_{0.2})O_{3-\delta}$ (BSFCu) and $(Ba_{0.5}Sr_{0.5})(Co_{0.8}Fe_{0.2})O_{3-\delta}$ (BSCF) membranes as a function of time at 1023 K.

Figure 5. Electrical conductivity of BSFCu pellet: a) σ as a function of temperature and b) σT in Arrhenius representation.

performed via JEMS software for each grain according to its orientation, which show good correlation with experimental results.

In order to be a candidate for a promising membrane material, a novel perovskite system must show a good oxygen permeation performance. Because the value of oxygen flux through a membrane strongly depends on the experimental conditions, such as the membrane thickness and oxygen partial pressures on the permeate and the feed side, it is problematic to compare the detected oxygen permeation flux with data given in the literature. Table 1 summarizes the results of oxygen permeation measurements of several related perovskite membranes of equal thickness (1.1 mm) conducted under the same conditions. Thus, it appears that the oxygen flux through the BSFCu membrane, both at intermediate (1023 K) and at high temperatures (1223 K), is significantly higher than the flux through $(Ba_{0.5}Sr_{0.5})(Fe_{0.8}Zn_{0.2})O_{3-\delta}$ and $(Ba_{0.5}Sr_{0.5})$-$(Fe_{0.9}Al_{0.1})O_{3-\delta}$ membranes. The permeation flux of $(Ba_{0.5}Sr_{0.5})(Co_{0.8}Fe_{0.2})O_{3-\delta}$, however, remains unrivalled. The activation energies were calculated from the temperature dependence of the oxygen permeation as given in Table 1.

For perspective application in the IT range, the most important factor for perovskite materials is a constant oxygen permeation performance owing to phase stability in addition to good mixed oxygen-ionic and electronic conductivity. For this reason, time-dependent oxygen permeation experiments were carried out for BSFCu and the prominent $(Ba_{0.5}Sr_{0.5})(Co_{0.8}Fe_{0.2})O_{3-\delta}$ perovskite in the IT range. Figure 4 shows the oxygen permeation flux through both membranes at 1023 K. The oxygen permeation of the BSFCu membrane maintains a value of

0.53 mL cm^{-2} min^{-1} for more than 200 h. The flux through the $(Ba_{0.5}Sr_{0.5})(Co_{0.8}Fe_{0.2})O_{3-\delta}$ membrane continuously decreases with time. The flux was reduced by one-half after 200 h, from 1.31 mL cm^{-2} min^{-1} to 0.66 mL cm^{2-} min^{-1}, which was caused by the intrinsic phase instability of the $(Ba_{0.5}Sr_{0.5})(Co_{0.8}Fe_{0.2})O_{3-\delta}$ perovskite at intermediate temperatures[5,8-12]. After the measurement, the microstructure of the BSFCu material was analyzed by SEM, EDXS, and XRD. SEM investigations combined with EDXS of the feed side, the permeate side, and the cross-section of the membrane exhibit the absence of cracks and coats in the ceramic. With the help of XRD, the BSFCu material was proved to maintain its cubic perovskite structure as a single pure phase during the performance test at 1023 K for 200 h. Thus, these results show the advantage of the BSFCu perovskite over $(Ba_{0.5}Sr_{0.5})(Co_{0.8}Fe_{0.2})O_{3-\delta}$ materials for operation in the IT range.

The total electrical conductivity of the BSFCu ceramic was studied via the four-point probe method at ambient air. As demonstrated in Figure 5a, the conductivity increases with increasing temperature and reaches a maximum value of 45 S cm^{-1} at around 890 K. This semiconducting behavior can be explained by a thermally activated p-type small polaron-hopping mechanism.[34] An activation energy of 23.2 kJ mol^{-1} was determined from the linear part of the Arrhenius plot (Figure 5b) in the temperature range of 300−500 K. The changeover from semiconduction to metallic conduction of the BSFCu above 890 K may be related to a spin-state transition of the Fe ions.[17,35,36] The

(34) Stevenson, J. W.; Armstrong, T. R.; Carneim, R. D.; Pederson, L. R.; Weber, W. J. *J. Electrochem. Soc.* **1996**, *143*, 2722.

Efimov et al.

total conductivity of BSFCu is comparable with that of $(Ba_{0.5}Sr_{0.5})(Co_{0.8}Fe_{0.2})O_{3-\delta}$, which shows a maximum value of approximately 45−50 S cm^{-1} at about 820 K.[37] The established Co-free material, such as $(Ba_{0.5}Sr_{0.5})(Fe_{0.8}Zn_{0.2})O_{3-\delta}$, shows a lower conductivity with a maximum of 9.4 S cm^{-1} at about 860 K.[38]

(35) Raccah, P. M.; Goodenough, J. B. *Phys. Rev.* **1967**, *155*, 932.
(36) Bhide, V. G.; Rao, G. R.; Rao, C. N. R.; Rajoria, D. S. *Phys. Rev. B* **1972**, *6*, 1021.
(37) Zhao, H.; Shen, W.; Zhu, Z.; Li, X.; Wang, Z. *J. Power Sources* **2008**, *182*, 503.
(38) Wei, B.; Lu, Z.; Huang, X.; Miao, J.; Sha, X.; Xin, X.; Su, W. *J. Power Sources* **2008**, *176*, 1.

Conclusions

The novel cubic perovskite BSFCu was designed to be an alternative to Co-based perovskites. This material exhibits a good phase stability at high and intermediate temperatures and a better oxygen permeation performance as compared to related Fe-based perovskites. With regard to thermal dilatation and electrical conductivity, BSFCu is comparable to $(Ba_{0.5}Sr_{0.5})(Co_{0.8}Fe_{0.2})O_{3-\delta}$. The stability of the BSFCu material during the operation in the IT range clearly exceeds that of $(Ba_{0.5}Sr_{0.5})(Co_{0.8}Fe_{0.2})O_{3-\delta}$.

4 Intolerance of alkaline earth-containing perovskite against CO_2

4.1 Summary

For numerous applications, where some CO_2 is present in a gaseous atmosphere, the alkaline earth-containing MIEC materials could not sustain their phase stability and oxygen transport properties because of the formation of carbonates. This chapter summarizes the poisoning effect of CO_2 on $Ba(Co_xFe_yZr_z)O_{3-\delta}$ and $(Ba_{0.5}Sr_{0.5})(Fe_{0.8}Zn_{0.2})O_{3-\delta}$ oxygen-transporting perovskites, which were developed to be an alternative to BSCF cobaltite because of their beneficial thermal and mechanical stabilities.

Section 4.2 demonstrates that the oxygen permeation performance of a $Ba(Co_xFe_yZr_z)O_{3-\delta}$ hollow fiber membrane was almost stopped after a dwell time of 30 minutes when 10 vol.% CO_2 was present in the sweep gas. To gain a deeper understanding of the processes occurring during application in CO_2-containing atmospheres, *in-situ* XRD and TEM studies were carried out on a two-phase perovskite having an average composition of $BaCo_{0.4}Fe_{0.4}Zr_{0.2}O_{3-\delta}$, which is similar to that of the $BaCo_xFe_yZr_zO_{3-\delta}$ hollow fiber. The initial powder consisted of 74 wt.% $BaCo_{0.5-\gamma}Fe_{0.5-\gamma}Zr_{2\gamma}O_{3-\delta}$ (γ = 0.015-0.025) with a cubic perovskite structure and 16 wt.% of cubic $BaZrO_3$ perovskite. Rapid formation of a high-temperature rhombohedral $BaCO_3$ polymorph was observed after exposure of the CO_2 at 1173 K on the costs of cobalt- and iron-containing perovskite phases. This carbonate structure is not quenchable and cannot be detected by *ex-situ* methods. Additionally, a reversible phase transition of $BaCO_3$ from orthorhombic to rhombohedral to cubic was detected at different temperatures, accompanied by the formation of CoO and the distortion of remaining iron-containing perovskite. Furthermore, full regeneration of the perovskite phase was obtained after high-temperature treatment under CO_2-free conditions.

The $(Ba_{0.5}Sr_{0.5})(Fe_{0.8}Zn_{0.2})O_{3-\delta}$ membrane exhibited a constant oxygen permeation flux for about 100 hours at 1023 K, while sweeping with helium gas, indicating good inherent phase stability of the perovskite over intermediate temperatures (Section 4.3). After insertion of CO_2 in the sweep gas, the oxygen permeation flux collapsed immediately, as a result of the formation of a tarnishing layer on the membrane surface. Using XRD and TEM, a several micrometer-thick layer was found to consist of mixed barium, strontium carbonate, zinc oxide and distorted perovskite phases. Complete recovery of the oxygen flux was achieved by membrane flushing with helium at 1223 K, pointing out the full decomposition of the tarnishing layer and regeneration of the perovskite structure.

4.2 *In-situ* X-ray diffraction study of carbonate formation and decomposition in perovskite-type BCFZ

Konstantin Efimov, Oliver Czuprat, and Armin Feldhoff

In-situ X-ray diffraction study of carbonate formation and decomposition in perovskite-type BCFZ

Konstantin Efimov*, Oliver Czuprat, Armin Feldhoff

Institute of Physical Chemistry and Electrochemistry, Leibniz Universität Hannover, Callinstr. 3A, D-30167 Hannover, Germany

ARTICLE INFO

ABSTRACT

The effect of CO_2 on the two phase perovskite with average composition of $BaCo_{0.4}Fe_{0.4}Zr_{0.2}O_{3-\delta}$ is investigated by *in-situ* X-ray diffraction (XRD) as well as transmission electron microscopy (TEM). Partial decomposition of the BCFZ into high-temperature rhombohedral $BaCO_3$ polymorph was observed during annealing in an atmosphere, which contained 50 vol% CO_2/50 vol% N_2 at 1173 K. This carbonate structure is not quenchable and cannot be detected by *ex-situ* methods. Additionally, the reversible phase transition of $BaCO_3$ from orthorhombic to rhombohedral to cubic at different temperatures accompanied by formation of CoO was shown by *in-situ* XRD and TEM. Furthermore, complete regeneration of perovskite phase was obtained after high-temperature treatment under CO_2-free conditions.

© 2011 Elsevier Inc. All rights reserved.

1. Introduction

Doped perovskites (ABO_3) with multivalent cations as mixed ionic and electronic conductors are a hot topic in materials science today, e.g. as membrane materials for the separation of oxygen from oxygen containing gases like air with unrivaled selectivities [1] or as cathode material in solid-oxide fuel cells [2]. In the last decade, these membranes have attracted great academic and industrial interest, since they have also large potential applications in chemical processes in which a constant supply or removal of oxygen is required [3]. For prospective industrial applications as membrane reactors for oxidative activation reactions of light hydrocarbons [4] or as oxygen separators in zero emission plants in which oxygen permeable membranes are flushed with CO_2-containing exhaust gases [5], a sufficient stability especially in reducing gas atmospheres or atmospheres containing CO_2 is essential.

The poisoning effect of CO_2 arises from alkaline earth metal cations in the perovskite structure, which tend to form carbonates. Carolan et al. [6] reported that the oxygen permeation flux of $La_{0.8}Ba_{0.2}Co_{0.8}Fe_{0.2}O_{3-\delta}$ decreased significantly when 430 ppm CO_2 was introduced into the operation gas. It was further discovered that $BaCe_{0.9}Y_{0.1}O_{3-\delta}$ is converted to the carbonate at 1123–1273 K under pure CO_2 atmosphere and the perovskite structure is disrupted [7].

Arnold et al. [8] investigated the influence of CO_2 on the oxygen permeation performance and the microstructure of perovskite-type $Ba_{0.5}Sr_{0.5}Co_{0.8}Fe_{0.2}O_{3-\delta}$ membranes. It was found that when having air on the feed side, using pure CO_2 as sweep gas at 1148 K caused an immediate stop of the oxygen permeation flux, which could be recovered by sweeping with pure helium. A detailed surface analysis of a BSCF cathode after operation in 1% CO_2/O_2 at 723 K for 24 h revealed that its surface was destroyed and mixed barium–strontium carbonate was formed as a top layer [9].

Systems using dense perovskite hollow fiber membranes of the composition $BaCo_xFe_yZr_zO_{3-\delta}$ ($x+y+z=1$), which is a novel oxygen permeable membrane material with high O_2 permeation fluxes and excellent thermal and mechanical stability [10], have been presented by our group, e.g. for the direct decomposition of nitrous oxide to nitrogen by *in-situ* oxygen removal [11], the simultaneous production of hydrogen and synthesis gas by combining water splitting with partial oxidation of methane [12] as well as the multi-step oxidative dehydrogenation of ethane [4] and propane (ODP) [13]. Furthermore, the oxidative coupling of methane to C_2 products could be successfully demonstrated in a $BaCo_xFe_yZr_zO_{3-\delta}$ hollow fiber membrane reactor [14].

Summarizing, the effect of CO_2 on the membrane permeation performance plays an important role and thus was examined recently [15]. Under exposure of 50 vol% CO_2 in He, the perovskite structure is impaired up to a depth of ca. 15 μm after 5 h and approximately 30 μm after 10 h, respectively. Furthermore, it was found that both microstructure as well as oxygen permeation are recovered in a CO_2-free atmosphere.

---

* Corresponding author.
  E-mail address: Konstantin.Efimov@pci.uni-hannover.de (K. Efimov).

In order to get a deeper understanding of the processes occurring during application in CO_2 containing atmospheres, we carried out an *in-situ* X-ray diffraction (XRD) as well as transmission electron microscopy (TEM) study on the powder with the composition of $BaCo_{0.4}Fe_{0.4}Zr_{0.2}O_{3-\delta}$, which is similar to that of $BaCo_xFe_yZr_zO_{3-\delta}$ hollow fiber, and can be considered as a model system.

2. Experimental

Powder with average composition of $BaCo_{0.4}Fe_{0.4}Zr_{0.2}O_{3-\delta}$ (denoted as BCFZ) was obtained from the Fraunhofer-Institute for Ceramic Technologies and Systems (IKTS, Hermsdorf) from the hydrolysis of corresponding metal nitrates by an ammonium hydroxide solution followed by calcination. $BaCo_xFe_yZr_zO_{3-\delta}$ $(x+y+z=1)$ hollow fiber membranes were manufactured by phase inversion spinning followed by sintering as described elsewhere [1]. The O_2 permeation experiments of the $BaCo_xFe_yZr_zO_{3-\delta}$ hollow fiber membrane, were carried out on a high-temperature permeation reactor which is described in detail elsewhere [1]. *In-situ* powder XRD was conducted on the Bruker D8 Advance diffractometer in Bragg-Brentano geometry using Cu-$K\alpha$ radiation with interval of 0.02 and count times of 0.3 s per step. The diffractometer was equipped with an Anton Paar 1200 N high-temperature chamber and superfast 1D Lynxeye detector. XRD data were analyzed using TOPAS 4.0 software (Bruker AXS). Quantitative analyses of XRD collected at isothermal conditions were carried out by Rietveld method. During the *in-situ* experiments at rising and falling temperatures, phases with unknown structures were observed. These phases were included in the refinement by Pawley fits. Then, the phase contents were estimated from the integrated scattered intensities of corresponding phases. The reliability of the both methods was controlled by XRD experiments on BCFZ powder at room temperature in ambient air using of known amount of $BaCO_3$ as internal standard. Structural data for the known phases were taken from ICSD database (FIZ Karlsruhe) with file numbers: $BaCoO_{2.23}$ [28865], $BaZrO_3$ [27048], $BaCO_3$ (orthorhombic) [15196], $BaCO_3$ (rhombohedral) [158389], $BaCO_3$ (cubic) [27449], CoO [28505], and FeO [24635]. Scanning TEM (STEM) was conducted at 200 kV on a JEOL JEM-2100 F-UHR field-emission instrument. A light-element energy dispersive X-ray (EDX) spectrometer, Oxford Instruments INCA-200 TEM, was used for elemental analysis. In order to obtain a TEM sample, the powder was glued between two alumina bodies, polished, and finally Ar^+ sputtered to electron transparency.

3. Results and discussion

The effect of CO_2 on the oxygen permeation performance of the $BaCo_xFe_yZr_zO_{3-\delta}$ hollow fiber at 1173 K is shown in Fig. 1. Insertion of 10 vol% CO_2 on the sweep side of a membrane leads to the diminution of oxygen permeation flux after only few minutes. Then, the oxygen flux through perovskite hollow fiber is almost stopped after dwell time of 30 min. However, the fast recovery of the oxygen permeation can be observed, if the sweep gas is changed to pure He. The value of oxygen flux reaches two-thirds of the initial performance after 5 min. The complete regeneration occurs after testing for 30 min.

According to Czuprat et al. [15], the decline of oxygen permeation flux in presence of CO_2 is due to formation of $BaCO_3$, which was observed by XRD and scanning electron microscopy (SEM) on the surface of quenched $BaCo_xFe_yZr_zO_{3-\delta}$ perovskite hollow fiber. The full recovery of the flux points out to the decomposition of poisoning $BaCO_3$ and the regeneration of the initial structure of hollow fiber.

To prove this hypothesis, the high-temperature *in-situ* XRD in CO_2 containing atmosphere was carried out on the BCFZ powder. Fig. 2 shows *in-situ* XRD-patterns of BCFZ collected at (a) room temperature, (b) at 1173 K in flowing synthetic air consisting 80 vol% N_2 and 20 vol% O_2, and (c) at 1173 K in an atmosphere
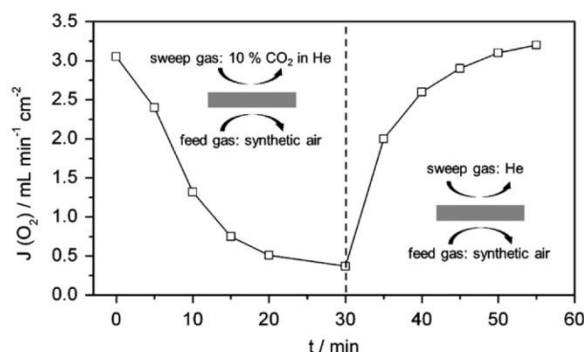
Fig. 1. Decline of O_2 permeation through a $BaCo_xFe_yZr_zO_{3-\delta}$ hollow fiber membrane with effective thickness of 140 μm under CO_2 exposure on the sweep side (sweep side: F_{total}=50 mL min⁻¹ 10 vol% CO_2 in He; feed side: 150 mL min⁻¹ synthetic air (80 vol% N_2, 20 vol% O_2,) and recovery as a function of time while sweeping with pure He at 1173 K (sweep side: 50 mL min⁻¹ He; feed site: 150 mL min⁻¹ synthetic air (80 vol% N_2, 20 vol% O_2,)).

containing 50 vol% CO_2 and 50 vol% N_2. As can be seen in the room temperature XRD (Fig. 2a), the original BCFZ powder consists of two perovskite systems as reported by Caro et al. [16] previously. The Rietveld analysis of XRD data combined with the EDXS investigation of the initial BCFZ powder exhibit, that the main compound is a $BaCo_{0.5-\gamma}Fe_{0.5-\gamma}Zr_{2\gamma}O_{3-\delta}$ (γ=0.015–0.025) with cubic structure (space group $Pm\bar{3}m$, a=4.072 Å). Furthermore, the powder contains approximately 16 wt% of cubic $BaZrO_3$ perovskite (space group $Pm\bar{3}m$, a=4.18 Å). Note, the co-existence of two cubic perovskite phases after doping of 5–10% Zr was also reported for similar perovskite systems like $Ba_{0.5}Sr_{0.5}Co_{0.8}Fe_{0.2-x}Zr_xO_{3-\delta}$ and $SrCo_{0.4}Fe_{0.6-x}Zr_xO_{3-\delta}$ [17,18]. The high-temperature XRD pattern taken from the BCFZ powder annealed at 1173 K for 30 min in the flowing synthetic air evidences no structural changes. Only slight shift of Bragg-reflection positions to smaller angles can be recognized here due to thermal lattice expansion. The annealing of the BCFZ powder at 1173 K for 90 min under 50 vol% CO_2/50 vol% N_2 leads to the partial decomposition of perovskite structure. $BaCO_3$ can be detected in the *in-situ* XRD pattern (Fig. 2c) alongside of BCFZ. The pattern of $BaCO_3$ relates to the high-temperature rhombohedral polymorph (space group $R3m$), which is stable in the temperature range from approximately 1073 K to 1233 K as reported by Antao et al. [19]. The structure of this phase is not quenchable and cannot be detected by *ex-situ* methods. Quantitative Rietveld analysis was applied to estimate the $BaCO_3$ content in the sample to be about 29 wt%. Additionally, the presence of a fourth phase is obvious by weak intensities at 36.3° and 42.1° 2Θ. This phase can be understood as CoO with help of TEM experiments (see Fig. 5) on the sample quenched in CO_2-containing atmosphere. Change-over of the gas atmosphere to the CO_2-free synthetic air or pure N_2 leads to the complete decomposition of $BaCO_3$ and regeneration of both perovskite phases.

In order to elucidate the kinetics of the carbonate formation and decomposition, series of *in-situ* XRD experiments accompanied by quantitative analysis were carried out determining the content of $BaCO_3$ in the BCFZ powder as function of time. Fig. 3 summarizes the results of quantitative analysis of diffraction patterns collected at 1173 K in time intervals of 15 min at different gas atmospheres. In presence of 50 vol% CO_2 in N_2, the content of $BaCO_3$ amounts to approximately 15 wt% after the first 15 min. After half an hour, the content of $BaCO_3$ reaches about 24 wt%. Then, the amount of carbonate increases slowly and reaches the value of approximately 29 wt% during 90 min. The sluggish kinetic of carbonate formation after the dwell time of 30 min may be explained by the development of the dense

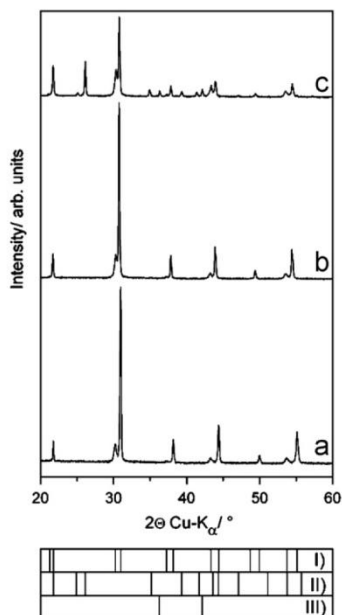**Fig. 2.** *In-situ* XRD-patterns of BCFZ powder collected (a) at room temperature; (b) at 1173 K in flowing synthetic air (80 vol% N_2, 20 vol% O_2) after 30 min, $F_{total}=100$ mL min^{-1}; (c) at 1173 K in an atmosphere containing 50% CO_2/50% N_2 after 90 min, $F_{total}=100$ mL min^{-1}. (I–III) Calculated Bragg position of (I) BCFZ (two phase system); (II) $BaCO_3$ rhombohedral polymorph; (III) CoO.
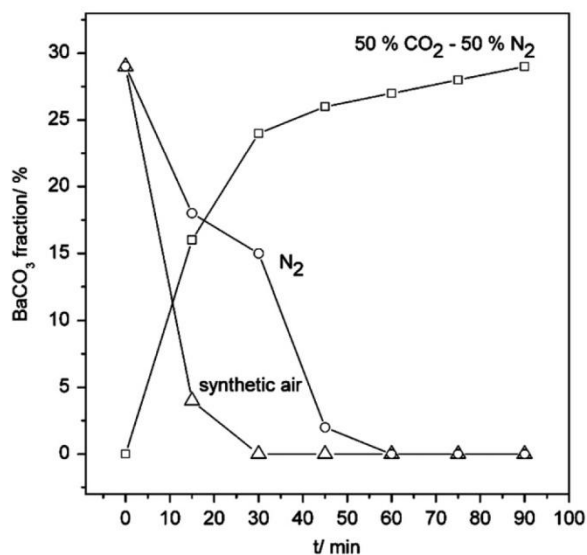

Fig. 3. Amount of $BaCO_3$ in the BCFZ sample as function of time at different atmospheres as observed by *in-situ* XRD. (Synthetic air: 80 vol% N_2, 20 vol% O_2, $F_{total}=100$ mL min^{-1}; N_2: $F_{total}=100$ mL min^{-1}).

carbonate layer on the surface of perovskite particles, which can be considered as a protective layer regarding further carbonate formation. Moreover, thermodynamical considerations deliver further approach to understand partial BCFZ decomposition. According to the Ellingham diagram presented by Feldhoff et al. [20], $BaCO_3$ is stable at 5×10^4 Pa CO_2 up to 1603 K. However, Kumar et al. [21] reported that the reaction of $BaCO_3$ with

transition metal oxide like TiO_2 leading to the formation of perovskite is thermodynamically possibly above 649 K in 10^5 Pa CO_2. Thus, we assume that the reaction of the carbonate with transition metal oxide counteracts the formation of the carbonate at 1173 K in 5×10^4 Pa CO_2 and the both processes are in equilibrium state. The composition of remaining BCFZ perovskite, which consists of the two above mentioned perovskite phases was also changed during the annealing in CO_2. We found that the ratio of $BaCo_{0.5-\gamma}Fe_{0.5-\gamma}Zr_{2\gamma}O_{3-\delta}$ component was significantly decreased and reached the value of approximately 46 wt%. In contrast, the ratio of $BaZrO_3$ phase was remained almost constant. It seems that carbonate formation occurs at the costs of Co- and Fe-containing perovskite phase. These phenomena points out to the higher stability of Zr-based perovskite as postulated by Yokokawa et al. [22].

Fig. 3 shows also the kinetics of the BCFZ regeneration, if the CO_2 atmosphere was changed over to synthetic air or pure N_2. In air, the carbonate was decomposed very rapidly. After 15 min, only approximately 4 wt% carbonate can be detected in the sample. After 30 min, the carbonate was removed completely. Carbonate decomposition proceeds in the N_2 atmosphere a little slower. The perovskite structure was fully recovered after testing for 60 min. The decomposition of $BaCO_3$ in CO_2-free atmospheres corresponds to thermodynamical calculations, which indicate that carbonate becomes unstable at 1173 K if CO_2 partial pressure is lower than 30 Pa [20]. Then, solid state reaction between carbonate and transition metal oxides can be considered as thermodynamically favored.

Effect of temperature on the carbonate formation in the atmosphere containing 50 vol% CO_2 in N_2 was also studied by *in-situ* XRD during heating and cooling in the range of 303–1273 K with steps of 100 K. Before each data acquisition, an equilibrium time of 30 min was set. The phase fractions were estimated by considering integrated intensities of corresponding phases in the refinements, which were carried out by combined Rietveld and Pawley methods. Fig. 4a and b display selected XRD data. An appreciable amount of $BaCO_3$ was detected not until 873 K by heating of the sample (Fig. 4a). A low temperature orthorhombic polymorph (space group *Pmcn*) was formed under these conditions. Additionally, a low amount of CoO can be observed in the powder. The carbonate remains in orthorhombic symmetry up to 973 K. Rising the temperature leads to the phase transition of the orthorhombic $BaCO_3$ to rhombohedral polymorph at 1073 K and to cubic carbonate phase at 1273 K. The high-temperature cubic carbonate (space group $Fm\overline{3}m$) exists only at temperatures above 1233 K as reported by Strømme [23]. Interestingly, the integrated intensity of carbonate phase in the scan collected at 1073 K was diminished from 42% at 1073 K to 10% at 1273 K, which can be explained by strong decline of the carbonate content in the sample. This finding can be related to an increasing of the Gibbs free enthalpy of carbonate formation with rising temperature accompanied by decline of the Gibbs free enthalpy of the reaction between carbonate and oxides leading to shift of equilibrium of the processes [21]. During cooling, $BaCO_3$ structure changes to rhombohedral polymorph at 1173 K (Fig. 4b) and the integrated intensity of carbonate phase reaches the value of about 21%. Further cooling to 873 K leads to formation of orthorhombic carbonate phase and rising of the ratio of the integrated intensity to 27%.

Thus, the maximum $BaCO_3$ content in the sample was observed in the sample at 1073 K during the heating. Furthermore, the XRD scan collected at these conditions exhibits apparently just one perovskite phase. However, the value of scattered intensity of this phase amounted to be 52%, which cannot be explained by complete loss of Co- and Fe-containing phases. The shape of the peaks as well as peak widths cannot be interpreted by single $BaZrO_3$ phase also. Rather, the formation of above 40 wt% carbonate
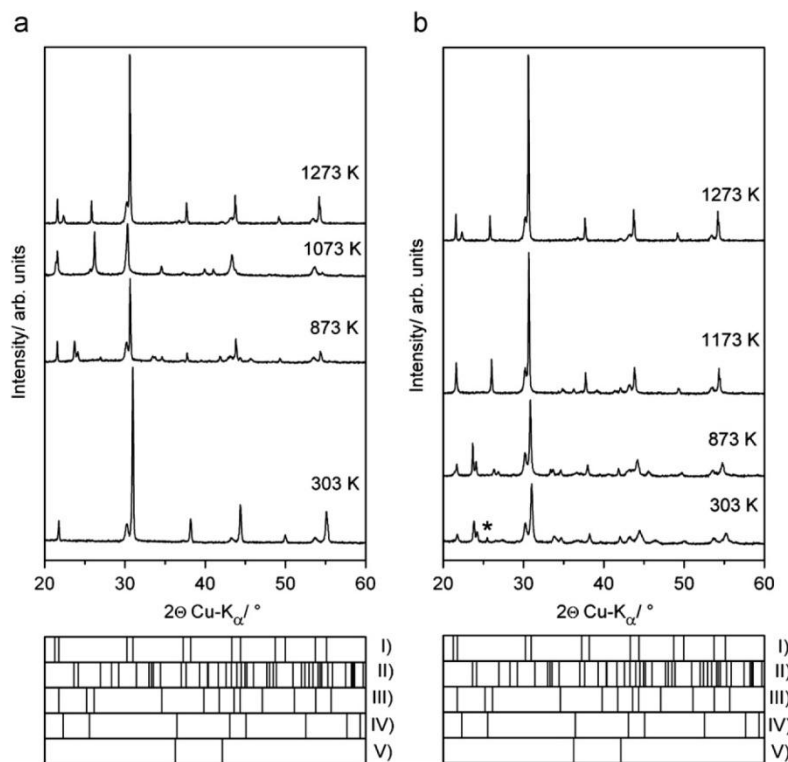
Fig. 4. *In-situ* XRD of BCFZ powder in the atmosphere containing 50 vol% CO_2 and 50 vol% N_2 $F_{total}=100$ mL min^{-1} (a) during heating; (b) during cooling. Before each data acquisition an equilibrium time of 30 min was set. (I–V) Calculated Bragg positions for (I) BCFZ; (II) orthorhombic $BaCO_3$; (III) rhombohedral $BaCO_3$; (IV) cubic $BaCO_3$; (V) CoO. Asterisks marks a reflection of tetragonal perovskite phase.
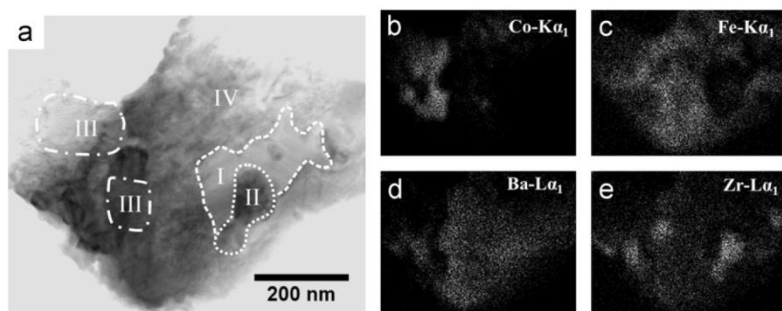
Fig. 5. (a) STEM bright field micrograph of BCFZ powder annealed and cooled in 50% CO_2 and 50% N_2. (b–e) Elemental distributions by EDXS.

leads to strong decline of Co- and Fe-ratio in the main perovskite phase followed by increase of lattice parameter due to high amount of Zr in the perovskite. Consequently, the increase of lattice parameter leads to a shift of the reflection positions to the smaller 2Θ angles and to the overlap of the reflection positions of both perovskite phases in the corresponding XRD scan. Increase of the temperature to 1273 K leads to partial decomposition of $BaCO_3$ due to the above-mentioned reasons and to a regeneration of $BaCo_{0.5-\gamma}Fe_{0.5-\gamma}Zr_{2\gamma}O_{3-\delta}$ phase. The composition of the sample was marginally changed after the complete cooling in CO_2. However, at room temperature we detected a new compound in XRD pattern, which cannot be attributed to the mentioned phases. The intensity of the phase at 25.4° 2Θ, which is marked by asterisks in Fig. 4b, relates to a tetragonal perovskite structure as reported by Martynczuk et al. [24].

In order to verify the results of *in-situ* XRD experiments, we investigated the sample, which was annealed and cooled down in CO_2 by TEM methods. The STEM bright-field micrograph in Fig. 5a shows a BCFZ powder particle, which consists of several grains. EDXS elemental distribution (Fig. 5b–e) clearly demonstrates that the grains exhibit a different chemical composition. The grain marked in Fig. 5a with "I" contains no metal cations besides of Ba and can be indicated as $BaCO_3$. Obviously, the carbonate phase does not form a dense layer around the BCFZ powder particle in contrast to the hollow fiber ceramic membrane [15]. Instead, the carbonate is located inside of the particle. This kind of behavior was also observed by Martynczuk et al. [24], who investigated the effect of CO_2 on the functional performance of related Zn-doped $(Ba,Sr)FeO_{3-\delta}$ perovskite. The phase "II" consisted of Ba and Zr in the ratio 1:1 relates to $BaZrO_3$. Cliff-Lorimer quantification of EDXS

data reveals a dramatical enrichment of Co in area "III" collateral to an almost entirely absence of other cations. Thus, this phase can be considered as CoO. Finally, the main phase marked with "IV" can be described as a Co-depleted $Ba(Co,Fe,Zr)O_{3-\delta}$ perovskite.

Based on the *in-situ* XRD study as well as TEM investigations, we summarize the BCFZ decomposition process in presence of CO_2. Firstly, the CO_2 reacts with BCFZ under formation of $BaCO_3$. The carbonate can exhibit different polymorphs depending on the temperature. The formation of carbonate does not lead to the complete destruction of perovskite. Based on TEM, partial BCFZ decomposition cannot be explained by slow kinetic of the reaction due to formation of protective layer on the surface of perovskite particle. The chemical equilibrium between formation of carbonate and reaction to the perovskite can be rather considered as an applicable approach. Second, we found that the carbonate formation occurs predominantly at the cost of Co/Fe containing component of BCFZ accompanied by development of CoO as by-product. Poor stability of Co-containing perovskite caused by flexible redox behavior of Co-cations was already discussed in some details in ours previous reports [25–27]. Furthermore, these results are in good agreement with reports of Yakovlev et al. [17] as well as Yi et al. [28] suggesting the stabilizing effect of higher valent B-site cation like Zr^{4+} or Nb^{5+} on the Co-, Fe-containing perovskite materials. The remaining perovskite phase was found to be Fe-enriched. According to the report of Yáng et al. [29], structures of perovskites with Ba/Fe-rich composition exhibit several distorted variants. One of them, the tetragonal distorted perovskite phase, we observed in the room temperature XRD pattern (Fig. 4b).

4. Conclusions

Decomposition process of BCFZ powder, which consists of two perovskite phases, in the CO_2-containing atmosphere was investigated by *in-situ* XRD as function of dwell time and temperature. Rapid formation of high-temperature rhombohedral $BaCO_3$ polymorph was observed after exposure of the CO_2 at 1173 K. This non-quenchable carbonate structure, which is stable at temperatures between 1073 and 1233 K, can be declared as the phase terminating the oxygen permeation transport through BCFZ membrane materials. Time-dependent experiments at isothermal conditions deliver the partial decomposition of two phase BCFZ system at the costs of Co- and Fe-containing perovskite phase, which is in close agreement with thermodynamical considerations. Furthermore, the complete regeneration of BCFZ was proven after removing of CO_2 from the gas atmosphere.

The reversible phase transition of $BaCO_3$ from orthorhombic at temperatures below 1073 K to rhombohedral to cubic at 1273 K was shown by *in-situ* XRD. Finally, formation of CoO as well as traces of tetragonal disordered Fe-enriched perovskite phase was observed as by-products of BCFZ decomposition by XRD and TEM methods.

References

[1] T. Schiestel, M. Kilgus, S. Peter, K.J. Caspary, H. Wang, J. Caro, J. Membr. Sci. 258 (2005) 1–4.
[2] Z. Shao, S. Haile, Nature 431 (2004) 170–173.
[3] H.J.M. Bouwmeester, A.J. Burggraaf, Dense ceramic membranes for oxygen separation, in: A.J. Burggraaf, L. Cot (Eds.), Fundamentals of Inorganic Membrane Science and Technology, Elsevier, Amsterdam, 1996, pp. 435–528.
[4] O. Czuprat, S. Werth, S. Schirrmeister, T. Schiestel, J. Caro, Chem. Catal. Chem. 1 (2009) 401–405.
[5] J.H. Horlock, Advanced Gas Turbine Cycles, Pergamon, Oxford, 2003.
[6] M.F. Carolan, P.N. Dyer, J.M LaBar, R.M. Thorogood, US Patent 5240473 (1993).
[7] N. Zakowsky, S. Williamson, J.T.S. Irvine, Solid State Ionics 176 (2005) 3019–3026.
[8] M. Arnold, H. Wang, A. Feldhoff, J. Membr. Sci. 293 (2007) 44–52.
[9] A. Yan, V. Maragou, A. Arico, M. Cheng, P. Tsiakaras, Appl. Catal. B 76 (2007) 320–327.
[10] S.M. Liu, G.R. Gavalas, J. Membr. Sci. 246 (2005) 103–108.
[11] H. Jiang, H. Wang, F. Liang, S. Werth, T. Schiestel, J. Caro, Angew. Chem. Int. Ed. 48 (2009) 2983–2986.
[12] H. Jiang, H. Wang, S. Werth, T. Schiestel, J. Caro, Angew. Chem. Int. Ed. 47 (2008) 9341–9344.
[13] O. Czuprat, S. Werth, J. Caro, T. Schiestel, AIChE J. 56 (2010) 2390–2396.
[14] O. Czuprat, T. Schiestel, H. Voss, J. Caro, Ind. Eng. Chem. Res. 46 (2010) 10230–10236.
[15] O. Czuprat, M. Arnold, S. Schirrmeister, T. Schiestel, J. Caro, J. Membr. Sci. 364 (2010) 132–137.
[16] J. Caro, H. Wang, C. Tablet, A. Kleinert, A. Feldhoff, T. Schiestel, M. Kilgus, P. Kölsch, S. Werth, Catal. Today 118 (2006) 128–135.
[17] S. Yakovlev, C.Y. Yoo, S. Fang, H.J.M. Bouwmeester, Appl. Phys. Lett. 96 (2010) 254101-1.
[18] L. Yang, L. Tan, X. Gu, W. Jin, L. Zhang, N. Xu, Ind. Eng. Chem. Res. 42 (2003) 2299–2305.
[19] S.M. Antao, E.I. Hassan, Phys. Chem. Miner. 34 (2007) 573–580.
[20] A. Feldhoff, M. Arnold, J. Martynczuk, Th.M. Gesing, H. Wang, Solid State Sci. 10 (2008) 689–701.
[21] S. Kumar, G.L. Messing, W.B. White, J. Am. Ceram. Soc. 76 (1993) 617–624.
[22] H. Yokokawa, N. Sakai, T. Kawada, M. Dokiya, Solid State Ionics 52 (1992) 43–56.
[23] K.O. Strømme, Acta Chem. Scand. A 29 (1975) 105–110.
[24] J. Martynczuk, K. Efimov, L. Robben, A. Feldhoff, J. Membr. Sci. 344 (2009) 62–70.
[25] K. Efimov, T. Halfer, A. Kuhn, P. Heitjans, J. Caro, A. Feldhoff, Chem. Mater. 22 (2010) 1540–1544.
[26] A. Feldhoff, J. Martynczuk, M. Arnold, M. Myndyk, I. Bergmann, V. Šepelák, W. Gruner, U. Vogt, A. Hähnel, J. Woltersdorf, J. Solid State Chem. 182 (2009) 2961–2971.
[27] K. Efimov, Q. Xu, A. Feldhoff, Chem. Mater. 22 (2010) 5866–5875.
[28] J. Yi, M. Schroeder, T. Weirich, J. Mayer, Chem. Mater. 22 (2010) 6246–6253.
[29] Z. Yáng, A.S. Harvey, A. Infortuna, L. Gauckler, J. Appl. Crystallogr. 42 (2009) 153–160.

4.3 Performance of zinc-doped perovskite-type membranes at intermediate temperatures for long-term oxygen permeation and under carbon dioxide atmosphere

Julia Martynczuk, Konstantin Efimov, Lars Robben, and Armin Feldhoff

Performance of zinc-doped perovskite-type membranes at intermediate temperatures for long-term oxygen permeation and under a carbon dioxide atmosphere

Julia Martynczuk[a,*], Konstantin Efimov[a], Lars Robben[b], Armin Feldhoff[a]

[a] Institute of Physical Chemistry and Electrochemistry, Leibniz Universität Hannover, Callinstr. 3-3a, D-30167 Hannover, Germany
[b] Institute of Mineralogy, Leibniz Universität Hannover, Callinstr. 3, D-30167 Hannover, Germany

ABSTRACT

Zinc-doped $(BaSr)FeO_{3-\delta}$ perovskite-type membranes were found to exhibit excellent long-term stability at high and intermediate temperatures under an oxygen partial pressure difference of $p^1/p^2 = 21/2.1 \times 10^3$ Pa at 950 °C and $p^1/p^2 = 21/0.8 \times 10^3$ Pa at 750 °C. After the change to carbon dioxide as the sweep gas, the oxygen permeation diminishes almost completely. By XRD, a phase mixture of hexagonal, tetragonal and cubic perovskite with a $(Ba_{0.4\pm0.1}Sr_{0.6\pm0.1})CO_3$ layer and some zinc oxide was found. TEM showed that the dense perovskite membrane is decomposed into phases with different morphologies accompanied by pore and crack formation in a surface layer with a depth of approximately 5 μm. After switching to helium as the sweep gas, the carbonate layer is decomposed, but a hexagonal and tetragonal perovskite phase in addition to the cubic phase are still present. A short heating to 950 °C regenerates the oxygen permeation flux due to the abatement of hexagonal perovskite for the benefit of the cubic and tetragonal perovskite phase. The appearance of the carbonate structure, even to a small amount of 8%, leads to a breakdown of the oxygen permeation ability, but also the hexagonal perovskite is disadvantageous. In contrast, the cubic and tetragonal perovskite modifications exhibit good oxygen permeation abilities. The effect of the carbon dioxide is totally reversible after a short high temperature treatment.

© 2009 Elsevier B.V. All rights reserved.

1. Introduction

Since the International Energy Agency released the actual World Energy Outlook in November 2008, declaring that current energy trends are socially, environmentally and economically unsustainable, energy is one of the main factors that must be considered in discussions of sustainable development [1,2]. Fuel cells as alternatives to the standard conversion of energy are rapidly increasing in interest, and fuel cell materials like perovskite-type oxides are being simultaneously investigated intensively. In solid-oxide fuel cells, the state-of-the-art cathodes are $(La_xSr_{1-x})MnO_{3-\delta}$ perovskites operating at high temperature (i.e., 800–1000 °C), or mixed conducting $(La_xSr_{1-x})(Co_yFe_{1-y})O_{3-\delta}$ perovskites for intermediate temperature operation, i.e., 500–800 °C. Among the variety of alternative materials, $(Sm_xSr_{1-x})CoO_{3-\delta}$ and $(Ba_xSr_{1-x})(Co_yFe_{1-y})O_{3-\delta}$ are perovskites that show very good oxygen reduction properties

and low polarization resistances, because of the extremely high amount of mobile oxygen vacancies [3–5]. Perovskites are not only employed as cathode, but also as electrolyte or anode materials and even full ceramic intermediate-temperature solid-oxide fuel cells (IT-SOFCs) are possible [6–10]. Furthermore, there is also considerable interest in mixed ionic and electronic conductors with perovskite structure for various other applications, especially for industrial processes, where the supply or removal of oxygen to or from reaction mixtures with high selectivity and oxygen fluxes is needed [11,12]. Perovskite-type ceramic membranes are a key technology, e.g., in the separation of oxygen from air, partial oxidation of hydrocarbons and oxygen-enrichment in air [13–16].

In the large field of perovskite materials, some materials stand out due to their exceptionally high oxygen fluxes. One of the highest oxygen permeation fluxes reported so far for a perovskite membrane exhibits the $(Ba_{0.5}Sr_{0.5})(Co_{0.8}Fe_{0.2})O_{3-\delta}$ perovskite-type oxide (BSCF) [6]. But recently, serious stability problems for long-term periods with this cobalt containing material in the IT range below 900 °C have been discussed in the literature [17,18]. Therefore, great effort has been put into the search for alternative materials and the development of cobalt-free perovskite-type oxides. Recently, a novel perovskite material of $A^{II}B^{IV}O_3$-type

* Corresponding author at: Nonmetallic Inorganic Materials, ETH Zurich, Wolfgang-Pauli-Str. 10, CH-8093 Zurich, Switzerland. Tel.: +41 44 633 69 97; fax: +41 44 632 11 32.
E-mail address: julia.martynczuk@mat.ethz.ch (J. Martynczuk).

with the stoichiometry $(Ba_{0.5}Sr_{0.5})(Fe_{0.8}Zn_{0.2})O_{3-\delta}$ (BSFZ) has been developed that shows high oxygen permeation fluxes (membrane disks: ~2.55 mL min^{-1} cm^{-2} for the partial catalytic oxidation of methane to syngas (POM)), as well as an excellent phase stability under a 2% H$_2$–Ar atmosphere with an oxygen partial pressure pO$_2$ of less than 1×10^{-8} Pa [19,20]. Doping of the B-site of the perovskite structure with a divalent metal like zinc leads to the diminution of non-stoichiometric oxygen variations and lattice expansion caused by the variation of temperature or chemical oxygen potential and improves the oxygen permeability due to higher ionic conductivity. BSFZ is a mixed conductor that can provide simultaneous transport of oxygen ions and electrons. Furthermore, Wei et al. demonstrated the use of BSFZ as a cathode material in an IT-SOFC at 500–650 °C at power densities of up to 180 mW cm^{-2} and quantified the polarization resistances of symmetrical BSFZ cathodes in air to be 0.23 Ω cm^2, 0.48 Ω cm^2, and 1.06 Ω cm^2 at 700 °C, 650 °C, and 600 °C, respectively [21,22]. Our aim was to further investigate this material concerning its performance at intermediate temperatures for long-term oxygen permeation and under carbon dioxide atmosphere.

It is well known that alkaline earth elements easily form stable carbonates and the stability increases with alkaline earth ionic radius [23,24]. That is why barium- and strontium-containing perovskites exhibit severe stability problems at high temperatures in the presence of carbon dioxide, e.g., for BaCe$_{0.9}$Y$_{0.1}$O$_{3-\delta}$, Sr(CoFe)O$_{3-\delta}$, and BaPr$_{0.7}$Gd$_{0.3}$O$_{3-\delta}$ [25–29]. Carbon dioxide is a component in natural air as well as it is a product of the synthesis gas production, hence its effect on the membrane performance is important for practical application and needs to be investigated. Therefore, depending on the potential application of the perovskite membrane several investigations concerning the effect of carbon dioxide on different materials with perovskite-type structure have been published in the recent years [8,25–44]. For $(Ba_{0.5}Sr_{0.5})(Co_{0.8}Fe_{0.2})O_{3-\delta}$, Arnold et al. showed that the perovskite structure is impaired up to a depth of 50 µm in the presence of carbon dioxide at 875 °C [30] and Yan et al. found that even small quantities of carbon dioxide (0.28–3.07%) seriously deteriorate the cathode performance in a fuel cell at 450 °C [31,32]. Also, calcium-containing perovskites exhibit the same problem as shown by Kalinkin for CaTiO$_3$ and by Nomura et al. for (BaCa)(CoFe)O$_{3-\delta}$ [33,34]. The partial substitution of the A-site ions with lanthanum does not solve the problem either, because the remaining strontium content, nevertheless, tends to form carbonates [35–38]. It was previously stated in 1991 by Yokokawa et al. that the stability of perovskites could not be determined merely by the stabilization energy, but required other thermodynamic factors and that the stable region of oxygen potential for double oxides was primarily determined by the stability of the less stable constituent oxide, like strontium in the Sr-doped lanthanum perovskites [39]. When a comparison is made between strontium and barium, the tendency of carbonate formation of the binary oxide is much stronger in barium oxide. On the other hand, the stabilization energy of barium perovskites is negatively larger. Thus, the stability against the carbonate formation is essentially the same in magnitude between strontium and barium perovskites [40].

The approaches found in the literature to diminish carbonate formation in a carbon dioxide atmosphere are the introduction of an A-site deficiency or the doping of the B-site position with a stabilizing ion. The former was done by Yaremchenko et al. [41] in the case of $(SrFeO_{3-\delta})_{0.7}(SrAl_2O_4)_{0.3}$ and by Yi et al. for $Sr_{0.95}Co_{0.8}Fe_{0.2}O_{3-\delta}$ [42]. The influence of a B-site doping has so far been reported only for proton conducting perovskites for the addition of zirconia for $Ba(Ce_{0.8-x}Zr_x)Y_2O_{3-\delta}$ by Fabbri et al. [43] or zinc for $Ba(Ce_{0.5}Zr_{0.3}Y_{0.16}Zn_{0.04})O_{3-\delta}$ by Tao et al. and for $Ba(Zr_{0.81}Y_{0.15}Zn_{0.04})O_{3-\delta}$ by Babilo et al. [8,44]. For the last two materials, the TGA analysis in pure CO$_2$ indicated no CO$_2$ uptake

on cycling to 1200 °C and resulted in no phase change according to XRD, in contrast to samples with the same Zr/Ce ratio without zinc or with samples containing only yttria and ceria on the perovskite B-site. Following, zinc doping stabilizes against carbonation.

In the present work, the stabilizing effect of zinc in the $(BaSr)FeO_{3-\delta}$ system was investigated by long-term oxygen permeation experiments and under a carbon dioxide atmosphere using XRD, SEM and analytical TEM analysis.

2. Experimental

A synthesis method with combined citric acid and ethylene-diamine-tetraacetic acid (EDTA) as the complexing agents was applied, which is described in detail elsewhere [23,24]. The nitrates of the cations (Ba(NO$_3$)$_2$, Sr(NO$_3$)$_2$, Zn(NO$_3$)$_2$, Fe(NO$_3$)$_3$) were dissolved in water, followed by the addition of EDTA acid and citric acid, with the molar ratio of EDTA acid:citric acid:total of metal cations controlled at around 2:3:2. The pH value of the solution was adjusted to around 9 by the addition of NH$_3$·H$_2$O. After water evaporation for several hours at 150 °C, further heat treatments were applied at temperatures up to 950 °C for 40 h. The calcined powders were uniaxially pressed under 140 kN into pellets and sintered pressurelessly at 1150 °C for 40 h to ceramic disks of 14 mm in diameter and a thickness of around 1.15 mm.

Oxygen permeation was measured in a high-temperature permeation cell [45] according to the method described in [46]. The sintered membranes were sealed onto an Al$_2$O$_3$ ceramic tube with gold paste (conducting paste, C5754, Heraeus) at 950 °C for 2 h. After sealing, gas flow rates were delivered to the reactor by mass flow controllers (Bronckhorst Hi-Tech) and continuously read by an on-line gas chromatograph (Agilent Technologies, HP 6890, equipped with a Carboxen 1000 column). Air was fed at a rate of 150 mL min^{-1} to the feed side; He (29.0 mL min^{-1}, 99.995%) and Ne (1.0 mL min^{-1}, 99.995%) as the internal standard gases were fed to the sweep side. The relative leakage of O$_2$ was found to be less than 8%.

X-ray diffraction (XRD) data for the Rietveld phase analysis of BSFZ membranes were recorded on a Bruker D8 Advance diffractometer using reflection geometry, and a Göbel mirror and Cu Kα$_{1,2}$ radiations. Three thousand data points were collected with a step width of 0.02° in the 2θ from 20° to 80°. Phase analysis by the Rietveld method was carried out by using TOPAS 2.0 (Bruker AXS) software. During refinements, general parameters such as scale factors, four background parameters, zero point error and sample tilt were optimized. Profile shape calculations were carried out on the basis of standard instrumental parameters using the fundamental parameter approach implemented in the program, varying also the average crystal size (integral breadth) of the reflections. The lattice parameters and crystallite size of all phases were refined. Structural data for the known phases were taken from ICSD PDF-2 database with PDF numbers: Al$_2$O$_3$ [46–1212], Au [4–784], ZnO [36–1451], and $(Ba_{0.5}Sr_{0.5})CO_3$ [47–224]. Structural data for the BSFZ cubic perovskite was taken from Feldhoff et al. [23,47]. Further XRD measurements for qualitative phase analysis were carried out on a Philips PW1800 diffractometer using Cu Kα$_{1,2}$ radiations and a secondary monochromator in reflection geometry to achieve high sample throughput. Reflections that could not be included in the refinement by the above-mentioned phases were compared with the PDF database if the sample contained other known phases, which was not the case. These reflections from unknown phases could be included in the refinements by adding phases deduced from the BSFZ perovskite by geometrical considerations as described in more detail in the following section. These phases were included in the refinement procedures by Pawley fits. Phase contents were calculated by considering the integrated scat-

J. Martynczuk et al. / Journal of Membrane Science 344 (2009) 62–70
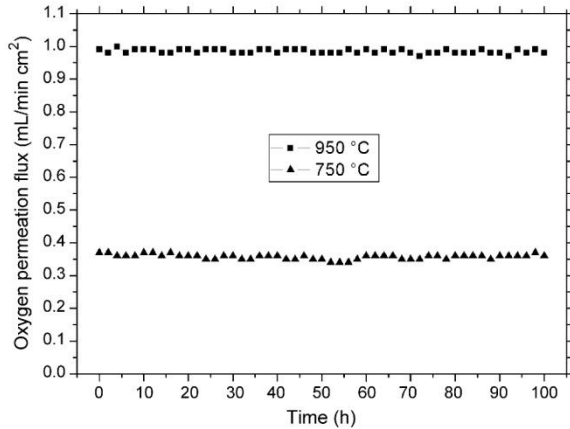
Fig. 1. Long-term oxygen permeation measurements, oxygen permeation flux as a function of time for 100 h at 950 °C and 750 °C for BSFZ membranes, which were sintered at 1150 °C for 40 h, membrane thickness = 1.15 mm. The oxygen partial pressure at the permeate side was in the range of $0.8–2.1 \times 10^3$ Pa, feed side: synthetic air (150 mL min⁻¹), sweep side: He (29.0 mL min⁻¹) and Ne (1.0 mL min⁻¹).

tering intensity of the respective phases in the refinement, whereas the tube sealing materials were excluded.

Scanning electron microscopy (SEM) was employed on a field-emission instrument of the type JEOL JSM-6700F. Secondary electron (SE) micrographs were taken at a low excitation voltage of 2 kV. In order to analyze the microstructure of the sintered membranes, SEM was conducted on both surfaces and on fracture surfaces and grain size distributions were evaluated. Fracture surfaces were etched with aqueous HCl (2 M) for 2–5 s in order to visualize grain boundaries. An EDX spectrometer of the type Oxford Instruments INCA-300 with ultra-thin window was used for elemental analysis. Adobe Photoshop CS2 (Version 9.0) and ImageJ (1.33 u) were used as the image analysis software for the determination of the grain size distribution.

Additionally, TEM was conducted at 200 kV with a JEOL JEM-2100F-UHR field-emission instrument equipped with a Gatan GIF 2001 energy filter and a 1k-CCD camera. EDXS was carried out by a light-element detector using the Cliff-Lorimer quantification technique (INCA 200 TEM, Oxford Instruments). In order to obtain elemental maps by energy-filtered transmission electron microscopy (EFTEM), the three windows method was used. For the Ba–M edge, 40 eV-width slits were centered at 661 eV, 751 eV (pre-edge) and 801 eV (post-edge). For the Fe–L edge, 40 eV-width slits were placed at 643 eV, 683 eV (pre-edge) and 728 eV (post-edge), For the C–K edge, 20 eV-width slits were placed at 248 eV,
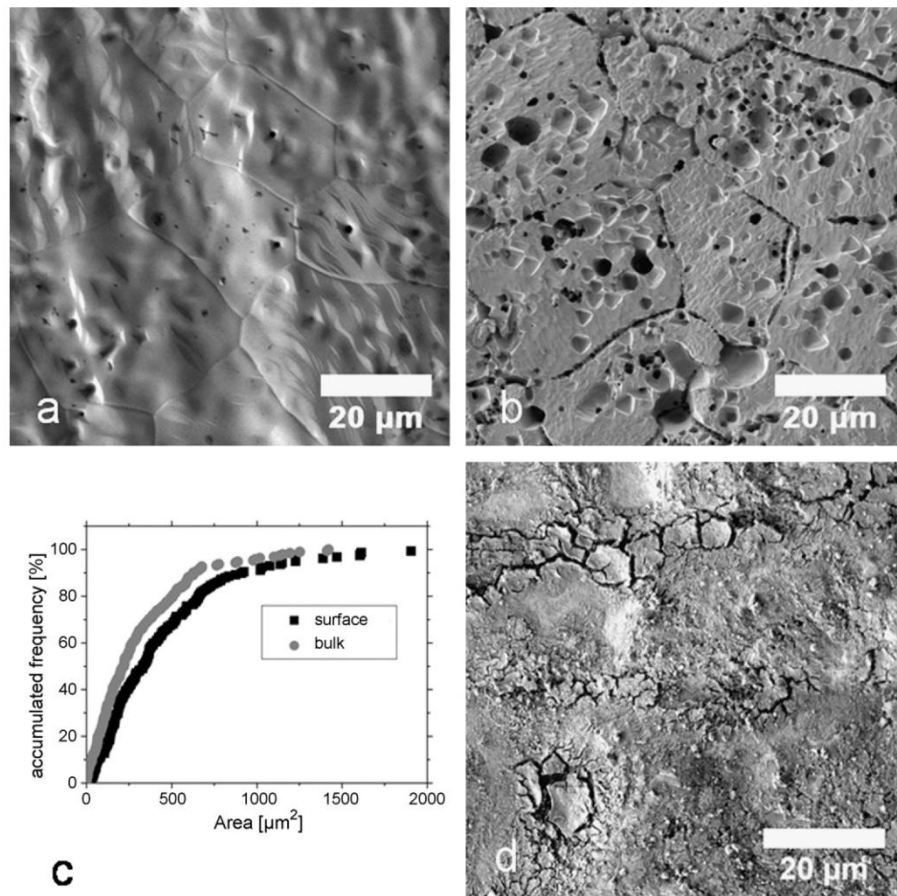
Fig. 2. Secondary electron micrographs of a sintered membrane (40 h at 1150 °C) with grain size distribution: (a) surface, (b) fracture surface (bulk) etched for 2 s with HCl (2 M), (c) grain size distribution of surface and bulk, (d) and the permeate side of a recovered membrane after CO₂ treatment.

270 eV (pre-edge) and 294 eV (post-edge). For the Zn–L edge, energy slits with the width of 40 eV were centered at 955 eV, 995 eV (pre-edge) and 1040 eV (post-edge). Furthermore, specimens after carbon dioxide treatment were prepared as follows for electron microscopy (SEM, TEM). First, the membrane permeate side was vaporized with gold in order to mark the surface area. Accordingly, the permeate side was glued with a polycrystalline corundum block using epoxy followed by cutting of the membrane into 1 mm × 1 mm × 2 mm pieces. The protected membrane pieces were polished on polymer-embedded diamond lapping films to approximately 0.01 mm × 1 mm × 2 mm (Allied High Tech, Multi-prep). Electron transparency was achieved by Ar$^+$ ion sputtering at 3 kV (Gatan, model 691 PIPS, precision ion polishing system) under shallow incident angles of 10°, 6°, and 4°.

3. Results and discussion

The main focus of the present work is on the performance of the zinc-doped perovskite membranes under carbon dioxide atmospheres. However, it should also be kept in mind that the perovskites are also exposed to quite low oxygen potentials at high temperatures, and so possibly thermal decomposition of the perovskite into component oxides or even metallic phases may also become an issue. To investigate the kinetic demixing of the perovskite membranes under oxygen pressure gradients and phase changes of the defect perovskite oxides at intermediate temperatures we investigated the performance of zinc-doped perovskite-type membranes at intermediate temperatures by long-term oxygen permeation experiments under an oxygen partial pressure gradient of synthetic air at the feed side (150 mL min^{-1} cm^{-2}, pO$_2$ = 2.1 × 10^4 Pa) and a helium/neon mixture at the sweep side (He: 29 mL min^{-1} cm^{-2}, Ne: 1 mL min^{-1} cm^{-2}, pO$_2$ (950 °C) = 2.1 × 10^3 Pa, pO$_2$ (750 °C) = 0.8 × 10^3 Pa). Fig. 1 shows the oxygen permeation flux of BSFZ membranes at two temperatures as a function of time. The oxygen permeation flux is constant for more than 100 h at 950 °C and at 750 °C, and it reaches values of 0.98 mL min^{-1} cm^{-2} and 0.36 mL min^{-1} cm^{-2}, respectively. Fig. 2a–c shows a SEM micrograph of a BSFZ membrane sintered at 1150 °C for 40 h before the permeation experiment. The grain size distribution at the surface (Fig. 2a) and in the bulk (Fig. 2b) before the permeation experiments is very similar and the exact evolution of the grain size distribution of surface and bulk (Fig. 2c) confirms this finding. After the long-term oxygen permeation experiment, the microstructure of the membranes was found to correspond still to that shown in Fig. 2a–c (not shown here). Phase stability of the cubic perovskite was investigated by XRD. Results for both long-term experiments (950 °C and 750 °C) are equal, thus, Fig. 3a shows the XRD data of a BSFZ membrane after long-term permeation (100 h) at 750 °C. The phase content of the sample was investigated by the Rietveld method and shows only gold, corundum – both from the tube sealing of the permeation experiment – and the cubic BSFZ perovskite phase. This proves that the BSFZ perovskite-type membranes exhibit long-term stability at high (950 °C) and intermediate (750 °C) temperatures.

The effect of CO$_2$ on the permeation behavior of BSFZ perovskite-type membranes is shown in Figs. 4 and 5. First, we conducted an oxygen permeation measurement at 750 °C with changes of sweep gas from helium to carbon dioxide and back and forth (He (2 h), CO$_2$ (2 h), He (4 h), CO$_2$ (2 h), He (12 h)) for a BSFZ membrane sintered at 1150 °C for 40 h (Fig. 4). The oxygen permeation behavior corresponds to Fig. 1 for helium as the sweep gas (0.36 mL min^{-1} cm^{-2}), but after the change to carbon dioxide as the sweep gas the oxygen permeation diminishes almost completely after an equilibrium time of 1/2 h and does not increase again during 2 h of carbon dioxide treatment. Switching to helium as the sweep gas does
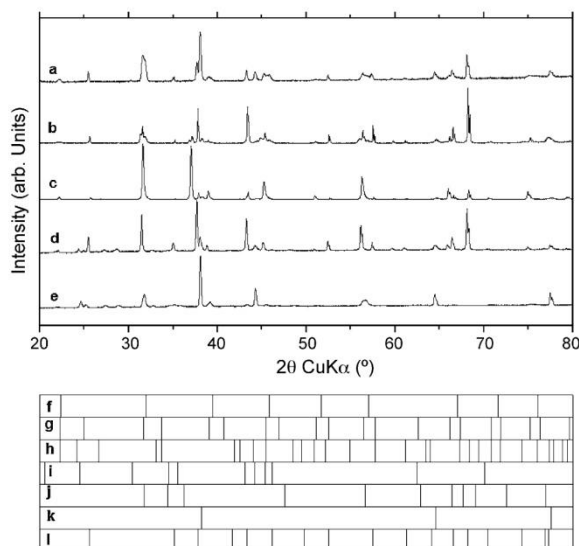
Fig. 3. X-ray diffraction data of BSFZ membranes after different permeation experiments (all measurements carried out with D8 except (b) and (c), where a visual shift of the pattern occurs due to sample height error, which was considered in the refinements): (a) long-term permeation for 100 h at 750 °C, (b) quenched from 750 °C with changes of the sweep gas from He (2 h) to CO$_2$ (2 h) to He (4 h) to CO$_2$ (2 h) to He (12 h), (c) quenched from 750 °C with changes of the sweep gas from He (2 h) to CO$_2$ (2 h) to He (1 h), followed by a heating step under helium atmosphere from 750 °C to 950 °C with 2°/min, 1/2 h equilibrium time at 950 °C, and a cooling step from 950 °C to 750 °C with 2°/min to He (2 h), (d) quenched from 750 °C with changes of the sweep gas from He (2 h) to CO$_2$ (2 h), (e) quenched after 100 h at 750 °C with CO$_2$ as the sweep and feed gas with a flow rate of 30 mL min^{-1} cm^{-2}, respectively. Reflex positions for different phases: (f) cubic perovskite, (g) tetragonal perovskite (calculated), (h) hexagonal perovskite (calculated), (i) (Ba$_{0.5}$Sr$_{0.5}$)CO$_3$ in aragonite modification, (j) ZnO, (k) Au (membrane sealing), and (l) Al$_2$O$_3$ (membrane reactor).

not give the same oxygen permeation flux as before, but rather half of the former flux (0.21–0.11 mL min^{-1} cm^{-2}). After a second switch to 2 h of carbon dioxide as the sweep gas, the oxygen permeation flux shows the same lower value. A sweeping of 12 h with helium increases the flux little by little but it stays as low as 0.22 mL min^{-1} cm^{-2}. The rapid total collapse of the oxygen permeation with carbon dioxide as the sweep gas can be explained
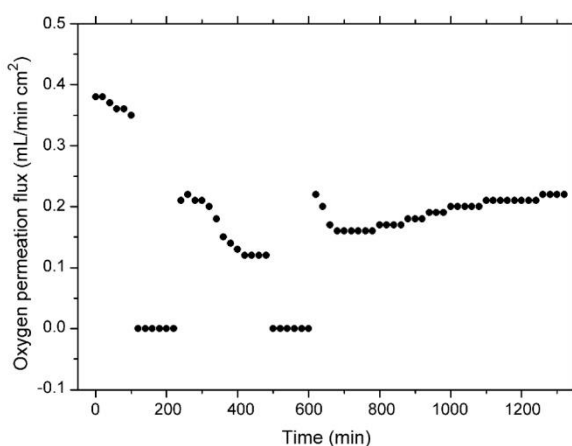
Fig. 4. Oxygen permeation measurements at 750 °C with changes of the sweep gas from He (2 h) to CO$_2$ (2 h) to He (4 h) to CO$_2$ (2 h) to He (12 h) of a BSFZ membrane sintered at 1150 °C for 40 h, membrane thickness = 1.15 mm. The oxygen partial pressure at the permeate side was in the range of 1 × 10^3 Pa to 6 Pa.
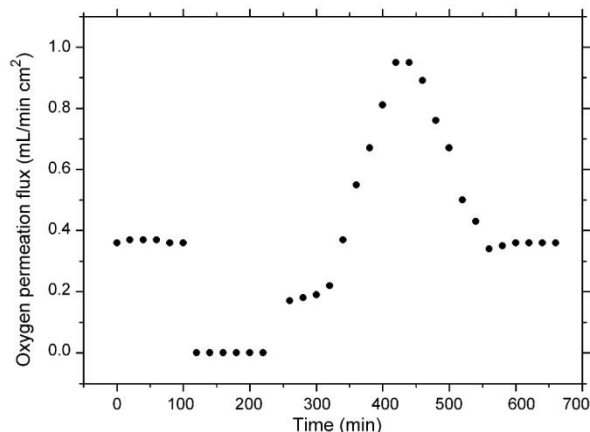
Fig. 5. Oxygen permeation measurements, oxygen permeation flux in dependence of time at 750 °C with changes of the sweep gas from He (2 h) to CO$_2$ (2 h) to He (1 h), followed by a heating step under helium atmosphere from 750 °C to 950 °C with 2°/min, 1/2 h equilibrium time at 950 °C, and a cooling step from 950 °C to 750 °C with 2°/min to He (2 h) for a BSFZ membrane sintered at 1150 °C for 40 h, membrane thickness = 1.15 mm. The oxygen partial pressure at the permeate side was in the range of 2.5 × 10^3 Pa to 6 Pa.

Table 1
Phase content in percent of the examined samples according to Rietveld refinements (calculated by integrated areas, tube sealing materials excluded; hexagonal and tetragonal perovskite phase included by Pawley fits).

	Fig. 3a	Fig. 3b	Fig. 3c	Fig. 3d	Fig. 3e
Measured with	D8	PW1800	PW1800	D8	D8
Cubic perovskite	100.0	52	67	49	9
Tetragonal perovskite	–	28	28	–	40
Hexagonal perovskite	–	20	5	42	16
(Ba$_x$,Sr$_{1-x}$)CO$_3$	–	–	–	8	35
				$x = 0.45$	$x = 0.31$
ZnO	–	–	–	1	–

often reported for perovskite-type structures) with lattice parameter $a_{tetra} = 3.99$ Å equal to the cubic lattice parameter and with a doubling of the cubic lattice parameter in c-direction (7.98 Å); and (b) a hexagonal phase (space group $P6_3/mmc$) with lattice parameter $a_{hexa} = 4.25$ Å and a doubling of the cubic lattice in c-direction. These phases were successfully included in the refinement procedures by Pawley fits. It has to be noted that these lattice parameters are the starting values for the Pawley fit refinements; the software modifies these lattice parameters and also the relative intensities for the reflections. The positions for the reflections given in Fig. 3g and h are calculated for the above given starting values and so not all reflections must necessarily be seen in the respective measurement. The addition of the hexagonal and the tetragonal phase allows the fitting of all reflections in the pattern. The reflection at approx. 27° 2θ can be attributed to the (0 1 1) reflection of the hexagonal phase. The refinement of the lattice parameters of these two new phases is in good accordance with the lattice parameters,

by the formation of a carbonate layer with the alkaline earth metal ions barium and strontium of the A-site of the perovskite or a transformation to another modification of the cubic perovskite. Because the operating temperature of 750 °C is in the intermediate range and the decomposition temperatures of the barium and strontium mixed carbonates is around 800 °C [23] the oxygen permeation might be reduced due to remaining carbonate or other perovskite modifications than the cubic phase [17]. Thus, above 750 °C, the oxygen permeation flux cannot be regenerated totally at this temperature. The BSFZ membrane needs to be heated for a short time to higher temperatures to decompose the carbonate layer. This is shown in Fig. 5 by the oxygen permeation flux as a function of time at 750 °C with changes of the sweep gas from He (2 h) to CO$_2$ (2 h) to He (1 h), followed by a heating step under helium atmosphere from 750 °C to 950 °C with 2°/min, 1/2 h equilibrium time at 950 °C, and a cooling step from 950 °C to 750 °C with 2°/min to He (2 h) for a BSFZ membrane sintered at 1150 °C for 40 h. The short heating regenerates the oxygen permeation flux and the membrane has the same performance as it did before the carbon dioxide treatment. These measurements show that the effect of the carbon dioxide on the oxygen permeation is totally reversible after a short high temperature treatment. Similar observations were made in Wang et al., however, without a correlation to the microstructure [48]. Although the effect on the oxygen permeation is totally reversible after a short high temperature treatment, the microstructure does not regenerate to its former appearance as shown in Fig. 2d. The permeate side of the regenerated membrane shows some cracks to a depth of approximately 5 μm. Several cycles of CO$_2$ treatment and regeneration at 950 °C will cause a slow destruction of the microstructure of the membrane.

To further investigate the microstructure of the different membranes, extensive XRD measurements were conducted (Fig. 3b–e) and evaluated by Rietveld refinements (Table 1). X-ray diffraction data of a BSFZ membrane quenched after the oxygen permeation measurements at 750 °C with changes of the sweep gas from helium to carbon dioxide (Fig. 4) is shown in Fig. 3b and it shows a quite different diffraction pattern with a number of unidentified reflections that cannot be attributed to known phases from the ICSD database. Thus, we deduced two additional phases from the cubic BSFZ perovskite: (a) a tetragonal phase (space group $P4/mmm$, which is
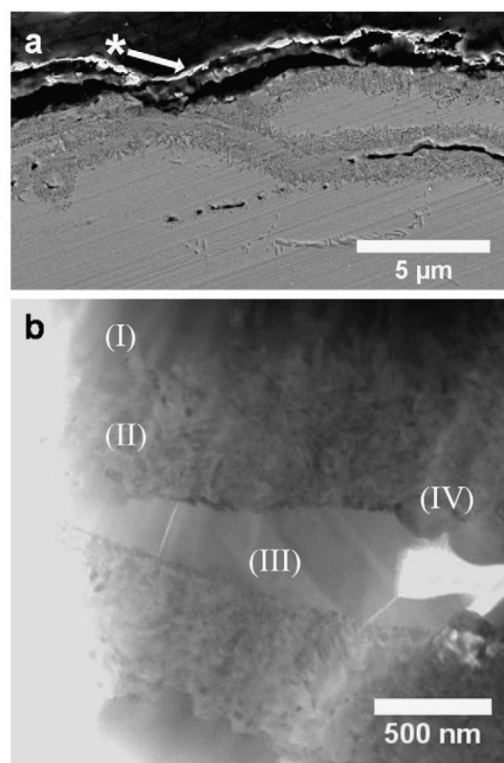

Fig. 6. (a) Scanning electron and (b) transmission electron bright-field micrographs of the membrane permeate side after treatment with CO$_2$ for 2 h at 750 °C. The asterisk (*) refers to unsoldered Au-coating, which was vaporized on the membrane permeate side in order to mark the surface area.
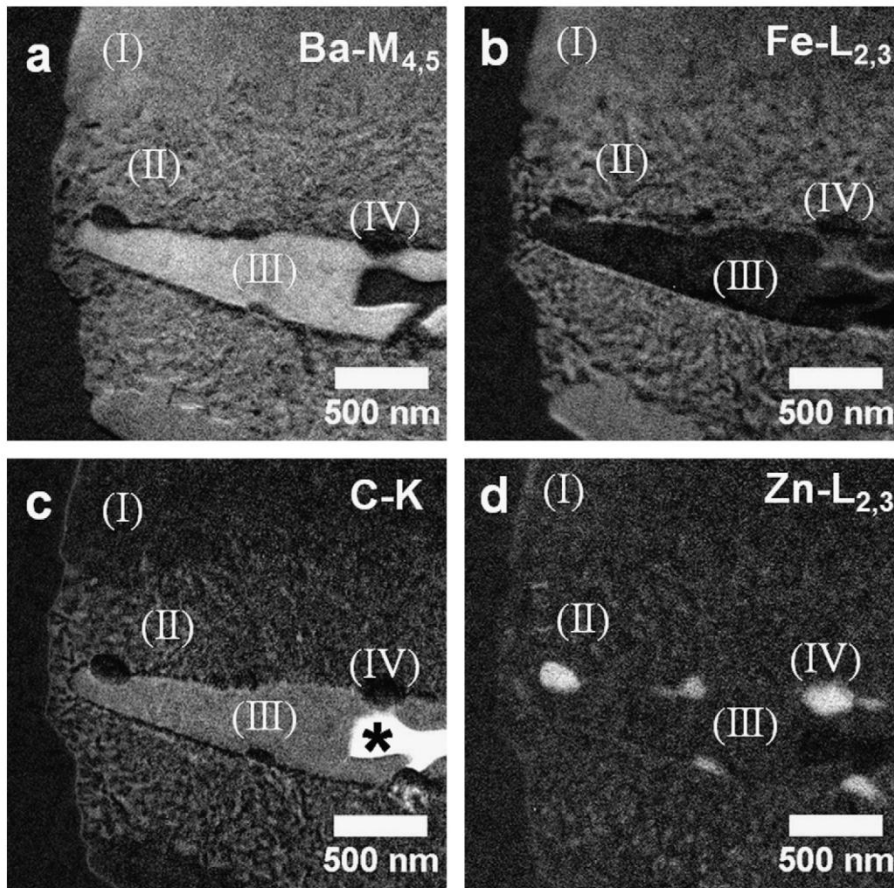
Fig. 7. Energy-filtered transmission electron micrographs of the intermediate phases at the permeate side after treatment with CO_2 for 2 h at 750 °C (same region as in Fig. 6b). High elemental concentration is shown by bright contrast: (a) barium, (b) iron, (c) carbon and (d) zinc. The asterisk (*) in (c) refers to a pore filled by epoxy due to TEM specimen preparation.

which have been deduced from the cubic structure. Thus, the sample shown in Fig. 3b was found to consist of perovskite in three different modifications: the cubic BSFZ starting material (52%), a tetragonal (28%) and a hexagonal (20%) perovskite. For this membrane, the oxygen permeation did not increase to its full value again even after helium treatment for 12 h, but the reason is not a carbonate layer, like suggested above, but different modifications of the perovskite. Conclusions about the structures of these new phases are limited to the crystal system considering the X-ray data available, but the data indicates clearly a modification of the cubic perovskite. This becomes also obvious when considering the peak shapes of the most intensive reflection of the cubic perovskite at approx. $32°$ 2θ, which shows the typical appearance of overlapping reflections with slightly different reflection positions and different crystallite sizes, where at least one phase clearly shows a higher crystallite size than the others.

Fig. 3c displays a BSFZ membrane quenched after oxygen permeation measurements at 750 °C with changes of sweep gas shown in Fig. 5 with a heating step to 950 °C consisting of 28% tetragonal, 5% hexagonal, and 67% cubic BSFZ perovskite phase. Since the oxygen permeation flux was regenerated again to its full value, we conclude that the tetragonal and cubic phases of the BSFZ perovskite have good oxygen permeation ability and the hexagonal phase is unfavorable for the oxygen permeation. The hexagonal perovskite phase was already reported to be oxygen non-permeable for sev-

eral perovskite compositions, e.g., for $Sr_{0.9}Ca_{0.1}CoO_{2.5+\delta}$, $SrMnO_{3-\delta}$, $SrCoO_{3-\delta}$ and $SrCo_{0.95}M_{0.05}O_{3-\delta}$ [49–52]. In the ideal hexagonal phase, chains of face-shared BO_6 (B = Fe, Zn) octahedron run parallel to the c-axis with A site cations (Ba, Sr) being distributed between the chains and the vacancy-ordered state [17,18,49,51]. Hence, the conduction for both oxide ions and electrons in such a structure is confined in one dimension along the c-axis at intermediate temperatures. It is considered that the oxide ion vacancies are unable to migrate as freely as these in the cubic or tetragonal perovskite-type structure and thus fail to give oxygen permeability to the oxide. When raising the temperature to 950 °C a phase transformation occurs from hexagonal to tetragonal or cubic perovskite, and thus the oxygen permeability and electrical conductivity increase.

Two other membranes were investigated in the XRD: a BSFZ membrane quenched after oxygen permeation measurements at 750 °C with changes of the sweep gas from He (2 h) to CO_2 (2 h) (Fig. 3d) and a BSFZ membrane quenched after oxygen permeation measurements for 100 h at 750 °C with CO_2 as the sweep and feed gas with a flow rate of 30 mL min^{-1} cm^{-2}, respectively (Fig. 3e). The phase content of the first sample shows the cubic BSFZ perovskite phase (49%), hexagonal perovskite (42%), $(Ba_{0.45}Sr_{0.55})CO_3$ (8%), and ZnO (1%). The Ba/Sr ratio in the carbonate was calculated by the unit cell volume according to Eq. (9) in [53]. The occurrence of the tetragonal perovskite and of zincite in this sample cannot be excluded from the data. Fig. 3e was refined to consist of the BSFZ
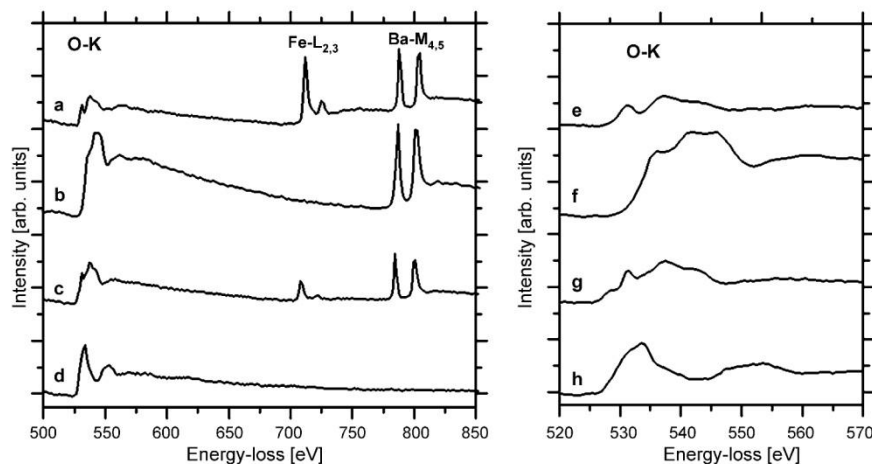
J. Martynczuk et al. / Journal of Membrane Science 344 (2009) 62–70

Fig. 8. Electron energy-loss spectra showing O–K, Fe–$L_{2,3}$ and Ba–$M_{4,5}$ ionization edges and close-ups of O–K energy-loss near-edge structures of different phases. (a and e) Perovskite-type $Ba_{0.5}Sr_{0.5}FeO_{3-\delta}$, (b and f) $(Ba_{0.4\pm0.1}Sr_{0.6\pm0.1})CO_3$ carbonate, (c and g) the phase mixture, (d and h) zinc oxide.

perovskite phase (9%) as well as the hexagonal (16%) and tetragonal (40%) perovskite phases. Additionally, a mixed $(Ba_{0.31}Sr_{0.69})CO_3$ can be identified in this sample (35%).

Since the XRD does not give local information for the different phases, SEM and TEM investigations were accomplished. Fig. 6a shows a cross-section secondary electron micrograph of the membrane reaction near-surface region after treatment with CO_2 for 2 h at 750 °C. Obviously, the dense perovskite membrane is decomposed into phases with different morphologies accompanied by pore and crack formation in a surface layer with a depth of approximately 5 μm. Fig. 6b displays a region of the surface near layer explicitly. Four phases have been distinguished here: a plate-like phase (I), a layer (II) with sponge-like morphology, a plate-like phase (III) and grains assigned with (IV), which are located at the boundaries between phases (II) and (III). Different chemical compositions of these phases have been found by EFTEM (Fig. 7), as well as EDXS. Fig. 7 displays the presence of barium (Fig. 7a) and iron (Fig. 7b) in phase (I) by bright contrast. No carbon (Fig. 7c) and no zinc (Fig. 7b) have been detected in the plate-like layer (I). Its EDXS quantification exhibits a stoichiometry like $(Ba_{0.5}Sr_{0.5})FeO_{3-\delta}$ perovskite. The sponge-like layer (II) contains all metal cations and a certain amount of carbon. Phase (III) is composed of barium, strontium, and carbon solely with a composition like $(Ba_{0.4\pm0.1}Sr_{0.6\pm0.1})CO_3$ carbonate determined by EDXS. Furthermore, Fig. 7 clearly indicates the exclusive presence of zinc in grains (IV) corresponding to zinc oxide. The appearance of layer (II) can be explained as a fine intermediate mixture of a perovskite-like phase (cubic or hexagonal), a carbonate, and a zinc oxide.

EEL spectra of the phases under consideration are given in Fig. 8. These demonstrate O–K, Fe–$L_{2,3}$, and Ba–$M_{4,5}$ ionization edges as well as close-ups of O–K energy-loss near-edge structures (ELNES). The spectra of the $(Ba_{0.5}Sr_{0.5})FeO_{3-\delta}$ perovskite phase (I) (Fig. 8a) and the $(Ba_{0.4\pm0.1}Sr_{0.6\pm0.1})CO_3$ carbonate (Fig. 8b) and the O–K ELNES (Fig. 8e and f) reveal typical characteristics of the spectra given in the literature for perovskite [23] and carbonate [23,54], respectively. The carbonate specific combined Sr–$M_{2,3}$ and C–K edges were also observed in the energy range of 260–320 eV (not shown here). The spectrum of the intermediate phase (II) in Fig. 8c exhibits Fe–$L_{2,3}$ and Ba–$M_{4,5}$ lines with other relative intensity proportions compared to perovskite. The fine structure of O–K ELNES (Fig. 8g) is affected by perovskite and carbonate phases. The ZnO EEL-spectrum shows an O–K line (Fig. 8d and h) in the energy loss-range of 500–850 eV with zinc oxide specific O–K ELNES [55]. Furthermore, the Zn–$L_{2,3}$ edge was detected at 1130 eV.

We come to the result that the appearance of the carbonate structure, even to a small amount of 8%, immediately leads to a breakdown of the oxygen permeation ability, but also the appearance of the perovskite in hexagonal modification is disadvantageous. In contrast, the cubic and tetragonal modifications of the perovskite exhibit good oxygen permeation abilities. The influence of hexagonal perovskite modification seems to be less severe than the appearance of a carbonate. The doping with zinc or the different methods described in the literature like the introduction of an A-site deficiency or the doping of the B-site position with a stabilizing ion [8,41–44] are all reducing the carbon dioxide damage, but in our opinion the only way to achieve overall carbon dioxide and phase stability is to choose barium and strontium free perovskites taking a loss of conductivity or permeability.

4. Conclusions

We proved that zinc-doped BSF perovskite-type membranes exhibit long-term stability at high (950 °C) and intermediate (750 °C) temperatures under an oxygen partial pressure difference of $\Delta pO_2 = 1.89 \times 10^4$ Pa at 950 °C and $\Delta pO_2 = 2.02 \times 10^4$ Pa at 750 °C. The oxygen permeation flux was found to be constant for more than 100 h at 950 °C (0.98 mL min^{-1} cm^{-2}) and at 750 °C (0.36 mL min^{-1} cm^{-2}). The phase content of the samples was investigated by XRD and Rietveld refinements, which show only the cubic BSFZ perovskite phase.

Additionally, the effect of CO_2 on the permeation behavior of BSFZ perovskite-type membranes was investigated and it was found that, after the change to carbon dioxide as the sweep gas, the oxygen permeation abates to a value of close to zero. The reason for that behavior was investigated by XRD, SEM and TEM. We found a phase mixture of hexagonal, tetragonal and cubic perovskite with a barium/strontium carbonate layer (($Ba_{0.4\pm0.1}Sr_{0.6\pm0.1})CO_3$) with ZnO inclusions at the surface and surface-near grain boundaries. The actual structural characteristics of the two modifications of the cubic perovskite considered could not be clarified by the available data. TEM showed that the dense perovskite membrane is decomposed into phases with different morphologies accompanied by pore and crack formation in a surface layer with a depth of approximately 5 μm. The phases were identified to be a plate-like $(Ba_{0.5}Sr_{0.5})FeO_{3-\delta}$ perovskite phase, an intermediate layer of a mixture of perovskite, carbonate and zinc oxide with sponge-like morphology, a plate-like $(Ba_{0.4\pm0.1}Sr_{0.6\pm0.1})CO_3$ phase and some zinc oxide grains, which are located at the boundaries. Those phases

where approved by EDXS and EELS. Switching to helium as the sweep gas does not give the same oxygen permeation flux as before, rather half of the former flux, even after 12 h of helium treatment. Our first suggestion of a remaining carbonate layer at 750 °C was wrong, but the decrease in oxygen permeation can be attributed to the formation of a hexagonal and tetragonal perovskite phase in addition to the cubic phase. A short heating under helium atmosphere to 950 °C regenerates the oxygen permeation flux and the membrane has the same performance as before. The investigations of the microstructure resulted in a mixture of cubic and tetragonal perovskite phase and a little hexagonal fraction. Since the oxygen permeation flux was regenerated to its full value, we conclude that the tetragonal and cubic phases of the BSFZ perovskite have good oxygen permeation ability and the hexagonal phase is unfavorable for the oxygen permeation. Besides, we come to the result that the appearance of the carbonate structure, even to a small amount of 8%, immediately leads to a breakdown of the oxygen permeation ability. The measurements show that the effect of the carbon dioxide is totally reversible after a short high temperature treatment.

Acknowledgements

References

[1] International Energy Agency, World Energy Outlook 2008, Presentation to the Press, OECD/IEA, London, 12th November 2008, http://www.iea.org/Textbase/speech/2008/Birol_WEO2008_PressConf.pdf.

[2] International Energy Agency, World Energy Outlook 2008, Fact Sheet, IEA/AIE, Paris, 2008, http://www.worldenergyoutlook.org/.

[3] L.J. Gauckler, D. Beckel, B.E. Buergler, E. Jud, U.P. Muecke, M. Prestat, J.L.M. Rupp, J. Richter, Solid oxide fuel cells: systems and materials, Chimia 58 (2004) 837–850.

[4] R. Merkle, J. Maier, How is oxygen incorporated into oxides? A comprehensive kinetic study of a simple solid-state reaction with SrTiO$_3$ as a model material, Angew. Chem. Int. Ed. 47 (2008) 3874–3894.

[5] R. Merkle, J. Maier, H.J.M. Bouwmeester, A linear free energy relationship for gas-solid interactions: correlation between surface rate constant and diffusion coefficient of oxygen tracer exchange for electron-rich perovskites, Angew. Chem. Int. Ed. 43 (2004) 5069–5073.

[6] Z. Shao, S. Haile, A high-performance cathode for the next generation of solid-oxide fuel cells, Nature 431 (2004) 170–173.

[7] A. Esquirol, N.P. Brandon, J.A. Kilner, M. Mogensen, Electrochemical characterization of La$_{0.6}$Sr$_{0.4}$Co$_{0.2}$Fe$_{0.8}$O$_3$ cathodes for intermediate-temperature SOFCs, J. Electrochem. Soc. 151 (2004) A1847–A1855.

[8] S. Tao, J.T.S. Irvine, A stable, easily sintered proton-conducting oxide electrolyte for moderate-temperature fuel cells and electrolyzers, Adv. Mater. 18 (2006) 1581–1584.

[9] Q.X. Fu, F. Tietz, F. Stöver, La$_{0.4}$Sr$_{0.6}$Co$_{1-x}$Fe$_x$O$_{3-\delta}$ perovskites as anode materials for solid oxide fuel cells, J. Electrochem. Soc. 153 (2006) D74–D83.

[10] M.-F. Hsu, L.-J. Wu, J.-M. Wu, Y.-H. Shiu, K.-F. Lin, Solid oxide fuel cell fabricated using all-perovskite materials, Electrochem. Solid-State Lett. 9 (2006) A193–A195.

[11] H.J.M. Bouwmeester, A.J. Burggraaf, Dense ceramic membranes for oxygen separation, in: A.J. Burggraaf, L. Cot (Eds.), Fundamentals of Inorganic Membrane Science and Technology, 1st edition, Elsevier, Amsterdam, 1996, p. 435ff.

[12] J. Martynczuk, M. Arnold, H. Wang, J. Caro, A. Feldhoff, How (Ba$_{0.5}$Sr$_{0.5}$)(Fe$_{0.8}$Zn$_{0.2}$)O$_{3-\delta}$ and (Ba$_{0.5}$Sr$_{0.5}$)(Co$_{0.8}$Fe$_{0.2}$)O$_{3-\delta}$ perovskites form via an EDTA/citric acid complexing method, Adv. Mater. 19 (2007) 2134–2140.

[13] J. Caro, Membranreaktoren für die katalytische Oxidation, Chemie Ingenieur Technik 78 (2006) 899–912.

[14] H. Wang, Y. Cong, X. Zhu, W. Yang, Oxidative dehydrogenation of propane in a dense tubular membrane reactor, React. Kinet. Catal. Lett. 79 (2003) 351–356.

[15] C. Hamel, A. Seidel-Morgenstern, T. Schiestel, S. Werth, H. Wang, C. Tablet, J. Caro, Experimental and modeling study of the O$_2$-enrichment by perovskite fibers, AIChE J. 52 (2006) 3118–3125.

[16] H. Wang, S. Werth, T. Schiestel, J. Caro, Perovskite hollow-fiber membranes for the production of oxygen-enriched air, Angew. Chem. Int. Ed. 44 (2005) 6906–6909.

[17] M. Arnold, T.M. Gesing, J. Martynczuk, A. Feldhoff, Correlation of the formation and the decomposition process of the BSCF perovskite at intermediate temperatures, Chem. Mater. 20 (2008) 5851–5858.

[18] S. Švarcová, K. Wiik, J. Tolchard, H.J.W. Bouwmeester, T. Grande, Structural instability of cubic perovskite (Ba$_x$Sr$_{1-x}$)(Co$_y$Fe$_{1-y}$)O$_{3-\delta}$, Solid State Ionics 178 (2008) 1787–1791.

[19] H. Wang, G. Grubert, C. Tablet, J. Caro, Sauerstofftransportierende Oxidkeramiken, Patent Application, EP 1630148/05102708.4, 2005.

[20] H. Wang, C. Tablet, A. Feldhoff, J. Caro, A cobalt-free oxygen-permeable membrane based on the perovskite-type oxide Ba$_{0.5}$Sr$_{0.5}$Zn$_{0.2}$Fe$_{0.8}$O$_{3-\delta}$, Adv. Mater. 17 (2005) 1785–1788.

[21] B. Wei, Z. Lü, X. Huang, Z. Liu, J. Miao, N. Li, W. Su, Ba$_{0.5}$Sr$_{0.5}$Zn$_{0.2}$Fe$_{0.8}$O$_{3-\delta}$ perovskite oxide as a novel cathode for intermediate-temperature solid-oxide fuel cells, J. Am. Ceram. Soc. 90 (10) (2007) 3364–3366.

[22] B. Wei, Z. Lü, X. Huang, Z. Liu, J. Miao, N. Li, W. Su, Synthesis, electrical and electrochemical properties of (Ba$_{0.5}$Sr$_{0.5}$)(Zn$_{0.2}$Fe$_{0.8}$)O$_{3-\delta}$ perovskite oxide for IT-SOFC cathode, J. Power Sources 176 (2008) 1–8.

[23] A. Feldhoff, M. Arnold, J. Martynczuk, Th.M. Gesing, H. Wang, The sol–gel synthesis of perovskites by an EDTA/citrate complexing method involves nanoscale solid state reactions, Solid State Sci. 10 (2008) 689–701.

[24] A. Feldhoff, J. Martynczuk, H. Wang, Advanced Ba$_{0.5}$Sr$_{0.5}$Zn$_{0.2}$Fe$_{0.8}$O$_{3-\delta}$ perovskite-type ceramics as oxygen selective membranes: evaluation of the synthetic process, Prog. Solid State Chem. 35 (2007) 339–353.

[25] N. Zakowsky, S. Williamson, J.T.S. Irvine, Elaboration of CO$_2$ tolerance limits of BaCe$_{0.9}$Y$_{0.1}$O$_{3-\delta}$ electrolytes for fuel cells and other applications, Solid State Ionics 176 (2005) 3019–3026.

[26] S. Pei, M.S. Kleefisch, T.P. Kobylinski, J. Faber, C.A. Udovich, V. Zhang-McCoy, B. Dabrowski, U. Balachandran, R.L. Mieville, R.B. Poeppel, Failure mechanisms of ceramic membrane reactors in partial oxidation of methane to synthesis gas, Catal. Lett. 30 (1995) 201–212.

[27] I. Kaus, K. Wiik, B. Krogh, M. Dahle, K.H. Hofstad, S. Aasland, Stability of SrFeO$_3$-based materials in H$_2$O/CO$_2$-containing atmospheres at high temperatures and pressures, J. Am. Ceram. Soc. 90 (7) (2007) 2226–2230.

[28] V.V. Kharton, A.A. Yaremchenko, A.V. Kovalevsky, A.P. Viskup, E.N. Naumovich, P.F. Kerko, Perovskite-type oxides for high-temperature oxygen separation membranes, J. Membr. Sci. 163 (1999) 307–317.

[29] A. Magrasó, F. Espiell, M. Segarra, J.T.S. Irvine, Chemical and electrical properties of BaPr$_{0.7}$Gd$_{0.3}$O$_{3-\delta}$, J. Power Sources 169 (2007) 53–58.

[30] M. Arnold, H. Wang, A. Feldhoff, Influence of CO$_2$ on the oxygen permeation performance and the microstructure of perovskite-type (Ba$_{0.5}$Sr$_{0.5}$)(Co$_{0.8}$Fe$_{0.2}$)O$_{3-\delta}$ membranes, J. Membr. Sci. 293 (2007) 44–52.

[31] A. Yan, M. Cheng, Y. Dong, W. Yang, V. Maragou, S. Song, P. Tsiakaras, Investigation of Ba$_{0.5}$Sr$_{0.5}$Co$_{0.8}$Fe$_{0.2}$O$_{3-\delta}$ based cathode IT-SOFC. I. The effect of CO$_2$ on the cell performance, Appl. Catal. B 66 (2006) 64–71.

[32] A. Yan, V. Maragou, A. Arico, M. Cheng, P. Tsiakaras, Investigation of Ba$_{0.5}$Sr$_{0.5}$Co$_{0.8}$Fe$_{0.2}$O$_{3-\delta}$ based cathode SOFC. II. The effect of CO$_2$ on the chemical stability, Appl. Catal. B 76 (2007) 320–327.

[33] A.M. Kalinkin, Mechanosorption of carbon dioxide by CaTiO$_3$ perovskite: structure-chemical changes, Russ. J. Phys. Chem. A 82 (2008) 263–268.

[34] K. Nomura, Y. Ujihira, T. Hayakawa, K. Takehira, CO$_2$ absorption properties and characterization of perovskite oxides, (Ba,Ca)(Co,Fe)O$_{3-\delta}$, Appl. Catal. A 137 (1996) 25–36.

[35] I.V. Khromushin, T.I. Aksenova, Zh.R. Zhotabaev, Mechanism of gas–solid exchange processes for some perovskites, Solid State Ionics 162–163 (2003) 37–40.

[36] J.E. ten Elshof, H.J.M. Bouwmeester, H. Verweij, Oxygen transport through La$_{1-x}$Sr$_x$FeO$_{3-\delta}$ membranes. II. Permeation in air/CO, CO$_2$ gradients, Solid State Ionics 89 (1996) 81–92.

[37] S.J. Benson, D. Waller, J.A. Kilner, Degradation of La$_{0.6}$Sr$_{0.4}$Fe$_{0.8}$Co$_{0.2}$O$_{3-\delta}$ in carbon dioxide and water atmospheres, J. Electrochem. Soc. 146 (4) (1999) 1305–1309.

[38] A. Sin, E. Kopnin, Y. Dubitsky, A. Zaopo, A.S. Aricò, L.R. Gullo, D. La Rosa, V. Antonucci, Stabilisation of composite LSFCO-CGO based anodes for methane oxidation in solid oxide fuel cells, J. Power Sources 145 (2005) 68–73.

[39] H. Yokokawa, N. Sakai, T. Kawada, M. Dokiya, Thermodynamic stability of perovskites and related compounds in some alkaline earth–transition metal–oxygen systems, J. Solid State Chem. 94 (1991) 106–120.

[40] H. Yokokawa, N. Sakai, T. Kawada, M. Dokiya, Thermodynamic stability of perovskite oxides for electrodes and other electrochemical materials, Solid State Ionics 52 (1992) 43–56.

[41] A.A. Yaremchenko, V.V. Kharton, A.A. Valente, F.M.M. Snijkers, J.F.C. Cooymans, J.J. Luyten, F.M.B. Marques, Performance of tubular SrFe(Al)O$_3$–SrAl$_2$O$_4$ composite membranes in CO$_2$- and CH$_4$-containing atmospheres, J. Membr. Sci. 319 (2008) 141–148.

[42] J. Yi, S. Feng, Y. Zuo, W. Liu, C. Chen, Oxygen permeability and stability of Sr$_{0.95}$Co$_{0.8}$Fe$_{0.2}$O$_{3-\delta}$ in a CO$_2$- and H$_2$O-containing atmosphere, Chem. Mater. 17 (2005) 5856–5861.

[43] E. Fabbri, A. D'Epifanio, E. Di Bartolomeo, S. Licoccia, E. Traversa, Tailoring the chemical stability of Ba(Ce$_{0.8-x}$Zr$_x$)Y$_{0.2}$O$_{3-\delta}$ protonic conductors for intermediate temperature solid oxide fuel cells (IT-SOFCs), Solid State Ionics 179 (2008) 558–564.

[44] P. Babilo, S.M. Haile, Enhanced sintering of yttrium-doped barium zirconate by addition of ZnO, J. Am. Ceram. Soc. 88 (9) (2005) 2362–2368.

[45] H. Wang, C. Tablet, A. Feldhoff, J. Caro, Investigation of phase structure, sintering, and permeability of perovskite-type Ba$_{0.5}$Sr$_{0.5}$Co$_{0.8}$Fe$_{0.2}$O$_{3-\delta}$ membranes, J. Membr. Sci. 262 (2005) 20–26.

[46] J. Martynczuk, M. Arnold, A. Feldhoff, Influence of grain size on the oxygen permeation performance of perovskite-type (Ba$_{0.5}$Sr$_{0.5}$)(Fe$_{0.8}$Zn$_{0.2}$)O$_{3-\delta}$ membranes, J. Membr. Sci. 322 (2008) 375–382.

70   *J. Martynczuk et al. / Journal of Membrane Science 344 (2009) 62–70*

[47] Further details of the crystal structure investigation may be obtained from Fachinformationszentrum Karlsruhe, 76344 Eggenstein-Leopoldshafen, Germany (fax: +49 7247 808 666; e mail: crysdata@fiz karlsruhe.de, http://www fiz karlsruhe de/request_for_deposited_data html on quoting the deposition number CSD 418850.

[48] H. Wang, C. Tablet, J. Caro, Oxygen production at low temperature using dense perovskite hollow fiber membranes, J. Membr. Sci. 322 (2008) 214–217.

[49] N. Miura, H. Murae, H. Kusaba, J. Tamaki, G. Sakai, N. Yamazoe, Oxygen permeability and phase transformation of Sr$_{0.9}$Ca$_{0.1}$CoO$_{2.5+\delta}$, J. Electrochem. Soc. 146 (7) (1999) 2581–2586.

[50] R.S. Tichy, J.B. Goodenough, Oxygen permeation in cubic, SrMnO$_{3-\delta}$, Solid State Sci. 4 (2002) 661–664.

[51] Z.Q. Deng, W.S. Yang, W. Liu, C.S. Chen, Relationship between transport properties and phase transformation in mixed-conducting oxides, J. Solid State Chem. 179 (2006) 362–369.

[52] P. Zeng, Z. Shao, S. Liu, Z.P. Xu, Influence of M cations on structural, thermal and electrical properties of new oxygen selective membranes based on SrCo$_{0.95}$M$_{0.05}$O$_{3-\delta}$ perovskites, Sep. Purif. Technol. 67 (2009) 304–311.

[53] L.A. Kiselva, A.R. Kotelnikov, K.V. Martynov, L.P. Ogorodova, Ju.K. Kabalov, Thermodynamic properties of strontianite–witherite solid solution (Sr,Ba)CO$_3$, Phys. Chem. Minerals 21 (1994) 392–400.

[54] J.L. Mansot, V. Golabkan, L. Romana, T. Cesaire, Chemical and physical characterization by EELS of strontium hexanoate reverse micelles and strontium carbonate nanophase produced during tribological experiments, J. Microsc. 210 (2003) 110–118.

[55] N. Sakaguchi, Y. Suzuki, K. Watanabe, S. Iwama, S. Watanabe, H. Ichinose, A HRTEM and EELS study of Pd/ZnO polar interfaces, Philos. Mag. 10 (2008) 1493–1509.

5   CO$_2$-stable MIEC materials

5.1   Summary

Because the majority of high performance oxygen transporting materials contain barium and/or strontium, their wide application is hindered by intolerance toward CO$_2$ due to the formation of carbonates. This chapter relates two original research articles concerning the development of CO$_2$-stable MIEC membranes.

In Section 5.2, the calcium-containing perovskite systems La$_{1-x}$Ca$_x$FeO$_{3-\delta}$ and La$_{1-x}$Ca$_x$Co$_{0.8}$Fe$_{0.2}$O$_{3-\delta}$ (x = 0.4-0.6) are discussed with respect to CO$_2$-stability. Thermodynamic considerations using an Ellingham diagram clearly revealed that calcium and lanthanum (oxy) carbonates are significantly less stable than barium and strontium carbonates. Hence, beneficial stability of calcium- and lanthanum-based materials in the presence of CO$_2$ can be expected. Because materials synthesized by the sol-gel method contain more calcium (x = 0.5-0.6), as exhibited by the considerable amount of by-phases (e.g., brownmillerite and/or spinel), further detailed investigations were carried out only on the first member of the systems (x = 0.4). The orthorhombicly distorted (La$_{0.6}$Ca$_{0.4}$)FeO$_{3-\delta}$ and rhombohedrally distorted (La$_{0.6}$Ca$_{0.4}$)(Co$_{0.8}$Fe$_{0.2}$)O$_{3-\delta}$ perovskites showed relatively high oxygen permeation fluxes, which could be improved by about 50% via the asymmetric configuration using a porous support and an approximately 10 µm thick dense layer with the same chemical composition. *In-situ* XRD in an atmosphere containing 50 vol.% CO$_2$ and experiments using pure CO$_2$ as the sweep gas revealed a high tolerance of Ca-based materials toward CO$_2$.

The concept of alkaline-earth-free dual phase membranes provides an alternative solution of the CO$_2$-intolerance problem. Improved stability against carbonate formation can be expected if both phases are made from oxides, which contain only transition metals and/or lanthanides caused by the low affinity of both groups of elements toward CO$_2$.

Section 5.3 introduces a novel dual phase material consisting of 40 wt.% NiFe$_2$O$_4$ with spinel structure and 60 wt.% Ce$_{0.9}$Gd$_{0.1}$O$_{2-\delta}$ with fluorite structure prepared by a one-pot sol-gel method. The MIEC properties of the membrane arise from two interpenetrating percolated networks of spinel phase as the electronic conductor and fluorite phase as the solid state electrolyte. *In-situ* XRD and TEM investigations showed that both phases were well separated and do not interact at high temperatures, but remained in their initial structures. The presented dual phase membrane exhibited very good CO$_2$-stability, as proven by *in-situ* XRD and long-term oxygen permeation measurements in the presence of CO$_2$.

5.2 Ca-containing CO$_2$-tolerant perovskite materials for oxygen separation

Konstantin Efimov, Tobias Klande, Nadine Juditzki, and Armin Feldhoff

Ca-containing CO$_2$-tolerant perovskite materials for oxygen separation

Konstantin Efimov, Tobias Klande, Nadine Juditzki, and Armin Feldhoff

Institute of Physical Chemistry and Electrochemistry, Leibniz Universität Hannover, Callinstraße 3-3A, D-30167 Hannover, Germany

Abstract

Perovskites $(La_{1-x}Ca_x)FeO_{3-\delta}$ and $(La_{1-x}Ca_x)(Co_{0.8}Fe_{0.2})O_{3-\delta}$ with varying La and Ca contents (x = 0.4-0.6) were designed by sol-gel route as model membrane materials to be an alternative to Ba- and Sr-based systems for operation in the presence of CO$_2$. It was found that only the first members of the systems with x = 0.4 consisted of almost pure perovskite phases. The materials containing more Ca (x = 0.5-0.6) exhibited a considerable amount of by-phase material, such as brownmillerite and/or spinel, after calcination at 1223 K. The orthorhombicly distorted $(La_{0.6}Ca_{0.4})FeO_{3-\delta}$ and rhombohedrally distorted $(La_{0.6}Ca_{0.4})(Co_{0.8}Fe_{0.2})O_{3-\delta}$ perovskites showed relatively high oxygen permeation fluxes at 1223 K of 0.26 cm^{3}min^{-1}cm^{-2} and 0.43 cm^{3}min^{-1}cm^{-2}, respectively. The oxygen-ionic conductivity of the materials was improved by about 50% via an asymmetric configuration using a porous support and an approximately 10 μm thick dense layer with the same chemical composition. *In-situ* XRD in an atmosphere containing 50 vol.% CO$_2$ and long-term oxygen permeation experiments using pure CO$_2$ as the sweep gas revealed a high tolerance of Ca-based materials toward CO$_2$. Thus, we suggest that Ca-containing perovskite can be considered promising membrane materials if operation in the presence of CO$_2$ is required.

Keywords: *Mixed ionic-electronic conductor; perovskite, CO$_2$-stability, asymmetric membrane; in-situ X-ray diffraction; transmission electron microscopy*

1. Introduction

Over the last two decades, mixed oxygen ionic and electronic conductors (MIEC) have attracted a lot of attention. Because of their very high oxygen-ionic transport rates over a wide temperature range, the Ba- and Sr-containing perovskites [e.g., $(Ba_{1-x}Sr_x)(Co_{0.8}Fe_{0.2})O_{3-\delta}$ and $(La_{1-x}Sr_x)(Co_{1-y}Fe_y)O_{3-\delta}$] rank among the state-of-the-art MIEC materials [1-3]. However, the wide practical employment of these materials is hindered by significant problems, like poor chemical and thermomechanical stability [4-10]. In particular, the degradation of these materials in the presence of CO$_2$, with the formation of carbonates, [11-16] handicaps their application in important processes, such as cathode materials in solid-oxide fuel cells (SOFCs) operated at intermediate temperatures, in oxyfuel processes or in hydrocarbon partial oxidations, where some

CO$_2$ is formed as a by-product of an undesired deeper oxidation [17-19].

Tolerance against CO$_2$ can be achieved by the complete replacement of Ba and Sr in the A-lattice site of the perovskite structure by rare-earth elements, like La. Unfortunately, this leads to a dramatic loss in the oxygen-ionic conductivity of the materials, as caused by a reduced lattice parameter, which induces lower oxygen mobility, and by a lower amount of mobile oxygen vacancies, which results from a higher oxidation state of the rare-earth cation [20]. To increase the oxygen deficiency in the perovskite lattice, a Ca cation with the stable valence state of 2+ can be regarded as a potential dopant.

The stability of alkaline earth-containing materials in the presence of CO$_2$ can be evaluated using the Ellingham diagram shown in Figure 1. This figure demonstrates the thermodynamic stability of carbonates at a given CO$_2$ partial pressure and temperature.
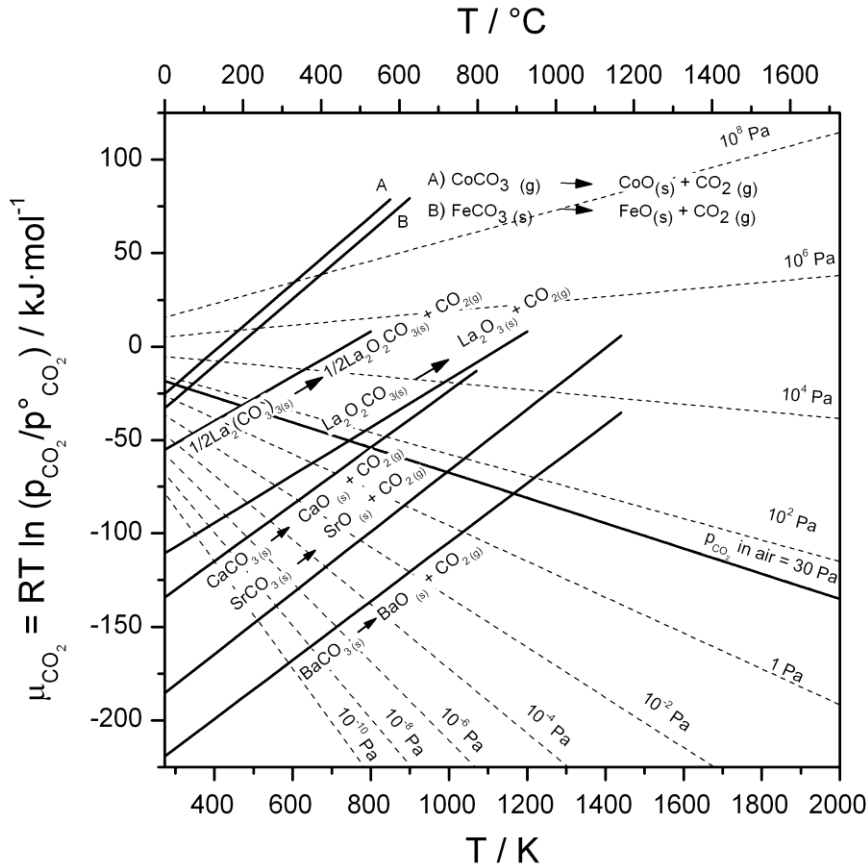
***Figure 1**. Ellingham diagram for the decomposition of carbonates under different partial pressures. Chemical potential of CO$_2$ above FeCO$_3$, CoCO$_3$, CaCO$_3$, La$_2$O$_2$CO$_3$, SrCO$_3$, and BaCO$_3$ have been calculated from thermodynamic data [21-23]. The chemical potential of La$_2$(CO$_3$)$_3$ has been determined experimentally [24]. The dashed lines represent the chemical potential of CO$_2$ in the surrounding atmosphere for different partial pressures. p°(CO$_2$) = 101.3 kPa refers to standard conditions.*

The compact lines with positive slope in the diagram represent chemical potentials of CO$_2$ during the decomposition of corresponding carbonate, as calculated with thermodynamic data or determined experimentally [21-24]. The dashed lines give the chemical potential of CO$_2$ at different partial pressures. In general, if the CO$_2$ chemical potential of the carbonate decomposition reaction at the present temperature is higher than at the corresponding partial pressure, the carbonates are thermodynamically unstable. As can be seen in the Ellingham diagram, CaCO$_3$ is significantly less stable than BaCO$_3$ and SrCO$_3$. The relatively small ionic radius of 135 pm of the Ca^{2+} cation, as compared with Ba^{2+} (r = 160 pm) Sr^{2+} and (r = 144 pm) cations, leads to a decline of the crystal lattice energy of carbonate and can be considered a reason for the lower stability of CaCO$_3$ [25,26]. Note, the Ellingham diagram gives only a rough

guide to estimate the possible tolerance of Ca-containing perovskite materials against CO$_2$ because the stabilization energy of perovskite may also play an important role [27,28]. Nevertheless, the desirable stability of Ca-containing materials in the presence of CO$_2$ can be expected from thermodynamic considerations and was reported for Ca(Ti$_{1-x}$Fe$_x$)O$_{3-\delta}$ [29].

Teraoka et al. have already reported a high oxygen permeation flux through the perovskite membrane with the composition (La$_{0.6}$Ca$_{0.4}$)(Co$_{0.8}$Fe$_{0.2}$)O$_{3-\delta}$ in 1988 [30]. Using a higher Ca content, Stevenson et al. have obtained a very high electrical conductivity using (La$_{0.4}$Ca$_{0.6}$)(Co$_{0.8}$Fe$_{0.2}$)O$_{3-\delta}$ perovskite in 1996 [31]. Since then, however, Ca-containing materials have gained little notice as promising MIEC materials [32-34]. One reason for this lack of attention may be the formation of secondary phases, like brownmillerite and/or

the Grenier phase, during the preparation and operation of the perovskites. It has also been reported that this problem appears more pronounced with rising Ca content in the materials [31,35].

Recently, the group around Teraoka has developed asymmetrically structured membranes consisting of a porous support and thin dense layer and having the chemical composition $(La_{0.6}Ca_{0.4})CoO_{3-\delta}$ [36]. The main advantage of self-supported membranes is a result of the good chemical compatibility and thermomechanical stability of the materials. The oxygen permeation flux of the $(La_{0.6}Ca_{0.4})CoO_{3-\delta}$ was enhanced by the asymmetric configuration up to 300%, which has yielded a value of 1.66 $cm^3min^{-1}cm^{-2}$ [37]. This feature draws a spotlight on the Ca-containing perovskites as promising candidate MIEC materials.

In the present work, model perovskite systems $(La_{1-x}Ca_x)FeO_{3-\delta}$ and $(La_{1-x}Ca_x)(Co_{0.8}Fe_{0.2})O_{3-\delta}$ (x = 0.4-0.6) were examined regarding phase purity and stability in the presence of CO_2. Furthermore, bulk and asymmetrically structured membranes were prepared and investigated for their oxygen-ionic conducting properties.

2. Experimental

2.1 Powder preparation

A sol-gel route using metal nitrates, citric acid, and ethylenediaminetetraacetic acid (EDTA) was applied to prepare the $La_{1-x}Ca_xFeO_{3-\delta}$ and $La_{1-x}Ca_xCo_{0.8}Fe_{0.2}O_{3-\delta}$ (x = 0.4-0.6) materials as described elsewhere [38,39]. Given amounts of $La(NO_3)_3$ and $Ni(NO_3)_2$ were dissolved in water followed by the addition of EDTA as an organic ligand and citric acid as a network former. The molar ratio of metal nitrates:EDTA:citric acid was equal to 2:1:1.5. The pH value of the solution was adjusted to the range of 7-9 with $NH_3 \cdot H_2O$. The transparent reaction solution was then heated at 423 K under constant stirring for several hours to obtain a gel. The gel was pre-calcined in the temperature range of 573-673 K in order to remove organic compounds, followed by calcination for 10 h at 1223 K in air.

2.2 Preparation of bulk and asymmetric membranes

To obtain the bulk membranes, the powders were uniaxially pressed under 140-150 kN for 20 min into green bodies. The pellets were then calcined for 10 h at 1423-1523 K with a heating and cooling rate of 3 K/min.

The asymmetric membranes were manufactured as follows: the as synthesized powders were ground in a mortar with 20 wt.% of a pore former block co-polymer Pluronic F 127 (BASF). The mixture was then press-formed into pellets and fired at 1423 K for 2 h. The dense layers were obtained by spin coating of porous supports with 3 cm^3 slurry (15 wt.% powder in ethanol), drying at room temperature for 5 h following by calcination at 1423-1523 K for 2-5 h.

2.3 Characterizations of materials

The phase structure of the powders and membranes were studied by X-ray diffraction (XRD, D8 Advance, Bruker-AXS, with Cu K$\alpha_{1,2}$ radiation). Data sets were recorded in a step–scan mode in the 2Θ range of 20°–60° with intervals of 0.02°. *In-situ* XRD tests were conducted in a high-temperature cell HTK 1200N (Anton-Paar) between room temperature and 1273 K. Tests in the atmosphere containing 50 vol.% CO_2 / 50 vol.% air and 50 vol.% CO_2 / 50 vol.% N_2 were carried out with heating and cooling rate of 12 K/min. At each temperature step, the temperature was held for 30 min before diffraction data collection.

Scanning electron microscopy (SEM) imaging was performed on a JEOL JSM-6700F field-emission instrument at a low excitation voltage of 2 kV. An energy-dispersive X-ray spectrometer (EDXS), Oxford Instruments INCA-300, with an ultrathin window was used for the elemental analysis at an excitation voltage of 15 kV.

Transmission electron microscopy (TEM) investigations were made at 200 kV on a JEOL JEM-2100F-UHR field-emission instrument (C_S = 0.5 mm, C_C = 1.2 mm) equipped with a light-element EDXS detector (INCA 200 TEM, Oxford Instruments). The microscope was operated as scanning TEM (STEM) in high-angle annular dark-field (HAADF) mode. An energy filter of the type Gatan GIF 2001 was employed to acquire electron energy-loss spectra (EELS).
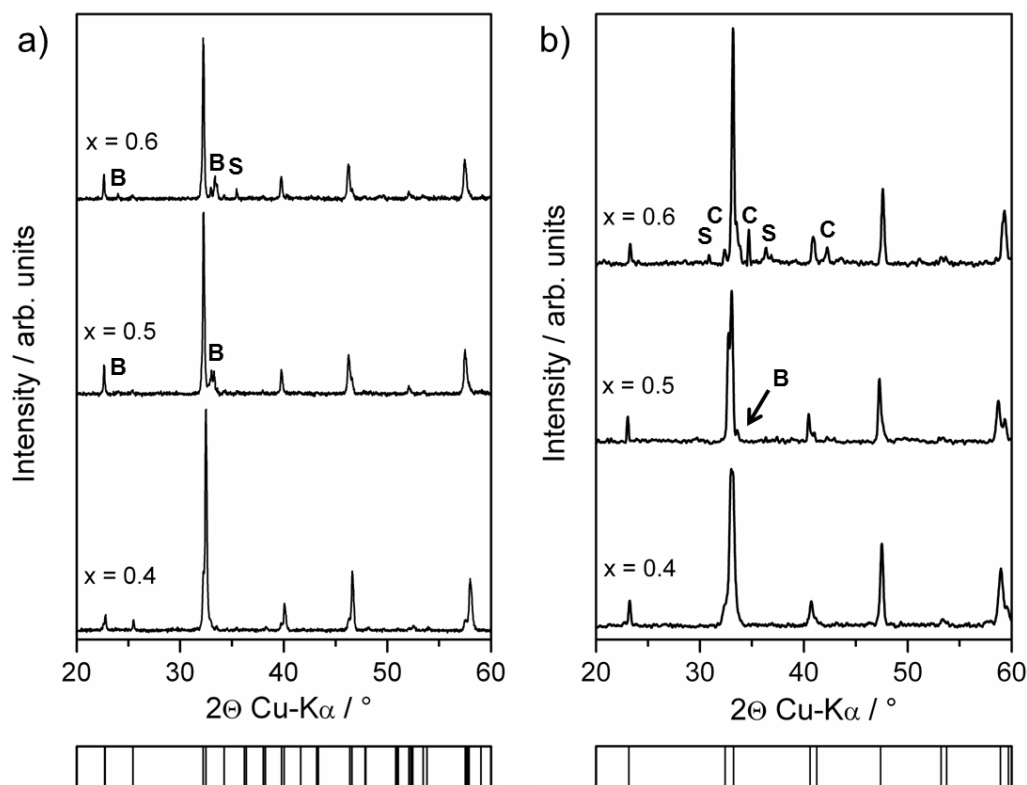
Figure 2. a) XRD pattern of $La_{1-x}Ca_xFeO_{3-\delta}$ (x = 0.4-0.6) powders. The calculated Bragg positions for orthorhombic perovskite (space group Pnma; a = 5.496 Å, b = 7.772 Å and c = 5.566 Å) are marked with ticks at the bottom of the figure. The intensities of non-perovskite phases are marked in the figure with b for $Ca_2Fe_2O_5$ brownmillerite and s for Ca_2FeO_4 spinel. b) XRD pattern of $La_{1-x}Ca_xCo_{0.8}Fe_{0.2}O_{3-\delta}$ (x = 0.4-0.6) powders. The calculated Bragg positions for rhombohedral perovskite (space group R-3c, a = 5.391 Å, b = 13.263 Å) are marked with ticks at the bottom. The intensity of impurity phases are marked in the figure with B for $Ca_2Co_{2-y}Fe_yO_5$, S for Co_3O_4 spinel and C for $Ca_3Co_{2-z}Fe_zO_6$.

Specimens for electron microscopy were prepared as follow. First, the permeate side was glued with a polycrystalline corundum block using epoxy followed by cutting of membrane into 1 mm x 1mm x 2 mm pieces. The protected membrane pieces were polished on polymer-embedded diamond lapping films to approximately 0.01 mm x 1 mm x 2 mm (Allied High Tech, Multiprep). Electron transparency for TEM was achieved by Ar⁺ ion sputtering at 3 kV (Gatan, model 691 PIPS, precision ion polishing system) under shallow incident angles of 10°, 6°, and 4°.

Oxygen permeation was measured in a high-temperature permeation cell according to the method described elsewhere [40,41]. Before measurements, the bulk membranes were polished with 30 µm polymer-embedded diamond lapping films. Air was fed at a rate of 150 cm³ min⁻¹ to the feed side; He or CO_2 (29.0 cm³ min⁻¹) and Ne (1.0 cm³ min⁻¹) gases were fed to the sweep side. The effluents were

analyzed by gas chromatography on an Agilent 6890 instrument equipped with a Carboxen 1000 column. The gas concentrations in the effluent stream were calculated from a gas chromatograph calibration. The absolute flux rate of the effluents was determined by using neon as an internal standard. The relative leakage of O_2, which was evaluated by measuring the amount of N_2 in the effluent stream, was subtracted in the calculation of the oxygen permeation flux.

3. Results and discussion

3.1 Characterization of powders

The Goldschmidt tolerance factors for perovskite systems $(La_{1-x}Ca_x)FeO_{3-\delta}$ and $(La_{1-x}Ca_x)(Co_{0.8}Fe_{0.2})O_{3-\delta}$ (x = 0.4-0.6) lie close to unity ($t \leq 1$), even for various ratios of Fe^{4+}/Fe^{3+} and $Co^{4+}/Co^{3+}/Co^{2+}$ cations [42,25]. Accordingly, it may be expected that both

systems crystallize in the perovskite structure. However, as can be seen in Figure 2a,b, only the first members of the systems ($La_{1-x}Ca_x)FeO_{3-\delta}$ and $(La_{1-x}Ca_x)(Co_{0.8}Fe_{0.2})O_{3-\delta}$ with x = 0.4 consisted of almost pure perovskites with the amount of the main phases at 97% and 98% respectively. The compounds with higher calcium contents include significant fractions of by-phases. For the iron-based system, these higher calcium contents were attributed to brownmillerite ($Ca_2Fe_2O_5$) and $CaFe_2O_4$ spinel. For cobalt-based materials, these were indexed as brownmillerite-like phase $Ca_2Co_{2-y}Fe_yO_5$, Co_3O_4 spinel and the layered complex oxide $Ca_3Co_{2-z}Fe_zO_6$. Brownmillerite exhibits ordered oxygen vacancies along the *c*-axis [43]. The $Ca_3Co_{2-z}Fe_zO_6$ structure contains chains of face-shared CoO_6 octahedra arranged along the *c*-axis [44]. These structures are unfavorable for oxygen-ionic transport. For this reason, the by-phase-containing compounds with high calcium ratios have not been considered for further investigations.

The crystal symmetry and lattice parameters of the materials were determined by the Pawley method [45]. It was found that both systems showed the distorted perovskite structure. The $(La_{0.6}Ca_{0.4})FeO_{3-\delta}$ (LCF) exhibited an orthorhombic symmetry (space group Pnma, number of formula units per unit cell Z = 4), corresponding to the LaFeO$_3$ oxide with lattice parameters of a = 5.496 Å, b = 7.772 Å and c = 5.566 Å [46]. The structure of $(La_{0.6}Ca_{0.4})(Co_{0.8}Fe_{0.2})O_{3-\delta}$ (denoted as LCCF) was rhombohedrally distorted (space group R-3c, Z = 6) likewise in the LaCoO$_3$ perovskite with the lattice parameters of a = 5.391Å and b = 13.263 Å [47].
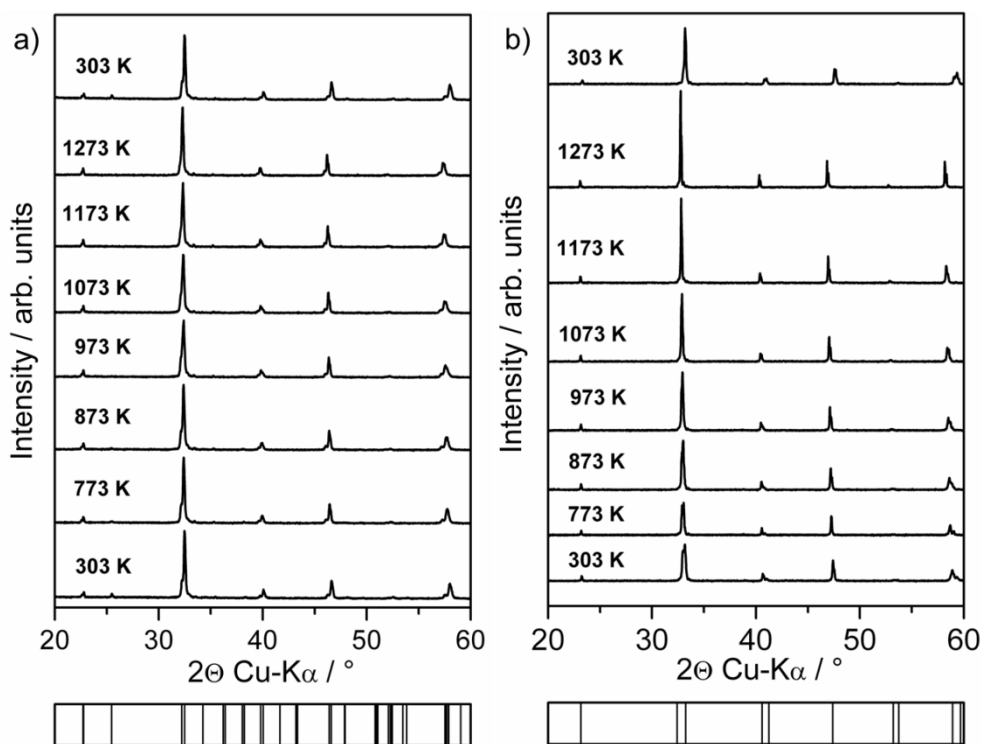
Figure 3. *In-situ XRD pattern of a) La$_{0.6}$Ca$_{0.4}$FeO$_{3-\delta}$ and b) La$_{0.6}$Ca$_{0.4}$Co$_{0.8}$Fe$_{0.2}$O$_{3-\delta}$. The data were collected during heating and cooling in an atmosphere containing 50 vol.% CO$_2$ / 50 vol.% air. F$_{total}$ = 100 cm^{3}min^{-1}.*

The stability of the LCF and LCCF perovskites in different gas atmospheres and temperatures was investigated using an *in-situ* XRD technique. Figure 3a shows the diffraction pattern of LCF collected in an atmosphere containing 50 vol.% air and 50 vol.% CO$_2$.

During heating and cooling in the temperature range of 303-1273 K, the oxide retained its perovskite structure. The formation of carbonates or additional phases was not observed in the measurements. However, an increase in the temperature above 973 K

resulted in the reversible adoption of cubic perovskite symmetry. Table 1 summarizes the calculated lattice parameters and unit cell volumes at corresponding temperatures. The orthorhombicity σ decreased continuously with increasing temperature [48]. The crystal unit cell of orthorhombic perovskite growth with the temperature was almost independent from the direction. Furthermore, the transition from orthorhombic to cubic symmetry occurred without a jump in unit cell volume. Hence, the thermal expansion coefficient (CTE) of the LCF oxide could be estimated from XRD data to be $15 \cdot 10^{-6}$ K^{-1}.

Table 1. Lattice parameters of the LCF perovskite system. The orthorhombicity σ was calculated by: $\sigma = 2(a-c)/(a+c)$ [48].

	Orthorhombic phase (Pnma, Z = 4)						Cubic phase (Pm-3m, Z =1)	
T/ K	a/ Å	b/ Å	c/ Å	V/ Å^3	VZ^{-1}/ Å^3	σ	a	V
303	5.522	7.774	5.487	235.525	58.881	0.0065		
773	5.533	7.813	5.521	238.670	59.667	0.0021		
873	5.542	7.836	5.536	240.480	60.120	0.001		
973							3.923	60.372
1073							3.929	60.68
1173							3.936	61.016
1273							3.944	61.359

Table 2. Lattice parameters of the LCCF perovskite system. The degree of rhombohedral strain ω was determined using the relationship: $\dfrac{c_H}{a_H} = \dfrac{\sqrt{6}}{cos\omega}$ [49].

	Rhombohedric phase (R-3c, Z=6)					Cubic phase (Pm-3m, Z =1)	
T/ K	a/ Å	c/ Å	V/ Å^3	VZ^{-1}/ Å^3	ω	a	V
303	5.391	13.263	333.837	55.639	5.5		
773	5.436	13.383	342.516	57.08	5.7		
873	5.449	13.411	344.819	57.46	5.6		
973	5.464	13.431	347.266	57.87	4.7		
1073	5.475	13.438	348.909	58.15	3.6		
1173						3.888	58.773
1273						3.898	59.227

Similar behavior was observed for the LCCF powder (Figure 3b). The perovskite material was stable over the whole temperature range. The reversible transformation of the rhombohedral to the cubic modification took place above 1173 K without a significant change of the cell volume per each formula unit (Table 2). The parameter of rhombohedral strain ω remained almost constant until 873 K and decreased with further

increasing temperature [49]. The lattice parameters of the LCCF perovskite unit cell expanded isotropically with increasing temperature. Thus, the CTE of the LCCF was evaluated from the XRD data to be $20 \cdot 10^{-6}$ K^{-1}.

Additionally, *in-situ* experiments in an atmosphere containing 50 vol.% N$_2$ and 50 vol.% CO$_2$ were carried out for both perovskite systems. The LCF and LCCF oxides remained stable at these conditions. This result is evidence of the high tolerance of the Ca-containing perovskite materials against CO$_2$, as well as the desirable stability of LCF and LCCF at low oxygen partial pressures and temperatures between 303 and 1273 K.
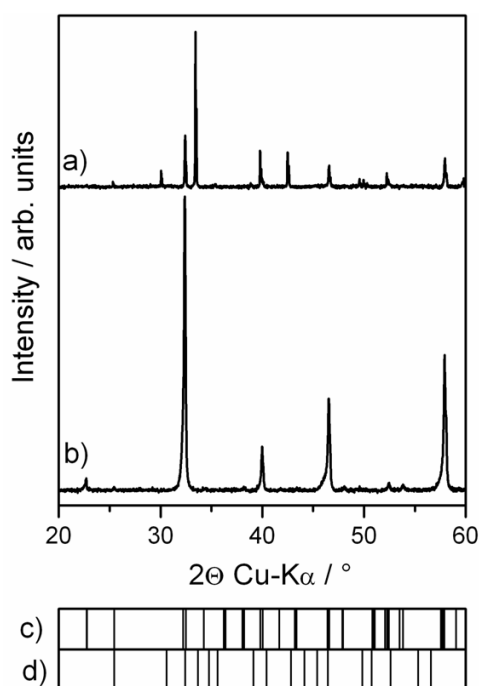

Figure 4. *XRD pattern a) of the LCF membrane after sintering at 1523 K for 10 h; b) of the polished LCF membrane. c) Bragg-positions of orthorhombic LCF perovskite. d) Bragg-positions of CaFe$_2$O$_4$.*

3.2 Membrane preparation and characterization

The bulk membranes, having a thickness of 1 mm, were prepared by uniaxial pressing and subsequent sintering. Gas-tight membranes with densities above 90% and low porosities were obtained only after sintering at 1523 K for 10 h. However, in the unpolished LCF membrane, pronounced growth of CaFe$_2$O$_4$ and La$_2$O$_3$ by-phases was observed by XRD,

as shown in Figure 4a. After polishing of the LCF membrane, the ratio of the by-phases declined to a value of 3 wt.%, as determined by XRD (Figure 4b), which equals their amount in the as-synthesized powder. To elucidate these findings, the unpolished LCF membrane surface was investigated by SEM. Figure 5a shows an SEM micrograph from the cross-section of the LCF membrane acquired with 15 kV acceleration voltages. It is obvious that a tarnish film with average thickness of 2 µm was accrued on the membrane surface. Elemental distribution by EDXS (Figure 5b-e) revealed the strong accumulation of iron and calcium combined with the absence of lanthanum in the tarnish layer. Using Cliff-Lorimer quantification, 66 at.% iron and 33 at.% calcium of the total value of cations were detected in the surface film. According to EDXS and XRD results, the tarnish layer on the unpolished LCF membrane can be understood as a CaFe$_2$O$_4$ phase. Thus, it can be concluded that the CaFe$_2$O$_4$ spinel formed in the LCF membrane at 1523 K preferentially on areas near the surface. A loss in oxygen from the perovskite structure, as induced by high temperatures, may be designated as the possible driving force for this process [35]. A decline in oxygen content led to the reduction of iron cations and formation of stoichiometric Fe^{3+} compounds, like CaFe$_2$O$_4$. A stoichiometric oxide arose at the membrane surface because oxygen loss on the membrane surface occurred faster than in bulk. Because of poor oxygen-ionic conductivity, the CaFe$_2$O$_4$ film can be considered a protective layer, which prevents further oxygen release and further perovskite decomposition. In addition, this hinders the recovery of the perovskite structure during cooling. Decomposition of the LCF ceramic at high temperatures due to irreversible oxygen release can be a handicap for operation of the material under long-term conditions with a steep oxygen gradient.

For the LCCF membrane, the formation of a tarnish layer was not observed by XRD or SEM. Traces of a Ca$_2$Co$_{2-y}$Fe$_y$O$_5$ phase could be detected only with the help of XRD. These findings point out to the advantageous stability of LCCF perovskite at extremely high temperatures, as compared with LCF.
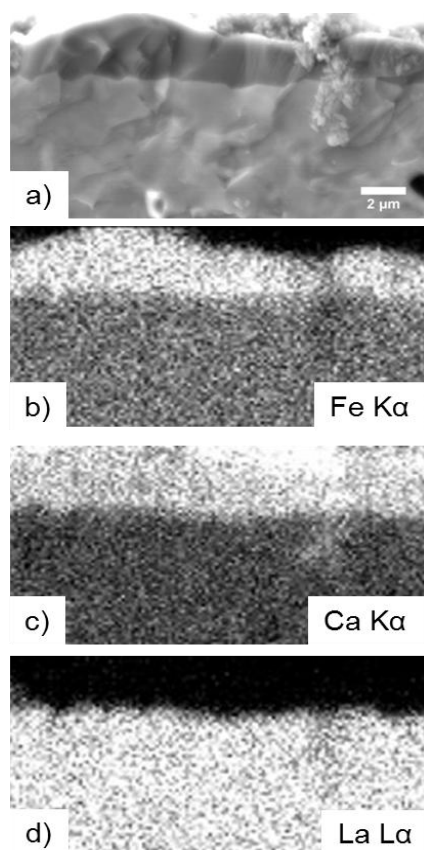
Figure 5. a) SEM micrograph from the cross-section of the unpolished LCF membrane sintered at 1523 K for 10 h showing formation of a tarnishing layer on the membrane surface (15 kV excitation voltage). b-d) Elemental distribution by EDXs of corresponding area b) Fe, c) Ca, d) La.

To prepare the LCCF and LCF asymmetric membranes, the powders obtained from the sol-gel synthesis were intermixed with 20 wt.% of block co-polymer Pluronic F 127 as a pore former. This material was utilized because the use of an organic pore former is widely applied for the fabrication of a porous support [50-53]. Then, porous membrane supports were constructed by press forming and calcination at 1423 K for 2 h. Figure 6a,b shows SEM micrographs from the surface of LCCF and LCF porous supports, respectively. Obviously, both supports had very high porosities. The pore size distribution of the LCCF support differed from that of LCF materials. The LCCF support exhibited some open pores, with sizes of about 10 µm, alongside 0.5-3 µm large pores. In contrast, the pore size distribution of the LCF support was in the mostly homogenously range of 0.5-2 µm. The high

amount of open pores leads to good air permeability through both supports, which was in the range of approximately 20-25 cm³min⁻¹cm⁻² between 1123 and 1223 K.
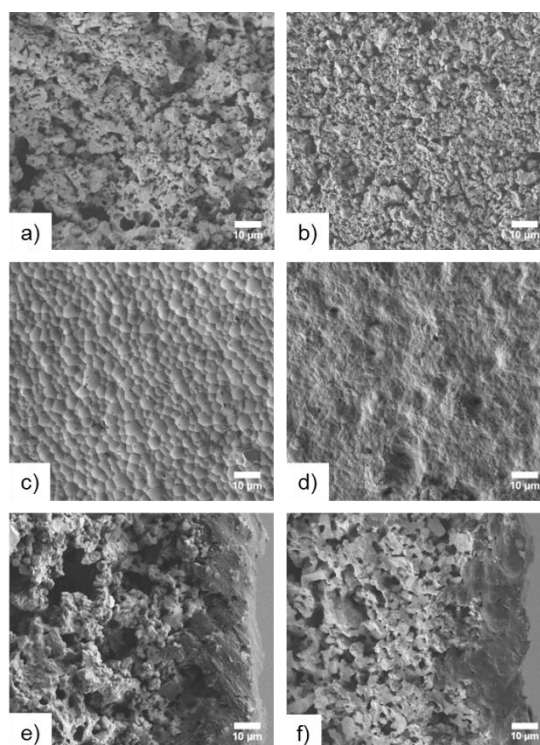
Figure 6. a,b) SEM micrographs of porous supports fired at 1423 K for 2 h a) LCCF, b) LCF. c,d) Surface of asymmetric membranes showing a dense layer obtained by spin coating and sintering c) LCCF sintered at 1443 K for 5 h, d) LCF sintered at 1473 K for 5 h. e,f) Fractured surface of asymmetric membranes e) LCCF sintered at 1443 K for 5 h, f) LCF sintered at 1473 K for 5 h. Excitation voltage 2 kV.

The spin-coating method was applied to obtain dense membranes on the porous supports. Subsequently, the LCCF membrane was sintered at 1448 K for 5 h. Very low porosities and no cracks were observed in the membrane surface using SEM (Figure 6c). Despite these occurrences, slightly elevated nitrogen leakage was detected during oxygen permeation measurements. This finding suggests that the dense layer was not completely homogeneously developed on the porous support. The size of the grains in the surface layer was found to be in the range of 2-6 µm. The LCF dense layer, shown in Figure 6d, was also formed after sintering at 1473 K

for 5 h. The LCF grains in the surface layer were smaller than that of LCCF and amounted to 1-3 µm. The average thickness of the dense layer of both materials was about 10 µm, as found in SEM micrographs from the cross-sections shown in Figures 6e,f. Both supports maintained their open pore structure after sintering. The distribution of the pore size in the bulk of LCCF and LCF materials after generation of dense layers was similar to that on the surface before sintering. EDXS of the cross-sections revealed that the LCCF dense layer retained its initial composition.
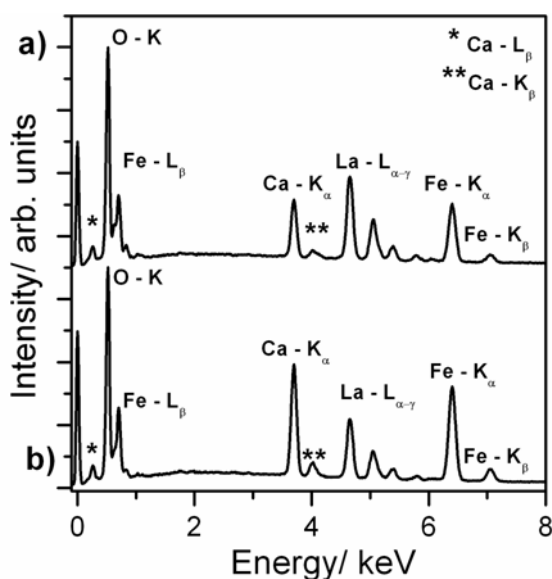

***Figure 7.** EDX spectra from the surface of a cross-sectioned LCF membrane. a) LCF porous support and b) LCF dense layer showing the slight accumulation of Ca and Fe in the dense layer.*

A slight accumulation of calcium in the LCF dense layer was detected by EDXS (Figure 7), which is related to the formation of $CaFe_2O_4$ at the membrane surface. The presence of the by-phase in the dense layer should be critically viewed because the impurities cannot be removed by polishing. Because the formation of a stoichiometric by-phase on the surface of the LCF membrane is due to oxygen loss, sintering of the ceramic material in an atmosphere with high oxygen content may be considered a possible method to prevent the perovskite decomposition and should be proven in a further investigation.

3.3 Measurements of oxygen permeation through LCCF and LCF membranes

Measurements of oxygen permeation flux through bulk and asymmetric membranes were carried out in air/He gradients at temperatures between 1223 K and 1023 K with 50 K steps. Prior to the experiments, the bulk membranes were polished with polymer-embedded 30 µm diamond lapping film to achieve a uniform surface appearance. The tarnish $CaFe_2O_4$ layer, which formed on the LCF bulk membrane after sintering, was thereby removed. Figure 8a shows the oxygen permeation fluxes of bulk and asymmetric membranes. For LCCF bulk membrane, a maximum flux of 0.43 $cm^3min^{-1}cm^{-2}$ was observed at 1223 K. This value is comparable to that of $La_{0.6}Ca_{0.4}CoO_{3-\delta}$, as reported by Watanabe et al. [37]. The oxygen permeation flux through the asymmetric LCCF membrane at 1223 K was improved by 50% to a value of 0.66 $cm^3min^{-1}cm^{-2}$. However, this value was approximately two orders of magnitude lower than expected from the Wagner equation, which states that the oxygen ionic conductivity is limited by bulk diffusion [54]. From our findings, we can assume that oxygen permeation through the asymmetric LCCF membrane is also strongly controlled by surface exchange reactions. Furthermore, the value of the oxygen permeation flux through the present asymmetric LCCF membrane was 2.5 times smaller than that reported by Watanabe et al. [37]. This result can be explained by the presence of low amount of by-phases, like $Ca_2Co_{2-y}Fe_yO_5$ and Co_3O_4, in the surface layer (see discussion related to Figures 9,10), which diminish the active area for oxygen exchange on the surface, as well as oxygen permeation through the membrane. Furthermore, the inhomogeneous distribution of the pore size in the porous support is unfavorable and is caused by a reduction of the effective area for oxygen permeation [37].

The activation energy of the oxygen ionic conductivity for bulk and asymmetric LCCF membranes was determined from the temperature dependency of oxygen fluxes by an Arrhenius plot, as given in Figure 8b. Although the asymmetric membrane structure has an effect on the oxygen permeability, which is considerably weaker than expected, the activation energy of the oxygen ionic

conductivity was found to be half that of the bulk membrane. For the asymmetric LCCF membrane, the activation energy was determined to be 65 kJmol^{-1}, compared with the activation energy of the bulk membrane, which had a value of 137 kJmol^{-1}. This fact indicates the different rate limiting steps for oxygen permeation through asymmetric and bulk membranes.
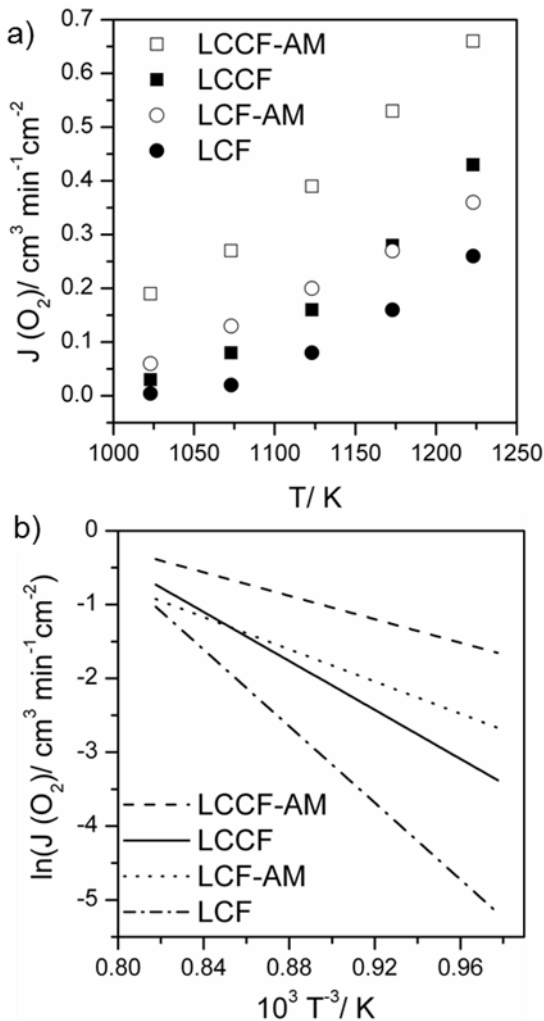

Figure 8. a) Oxygen permeation flux of 1 mm thick bulk membranes and asymmetrically structured membranes. Conditions: sweep flow rates: He = 29 cm^{3}min^{-1}, Ne =1 cm^{3}min^{-1}; feed flow rates: 150 cm^{3}min^{-1} synthetic air (80 vol.% N$_2$, 20 vol.% O$_2$,). b) Arrhenius presentation of oxygen permeation.

The activation energy for bulk LCCF membrane corresponds to the value that was calculated by Carter et al. from self-diffusion coefficients as a function of temperature [50]. Moreover, if activation energy is determined from the temperature dependency of surface exchange coefficients, it is around 70 kJmol^{-1} [55]. Accordingly, we can assume that the oxygen surface exchange reaction is the rate limiting step for the asymmetric membrane. In contrast, oxygen permeability through a bulk membrane is limited by bulk diffusion.

The LCF material exhibited an oxygen permeation of 0.26 cm^{3}min^{-1}cm^{-2} at 1223 K for the bulk membrane and 0.36 cm^{3}min^{-1}cm^{-2} for the asymmetric membrane at 1223 K (Figure 8a). The activation energies for bulk and asymmetric membranes were calculated to be 215 kJmol^{-1} and 91 kJmol^{-1}, respectively. It can be concluded that oxygen permeation through the bulk membrane is controlled by diffusion and by surface exchange reaction for the asymmetric membrane. Relatively low flux through the asymmetric LCF membrane can be explained by the accumulation of an CaFe$_2$O$_4$ phase in the surface layer during preparation.

3.4 Stability of LCCF material against CO$_2$

To examine the stability of Ca-containing materials during operation in the presence of CO$_2$, a time-dependent oxygen permeation experiment on 1µm thick LCCF bulk membrane was carried out using pure CO$_2$ as a sweep gas. As can be seen in Figure 9, a steady state of oxygen flux was reached within 3 h after switching the sweep gas from He to CO$_2$ at 1173 K. Subsequently, the oxygen permeation declined from 0.27 cm^{3}min^{-1}cm^{-2} to 0.16 cm^{3}min^{-1}cm^{-2} and maintained this value for 100 h. The decrease of oxygen flux at the start of the measurement may be explained by the inhibiting effect of CO$_2$ on the surface exchange reaction, which hinders the release of oxygen from the solid surface. The fact that the oxygen surface exchange had various rates in different gas atmospheres is well known and has been discussed in detail elsewhere [56-58]. The constant oxygen permeation flux through the LCCF membrane after steady state conditions were achieved suggests a high tolerance of the LCCF material toward CO$_2$. In contrast, the functional performance of Ba- and Sr-containing perovskites completely collapses, even at lower CO$_2$ partial pressures, after a very short time.
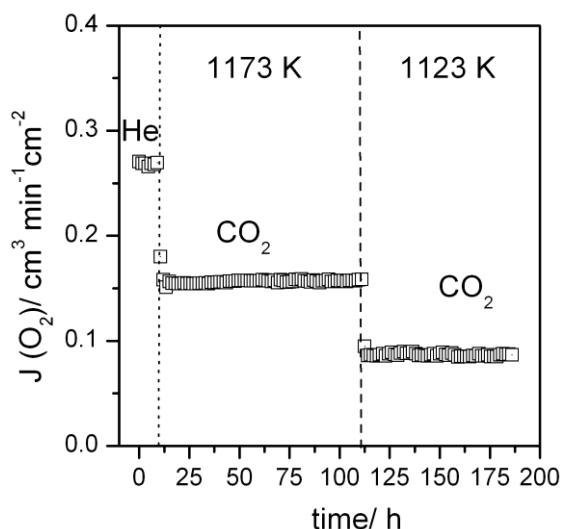
Figure 9. *Oxygen permeation flux of the LCCF bulk membrane with a thickness of 1 mm at 1173 and 1123 K. Conditions: sweep flow rate He or $CO_2 = 29$ cm^3min^{-1}, Ne $=1$ cm^3min^{-1}; feed flow rate 150 cm^3min^{-1} synthetic air (80 vol.% N_2, 20 vol.% O_2,).*

The LCCF perovskite also exhibited constant oxygen permeation performance at 1123 K (Figure 9). This result points to the desirable inherent stability of LCCF alongside its high CO_2 tolerance at temperatures below 1173 K. The temperature of 1173 K can be considered critical for many Co-containing perovskites because they tend to form hexagonal distorted perovskite phases below this temperature [7,9,10]. The reason for this issue is a reduction of cobalt cations combined with the spin-state transition leading to a significant decrease in ionic radius from Co^{2+} (high spin) = 74.5 pm to Co^{3+} (high spin) = 61 pm, Co^{3+} (low spin) = 54.5 pm, and Co^{4+} (high spin) = 53 pm [25]. The small Co^{3+} (low spin) and Co^{4+} cations, especially together with large A-site cations like Ba^{2+} and/or Sr^{2+}, resulted in a Goldschmidt tolerance factor higher than unity for corresponding perovskites, which is unfavorable for cubic and orthorhombic symmetries [7-9]. As mentioned in section 3.1, the tolerance factor for LCCF perovskite did not exceed the value of 1 by any ratio of $Co^{4+}/Co^{3+}/Co^{2+}$, because of the relatively small ionic radii of La^{3+} and Ca^{2+} cations. Furthermore, the high amount of La^{3+} cations in the LCCF may stabilize the valence and spin state of cobalt in a similar way as doping of Zr^{4+} or Ti^{4+}, which is beneficial for the delayed

phase transition kinetics of Ba- and Sr-containing cobaltites [10,59].

After the long-term oxygen permeation experiment, the LCCF membrane was quenched in a CO_2 atmosphere down to room temperature and investigated by XRD, SEM and TEM methods. XRD of the permeate site of the membrane revealed no $CaCO_3$ formation. Except for traces of $Ca_2Co_{2-y}Fe_yO_5$ and Co_3O_4, the LCCF material was found to consist of rhombohedrally distorted perovskite. SEM examination of the fractured surface of the permeate side proved that neither a tarnish layer nor cracks were formed on the membrane. However, the inclusion of phases, which have different chemical compositions than LCCF perovskite, in the regions near the surface and in the bulk were observed by the STEM HAADF technique (Figure 10a) by areas with dark Z contrast. Selected area electron diffraction was applied to the area marked with an asterisk in Figure 10a and showed no perovskite structures. The intensity distribution of the diffraction data in Figure 10b from the corresponding area can be attributed to a brownmillerite phase with an orthorhombic symmetry (space group Pnma) oriented along the [1,0,1] zone axis. The elemental distribution by EDXS in Figure 10 c-f reveals the accumulation of calcium, combined with the depletion of lanthanum in this area. Using Cliff-Lorimer quantification, the composition of the brownmillerite phase was found to be approximately $Ca_2Co_{1.5}Fe_{0.5}O_5$. Furthermore, some additional areas in the sample, which contained a brownmillerite phase or cobalt oxide, were detected by EDXS in the LCCF membrane.

Additionally, Figure 11a shows an HRTEM micrograph from the membrane surface, demonstrating the presence of two phases in this area. The phase on the left-hand side exhibited lattice fringes with a separation distance of approximately 7.4 Å, which corresponds to the (020) planes of the brownmillerite phase. The EEL spectra, which were acquired from both phase areas marked in Figure 11a, showed lanthanum-$M_{4,5}$, cobalt-$L_{2,3}$, iron-$L_{2,3}$, and oxygen-K ionization edges (Figure 11b,c). The weak intensities of the lanthanum-$M_{4,5}$ edge in Figure 11c clearly reveal that the phases had different chemical compositions. Furthermore, unequal chemical environments of the cations in these phases

were detected via analysis of the O-K energy-loss near edge structure (ELNES), which is sensitive to cation coordination, valence, and spin-state [8,60]. The O-K ELNES in Figure 11d is typical for perovskite oxides [38,39]. In contrast, the pattern of the O-K ELNES in Figure 11e cannot be attributed to a perovskite structure. According to HRTEM and EELS experiments, the phase in the LCCF membrane surface shown in Figure 11a can be indexed as brownmillerite and perovskite oxides. The presence of lanthanum traces in the brownmillerite phase may be explained by the limited substitution of calcium due to similar ionic sizes [25].
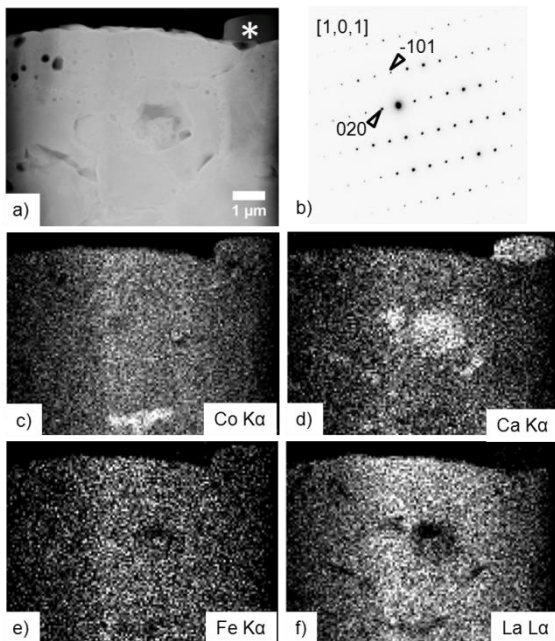

Figure 10. a) STEM-HAADF micrograph of the permeate side of an LCCF membrane quenched in the presence of CO_2. b) SAED pattern from the area marked with an asterisk in a). c-f) Elemental distribution by EDXS of the area shown in a. c) Co, d) Ca, e) Fe, f) La.

Because the traces of brownmillerite and cobalt oxide were observed in the as-prepared powder and in the sintered ceramic, we assumed that the formation of foreign phases in the LCCF membrane was not due to operation in a CO_2-containing atmosphere. The non-perovskite phases developed during the synthesis of LCCF materials and sintering of the ceramic, which is a general problem of this type of solid solutions. Nevertheless, Ca-based materials can be considered promising

for operation in the presence of CO_2, as LCCF ceramics exhibit stable functional performance in CO_2-containing atmospheres and no carbonate formation was observed by different analytical methods.
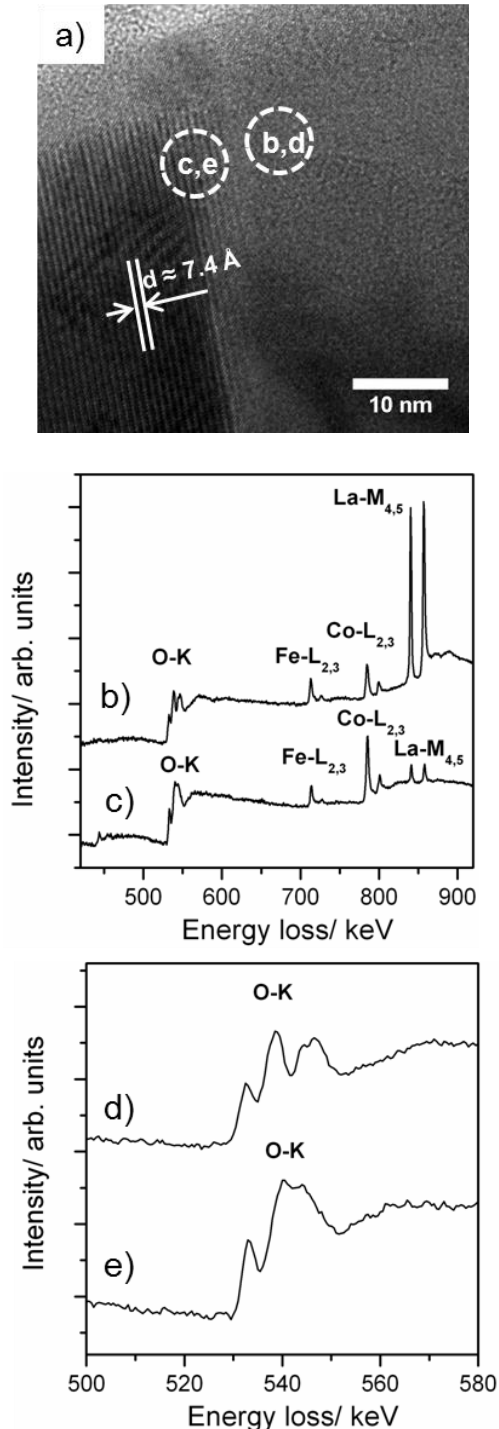

Figure 11. a) HRTEM micrograph showing two different phases on the cross-sectioned permeate side of LCCF membrane quenched in the presence of CO_2. b,c) EEL spectra from the areas marked in (a). d,e) O-K ELNES from the areas marked in (a).

Table 3. *Comparison of oxygen permeation flux through several relevant MIEC materials under CO_2-free conditions; sweep flow rates: He = 29 cm^3min^{-1}, Ne =1 cm^3min^{-1}; feed flow rates: 150 cm^3min^{-1} synthetic air (80 vol.% N_2, 20 vol.% $O_{2,}$).*

	$J(O_2)/$ $cm^3min^{-1}cm^{-2}$	
	1073 K	1173 K
$(Ba_{0.5}Sr_{0.5})(Co_{0.8}Fe_{0.2})O_{3-\delta}$ *	1.48	2.26
$(La_{0.4}Sr_{0.6})(Co_{0.8}Fe_{0.2})O_{3-\delta}$ *	0.31	0.61
$La_2NiO_{4+\delta}$	0.22	0.38
$(La_{0.6}Ca_{0.4})(Co_{0.8}Fe_{0.2})O_{3-\delta}$ (LCCF)	0.08	0.27
$(La_{0.6}Ca_{0.4})FeO_{3-\delta}$ (LCF)	0.02	0.16

* Useable only under CO_2-free conditions

3.5 Comparison of the oxygen permeation flux through LCCF and LCF perovskite with established MIEC materials

To evaluate whether Ca-containing perovskites are candidate membrane materials, the oxygen permeation flux through LCCF and LCF bulk membranes were compared with that of established MIEC materials. Table 3 summarizes the oxygen permeation fluxes of relevant MIEC membranes with equal thicknesses of 1 mm. These experiments were conducted under the same conditions as for our measurement setup. Obviously, the LCCF and LCF membranes exhibited lower oxygen permeation fluxes compared with Ba- and/or Sr-containing materials, as well as $La_2NiO_{4+\delta}$. Nevertheless, Ba- and/or Sr-containing membranes cannot be operated in the presence of CO_2 because of the formation of $(Ba,Sr)CO_3$. The tolerance of $La_2NiO_{4+\delta}$ material toward CO_2 is just as desirable as that of our presented LCCF and LCF membranes. In terms of electrical conductivity, however, Ca-containing materials clearly exceeded $La_2NiO_{4+\delta}$ [31,61,62]. Thus, we propose that Ca-based perovskites can be considered promising membrane materials for operation in CO_2-containing atmospheres, especially when

high electrical conductivity is required as, for example, with cathode material applications in SOFCs [63,64].

4. Conclusions

$(La_{1-x}Ca_x)FeO_{3-\delta}$ and $(La_{1-x}Ca_x)(Co_{0.8}Fe_{0.2})$ $O_{3-\delta}$ (x = 0.4-0.6) perovskite systems were fabricated as alternative materials to Ba- and/or Sr-based perovskite for operation in the presence of CO_2. Because only the first member of the systems with low Ca content (x=0.4) consisted mainly of a perovskite phase, these were investigated regarding chemical stability and oxygen ionic conducting properties. The $La_{0.6}Ca_{0.4}FeO_{3-\delta}$ (LCF) perovskite was found to be orthorhombically distorted, adopting a cubic symmetry at temperatures above 1173 K. The lattice symmetry of $La_{0.6}Ca_{0.4}Co_{0.8}Fe_{0.2}O_{3-\delta}$ (LCCF) perovskite was reversibly transformed from rhomohedral to cubic above 873 K. Furthermore, *in-situ* XRD experiments in the CO_2-containing atmosphere reveal the high tolerance of both materials toward CO_2, as expected from the thermodynamic considerations. The bulk and self-supported asymmetrically structured membranes were designed from both materials. Here, the LCF material was found to not be stable at extremely high temperatures because of the formation of a tarnish layer consisting of Ca_2FeO_4 spinel during sintering at 1523 K. The bulk LCCF membrane exhibited an oxygen permeation flux with a maximal value of 0.43 $cm^3min^{-1}cm^{-2}$ at 1223 K. The flux of 0.66 $cm^3min^{-1}cm^{-2}$ through asymmetric membranes with a dense layer thickness of about 10 μm was found to be two orders of magnitude lower than the value expected from theoretical calculations. The activation energies of oxygen ionic conductivity of bulk and self-supported membranes were determined to be 137 $kJmol^{-1}$ and 65 $kJmol^{-1}$, respectively. These results point out that oxygen permeation through a bulk membrane is limited by self-diffusion. In contrast, the limiting step for the oxygen permeation performance of asymmetric membranes lies in the surface exchange reaction. Similar behaviors were also observed for the LCF membrane. Additionally, the relatively low oxygen permeation flux through asymmetric membranes can be explained by the accumulation of impurities, like

brownmillerite and spinel phases, in the surface layer, as well as by the poor distribution of pore sizes in the porous support. The LCCF bulk membrane showed a constant oxygen permeation performance during long-term operation in the presence of CO_2. No formation of carbonate was detected in the membrane after testing for 100 h at 1173 K and for 60 h at 1123 K. Therefore, both the high tolerance against CO_2 and good inherent phase stability of the LCCF was confirmed. Thus, we propose that Ca-containing perovskites, LCCF, can be considered alternative membrane materials to Ba- and/or Sr-based perovskite for operation in CO_2-containing atmospheres. The synthesis and sintering conditions, however, should be optimized to prevent the formation of non-perovskite phases, which are primarily critical for performance of an asymmetrically structured membrane.

5. Acknowledgements

6. References

[1] Z. Shao, W. Yang, Y. Cong, H. Dong, J. Tong, G. Xiong, Investigation of the permeation behavior and stability of a $Ba_{0.5}Sr_{0.5}Co_{0.8}Fe_{0.2}O_{3-d}$ oxygen membrane, *J. Membr. Sci.* 172 (2000) 177-188.

[2] W. Zhou, R. Ran, Z. Shao, Progress in understanding and development of $Ba_{0.5}Sr_{0.5}Co_{0.8}Fe_{0.2}O_{3-\delta}$-based cathodes for intermediate-temperature solid-oxide fuel cells: A review, *J. Power Sources* 192 (2009) 231-246.

[3] Y. Teraoka, H. Zhang, S. Furukawa, N. Yamazoe, Oxygen permeation through perovskite oxides, *Chem. Lett.* 11 (1985) 1743-1746.

[4] J. Yi, H. Lein, T. Grande, S. Yakovlev, H.J.M. Bouwmeester, High-temperature compressive creep behaviour of the perovskite-type oxide $Ba_{0.5}Sr_{0.5}Co_{0.8}Fe_{0.2}O_{3-\delta}$, *Solid State Ionics* 180 (2009) 1564-1568.

[5] S. McIntosh, J.F. Vente, W.G. Haije, D.H.A. Blank, H.J.M. Bouwmeester, Oxygen stoichiometry and chemical expansion of $Ba_{0.5}Sr_{0.5}Co_{0.8}Fe_{0.2}O_{3-delta}$ measured by in-situ neutron diffraction, *Chem. Mater.* 18 (2006) 2187-2193.

[6] J. Vente, W. Haije, Z. Rak, Performance of functional perovskite membranes for oxygen production, *J.Membr.Sci.* 276 (2006) 178-184.

[7] S. Švarcova, K. Wiik, J. Tolchard, H.J.M. Bouwmeester, T. Grande, Structural instability of cubic perovskite $Ba_xSr_{1-x}Co_{0.8}Fe_{0.2}O_{3-\delta}$, *Solid State Ionics* 178 (2008) 1787-1791.

[8] M. Arnold, T. Gesing, J. Martynczuk, A. Feldhoff, Local charge disproportion in a high-performance perovskite, *Chem. Mater.* 20 (2008) 5858-5881.

[9] K. Efimov, Q. Xu, A. Feldhoff, TEM study of BSCF perovskite decomposition at intermediate temperatures, *Chem. Mater.* 22 (2010) 5866-5875.

[10] T. Nagai, W. Ito, T. Sakon, Relationship between cation substitution and stability of perovskite structure in $SrCoO_{3-\delta}$-based mixed conductors, *Solid State Ionics* 177 (2007) 3433-3444.

[11] M. Arnold, H. Wang, A. Feldhoff, Influence of CO_2 on the oxygen permeation performance and the microstructure of perovskite-type $(Ba_{0.5}Sr_{0.5})(Co_{0.8}Fe_{0.2})O_{3-\delta}$ membranes, *J. Membr. Sci.* 293 (2007) 44-52.

[12] O. Czuprat, M. Arnold, S. Schirrmeister, T. Schiestel, J. Caro, Influence of CO_2 on the oxygen permeation performance of perovskite-type $BaCo_xFe_yZr_zO_{3-\delta}$ hollow fiber membranes, *J. Membr. Sci.* 364 (2010) 132-137.

[13] J. Martynczuk, K. Efimov, L. Robben, A. Feldhoff, Performance of zinc-doped perovskite-type membranes at intermediate temperatures for long term oxygen permeation and under carbon dioxide atmosphere, *J. Membr. Sci.* 344 (2009) 62-70.

[14] J. Tong, W. Yang, B. Zhu, R. Cai, Investigation of ideal zirconium-doped perovskite-type ceramic membrane materials for oxygen separation, *J. Membr. Sci.* 203 (2002) 175-189.

[15] J.E. ten Elshof, H.J.M. Bouwmeester, H. Verweij, Oxygen transport through $La_{1-x}Sr_xFeO_{3-\delta}$ membranes II. Permeation in

air/CO, CO$_2$ gradients, *Solid State Ionics* 89 (1996) 81-92.

[16] S.J. Benson, D. Waller, J.A. Kilner, Degradation of La$_{0.6}$Sr$_{0.4}$Fe$_{0.8}$Co$_{0.2}$O$_{3-delta}$ in carbon dioxide and water atmospheres, *J. Electrochem. Soc.* 146 (4) (1999) 1305-1309.

[17] Z. Shao, S.M. Haile, A high-performance cathode for the next generation of solid-oxide fuel cells, *Nature* 431 (2004) 170-173.

[18] H. Wang, Y. Cong, W. Xang, Investigation on the partial oxidation of methane to syngas in a tubular Ba$_{0.5}$Sr$_{0.5}$Co$_{0.8}$Fe$_{0.2}$O$_{3-delta}$ membrane reactor, *Catal. Today* 82 (2003) 157-166.

[19] J. Caro, H. Wang, C. Tablet, A. Kleinert, A. Feldhoff, T. Schiestel, M. Kilgus, P. Kölsch, S. Werth, Evaluation of perovskites in hollow fibre and disk geometry in catalytic membrane reactors and in oxygen separators, *Catal. Today* 118 (2006) 128-135.

[20] J. Sunarso, S. Baumann, J.M. Serra, W.A. Meulenberg, S. Liu, Y.S. Lin, J.C. Diniz da Costa, Mixed ionic-electronic conducting (MIEC) ceramic-based membranes for oxygen separation, *J. Membr. Sci.* 320 (2008) 13-41

[21] I. Barin, F. Sauert, G. Patzki, "Thermochemical data of pure substances", third ed., vols. I and II, VCH, Weinheim, 1995.

[22] A.N. Shirsat, M. Ali, K.N.G. Kaimal, S.R. Bharadwaj, D. Das, Thermochemistry of La$_2$O$_2$CO$_3$ decomposition, *Thermochim. Acta* 399 (2003) 167-170.

[23] Y. Watanabe, S. Miyazaki, T. Maruyama, Y. Saito, Dissociation pressure of lanthanum dioxide carbonate, *J. Mater. Sci. Lett.* 5 (1996) 135-136.

[24] K. Efimov, M. Arnold, J. Martynczuk, A. Feldhoff, Crystalline intermediate phases in the sol gel-based synthesis of La$_2$NiO$_{4+\delta}$, *J. Am. Ceram. Soc.* 92 (2008) 876-880.

[25] R.D. Shannon, Revised effective ionic radii and systematic studies of interatomic distances in halides and chalcogenides, *Acta Crystallogr., Sect. A* 32 (1976) 751-767

[26] K.H. Stern, E.L. Weise, High temperature properties and decomposition of inorganic salts. Part 2 Carbonates, NSDRS, Washington, 1969.

[27] H. Yokokawa, N. Sakai, T. Kawada, M. Dokiya, Thermodynamic stability of perovskites and related compounds in some alkaline earth-transition metal-oxygen systems *J. Solid State Chem.* 94 (1991) 106–120.

[28] H. Yokokawa, N. Sakai, T. Kawada, M. Dokiya, Thermodynamic stabilities of perovskite oxides for electrodes and other electrochemical materials, *Solid State Ionics* 52 (1992) 43-56.

[29] F.M. Figueiredo, M.R. Soares, V.V. Kharton, E.N. Naumovich, J.C. Waerenborg, J.R. Frade, Properties of CaTi$_{1-x}$Fe$_x$O$_{3-delta}$ ceramic membranes, *J. Electroceram.* 13 (2004) 627-636.

[30] Y. Teraoka, T. Nobunaga, N. Yamazoe, Effect of cation substitution on the oxygen semipermeability of perovskite-type oxides, *Chem. Lett.* 17 (1988) 503–506.

[31] J.W. Stevenson, T.R. Armstrong, R.D. Carneim, L.R. Pederson, W. J. Weber, Electrochemical properties of mixed conducting perovskites La$_{1-x}$M$_x$Co$_{1-y}$Fe$_y$O$_{3-\delta}$ (M = Sr, Ba, Ca), *J. Electrochem. Soc.* 143 (1996) 2722-2729.

[32] M. Trunec, J. Cihlar, S. Diethelm, J. Van Herle, Tubular La$_{0.7}$Ca$_{0.3}$Fe$_{0.85}$Co$_{0.15}$O$_{3-\delta}$ Perovskite membranes, Part I: Preparation and properties, *J. Am. Ceram. Soc.* 89 (2006) 949-955.

[33] C.Y. Tsai, A.G. Dixon, Y.H. Ma, W.R. Moser, M.R. Pascucci, Dense perovskite, La$_{1-x}$A*$_x$Fe$_{1-y}$Co$_y$O$_{3-\delta}$ (A* = Ba, Sr, Ca), membrane synthesis, applications, and characterization, *J. Am. Ceram. Soc.* 81 (1998) 1437-1444.

[34] S. Diethelm, J. Van Herle, P.H. Middleton, D. Favrat, Oxygen permeation and stability of La$_{0.4}$Ca$_{0.6}$Fe$_{1-x}$Co$_x$O$_{3-\delta}$ (x= 0, 0.25, 0.5) membranes, *J. Power Sourc.* 118 (2003) 270-275.

[35] A.N. Nadeev, S.V. Tsybulya, E.Y. Gerasimov, N.A. Kulikovskaya, L.A. Isupova, Structural features of the formation of La$_{1-x}$Ca$_x$FeO$_{3-\delta}$ (0≤x≤0.7) heterovalent solid solutions, *J. Struct. Chem.* 51 (2010) 891-897.

[36] K. Watanabe, M. Yuasa, T. Kida, K. Shimanoe, Y. Teraoka, N. Yamazoe, Preparation of oxygen evolution layer/La$_{0.6}$Ca$_{0.4}$CoO$_3$ dense membrane /porous support asymmetric structure for

high-performance oxygen permeation, *Solid State Ionics* 179 (2008) 1377-1381.

[37] K. Watanabe, M. Yuasa, T. Kida, K. Shimanoe, Y. Teraoka, N. Yamazoe, Dense/porous asymmetric-structured oxygen permeable membranes based on La$_{0.6}$Ca$_{0.4}$CoO$_3$ perovskite-type oxide, *Chem. Mater.* 20 (2008) 6965-6973.

[38] A. Feldhoff, M. Arnold, J. Martynczuk, T.M. Gesing, H. Wang. The sol-gel synthesis of perovskites by an EDTA/citrate complexing method involves nanoscale solid state reactions. *Solid State Sciences*, 10 (2008) 689-701.

[39] A. Feldhoff, J. Martynczuk, H.H. Wang, Advanced Ba$_{0.5}$Sr$_{0.5}$Zn$_{0.2}$Fe$_{0.8}$O$_{3-\delta}$ perovs-kite-type ceramics as oxygen selective membranes: Evaluation of the synthetic process, *Progress Solid State Chem.* 35 (2007) 339–353

[40] H. Wang, C. Tablet, A. Feldhoff, J. Caro, Investigation of phase structure, sintering, and permeability of perovskite-type Ba$_{0.5}$Sr$_{0.5}$Co$_{0.8}$Fe$_{0.2}$O$_{3-delta}$ membranes, *J. Membr. Sci.* 262 (2005) 20-26.

[41] J. Martynczuk, M. Arnold, A. Feldhoff, Influence of grain size on the oxygen permeation performance of perovskite-type (Ba$_{0.5}$Sr$_{0.5}$)(Fe$_{0.8}$Zn$_{0.2}$)O$_{3-\delta}$ membranes, *J. Membr. Sci.* 322 (2008) 375-382.

[42] V.M. Goldschmidt, Die Gesetze der Kristallchemie, *Naturwiss.* 14, (1926) 477-485.

[43] G.J. Redhammer, G.Tippelt, G. Roth, G. Amthauer, Structural variations in the brownmillerite series Ca$_2$(Fe$_{2-x}$Al$_x$)O$_5$: Single-crystal X-ray diffraction at 25 degrees C and high-temperature X-ray powder diffraction (25 degrees C <= T <= 1000 degrees C), *Am. Mineral.* 89 (2004) 405-420.

[44] P. Boullay, V. Dorcet, O. Pérez, C. Grygiel, W. Prellier, B. Mercey, M. Hervieu, Structure determination of a brownmillerite Ca$_2$Co$_2$O$_5$ thin film by precession electron diffraction, *Phys. Rev.* 79 (2009) 184108.

[45] G.S. Pawley, Unit cell refinement from powder diffraction scans, *J. Appl. Cryst.* 14 (1981) 357-361.

[46] H. Fjellvag, E. Gulbrandsen, S. Aasland, A. Olsen, B.C. Hauback, Crystal structure and possible charge ordering in one-dimensional Ca$_3$Co$_2$O$_6$, *J. Solid State Chem.* 124 (1996) 190-194.

[47] H. Falcon, A.E. Goeta, G. Punte, E. Carbonio, Crystal structure refinement and stability of LaFe$_x$Ni$_{1-x}$O$_3$ solid solutions, *J. Solid State Chem.* 133 (1997) 379-385.

[48] M. Ain, J.M. Delrieu, A. Menelle, G. Parette, J. Jegoudez, Orthorhombicity and oxygen uptake by YBa$_2$Cu$_3$O$_{6+x}$, *J. Phys. France* 50 (1989) 1455-1461.

[49] R.H. Mitchell, Perovskites: Modern and ancient; Almaz Press Inc.: Ontario, Canada, 2002

[50] M.L. Fontaine, J.B. Smith, Y. Larring, R. Bredesen, On the preparation of asymmetric CaTi$_{0.9}$Fe$_{0.1}$O$_{3-\delta}$ membranes by tape-casting and co-sintering process, *J. Membr. Sci.* 326 (2009) 310–315.

[51] A.V. Kovalevsky, V.V. Kharton, F.M.M. Snijkers, J.F.C. Cooymans, J.J. Luyten, F.M.B. Marques, Oxygen transport and stability of asymmetric SrFe(Al)O$_{3-delta}$-SrAl$_2$O$_4$ composite membranes, *J. Membr. Sci.* 301(2007) 238–244.

[52] G. Etchegoyen, T. Chartier, P.D. Gallo, An architectural approach to the oxygen permeability of a La$_{0.6}$Sr$_{0.4}$Fe$_{0.9}$Ga$_{0.1}$O$_{3-delta}$ perovskite membrane, *J. Eur. Ceram. Soc.* 26 (2006) 2807-2815.

[53] S. Araki, Y. Hoshi, S. Hamakawa, S. Hikazudani, F. Mizukami, Synthesis and characterization of mixed ionic-electronic conducting Ca$_{0.8}$Sr$_{0.2}$Ti$_{0.7}$Fe$_{0.3}$O$_{3-alpha}$ thin film, *Solid State Ionics* 178 (2008) 1740–1745.

[54] C. Wagner, Equations for transport in solid oxides and sulfides of transition metals, *Prog. Solid State Chem.* 10 (1975) 3-16.

[55] S. Carter, A. Selcuk, R.J. Chater, J. Kajda, J.A. Kilner, B.C.H. Steele, Oxygen transport in selected nonstoichiometric perovskite-structure oxide, *Solid State Ionics* 53-56 (1992) 597–605.

[56] J.A. Lane, J.A. Kilner, Oxygen surface exchange on gadolinia doped ceria, *Solid State Ionics* 136-137 (2000) 927-932.

[57] K. Yashiro, S. Onuma, A. Kaimai, Y. Nigara, T. Kawada, J. Mizusaki, K. Kawamura, T. Horita, H. Yokokawa, Mass transport properties of Ce$_{0.9}$Gd$_{0.1}$O$_{2-delta}$ at the surface and in the bulk *Solid State Ionics* 152-153 (2002) 469-476.

[58] I.V. Khromushin, T.I. Aksenova, Zh.R. Zhotabaev, Mechanism of gas–solid

exchange processes for some perovskites, *Solid State Ionics* 162-163 (2003) 37-40.

[59] S. Yakovlev, C.Y. Yoo, S. Fang, H.J.M. Bouwmeester, Phase transformation and oxygen equilibration kinetics of pure and Zr-doped Ba$_{0.5}$Sr$_{0.5}$Co$_{0.8}$Fe$_{0.2}$O$_{3-\delta}$ perovskite oxide probed by electrical conductivity relaxation, *Appl. Phys.Lett.* 96 (2010) 254101.

[60] J. Martynczuk, M. Arnold, H. Wang, J. Caro, A. Feldhoff, How (Ba$_{0.5}$Sr$_{0.5}$)(Fe$_{0.8}$Zn$_{0.2}$)O$_{3-\delta}$ and (Ba$_{0.5}$Sr$_{0.5}$)(Co$_{0.8}$ Fe$_{0.2}$)O$_{3-\delta}$ Perovskites form via an EDTA/citric acid complexing method, *Adv. Mater.* 19 (2007) 2134-2140.

[61] G. Amow, I.J. Davidson, S.J. Skinner, A comparative study of the Ruddlesden-Popper series, La$_{n+1}$Ni$_n$O$_{3n+1}$ (n=1, 2 and 3), for solid-oxide fuel-cell cathode applications, *Solid State Ionics* 177 (2006) 1205-1210.

[62] N. Ortiz-Vitoriano, I. Ruiz de Larramendi, J.I. Ruiz de Larramendi, M.I. Arriortua, T. Rojo, Synthesis and electrochemical performance of La$_{0.6}$Ca$_{0.4}$Fe$_{1-x}$Ni$_x$O$_3$ (x = 0.1, 0.2, 0.3) material for solid oxide fuel cell cathode, *J. Power Sourc.* 192 (2009) 63-69.

[63] K. Kendall, Progress in solid oxide fuel cell materials, *Int. Mat. Rev.* 2005 (2005) 257-264.

[64] J. Richter, P. Holtappels, T. Graule, T. Nakamura, L.J. Gauckler, Materials design for perovskite SOFC cathodes, *Monatsh. Chem.* 140 (2009) 985-999.

5.3 CO$_2$-stable and cobalt-free dual phase membrane foroxygen separation

Huixia Luo, Konstantin Efimov, Heqing Jiang, Armin Feldhoff, Haihui Wang, and Jürgen Caro

Angewandte Chemie

Gas Separation

CO$_2$-Stable and Cobalt-Free Dual-Phase Membrane for Oxygen Separation**

Huixia Luo, Konstantin Efimov, Heqing Jiang, Armin Feldhoff, Haihui Wang, and Jürgen Caro**

The increase in carbon dioxide emissions is considered to be the main contribution to global warming. Therefore, there is an urgent need to reduce the emissions of CO$_2$ into the atmosphere. Recently, CO$_2$ capture and storage technologies to reduce the CO$_2$ emissions from coal-fired power plants have gained the attention of decision makers in governments, industry, and academia. There are three major concepts for CO$_2$ sequestration: post-combustion capture, pre-combustion separation, and oxyfuel techniques.[1] MIECMs, which are ceramic membranes with mixed oxygen ionic and electronic oxygen conductivity, have gained increasing attention owing to their potential applications in oxygen supply[2] to power stations for CO$_2$ capture according to the oxyfuel concept.[3] This concept involves burning natural gas with nitrogen-free oxygen, thus allowing CO$_2$ to be sequestered after steam condensation. Dense MIECMs are promising candidates for this oxygen separation from air. However, when MIECMs are used for this purpose, some of the CO$_2$ is recycled and used as the sweep gas for the oxygen separation, simultaneously lowering the temperature in the burner. Furthermore, CO$_2$-stable MIECMs could be promising for dry reforming and the thermal decomposition of carbon dioxide in combination with the partial oxidation of methane to syngas.[4]

Many complex oxides have been investigated as membranes for oxygen separation and in membrane reactors. However, there are two main problems for the proper application of this kind of membrane. First, perovskite membranes with cobalt doping usually show high permeability but poor stability under harsh working conditions;[5] by avoiding cobalt, the stability of MIEC membrane materials

can be enhanced.[6] Second, for numerous applications such as the oxyfuel process or hydrocarbon partial oxidations, where some CO$_2$ is formed as a byproduct of an undesired deeper oxidation, the oxygen transporting membranes must sustain their phase stability and oxygen transport properties. Usually, the perovskite-type membranes contain alkaline earth metal ions on the A site, such as barium and strontium, which tend to react with CO$_2$ and form carbonates.[7] However, when using perovskites as oxidation catalysts, the negative effect of CO$_2$ as product molecule can be reduced if the reaction is carried out in a microwave field.[8,9] Also in the case of CO$_2$ decomposition with a hydrocarbon as oxidant on the other side of the MIECM, the negative influence of CO$_2$ can be reduced. The aforementioned problems can be overcome by using a cobalt-free and alkaline-earth-metal-free dual-phase membrane, which is composed of two interpenetrating percolated networks of an oxygen conductor (solid oxide electrolyte) and an electron conductor (internally short-circuiting electrode). In an extension of this concept, the dual phases might also consist of MIECMs with deviating transfer rates for oxygen and electrons.[10]

The first dual-phase membranes were made of oxygen conductors and noble metals: $(Bi_2O_3)_{0.74}SrO_{0.26}$-Ag,[11] $Bi_{1.5}Y_{0.3}Sm_{0.2}O_3$-Ag,[12] $Bi_{1.5}Er_{0.5}O_3$-Ag,[13] $Bi_{1.6}Y_{0.4}O_3$-Ag,[14] and YSZ-Pd.[15] However, the application of these materials is limited owing to high materials costs, a mismatch of the coefficient of thermal expansion (CTE) between the ceramic and metallic phases, and poor oxygen permeabilities. In another concept, perovskite- or fluorite-type oxides are used instead of noble metals as electron conductors.[16–18] However, these dual-phase membranes have a perovskite phase as electron conductor in which the A site is often occupied by alkaline earth metals, which can be easily eroded by forming carbonates if CO$_2$ is present. Improved stability against carbonate formation can be expected if both phases are made from oxides, which contain only transition metals and/or lanthanides. Both groups of elements are very tolerant against carbonate formation as shown by thermodynamics as well as by gravimetric considerations.[19,20]

Herein, we have prepared a novel alkaline-earth-free CO$_2$-stable and cobalt-free composite dual-phase membrane containing 40 wt% NiFe$_2$O$_4$ with a spinel structure and 60 wt% Ce$_{0.9}$Gd$_{0.1}$O$_{2-\delta}$ with a fluorite structure (abbreviated as 40NFO–60CGO). In the mixture of the two phases, NFO is the electron conductor and CGO is the oxygen-ion conductor. Phase structure and stability and also oxygen permeability were investigated under different atmospheres at high temperatures. Special attention is paid to the CO$_2$ stability.

The dual phase membrane was synthesized using powder mixing and the one-pot method. X-ray diffraction (Figure 1)

[*] H. Luo, K. Efimov, Dr. H. Jiang, Dr. A. Feldhoff, Prof. Dr. J. Caro
Institute for Physical Chemistry and Electrochemistry
Leibniz University Hannover
Callinstrasse 3–3A, 30167 Hannover (Germany)
Fax: (+49) 511-762-19121
E-mail: juergen.caro@pci.uni-hannover.de

Prof. Dr. H. Wang
School of Chemistry & Chemical Engineering
South China University of Technology
No. 381 Wushan Road, Guangzhou 510640 (China)
Fax: (+86) 20-8711-0131
E-mail: hhwang@scut.edu.cn

Supporting information for this article is available on the WWW under http://dx.doi.org/10.1002/anie.201003723.
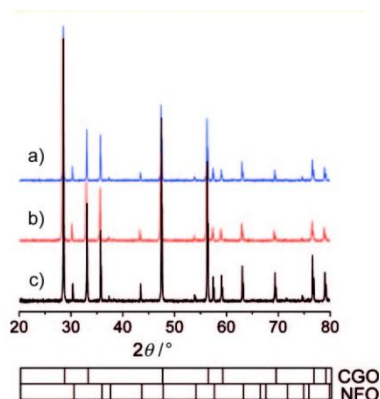
Communications

Figure 1. XRD pattern of 40NFO–60CGO membranes prepared by different methods and sintered at 1350°C for 10 h in air. a) Mixing NFO and CGO powders by hand; b) direct one-pot method; c) spent one-pot membrane after the CO_2 stability test shown in Figure 6.

Figure 2. Grain structure of the surface (top view) of the 40NFO–60CGO composite membrane after sintering at 1350°C for 10 h and prepared by different methods. Left line: powder mixing in a mortar by hand (a,c,e); right line: direct one-pot method (b,d,f). a,b) SEM, c,d) BSEM, e,f) EDXS.

clearly confirmed that both 40NFO–60CGO membranes consist of only the two phases NFO and CGO. The unit-cell parameter of the pure phases NFO (0.83455 nm) and CGO (0.54209 nm) are almost the same as in the 40NFO–60CGO dual-phase material (NFO: 0.83350 nm, CGO: 0.54186 nm). The phase composition was stable with time. As an example, Figure 1c shows the XRD of the spent 40NFO–60CGO membrane after the long-term oxygen separation with CO_2 as sweep gas (Figure 6).

Figure 2 shows the results of scanning electron microscopy (SEM), back-scattered SEM (BSEM), and energy-dispersive X-ray spectroscopy (EDXS) of both membranes. For the membrane prepared by powder mixing (Figure 2 a,c,e), the grain size of CGO in these composite membranes is smaller (2–4 μm) than that of NFO (3–7 μm). BSEM in particular (Figure 2 c) shows that there is clustering of grains of one and the same type; that is, NFO-NFO and CGO-CGO aggregation. In comparison to powder mixing, the membrane prepared by the direct one-pot method shows much smaller grains and a higher homogenization of the NFO and CGO phases (Figure 2 b,d,f). The NFO and CGO grains could be distinguished by BSEM and EDXS. The dark grains in BSEM are NFO and the light grains are CGO, as the contribution of the back-scattered electrons to the SEM signal intensity is proportional to the atomic number. The same information is provided by EDXS. The green color (dark in the black-and-white version) is an overlap of the Fe and Ni signals, whereas the yellow color (light) stems from an average of the Ce and Gd signals.

In situ XRD provides an effective and direct way to characterize the high-temperature structure changes while increasing and decreasing temperatures under certain gas atmospheres. The in situ XRD patterns of the one-pot 40NFO–60CGO in air upon increasing and decreasing the temperature from 30°C to 1000°C and back to 30°C (Supporting Information, Figure S1) indicate that the CGO and NFO phases remain unchanged in the 40NFO–60CGO dual-phase materials. During the oxygen supply for coal-
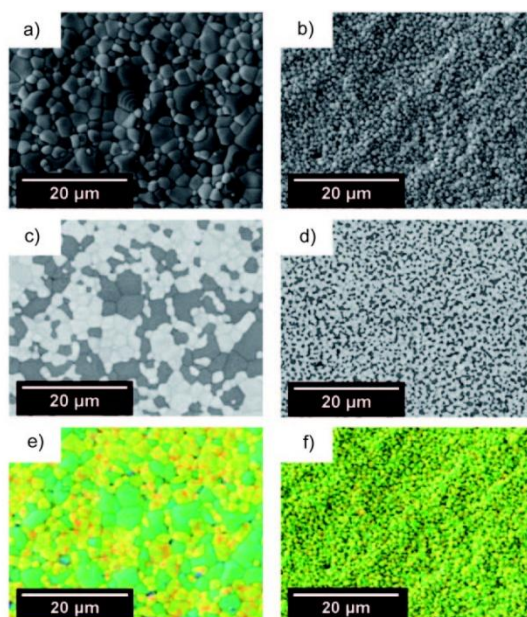
based power stations, the membrane would be exposed to CO_2. Therefore, the high-temperature phase stability in a CO_2-containing atmosphere was studied by in situ XRD (Supporting Information, Figure S2). The in situ XRD patterns of 40NFO–60CGO dual-phase membranes between room temperature and 1000°C in an atmosphere of 50 vol% CO_2 and 50 vol% N_2 (Supporting Information, Figure S2) shows that the composite membrane retains its dual phases over the entire temperature range. In an atmosphere of 50 vol% CO_2 and 50 vol% N_2, no carbonate formation could be detected. These results show that the composite membrane 40NFO–60CGO is stable in a CO_2 atmosphere. The time dependence of the oxygen flux with pure CO_2 as sweep gas also confirmed that the dual-phase membrane was CO_2-stable (Figure 6).

The scanning transmission electron microscope (STEM) high-angle annular dark-field (HAADF) micrograph in Figure 3a and also the EDXS elemental distributions in Figure 3c reveal a clear phase separation of CGO and NFO in the membrane. The grain size can be determined from these figures to be in the range of 500 nm to 1 μm, which is in accordance with the SEM findings. Similar to BSEM (Figure 2 c,d), in the STEM-HAADF micrograph the dark grains are NFO and light grains are CGO (Figure 3a). The electron energy-loss (EEL) spectra (Figure 3b) were taken from circa 150 nm circular areas in the volume of CGO (top) and NFO grains (bottom). The fine-structure of the O_K ionization edge is characteristic to the respective oxide. No intermixing of cations between the two phases can be observed (that is, CGO
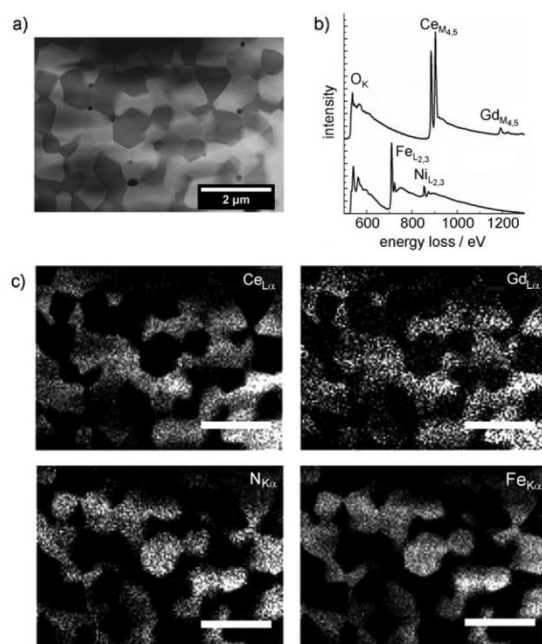
98

Figure 3. a) STEM-HAADF micrograph of a dual-phase membrane obtained by the direct one-pot method, showing CGO by bright contrast and NFO by dark contrast. Very dark contrast corresponds to holes in the as-prepared specimen. b) EEL spectra from the grain volume of CGO and NFO giving clear indication of phase separation. c) EDXS elemental distributions of Ce, Gd, Ni, and Fe. Scale bars: 2 μm.

Figure 4. HRTEM of a CGO–NFO contact in a dual-phase membrane that was obtained from the direct one-pot method. a) Medium magnification with SAED pattern as insets (CGO at top, NFO at bottom); b) close-up of the marked area in (a).

contains neither Fe nor Ni, and NFO contains neither Ce nor Gd), which shows that a dual-phase membrane with well-separated grains was obtained by the direct one-pot method.

Figure S3a in the Supporting Information shows a CGO–CGO interface with the grain to the left being imaged along $[111]_{CGO}$ zone axis and the grain to the right exhibiting $(111)_{CGO}$ planes. Figure S3b in the Supporting Information shows an NFO–NFO interface with both grains exhibiting $(202)_{NFO}$ lattice planes. In both cases of interfaces between grains of the same kind, the grains are in intimate contact with no interphase between them, which is obvious from the HRTEM micrographs of Figure S3. This result was supported by EDXS and EELS, which could not identify any Fe or Ni at CGO–CGO interfaces and no Ce or Gd at NFO–NFO interfaces.

Figure 4 displays a contact between grains of different type (CGO and NFO). The grain at top is CGO imaged along the $[110]_{CGO}$ zone axis, and the grain at bottom is NFO imaged along $[110]_{NFO}$ zone axis (see the selected-area electron diffraction (SAED) pattern as insets in Figure 4a). Some Moiré fringes are noted in the right part of Figure 4a, which appear to be due to a slight inclination of the grain boundary with respect to the electron beam and give rise to a circa 1 nm-thick bright contrast feature along the whole grain boundary. Figure 4b shows a close-up of the marked area in Figure 4a and gives no indication of any interphases. Locally varying phase contrast in Figure 4a and b can be attributed to changes
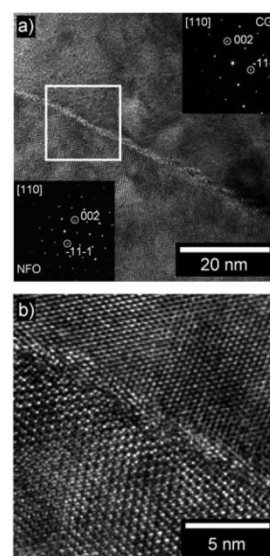
in the thickness of the as-prepared TEM specimen after ion sputtering. Thus, it is concluded that all interfaces in the dual-phase membrane, which was obtained from direct one-pot method, exhibit well-separated grains in intimate contact.

Figure 5 shows the oxygen permeation fluxes of our dual phase composite membranes prepared by the one-pot method, and by mixing the powders by hand in a mortar, using He and CO_2, respectively, as sweep gases. For the membrane prepared by one-pot synthesis, oxygen permeation fluxes of 0.31 and 0.27 mL min^{-1}cm^{-2} are found at 1000°C when pure He and CO_2 are used as sweep gases.

If the two powders NFO and CGO are mixed by hand in a mortar, only 50% of the oxygen permeances of the one-pot membrane are obtained (Figure 5). This experimental finding clearly indicates that a homogeneous grain size distribution and a small grain size are a condition for high oxygen fluxes, as mentioned before by Yang[21] who reported that the uniformity of dual-phase membrane effects the oxygen permeability. However, when pure CO_2 was taken as the sweep gas, the oxygen permeation flux was only slightly decreased (Figure 5), which demonstrates the high CO_2 stability of the material. On the other hand, there is a slight but remarkable reduction of the oxygen flux when CO_2 instead of He is used as sweep gas. This experimental finding can be explained by the inhibiting effect of carbon dioxide on the oxygen surface exchange reaction; that is, the presence of CO_2 decreases the rate of the oxygen release from the solid. This assumption is in complete agreement with previous findings,[22] which state that the oxygen surface-exchange reaction is not the same under different gas atmospheres. From an Arrhenius plot of the oxygen permeation fluxes when He and CO_2 were applied as sweep gases, the apparent
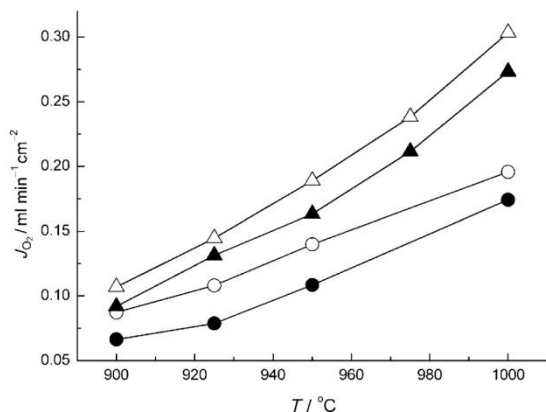
Communications

Figure 5. Oxygen flux J_{O_2} of 40NFO–60CGO dual-phase membranes prepared by different methods, and with a thickness of 0.5 mm, at different temperatures and with CO$_2$ and He as sweep gases. The air flow on the feed side was always $F_{air} = 150$ mL min^{-1}, the sweep flow was always 30 mL min^{-1}. He sweep with $F_{He} = 29$ mL min^{-1}, $F_{Ne} = 1$ mL min^{-1}: △ = one-pot membrane, ○ = powder mixing. CO$_2$ sweep with $F_{CO_2} = 29$ mL min^{-1}, $F_{Ne} = 1$ mL min^{-1}: ▲ = one-pot membrane, ● = powder-mixing method.

Figure 6. Oxygen permeation flux J_{O_2} through the 40NFO–60CGO composite membrane, prepared by the one-pot method, as a function of time at 1000°C. Conditions: 29 mL min^{-1} CO$_2$ as sweep gas, 1 mL min^{-1} Ne as internal standard gas, 150 mL min^{-1} air as feed gas.

activation energies $E_a = (128 \pm 4)$ kJ mol^{-1} were found to be the same for the two membrane preparations within experimental error. Tong et al.[23] reported that a single activation energy is an important feature for a good stability of oxygen permeation through a oxygen membrane. In our case, a single activation energy was found in the range of 900–1000°C.

The effect of the sweep rate on the oxygen permeation flux at temperature 1000°C is shown in Supporting Information, Figure S4. Even when using CO$_2$ as the sweep gas, we observe the usual behavior, namely that oxygen permeances increase if the gradient of the oxygen partial pressure across the membrane is increased; this increase can be achieved by off-transporting the permeated oxygen as fast as possible, which can be realized with an increased sweep flow.

Figure 6 shows the long-term behavior of oxygen permeation flux through 40NFO–60CGO composite membrane at 1000°C. During this oxygen permeation test, an oxygen permeation flux of about 0.30 mL min^{-1} cm^{-2} was obtained at 1000°C, and no decrease of the oxygen permeation flux was found during the permeation test. After the oxygen permeation test, the sample was characterized by XRD (Figure 1c). The dual-phase structure was retained, which indicates that 40NFO–60CGO exhibits excellent structure stability under a CO$_2$ atmosphere. The result is in agreement with the finding of in situ high-temperature XRD, indicating that the membrane is CO$_2$-stable. It is not like Ba$_{0.5}$Sr$_{0.5}$Fe$_{0.8}$Zn$_{0.2}$O$_{3-\delta}$ (BSFZ) or Ba$_{0.5}$Sr$_{0.5}$Co$_{0.8}$Fe$_{0.2}$O$_{3-\delta}$ (BSCF) perovskite materials, where carbonate was formed when CO$_2$ was the feed gas and the oxygen flux decreased rapidly.[7]

In conclusion, a novel CO$_2$-stable and cobalt-free dual-phase membrane of the composition 40 wt% NiFe$_2$O$_4$–60 wt% Ce$_{0.9}$Gd$_{0.1}$O$_{2-\delta}$ (40NFO–60CGO) was synthesized by a direct one-pot method, and for comparison by powder mixing in a mortar. In situ high-temperature X-ray diffraction
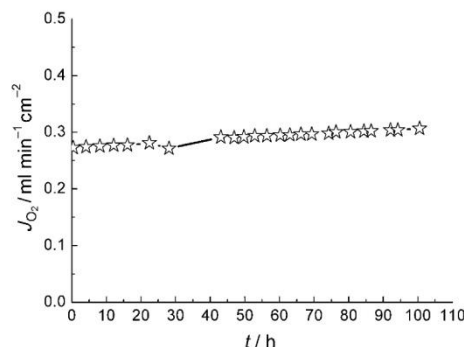
demonstrated that the two phases NFO and CGO were stable upon repeated heating and cooling cycles between room temperature and 1000°C in air and in an atmosphere with 50 vol% CO$_2$ and 50 vol% N$_2$. Energy-dispersive X-ray spectroscopy and back-scattered electron microscopy showed that the one-pot synthesis results in a dual-phase membrane with smaller NFO or CGO grains of uniform size distribution without homoaggregation of grains of the same phase, in comparison with a dual-phase membrane prepared by mixing the two powders. At 1000°C, oxygen permeation fluxes of 0.31 and 0.27 mL min^{-1} cm^{-2} were obtained on the membrane prepared with the one-pot material for the sweep gases He and CO$_2$, respectively. This value is comparable with that of La$_2$NiO$_{4+\delta}$ and of La$_2$Ni$_{0.9}$Fe$_{0.1}$O$_{4+\delta}$, which are promising CO$_2$-stable membrane materials.[24] In a 100 h oxygen permeation using CO$_2$ as the sweep gas, no decline of the oxygen permeation flux was found, thus indicating that our dual phase membrane is CO$_2$-stable.

[1] R. Kneer, D. Toporov, M. Förster, D. Christ, C. Broeckmann, E. Pfaff, M. Zwick, S. Engels M. Modigell, *Energy Environ. Sci.* **2010**, *3*, 198–207.

[2] a) H. Q. Jiang, Z. W. Cao, S. Schirrmeister, T. Schiestel, J. Caro, *Angew. Chem.* **2010**, *122*, 5790–5794; *Angew. Chem. Int. Ed.* **2010**, *49*, 5656–5660; b) H. Q. Jiang, H. H. Wang, F. Y. Liang, S. Werth, T. Schiestel, J. Caro, *Angew. Chem.* **2009**, *121*, 3027–3030; *Angew. Chem. Int. Ed.* **2009**, *48*, 2983–2986; c) H. Q. Jiang, H. H. Wang, S. Werth, T. Schiestel, J. Caro, *Angew. Chem.* **2008**, *120*, 9481–9484; *Angew. Chem. Int. Ed.* **2008**, *47*, 9341–9344; d) H. H. Wang, Y. Cong, W. S. Yang, *Chem. Commun.* **2002**, 1468–1469; e) H. Q. Jiang, F. Y. Liang, O. Czuprat, K. Efimov, A. Feldhoff, S. Schirrmeister, T. Schiestel, H. H. Wang, J. Caro, *Chem. Eur. J.* **2010**, *16*, 7898–7903; f) H. Q. Jiang, L. Xing, O. Czuprat, H. H. Wang, S. Schirrmeister, T. Schiestel, J. Caro,

© 2011 Wiley-VCH Verlag GmbH & Co. KGaA, Weinheim

Chem. Commun. **2009**, 6738–6740; g) J. Pérez-Ramírez, B. Vigeland, *Angew. Chem.* **2005**, *117*, 1136–1139; *Angew. Chem. Int. Ed.* **2005**, *44*, 1112–1115.

[3] a) H. H. Wang, S. Werth, T. Schiestel, J. Caro, *Angew. Chem.* **2005**, *117*, 7066–7069; *Angew. Chem. Int. Ed.* **2005**, *44*, 6906–6909; b) G. A. Richards, K. H. Casleton, B. T. Chorpening, *Proc. IMechE Part A* **2005**, *219*, 121–126; c) S. Rezvani, Y. Huang, D. McIlveen-Wright, N. Hewitt, J. D. Mondol, *Fuel* **2009**, *88*, 2463–2472; d) B. J. P. Buhre, L. K. Elliott, C. D. Sheng, R. P. Gupta, T. F. Wall, *Prog. Energy Combust. Sci.* **2005**, *31*, 283–307.

[4] a) W. J. Jin , C. Zhang, X. F. Chang, Y. Q. Fan, W. H. Xin, N. P. Xu, *Environ. Sci. Technol.* **2008**, *42*, 3064–3068; b) W. Q. Jin, C. Zhang, P. Zhang, Y. Q. Fan, N. P. Xu, *AIChE J.* **2006**, *52*, 2545–2550.

[5] a) C. S. Chen, S. J. Feng, S. Ran, D. C. Zhu, W. Liu, H. J. M. Bouwmeester, *Angew. Chem.* **2003**, *115*, 5354–5356; *Angew. Chem. Int. Ed.* **2003**, *42*, 5196–5198; b) X. Y. Tan, Y. T. Liu, K. L, *AIChE J.* **2005**, *51*, 1991–2000; c) Z. P. Shao, W. S. Yang, Y. Cong, H. Dong, J. H. Tong, G. X. Xiong, *J. Membr. Sci.* **2000**, *172*, 177–188.

[6] a) H. H. Wang, C. Tablet, A. Feldhoff, J. Caro, *Adv. Mater.* **2005**, *17*, 1785–1788; b) X. F. Zhu, H. H. Wang, W. S. Yang, *Chem. Commun.* **2004**, 1130–1131; c) K. Watenabe, M. Yuasa, T. Kida, Y. Teraoka, N. Yamazoe, K. Shimanoe, *Adv. Mater.* **2010**, *22*, 2367–2370; d) K. Efimov, T. Halfer, A. Kuhn, P. Heitjans, J. Caro, A. Feldhoff, *Chem. Mater.* **2010**, *22*, 1540–1544.

[7] a) J. Martynczuk, K. Efimov, L. Robben, A. Feldhoff, *J. Membr. Sci.* **2009**, *344*, 62–70; b) M. Arnold, H. H. Wang, A. Feldhoff, *J. Membr. Sci.* **2007**, *293*, 44–52.

[8] J. Beckers, G. Rothenberg, *ChemPhysChem* **2005**, *6*, 223–225.

[9] C. Zhang, X. Chang, Y. Fan, W. Jin, N Xu, *Ind. Eng. Chem. Res.* **2007**, *46*, 2000–2005.

[10] a) I. Kagomiya, T. Iijima, H. Takamura, *J. Membr. Sci.* **2006**, *286*, 180–184; b) S. G. Lia, W. Q. Jin, N. P. Xu, J. Shi, *J. Membr. Sci.* **2001**, *186*, 195–204; c) J. Sunarso, S. Baumann, J. M. Serra, W. A. Meulenberg, S. Liu, Y. S. Lin, J. C. Diniz da Costa, *J. Membr. Sci.* **2008**, *320*, 13–41.

[11] K. Wu, S. Xie, G. S. Jiang, W. Liu, C. S. Chen, *J. Membr. Sci.* **2001**, *188*, 189–193.

[12] a) F. T. Akin, Y. S. J. Lin, *J. Membr. Sci.* **2004**, *231*, 133–146; b) J. Kim, Y. S. Lin, *J. Membr. Sci.* **2000**, *167*, 123–133.

[13] J. E. ten Elshof, N. Q. Nguyen, M. W. den Otter, H. J. M. Bouwmeester, *J. Electrochem. Soc.* **1997**, *144*, 4361–4366.

[14] K. Kobayashi, T. Tsunoda, *Solid State Ionics* **2004**, *175*, 405–408.

[15] C. S. Chen, Ph.D. Thesis, University of Twente, The Netherlands, **1994**.

[16] a) V. V. Kharton, A. V. Kovalevsky, A. P. Viskup, F. M. Figueiredo, A. A. Yaremchenko, E. N. Naumovich, F. M. B. Marques, *J. Electrochem. Soc.* **2000**, *147*, 2814–2821; b) A. L. Shaula, V. V. Kharton, F. M. B. Marques, *J. Electrochem. Soc.* **2004**, *24*, 2631–2639; c) V. V. Kharton, A. V. Kovalevsky, A. P. Viskup, A. L. Shaula, F. M. Figueiredo, E. N. Naumovich, F. M. B. Marques, *Solid State Ionics* **2003**, *160*, 247–258.

[17] a) Q. M. Li, X. F. Zhu, W. S. Yang, *J. Membr. Sci.* **2008**, *325*, 11–15; b) X. F. Zhu, Q. M. Li, Y. Cong, W. S. Yang, *Catal. Commun.* **2008**, *10*, 309–312; c) H. H. Wang, W. S. Yang, Y. Cong, X. F. Zhu, Y. S. Lin, *J. Membr. Sci.* **2003**, *224*, 107–115.

[18] a) J. X. Yi, Y. B. Zuo, W. Liu, L. Winnubst, C. S. Chen, *J. Membr. Sci.* **2006**, *280*, 849–855; b) W. Li, T. F. Tian, F. Y. Shi, Y. S. Wang, C. S. Chen, *Ind. Eng. Chem. Res.* **2009**, *48*, 5789–5793; c) B. Wang, M. Zhan, D. C. Zhu, W. Liu, C. S. Chen, *J. Solid State Electrochem.* **2006**, *10*, 625–628; d) W. Li, J. J. Liu, C. S. Chen, *J. Membr. Sci.* **2009**, *340*, 266–271.

[19] a) K. Efimov, M. Arnold, J. Martynczuk, A. Feldhoff, *J. Am. Ceram. Soc.* **2008**, *92*, 876–880; b) A. Feldhoff, M. Arnold, J. Martynczuk, T. M. Gesing, H. Wang, *Solid State Sci.* **2008**, *10*, 689–701.

[20] S. Liu, R. Ma, R. Jiang, F. Luo, *J. Cryst. Growth* **1999**, *206*, 88–92.

[21] X. F. Zhu, H. H. Wang, W. S. Yang, *J. Membr. Sci.* **2008**, *309*, 120–127.

[22] a) J. A. Lane, J. A. Kilner, *Solid State Ionics* **2000**, *136–137*, 927–932; b) K. Yashiro, S. Onuma, A. Kaimai, Y. Nigara, T. Kawada, J. Mizusaki, K. Kawwamura, T. Horita, H. Yokokawa, *Solid State Ionics* **2002**, *152–153*, 469–476; c) J. E. ten Elshof, H. J. M. Bouwmeester, H. Verweij, *Solid State Ionics* **1996**, *89*, 81–92.

[23] J. H. Tong, W. S. Yang, B. C. Zhu, R. Cai, *J. Membr. Sci.* **2002**, *203*, 175–189.

[24] V. V. Kharton, E. V. Tsipis, E. N. Naumovich, A. Thursfield, M. V. Patrakeev, V. A. Kolotygin, J. C. Waerenborgh, I. S. Metcalfe, *J. Solid State Chem.* **2008**, *181*, 1425–1433.

Publications and contributions to conferences

Publications included in this work (in chronological order)

(1)   Performance of zinc-doped perovskite-type membranes at intermediate temperatures for long-term oxygen permeation and under a carbon dioxide atmosphere
J. Martynczuk, K. Efimov, L. Robben, and A. Feldhoff
Journal of Membrane Science 334 (2009) 62-70.

(2)   Novel cobalt-free oxygen-permeable perovskite-type membrane
K. Efimov, T. Halfer, A. Kuhn, P. Heitjans, J. Caro, and A. Feldhoff
Chemistry of Materials 22 (2010) 1540-1544.

(3)   Transmission electron microscopy study of $Ba_{0.5}Sr_{0.5}Co_{0.8}Fe_{0.2}O_{3-\delta}$ perovskite decomposition at intermediate temperatures
K. Efimov, Q. Xu, and A. Feldhoff
Chemistry of Materials 22 (2010) 5866-5875.

(4) CO_2-stable and cobalt-free dual-phase membrane for oxygen separation
H. Luo, K. Efimov, H. Jiang, A. Feldhoff, H. Wang, and J. Caro
Angewandte Chemie International Edition 123 (2011) 785-789.

(5)   *In-situ* X-ray diffraction study of carbonate formation and decomposition in perovskite-type BCFZ
K. Efimov, O. Czuprat, and A. Feldhoff
Journal of Solid State Chemistry 184 (2011) 1085–1089.

(6)   Oxygen-vacancy related structural phase transition of $Ba_{0.8}Sr_{0.2}Co_{0.8}Fe_{0.2}O_{3-\delta}$
Z. Yáng, J. Martynczuk, K. Efimov, A.S. Harvey, A. Infortuna, P. Kocher, and L.J. Gauckler,
Chemistry of Materials 23 (2011) 3169-3175.

(7)   Ca-containing CO_2-tolerant perovskite materials for oxygen separation
K. Efimov, T. Klande, N. Juditzki, and A. Feldhoff,
Journal of Membrane Science (submitted, Mai 2011).

Publications not included in this work

(8)   Grain boundaries as barrier for oxygen transport in perovskite-type membranes
M. Arnold, J. Martynczuk, K. Efimov, H. Wang, and A. Feldhoff
Journal of Membrane Science 316 (2008) 137–144.

(9)   Crystalline intermediate phases in the sol gel-based synthesis of $La_2NiO_{4+\delta}$
      K. Efimov, M. Arnold, J. Martynczuk, and A. Feldhoff
      Journal of the American Ceramic Society 92 (2009) 876-880.

(10) Preparation and hydrogen permeation of $BaCe_{0.95}Nd_{0.05}O_{3-\delta}$ membranes
      M. Cai, S. Liu, K. Efimov, J. Caro, A. Feldhoff, and H. Wang
      Journal of Membrane Science, 343 (2009) 90-96.

(11) Hydrogen production by water dissociation in surface-modified $BaCo_xFe_yZr_{1-x-y}O_{3-\delta}$ hollow-fiber membrane reactor with improved oxygen permeation
      H. Jiang, F. Liang, O. Czuprat, K. Efimov, A. Feldhoff, S. Schirrmeister, S. Schiestel, H. Wang, and J. Caro
      Chemistry-a European Journal 16 (2010) 7898-7903.

(12) CO_2-stabile und cobaltfreie Zweiphasenmembranen zur Sauerstoffabtrennung
      H. Luo, K. Efimov, H. Jiang, A. Feldhoff, H. Wang, and J. Caro
      Angewandte Chemie 123 (2011) 785-789.

(13) Access to metastable complex ion conductors via mechanosynthesis: Preparation, microstructure and conductivity of $(Ba,Sr)LiF_3$ with inverse perovskite structure
      A. Düvel, K. Efimov, A. Feldhoff, P. Heitjans, S. Wegner, M. Wilkening
      Journal of Materials Chemistry 21 (2011) 6238-6250.

(14) Influence of the Preparation methods on the microstructure and oxygen permeability of a CO_2-stable dual phase membrane
      H. Luo, H. Jiang, K. Efimov, and J. Caro
      AIChE Journal, 57 (2011) 2738-2745.

(15) CO_2-tolerant oxygen-permeable Fe_2O_3-$Ce_{0.9}Gd_{0.1}O_{2-\delta}$ dual-phase membranes
      H. Luo, H. Jiang, K. Efimov, F. Liang, H. Wang, and J. Caro
      Industrial and engineering chemistry research, (submitted, March 2011).

(16) CO_2-stable MIEC $La_2Ni_{0.9}(M_{0.1})O_{4+\delta}$ membrane materials
      T. Klande, K. Efimov, and A. Feldhoff
      Proceedings of the 12th Conference of the European Ceramic Society – ECerS XII Stockholm, Sweden – 2011.

(17) Effect of doping and microstructure on CO_2-stable La_2NiO_{4+d}-based oxygen transporting materials
      T. Klande, K. Efimov, S. Cusenza, K.D. Becker, and A. Feldhoff
      Journal of Solid State Chemistry, (accepted, October 2011).

(18) Gasphasensynthese von Core/Shell-Partikeln
      B. Poller, K. Efimov, A. Feldhoff, M. Binnewies
      Chemie Ingenieur Technik (submitted, August 2011)

Contributions to conferences

(1)   Crystalline intermediate phases in the sol-gel synthesis of the mixed ionic-electronic conductor $La_2NiO_{4+\delta}$ studied by transmission electron microscopy and X-ray diffraction
K. Efimov*, M. Arnold, J. Martynczuk, and A. Feldhoff
Poster, *Electroceramics XI*, Manchester, 31 August-03 September 2008.

(2)   Stability of oxygen-ion and electron mixed conducting perovskite-based ceramics at intermediate and high temperatures
A. Feldhoff*, K. Efimov, and M. Arnold
Talk, *11th ECerS Conference and Exhibition*, Cracow, 21–25 Juni 2009.

(3)   TEM study of the BSCF perovskite decomposition at intermediate temperature
K. Efimov*, M. Arnold, and A. Feldhoff
Talk, *42nd IUPAC Congress*, Glasgow, 2-7 August 2009.

(4)   Decomposition process of a high-performance perovskite at intermediate temperatures studied by analytical TEM
A. Feldhoff*, K. Efimov, M. Arnold, Q. Xu, and F. D. Tichelaar
Poster, *Microscopy Conference MC2009*, Graz 30 August-4 September 2009.

(5)   TEM Study of the BSCF perovskite decomposition at intermediate temperature
K. Efimov*, M. Arnold, and A. Feldhoff
Talk, *Euromat 2009*, Glasgow, 7-10 September 2009.

(6)   *In-situ* electron energy-loss spectroscopy of cobalt and iron valences in a mixed conducting perovskite and the correlation to a phase decomposition at intermediate temperatures
A. Feldhoff*, K. Efimov, M. Arnold, Q. Xu, F. D. Tichelaar
Poster, *Bunsen Kolloquium*, Hannover, 24-25 September 2009.

(7)   Phasenstabilität von Perowskiten für Membranen zur Sauerstoffabtrennung
A. Feldhoff*, K. Efimov, Q. Xu
Poster, *Bunsentagung2010*, Bielefeld, 13-15 Mai 2010.

(8)   Novel cobalt-free oxygen-permeable perovskite-type membranes
K. Efimov* and A. Feldhoff
Talk, *Electroceramics XII*, Trondheim, 13-16 Juni 2010.

(9)   Grain boundaries as barriers to the oxygen transport in perovskitetype membranes
A. Feldhoff*, K. Efimov, T. Klande, J. Martynczuk
Talk, *Electroceramics XII*, Trondheim, 13-16 Juni 2010.

(10) Effect of doping and grain size on oxygen permeation of $La_2NiO_{4+\delta}$-based mixed conducting ceramics
A. Feldhoff*, T. Klande, and K. Efimov,
Talk*, Solid State Ionics 18*, Warsaw, 3-8 July 2011.

(11) CO_2-stable mixed ionic electronic conducting $La_2Ni_{0.9}(M_{0.1})O_{4+d}$ membrane materials
T. Klande*, K. Efimov, and A. Feldhoff,

Talk*, 12th International Conference and Exhibition of the European Ceramic Society*, Stockholm 19-23 June 2011..

Curriculum Vitale

Personal data

Name	Konstantin Efimov
Date of birth	29th/March/1980
Place of birt	Ivanovo, Russia
Nationality	German
Marital status	married, two children

Higher Education

06/2011
Leibniz Universität Hannover
Naturwissenschaftliche Fakultät
Submission of the doctoral thesis:
"Mixed oxygen ionic and electron-conducting perovskite oxides: issues and possible solutions"

06/2008-05/2011
Leibniz Universität Hannover
Institut für Physikalische Chemie und Elektrochemie
Scientific co-worker at the group of Priv. Doz. Dr. Armin Feldhoff.

10/2003-05/2008
Leibniz Universität Hannover,
Chemistry Degree: Diplom-Chemiker
Diploma thesis: „Festkörperchemische Untersuchungen zur Sol-Gel-gestützten Synthese des gemischtleitenden $La_2NiO_{4+\delta}$"

09/1997-10/2001
Ivanovo State University of Chemistry and Technology
Student of chemical technology

Awards

12/2008
Award of Christian-Kuhlemann-Foundation
Award for an excellent performance within the chemistry degree course and for a special social commitment

Education

09/1987-06/1997
Secondary School, Ivanovo
Degree: baccalaureate

.

Erklärung zu dieser Dissertation

Hiermit erkläre ich, dass ich die vorliegende Dissertationsschrift selbstständig verfasst und alle benutzten Hilfsmittel sowie zur Hilfeleistung herangezogene Institutionen vollständig angegeben habe.

Diese Dissertation wurde nicht schon als Diplom- oder ähnliche Prüfungsarbeit verwendet.

Hannover, den